UNIVERSITY OF TRENTO

DOCTORAL SCHOOL IN PHYSICS

XXIX cycle

Wettability of graphitic materials and development of graphene layer as barriers to prevent the surface degradation induced by water.

Supervisor: Dr. Nadhira Bensaada Laidani

PhD candidate: Bartali Ruben

Trento, Italy

November 2017

Acknowledgements

The author would like to thank the supervisor, Dr Nadhira Bensaada Laidani, for precious helping, for teaching for the sharing of the scientific experience. The PhD candidate sincerely appreciates the opportunity that supervisor gave to the author to developed a new scientific skill and as well as improve the scientific network. During this thesis work, the author has had the opportunity to collaborate with various national and international group as ; the group of Lamberti Andrea at the Politecnico di Torino, the group of Michal Otypkea and Martin Pykal of the University of Omoluc, and the group of Professor Ana Tavares of Institute on the National Research (INRS) Canada. All these collaborations have been stimulating, and the discussion with the scientific partners helped the authors to improve the scientific level of research and as well the standard of this PhD dissertation. Therefore Ruben Bartali would like to thank Dr Andrea Lamberti, Michal Otyepka, Martin Pikal, and Ana Tavares. The candidate would like to thank all colleagues from Functional Material and Photonic Structures from Fondazione Bruno Kessler for their support in the research activity, in particular, Gianni Coser for the technical help and the encouragements.

Ruben Bartali would like to thank Sara and Giosue and all parents who made the time more pleasant and for their moral support and encouragements.

Abstract

Graphitic materials, thanks to the lamellar structure and chemical stability, are of particular interest to realize barriers against the degradation of surface properties induced by water. Many studies showed that water could be a source of degradation of surface properties. To develop a method to overcome the problem related to the deterioration of the surface it is fundamental to study the water- material interaction. For this reason, in this thesis, the water-surface interaction of graphitic-materials and the use of graphitic materials as impermeable barriers against water were explored. Different experimental set up were realized to study the liquid-gas-solid interaction, such as time evolution of the sessile water drop contact angle, captive bubble contact angle and contact angle measurements in a controlled atmosphere. Moreover, a method of deposition of protective graphene-based films using a Meyer rod to apply graphene-inks onto a surface was developed. To understand the intrinsic wettability of graphitic materials a detailed study of the gas-liquid-solid interactions of graphite was conducted in a wide range of experimental conditions. The surface chemical properties and morphology were studied by X-ray photoelectron spectroscopy (XPS), profilometry and atomic force microscopy(AFM), sessile drop contact angle, captive bubble and secondary emission microscopy (SEM). The results of the gas-liquid–surface interaction study indicated that HOPG surface was sensitive to experimental conditions like airborne contamination and the presence of gases. Similarly, a detailed study of the interaction of water with PDMS surface in various experimental conditions (in the air and immersed in water) were conducted. The findings showed that when PDMS was immersed in water, its surface changed. In fact, the volume of air bubbles in contact with the surface of PDMS increased by increasing immersion time in the water. The experimental results indicated that such dynamic evolution of the air bubbles was related to the rearrangement of surface polymer chains via the migration of the polar groups. This phenomenon induced a degradation of the surface properties of PDMS when it is immersed in water. When graphene monolayer was added to PDMS surface, it acted as a barrier against water, suppressing the dynamic evolution of the bubble. We studied the protective properties also of graphene-based films deposited on lead (Pb). We observed that Pb surface degradation occurred when Pb was in contact with a drop of water. The results showed that degradation of Pb surface in contact with water happened very rapidly but graphene-based films, in particular, graphene oxides films, were able to reduce degradation of the surface significantly.

Contents

1. Introduction and motivation

Everyday matter is in contact with water and air, sometimes this interaction is useful from an aesthetic point of view, like dew on the leafs, sometimes it is necessary as in fish respiration, and sometimes it is at the origin of practical problems as corrosion [1,2,3]. For all these reasons humanity has been attracted by the observation of liquid-solid interaction, as extensively reported in literature, for instance from Talete (philosopher), Galileo (scientist), D'Annunzio (poet) to Young (scientist). In the last century, scientific studies have been focused on the interaction of water drops on a surface in air environment because it represents a working condition which can be found in many real applications as water drops on the windows. In 1805 Thomas Young studied the interaction of a drop of water on a surface and described mathematically this interaction as a mechanical equilibrium between three interfacial tensions: solid-liquid, liquid gas and gas-solid. Wenzel in 1936 studied the influence of roughness on wettability and demonstrated that intrinsic wetting of a surface is different from that of a rough surface. In 1944 Cassie and Baxter described the self-cleaning properties of the lotus leaf, and they explained the fundamental role of micro- and nanobubbles entrapped between the drop and the surface to obtain hydrophobic surfaces. Between the '50 and '80 using a pure liquid drop as a probe, different methods have been developed to determine the thermodynamic properties of surfaces as surface free energy and to determine the polar and the dispersive components of the surface. The mains study have been done by Fowkes [4], Owens-Wendt [5], Van Oss Chaundry and Good [6]. After 2000, using nanotechnologies, the researchers have extensively studied the fabrication of artificial self-cleaning surfaces and the active effect on wettability induced by the light on the surface of specific type ceramic as TiO_2 (photoactivity) [7]. In the last five years, the broad use of graphene and the 2D materials in many field have renovated the interest on the wetting properties of a surface and as results the intrinsic wettability of graphite has been actively studied, e.g. by Rafiee, Kozbial, Li, Wei, but some results are still debated e.g the graphene wetting transparency [8,9,10]. Similarly to the interaction of the drop with a surface the system composed by a bubble of gas in contact with a surface immersed in liquid media is significant from a technological point of view [11]. The avoidance of the intravascular gas bubbles, (embolism) for instance, is vital to health because it is one of the leading causes of neurocognitive dysfunction in cardiopulmonary surgery [12]. In Europe 1.1 million persons die for pathologies related to embolism like venous thromboembolism (Cohen et al., 2007). One person dies each 30 second. A deep comprehension of the interaction of gas bubbles with a surface could be vital to developing strategies and materials as well as biomedical devices that can reduce this risk

factor. Another interesting example where the bubbles in contact with a surface could play an important role is in the direct methanol fuel cell (DMFC). The behaviour of the CO_2 bubbles in anode channels of DMFC is essential to improve the performance of fuel cells [13]. Unfortunately, the adhesion of the gas bubbles on a material immersed in water is not entirely understood; an example is the unexpected nanobubbles stability on graphite surface immersed in water [14].

One of the most important phenomena where the gas-liquid-solid interaction is extremely important is the degradation of surface induced by water. Water, in fact, can induce the degradation of the surface of materials in many different paths like absorption, hydrolysis, dissolution of the components and corrosion. For that reason, in many applications, it is vital to develop a thin barrier to protect the surface of materials by degradation induced by water. Many methods are used to protect the surface of materials against the degradation, such as painting using varnishing, deposition of thick and thin coating as well as passivation of the surface [15-18] . However, the use single layer of graphite, graphene is one of the most interesting ways because graphene could be the thinnest barrier against corrosion.[19].

For these reasons, the thesis is focalized on the study of wetting on graphitic materials in different experimental conditions and the development of protective barriers based on graphitic materials against water degradation. Particular interest was dedicated to correlate the fundamental study and the potentials applications of graphitic materials as impermeable barriers against water. In the first part of the dissertation, we will pay attention to the interaction of the different liquid and gases with highly oriented pyrolytic graphite (HOPG) and nano-graphite. HOPG is an interesting material because it is widely used in many applications such as electrodes, and it is the fundamental material to realise a wide range of graphitic materials, nano graphite and graphene [16]. Moreover, HOPG shows a well-defined honeycomb structure, and by exfoliation, it is quite easy to realise a surface in a controlled mode [20]. For this reason, we used HOPG as an excellent model surface to study the interaction of the graphitic material with pure liquids and gases in a controlled environment [21]. Particular attention was dedicated to the investigation of the interaction of HOPG with water with a vast number of solvents and using monoatomic and diatomic gases (He,Ar, N_2, Air,H_2). The effect of the morphological nano-structuring was studied. Particular interest was dedicated to the role of Lifshitz -Van der Waals interaction on graphite surfaces. Under the experimental point of view, two set-ups were realised to improve the description of the physicochemical surface properties: a) contact angle measurements by captive bubble method to study gas –solid-liquid interaction b) study of liquid-surface interaction in a controlled atmosphere.

In the second part of the dissertation, we will investigate the degradation of polydimethylsiloxane

(PDMS) in water. PDMS, in fact, show surface properties similar to those of graphite because it is a dispersive surface even if the structure and the chemical composition of PDMS is different. A comparison water-surface interaction between PDMS, graphite and on single-layer graphene deposited on PDMS surface was explored. X-ray photoelectron spectroscopy (XPS) analysis allowed determining the elemental surface composition while Raman spectroscopy was used to assess the effectiveness of graphene monolayer transfer on PDMS. Atomic force microscopy (AFM) was used to study the surface modification of samples immersed in water. The surface wettability was investigated by sessile drop contact angle measurements and the stability of gas bubbles on the surfaces was determined by captive bubble contact angle (CCA) measurements. CCA measurements showed that air bubbles on graphite surface exhibited a stable behaviour while on PDMS they underwent a dynamic phenomenon. Indeed, the air bubble volume on the PDMS rose by increasing immersion time in the water. The experimental results indicated that the dynamic evolution of air bubbles in contact with PDMS was related to the rearrangement of surface polymer chains via the migration of polar groups and this induced a degradation of the surface properties of PDMS. Therefore, the protection of PDMS using a single layer of graphite, graphene, against water degradation was studied. When graphene monolayer wass present on PDMS it acted as barrier, suppressing the dynamic evolution of the bubbles and preserving the surface of PDMS from any degradation process as well as preserving the optical transparency.

Finally, we investigated the barrier properties of graphene layers deposited on lead (Pb) using a simple method based on graphene inks [22]. The graphene-based inks were developed using graphene oxide, graphene and their mixture using a non- toxic solvent. We described the corrosion effects of water drops on Pb surface and particular interest was focused on the method for a qualitative estimation of the surface reactivity-degradation using sessile drop contact angle and profilometry. The physical and chemical properties of the films deposited on Pb will be reported and in particular the protective effect of the membranes on lead (Pb) surfaces against water corrosion will be discussed.

Reference

1. Zhang M, Feng S, Wang L, Zheng Y. Lotus effect in wetting and self-cleaning. *Biotribology*. 2015:1-13. doi:10.1016/j.biotri.2015.08.002.

2. Akanyeti O, Thornycroft PJM, Lauder G V., Yanagitsuru YR, Peterson AN, Liao JC. Fish optimize sensing and respiration during undulatory swimming. *Nat Commun*. 2016;7:11044. doi:10.1038/ncomms11044.

3. Kantürk Figen A, Coşkuner Filiz B. Hydrogen production by the hydrolysis of milled waste magnesium scraps in nickel chloride solutions and nickel chloride added in Marmara Sea and Aegean Sea Water. *Int J Hydrogen Energy*. 2015;40(46):16169-16177. doi:10.1016/j.ijhydene.2015.07.170.

4. Restolho J, Mata JL, Saramago B. On the interfacial behavior of ionic liquids: surface tensions and contact angles. *J Colloid Interface Sci*. 2009;340(1):82-86. doi:10.1016/j.jcis.2009.08.013.

5. Rudawska A, Jacniacka E. Analysis for determining surface free energy uncertainty by the Owen–Wendt method. *Int J Adhes Adhes*. 2009;29(4):451-457. doi:10.1016/j.ijadhadh.2008.09.008.

6. Van Oss CJ, Chaudhury MK, Good RJ. Interfacial Lifshitz-van der Waals and polar interactions in macroscopic systems. *Chem Rev*. 1988;88(6):927-941. doi:10.1021/cr00088a006.

7. Rico V, López C, Borrás A, Espinós JP, González-Elipe AR. Effect of visible light on the water contact angles on illuminated oxide semiconductors other than TiO2. *Sol Energy Mater Sol Cells*. 2006;90(17):2944-2949. doi:10.1016/j.solmat.2006.05.005.

8. Kozbial A, Li Z, Sun J, et al. Understanding the intrinsic water wettability of graphite. *Carbon N Y*. 2014;74:218-225. doi:10.1016/j.carbon.2014.03.025.

9. Li Z, Wang Y, Kozbial A, et al. Effect of airborne contaminants on the wettability of supported graphene and graphite. *Nat Mater*. 2013;12(10):925-931. doi:10.1038/nmat3709.

10. Wei Y, Jia CQ. Intrinsic wettability of graphitic carbon. *Carbon N Y*. 2015;87:10-17. doi:10.1016/j.carbon.2015.02.019.

11. Zhao C, Liu Y, Zhao Y, Fang N, Huang TJ. A reconfigurable plasmofluidic lens. *Nat Commun*. 2013;4:2305. doi:10.1038/ncomms3305.

12. Suzuki A, Eckmann DM. Embolism Bubble Adhesion Force in Excised Perfused. *Anesthesiology*. 2003;99:400-408.

13. Liao Q, Zhu X, Zheng X, Ding Y. Visualization study on the dynamics of CO2 bubbles in anode channels and performance of a DMFC. *J Power Sources*. 2007;171(2):644-651. doi:10.1016/j.jpowsour.2007.06.257.

14. Sun Y, Xie G, Peng Y, Xia W, Sha J. Stability theories of nanobubbles at solid–liquid interface: A review. *Colloids Surfaces A Physicochem Eng Asp*. 2016;495:176-186. doi:10.1016/j.colsurfa.2016.01.050.

15. Wang B, Cunning B V., Park S-Y, Huang M, Kim J-Y, Ruoff RS. Graphene Coatings as Barrier Layers to. *ACS Nano*. 2016;10:9797-9800. doi:10.1021/acsnano.6b04363.

16. Laidani N, Bartali R, Gottardi G, Anderle M, Chuste G, Bellachioma C. Production and characterization of thin a-C:(H) films for gas permeation barrier functionality against He,

CO(2), N(2), O(2) and H(2)O. *J Phys Condens Matter*. 2006;18(26):5945-5959. doi:10.1088/0953-8984/18/26/014.

17. Shan CX, Hou X, Choy K. Corrosion resistance of TiO 2 films grown on stainless steel by atomic layer deposition. 2008;202:2399-2402. doi:10.1016/j.surfcoat.2007.08.066.

18. Sathiyanarayanan S, Muthukrishnan S, Venkatachari G, Trivedi DC. Corrosion protection of steel by polyaniline (PANI) pigmented paint coating. 2005;53:297-301. doi:10.1016/j.porgcoat.2005.03.007.

19. Wang B, Cunning B V., Par S-Y, Huang M, Kim J-Y, Ruoff RS. Graphene Coatings as Barrier Layers to Prevent the Water-Induced Corrosin of Silicate Glass. *ACS Nano*. 2016;10:9794-9800. doi:10.1021/acsnano.6b04363.

20. Cai M, Thorpe D, Adamson DH, Schniepp HC. Methods of graphite exfoliation. *J Mater Chem*. 2012;(November):24992-25002. doi:10.1039/c2jm34517j.

21. Jeloaica L, Sidis V. DFT investigation of the adsorption of atomic hydrogen on a cluster-model graphite surface. *Chem Phys Lett*. 1999;300(1-2):157-162. doi:10.1016/S0009-2614(98)01337-2.

22. Van Nguyen C, Bartali R, Crema L, Speranza G. Effect of glass surface treatments on the deposition of highly transparent reduced graphene oxide films by dropcasting method. *Colloids Surfaces A Physicochem Eng Asp*. 2016;498:231-238. doi:10.1016/j.colsurfa.2016.03.051.

2. Scientific background and literature survey

2 Introduction

This thesis is focused on the study of the wettability properties of the graphitic materials and how to use the intrinsic impermeable properties of graphitic materials to protect the surface against degradation induced by water. In this chapter, after a brief overview on graphitic materials, a literature review will be given on a) theory about water surface interaction, b) the degradation of surfaces induced by water and c) barrier layers against water degradation. Water surface interaction, in fact, is crucial for many fields such as self-cleaning surfaces, micro/nanofluidics, capillarity, fundamental studies of thermodynamic properties of surfaces, corrosion, barrier coatings, biocompatibility[1-16]. The interaction of water with surfaces can be passive, a typical case of impermeable surfaces (e.g. that of carbon materials) [17,18,] or active, e.g. in differential aeration corrosion or surface modification induced by water on polymers. The basic concept of interpretation of passive liquid-solid interaction was introduced in 1805 by Thomas Young who studied the interaction of a drop of water on a surface and described this interaction mathematically as the mechanical equilibrium of the three interfacial tensions; solid-liquid, liquid gas and gas-solid. After year 2000, using nanotechnologies, the researchers started to study the active interaction of water with a surface as under the effect of light on the surface wettability of ceramic as TiO_2. The active wettability under UV light illumination was studied because of the great interest in many applications as photovoltaics and photocatalysis [19]. In the last five years, the influence of 2D materials as graphene on the wetting properties of a surface and the intrinsic wettability of graphite as well as the graphene transparency were actively studied, [20,21,18] but the results are still debated. A tremendous scientific interest in water-surface interaction has been continuously renewed in the scientific community as demonstrated by the fundamental studies of the wetting theory of textured surfaces by of small droplets reported by Kim *et al.*[22]. The study of the interaction of water with a surface is crucial, and for this reason, in this chapter, we will describe how a solid-liquid interaction can be characterized under different points of view: empirical, chemical and physical. In the last part, we describe how the water can degrade the surface properties and the primary strategies reported in the literature to reduce the degradation process induced by water.

2.1.1. Graphitic materials

Carbon belongs to the fourth group, and the second period of the periodic table of Mendeleev,

therefore, it occupies an intermediate position between metals and non-metal typical, figure 2.1. This position allows carbon to combine with electropositive and electronegative elements, resulting in hydrocarbons and halides of the same stability. Free state in nature is present as diamond, graphite and fullerene. The atomic number is 6, and the atomic weight is 12,011 [23]. Carbon form materials with very different properties, like diamond, methane and acetylene. Despite the electronic ground state of carbon being $1s^2$, $2s^2$ $2p^2$ the energetic advantage is gained from involving all four outer orbital electrons in bonding between other atoms or carbon atom themselves, figure [24,25,26].

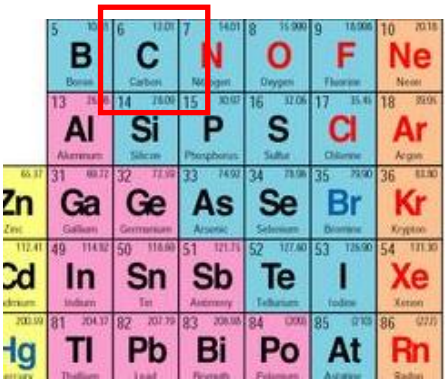

Figure 2.1 Carbon in Mendeleyev element table

Carbon forms a broad variety of crystalline and disordered structures because it can exist in three hybridisation sp^3,sp^2 and sp^1. In the sp^3 configuration as in diamond a carbon atom's four valence electrons are each assigned to tetragonally directed sp^3 orbital which makes strong sigma bond to an adjacent atom, In the sp^2 one of the 2s orbital electrons has been promoted to a 2p orbital, combine with each other only three orbitals to form three equivalent orbitals hybridised sp^2. These orbitals stay on a plane and are divided into the corners of an equilateral triangle. The angle that is formed is 120°, to minimise the electronic repulsion. The valence electron, which has not been let said "used", is in the orbital 2p, whose axis is perpendicular to the plane of the three sp^2 hybrids. The carbon-carbon double bond consists of a bond σ and a bond π. The two electrons of the link σ are along the line joining the nuclei while those of the link π is located in an area of the space arranged above and below the plane defined by two carbon atoms and four atoms linked to them. With this type of electronic structure, the angle between the orbital is 120°, the allotropic form of carbon that typically presents this bond is graphite. In the sp1 hybridization two of the four valence electrons enter sigma orbitals each forming a sigma bond directed along the ±x axis and other two-electron enter in pπ orbitals in the y and z-direction [27]

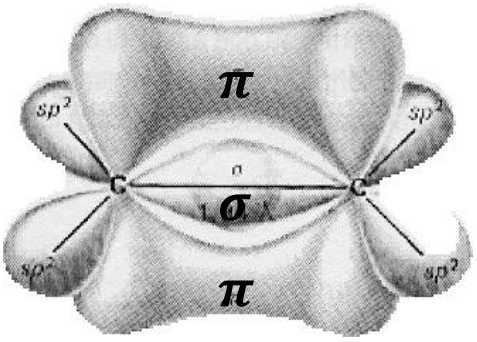

Figure 2.2 A trigonal carbon atom with three sp² orbital's that are on the same plane and at angles of 120° between them.

2.1.2 Graphite

Graphite consists of crystallised carbon with sp^2 hybridization in a stable phase at ambient pressure. Graphite is crystallized in the trigonal system in the form of solid with a lamellar structure. Natural graphite is soft to touch, has dark grey or black colour, its specific gravity is 2.2 gr/cm[3,28] and has a hardness of 1,5 Mohs that corresponds to an indentation hardness 100 MPa(Vickers), Figure2.3. (Diamond, for instance, have and hardness of 100 Gpa [29,30]. The natural graphite is softer of Gypsum and Talc due to the weaker interaction between the graphite layer, but as observed by Wolf the hardness of graphite in the plane should be higher than 2.5 GPa [29]. The refractive index is in the range of 1.93-2.07, it is a good conductor of heat and current, and its melting point is higher than 3000°C. Acids and bases do not attack it and it burns in the presence of oxygen between 620°C and 670°C. Natural graphite should be present in a variety of forms: lamellar Flinz, and compact fibrous or amorphous form. As mentioned the crystal of graphite is formed by a set of lattice planes (called basal planes) in which the carbon atoms form a hexagonal/honeycomb network where each atom has three nearest neighbours. It has a double bond for every two single bonds, through π bond In graphite is interesting to note that the double bond is not localised, but there is a resonance, similar to what occurs in benzene. The easy mobility of electrons in the graphite structure explains the excellent conduction of graphite. The basal planes are held together by Van der Waals forces, much weaker than those of valence.

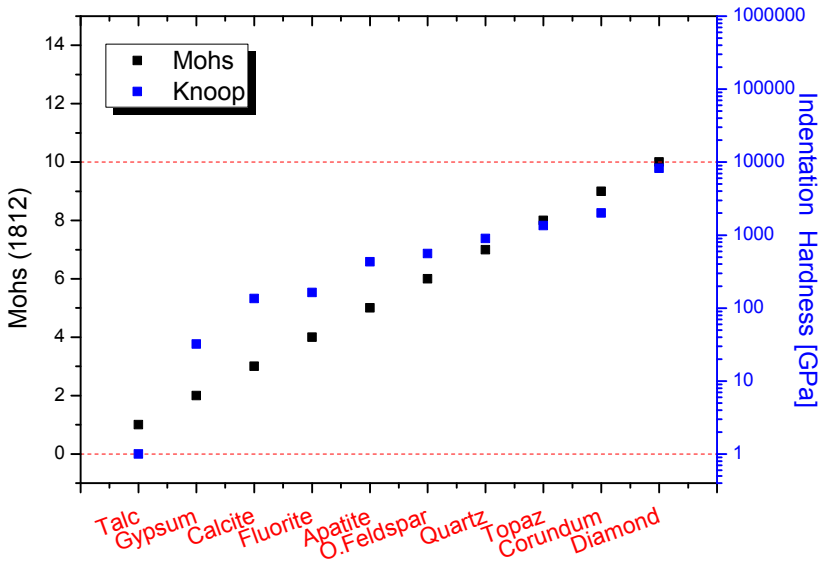

Figure 2.3 Mechanical properties of materials Mohs scale and indentation hardness, the red line indicates the hardness of graphite (the lowest) and diamond (the highest).

Due to this interplanar interaction, the graphite is particular easily to exfoliate, because the plans slip on each other. This is the origin of the low hardness of graphite, in fact even if the bond energy of C=C is 6.11 kJ mol^{-1} that is the almost the double of C-C 3.47 kJ mol. Which is the bond energy in diamond.

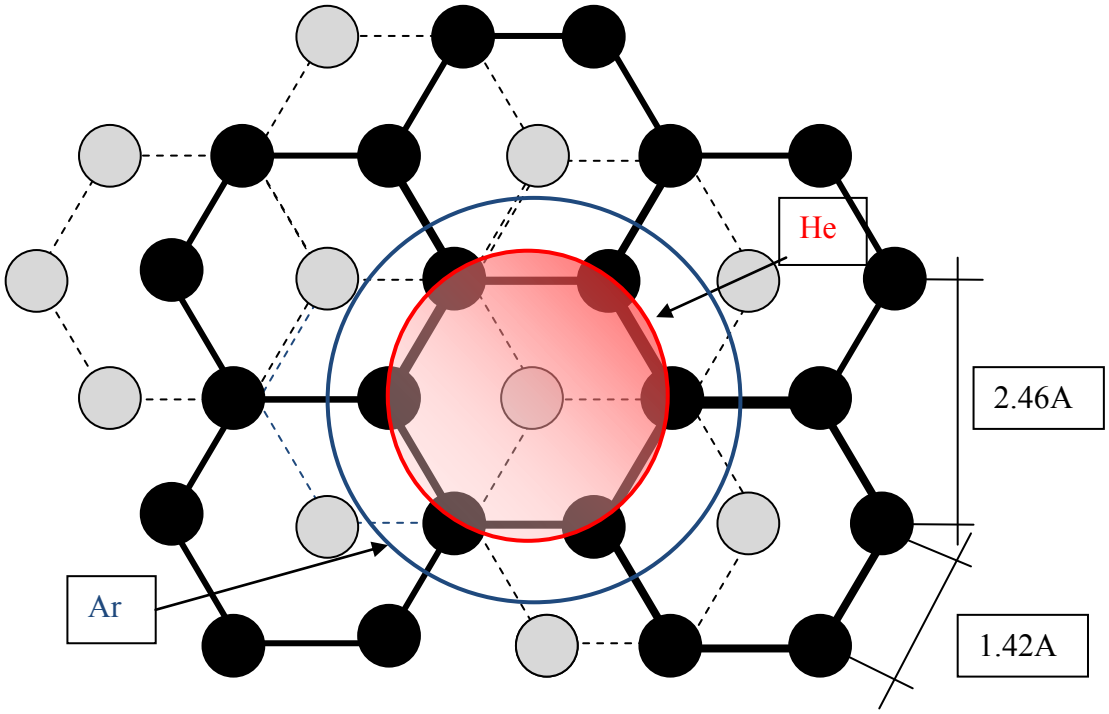

Figure 2.4 Structure of oriented graphite with the typical distance between the atom. The read sphere and the blue circle are the diameter dimension of Helium and Argon

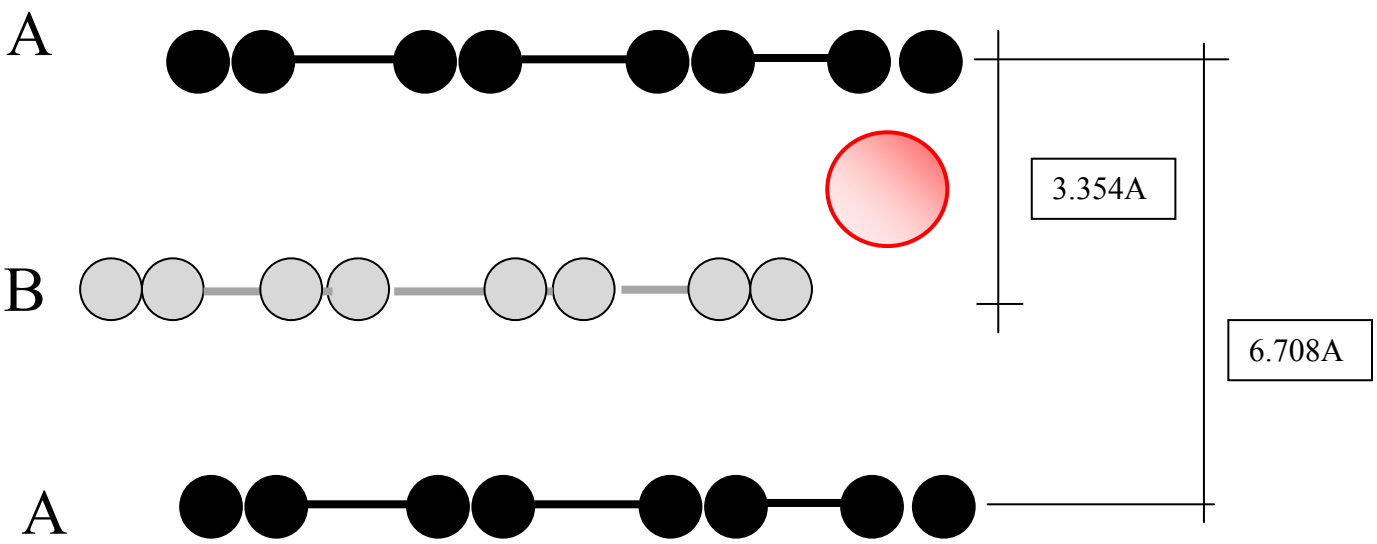

Figure 2.5 Sketch of the lamellar structure of graphite, the distance between the graphite layer are reported. The red sphere represents the diameter of helium

The distance between atom and atom in the hexagonal network is only 1.42Å, while the distance between the basal planes is 3.35Å, Figure 2.4 and Figure 2.5. The maximum diameter of the carbon ring is 246 pm, higher than the kinetic diameter of helium and hydrogen 269pm and 289pm respectively, Figure 2.4. The distance between the planes is higher than the diameter of many monoatomic and diatomic gases like CO_2 (kinetic diameter 330 pm) Figure 2.4. There are many types of available graphite, Ceylon graphite, Kish graphite, pyrolytic graphite, highly oriented pyrolytic graphite (HOPG). All these kinds of graphite have a large panel of structural defects or contaminations. To obtain a bulk piece of the well-ordered graphite, a controlled pyrolysis of an organic compound or chemical vapour deposition process at high temperature, >2500°K, are used to produce pyrolytic graphite (PG). An annealing at 3000°K at high pressure promotes a highly oriented form of graphite, named highly oriented graphite (HOPG), with a low degree of impurity, less than 10ppm and the highest degree of three-dimensional ordering. The structure of HOPG analysed by x-ray diffraction shows a low angular dispersion of c-axes, full with at half maximum, FWHM, usually less 1. The theoretical density of HOPG is 2.265 g/cm3. In many studies, due to the low level of contamination, the highly oriented structure is used as model surface [28,31,32]. HOPG bulk material shows a mosaic structure composed of different collumar structures and grain boundaries. The grains are slightly disoriented concerning each other. an angular spread of the c-axes of the crystallites is usually less than1°. The surface is composed of several dozens of lamella;

the single step has a well-defined height of 0.34 nm, The deviations of grain boundaries from the perpendicular axis give the perfectness level of HOPG samples (mosaic spread). Disorder results in the broadening of the 002 diffraction peak. The lower mosaic spread is found in a freshly cleaved surface which exhibits the smaller number of steps due to a larger size of the grains. The pencil is an example of the application of graphite, solid lubricant. In many cases, graphite is used as an additive to improve the thermal conductivity of the polymer or to increase the chemical resistance, for these reasons in many cases graphite is provided as a powder of micro graphite, nano graphite and graphene [33].

Figure 2.6 Natural graphite, graphite nanoplatelets and graphene

2.1.3 NanoGraphite and graphite nanoplatelets (GnP)

Graphite nanoplatelets (GnP) is a powder composed of graphite with a high surface area material from 100 m2 to 400 m^2/gr. GnP shows a lateral size is in the 100 nm - 500 nm range, and the thickness 10 nm - 300 nm, Figure 2.6. GnP shows excellent electrical and thermal conductivity, better than carbon black thanks to in particular to the more ordered structure [34]. Due to this properties, these nanomaterials are used to realize supercapacitors, batteries, printed electronics, solar cells and protective layers [35]. The nanographite materials are prepared by sonication of graphite in solution, by jet solution, ball milling, wet grinding and homogenizer processing [36]. Due to the relatively low cost in the production and the wide range of methods to produce the nanographite, and the opportunity to generate significant amounts, nanographite is a valuable solution to realise new materials at industrial scale and large-scale processes [37]. Graphene nanoplatelets are powder derived from graphite as nanographite but the mixture of the powder composed of flakes with a lateral width from 0,1 μm to several μm microns and a thickness from 1

to 15 layers of basal planes. This is usually synthesize by mechanical exfoliation of graphite. The surface area of graphene nanoplatelets can be higher than 500 m^2/gr [38,39,40]. Similarly to nanographite it is used to improve the electrical an thermal conductivity of materials [41,42], to support catalyst used in the fuel cells as reported by Shao et al. or [43] or used to realisze functional [44] inks for microfluidic devices.

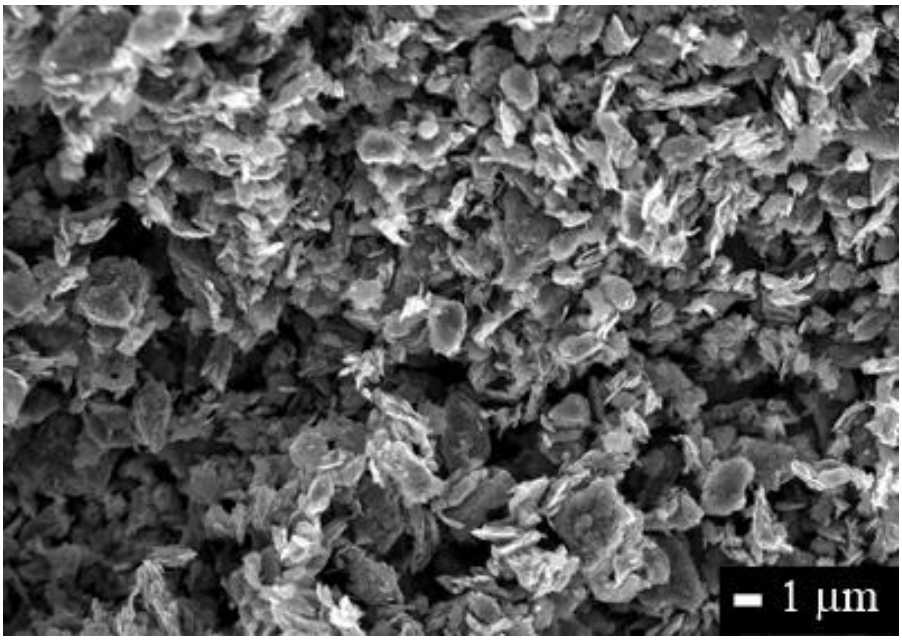

Figure 2.7 SEM image of nano graphite powder, (Graphene-supermarket supplier).

2.1.4 Graphene

The fundamental building block of 3D graphite, nano graphite and graphite nanoplatelets is graphene [45]. Graphene is a single layer of carbon packed in a hexagonal (honeycomb) lattice, with a carbon-carbon distance of 0.142 nm and a theoretical thickness of only 0.335 nm. [46]. Thanks to this structure it is considered a two-dimensional material. The physical properties of graphene are slightly different from the usual 3D materials. It is harder than steel but very stretchable. It shows a thermal conductivity much higher than that of silver; it is practically transparent, it absorbs only 2.3% of the light in the visible range [45]. Due to the excellent conductivity and high transparency, the excellent mechanical properties, it is a suitable material to realize flexible and transparent devices [47]. The extraordinary mechanical properties are due to the honeycomb structure which is considered the strongest among covalent bonds [48]. Figure 2.8 shows the 3D plot of the nearest neighbour tight – binding model (NNTB) dispersion throughout the Brillouin zone [49]. The upper half of the dispersion

is the conduction (π^*) band and the lower half is the valence band (π). Owing to the absence of a bandgap at the Fermi energy (Ef) and the fact that conduction and valence bands touch at Ef, graphene is considered a semi-metal or zero bandgap semiconductor, in contrast to a regular metal, where Ef is typically in the conduction band and a regular semiconductor where Ef is located inside a finite bandgap. Under no equilibrium conditions (applied electric, magnetic field) or extrinsic conditions (impurity doping), the Fermi energy will depart from its equilibrium value, 0 eV [50]. The deviations of Ef from its equilibrium value are often valuable in determining of concentration of impurity atoms. Since the density of states of the material is zero at that point, the electrical conductivity of intrinsic graphene is quite low and is the order of the conductance quantum, σ ~ e two /h [45]. The electrical conductivity of doped graphene is potentially quite high, at room temperature it may even be superior to that of copper [51,52]. Close to the Fermi level, the dispersion relation for electrons and holes is linear, which is representative of so-called massless particles (particles with zero effective mass)[53]. The equation describing the excitations in graphene is formally identical to the Dirac equation for massless fermions which travel at a constant speed [52]. The connection points of the cones are therefore called Dirac points. This gives rise to interesting analogies between graphene and particle physics, which are valid for energies up to approximately 1 eV, where the dispersion relation starts to be nonlinear [54].One result of this particular dispersion relation is that the quantum Hall effect becomes unusual in graphene [55]. Graphene, similarly to the other graphitic materials, show an excellent chemical resistance but thanks to its thickness it represents the thinnest protective layer against corrosion and oxidation. [17,56].

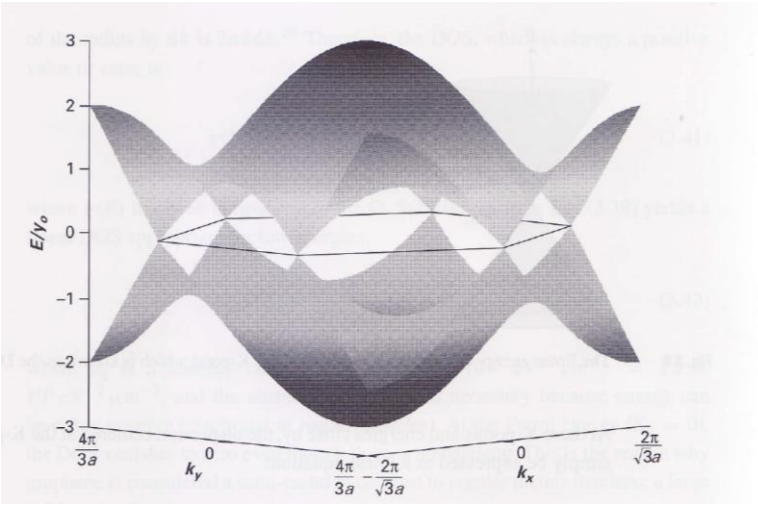

Figure 2.8. The nearest neighbour tight-binding band structure of graphene. The hexagonal Brillouin zone is superimposed and touches the energy bands at K points [54]

2.1.5 Amorphous carbon

The amorphous carbon does not have an ordered structure with a well-defined crystalline lattice, but a disordered structure that still allows a solid phase. In this form are present, in different percentages, the three different types of the hybridization, sp^1, sp^2 and sp^3, even if sp^2 is the main hybridization in this kind of material. This kind of material is present as a mixture of the two allotropic forms, which allows it to have the electronic, optical and tribological often very different from that of graphite and diamond.[57] There are many variations of such a structural material and, consequently, a wide range of physical properties [58]. Despite being a material in a condition of structural disorder, the atoms of which it is composed are not arranged in an entirely random manner [59]. When in a material the conditions of long-range symmetry and periodicity are absent, the solid is defined amorphous; In amorphous carbon the bonds there are small distortions in the length or angle of the bonds between first neighbours [59]. To describe this structure, some models consider a structure globally disordered as a random packing of hard spheres, the interweaving of disordered chains and linear structures, or a periodic lattice in which the distances and angles between first neighbours have statistical distributions [57]. The amorphous carbon film is deposited using physical vapor deposition (PVD) and chemical vapor deposition (CVD) processes, and they are used for a wide range of applications. The hardness is the range of 4 GPa to 60GPa, and the variation of mechanical properties is strictly related to the amount of the sp^3 bonds in the materials [57]. Amorphous carbon usually shows low friction coefficient values and excellent resistance to acid or basic solutions. In contrast to diamond films, amorphous carbon films can also be deposited at relatively low temperature, less than 200°C, for this reason, they are studied and also used as protective coatings against corrosion and gas permeation[60,61].

2.2.1 Solid-liquid interaction

The wettability is the tendency of a fluid to spread on a solid. In the scientific literature, the wettability is studied in a wide range of fields from fluid dynamics to bacterial adhesion, mathematics to the physical chemistry of the surface [62,63,64]. The proliferation of a vast number of scientific papers, in many cases with a considerable interdisciplinarity, is due to the fact that in many processes in the life sciences, in industrial applications wetting is a remarkable phenomenon,

and it is crucial to know how to check or how to change a wetting of surface [65]. The adhesion of varnish, the adhesion of lubricants, deposition, welding, condensation are just a few examples where this property, wettability, has a significant weight. Some applications require an excellent wettability while others require little wettability[66]. Welding is a process that needs a good wettability between the molten metal and the junction to ensure stability and quality[67]. The opposite case is represented by the "lotus flower" effect[1], which has a vital role in the mechanism of self-cleaning. The removal of contaminants from the surface of the plants is obtainable from water droplets that roll and do not stick to the surface. The estimation of wettability can be done in many ways. One of the most used is the measurement of a sessile drop contact angle. The contact angle is defined as the angle between the tangents drawn at the triple point among the three phases (solid-liquid - vapour) of a drop of liquid placed on the surface of a solid [68] figure 2.9.

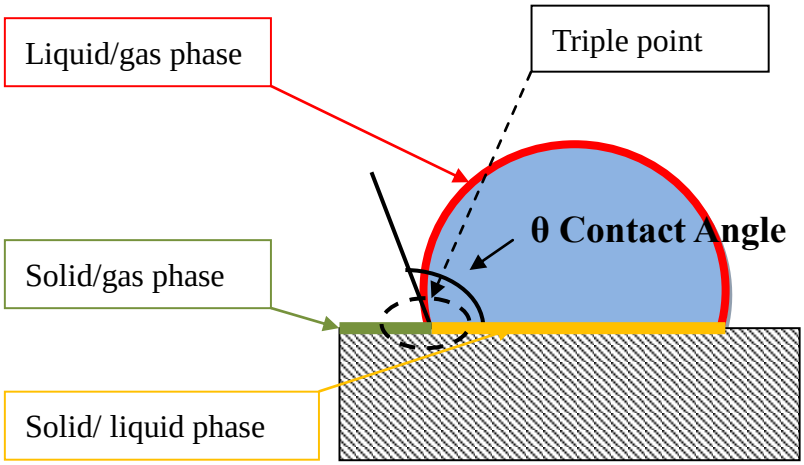

Figure 2.9 The angle of the three phases present in a system composed of drop put on the material.

The same liquid, in fact, may have different contact angles depending on the nature of the solid: for example, the water wets almost entirely glass or acrylic surfaces but does not wet the Teflon. A contact angle of 90° is the boundary value that separates wettability and non-wettability behavior. When the contact angle is less than 90° the surface is defined wettable (or hydrophilic in case of water), and if the contact angle is greater than 90° degrees the surface is defined not wettable (or hydrophobic in case of water). For a drop of water on glass, the contact angle is less than 25° and higher than 100° on Teflon. The wetting phenomena have been studied with a scientific approach already for 200 years with Thomas Young, introduced in 1805 a simple equation to estimate the surface tension of a solid [32]. The contact angle of a drop of liquid on a solid surface is determined by the balance of mechanical reduction under the action of the three interfacial tensions, as seen in

Figure 2.10:

- solid-vapour interfacial tension, γ_{sv}
- solid-liquid interfacial tension, γ_{sl}
- liquid-vapour interfacial tension. γ_{lv}

The equilibrium equation is known as a Young equation:

$$\gamma_{lv} \cos\theta = \gamma_{sv} - \gamma_{sl} \quad (2.1)$$

Where θ is the contact angle.

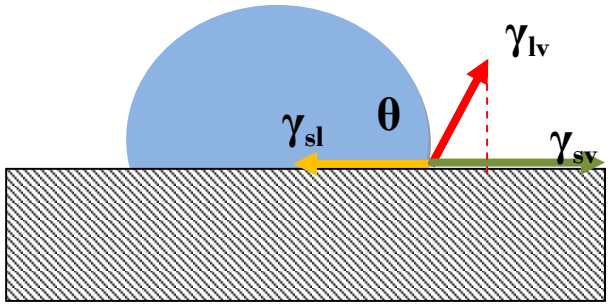

Figure 2.10 Drop contact angle at equilibrium

Dupré made another key step in the description of the interaction liquid-solid [69]. Dupré defined the work of adhesion as the work to be done to separate the liquid phase from the solid interface as described in detail as follows:

$$W_{SL} = \gamma_{sv} + \gamma_{lv} + \gamma_{sl} \quad (2.2)$$

where W_{SL}, the work of adhesion, gives an estimation of the adhesion of a liquid to a solid. Combining the Duprè equation with the Young equation gives

$$W_{SL} = \gamma_{lv} \ (1 + \cos\theta) \quad (2.3)$$

The equation of Young - Dupre shows that given a liquid with a specific γ_{lv} the contact angle increases if the liquid-solid adhesion decreases [24]. The extreme case is given for a contact angle of 180 °, where the adhesion is zero. The equation of Young and Young-Duprè have been designed

assuming that the solid-liquid interaction is not reactive and the drop is placed on an ideal flat surface. A further limitation of the equation of Young is that only two parameters are measurable, the contact angle (θ) and the liquid-vapour tension (γ_{lv}): then to determine precisely new relationships between γ_{sv} and γ_{sl} . assumptions are necessary. In any case, this expression remains to date the most widely used in the study of surface wettability and the determination of the surface tension. The drop contact angle measurement appears at first glance a straightforward and intuitive but is affected by a large number of factors, the variation of the surface tension (γsl), roughness, morphological heterogeneity of the surface and chemical interactions between liquid and solid [70]. For this reason, it is essential to classify the types of drop contact angles. The contact angle formed by the equilibrium of three interfaces tension, solid-vapour (γsv), solid-liquid (γsl), liquid-vapour(γlv), equilibrium conditions on a perfect surface and not reactive are defined as the equilibrium contact angle. The contact angle formed in a situation of absence of surface oxidation or a contaminant layer is defined as intrinsic contact angle. The contact angle defined with the balance of the forces induced by the surface tension is known as Young's contact angle for a surface in equilibrium. The contact angle obtained on a real surface is defined as the apparent contact angle and is given by the angle formed by the macroscopic three phases where the tangent is drawn to the nominal surface of the drop. The apparent contact angle is, of course, influenced by the surface chemistry of the solid, but also by two other factors: roughness and heterogeneity of the surface.

2.2.2 Effect of surface roughness on the contact angle apparent

Wenzel studied the effect of roughness on the contact angle in equilibrium and proposed an equation which correlates the contact angle and the apparent contact angle [22].

$$cos\theta_w = r\ cos\theta \quad (2.4)$$

Where θ is the intrinsic contact angle and θ_W is the apparent contact angle and r is the ratio between the area of the rough surface and the area of the original surface. The factor r is equal to 1 when the surface is entirely smooth. This law indicates that on a surface with a contact angle of 90°, the apparent contact angle tends to decrease by increasing the roughness. In the mechanism of Wenzel roughness acts as an amplifier of the intrinsic wettability of a surface.

2.2.3 Effect of heterogeneity of the surface on contact angle

Cassie-Baxter studied the effect of surface heterogeneity and described it with the following equation[1]:

$$cos\theta_c = f_1 cos\theta_1 + f_2 cos\theta_2 \quad (2.5)$$

Where f1 and f2 are the fractions of the surface occupied by two different types of surfaces: surface type 1 and type 2 surface having the contact angles respectively θ_1 and θ_2. A fascinating case of the different surface is what happens when one of the two surfaces is air. In this case, since the water droplet has a contact angle of 180 ° with the air the formula can be reduced as follows:

$$cos\theta_c = f_1 cos\theta_1 - f_2 \quad (2.6)$$

The attractive aspect to note is that, even if the material is inherently hydrophilic, it is possible to obtain a hydrophobic behaviour. For instance, when the drop wets the surface with corrugation, the air bubbles the air is entrapped between drop and surface the air increase the contact angle and a hydrophilic surface can show hydrophobic behavior (air-water interaction is hydrophobic). In this case, the contact angle can be described as follows:

$$cos\theta_c = rf_1 cos\theta_1 - f_2 \quad (2.7)$$

2.2.4 Fowkes theory and estimation of surface energy by Owens Wendt.

Beside the surface morphology, the chemical interactions can affect the contact angle in two ways: a) by intermolecular interaction between liquid and surface and b) by a chemical reaction between the liquid and solid (reactivity). In the determination of surface thermodynamic properties of the surface, the intermolecular interaction is fundamental. Fowkes realised the importance of the acid-based interaction (including hydrogen bonding) and modified of the expression of the work adhesion as follows [70]:

$$Wa = Wa_d + Wa_{AB} \quad (2.8)$$

Where AB is the acid-based component of the work of adhesion and Wa_d is the component due to the dispersive interaction. In the same manner, Fowkes assumed that the surface tension components have also been split into different terms:

$$\gamma = \gamma^d + \gamma^p + \gamma^{ind} + \gamma^H + \cdots \qquad (2.9)$$

where

γ= total surface energy
γ^d= London or dispersive interaction
γ^p= Keesom (dipole-dipole) interaction
γ^{ind}=Debye dipole interaction
γ^H =hydrogen bond interaction

Fowkes considered a simplification the surface tension is duet two dominant terms one due to non-bonding interaction e.g. London forces, and one due non-London forces.:

$$\gamma = \gamma^d + \gamma^{AB}$$

where

$$\gamma^{AB} = \gamma^p + \gamma^{ind} + \gamma^H + \cdots$$

A geometric mean relationship was postulated both for solid-liquid and liquid-liquid interfacial tensions

$\gamma_{ls} = \gamma_l + \gamma_s - 2\sqrt{\gamma_l \gamma_{ls}}$ *(2.10)*

Combining this equation with the Young equation, for a dispersive interaction the following equation is obtained:

$\gamma_l(cos\theta) = -\gamma_l - 2\sqrt{\gamma_s^d \gamma_l^d}$ *(2.11)*

Using two dispersive liquids as probes, the surface tension of surface can be estimated. The Owens-Wendt-Kaelble approach [15] extended the Fowkes' concept to cases where both dispersion and hydrogen bonding forces may operate.

$\gamma = \gamma^d + \gamma^H$ *(2.12)*

They regarded the surface tension as composed of two components: γ_H and γ^d, which are the

component of surface tension due hydrogen bonding and dipole-dipole interactions respectively. They postulate that

$$\gamma_{sl} = \gamma_s + \gamma_l - 2\sqrt{\gamma_s^d \gamma_l^d} - 2\sqrt{\gamma_s^H \gamma_l^H} \quad (2\ 13)$$

Combining this equation with Young's equation:

$$\gamma_l(1 + cos\theta) = 2\sqrt{\gamma_s^d \gamma_l^d} + 2\sqrt{\gamma_s^H \gamma_l^H} \qquad (2.14)$$

Since equation 5 contains two unknown parameters γ_s^d and γ_s^H of the solid, it is necessary to use drop contact angle measurements of at least two known liquid probes on the same solid surface, by solving two simultaneous equations. The use of one pure dispersive liquid and another with polar components is necessary. The typical dispersive liquids used to estimate the surface energy by the Owens-Wendt methods are diiodomethane, bromonaphthalene and paraffin oil. The typical polar liquids are water, ethylene glycol and formamide. This approach produces more robust results then the Fowkes one and gives more information on the surface such as dispersive components and polar components of the surface tension. However, by this approach variations due to the probe liquids are possible. The use of liquids with a high surface tension is suggested to avoid the underestimation of the surface tension.

2.2.5 Lifshitz - van der Waals / Acid-Base (van Oss) Approach

The Lifshitz - Van der Waals / acid-base (Van Oss) approach was claimed to be a generalisation of the Fowkes approach, by considering perceived acid-base interactions at the interface [70]. A hydrogen bond, in fact, is a proton-sharing interaction between a negative electron-molecule (e.g. a carbonyl) and a molecule or group that contains a proton bond in another electronegative group. e.g. hydroxyl. A hydrogen bond is an example of Lewis acid (electron acceptor) and Lewis base (electron donor) interaction. Van Oss, therefore, suggested that it is desirable to use the Lewis acid and base concept and approach in the estimation of surface tension. Therefore, Van Oss et al. divided the surface tension into different components, LW the so-called Lifshitz-van der Waals (LW), and the acid (+), and base (-) components, such that the total surface tension is given by

$$\gamma_i = \gamma_i^{LW} - 2\sqrt{\gamma_i^+ \gamma_i^-} \quad (2.15)$$

where "*i*" denotes either the solid or the liquid phase. The interfacial tension was postulated for both of solid-liquid and liquid-liquid systems as

$$\gamma_{12} = \gamma_1 + \gamma_2 - 2\sqrt{\gamma_1^{LW}\gamma_2^{LW}} - 2\sqrt{\gamma_1^+\gamma_2^-} - 2\sqrt{\gamma_1^-\gamma_2^+} \quad (2.16)$$

For solid-liquid systems, combining equation 16 with Young' s equation yields

$$\gamma_l(1 + cos\theta) = 2\sqrt{\gamma_s^{LW}\gamma_l^{LW}} + 2\sqrt{\gamma_l^+\gamma_s^-} - 2\sqrt{\gamma_s^-\gamma_l^+} \quad (2.17)$$

This equation is often used to determine the solid surface tension components using the drop contact angle, for three different liquids [71]. The acid-base approach is more informative than the Owens's and Wendt because it allows to determine the Lifthis-van der Walls components, the electron acceptor component and the electron donor element of a surface. This approach can predict many molecular properties: nonpolar components, negative and positive acidic and basic components as well as the total solid-liquid interfacial tension [72].

2.2.6 Equation of State Approach

In this and the following sections, an equation of state approach will be briefly discussed. The equation of state approach is based on pure thermodynamics consideration. The most fundamental equation are Antonow and Berthelot's equations. Antonow's relationship considered the final surface tension between a liquid and a surface, γ_{sl} , as the excess of the difference between γ_{lv} and γ_{sv}.

$$\gamma_{sl} = |\gamma_{lv} - \gamma_{sv}| \quad (2.18)$$

Combining the Antonow relation with Young's equation gives

$$cos\theta = -1 + 2\frac{\gamma_{sv}}{\gamma_{lv}} \quad (2.19)$$

.By Berthelot is the long-range dispersion energy for two identical molecules is given by the

relationship based on dispersion energy coefficients C_6^{ij} that can be written regarding C_6^{ii} and C_6^{jj} [70]:

$$C_6^{ij} = \sqrt{C_6^{ii} C_6^{jj}} \qquad (2.20)$$

This relationship forms the basis of the Berthelot combining rule

$$\frac{\varepsilon_{ij}}{\sqrt{\varepsilon_{ii}\varepsilon_{jj}}} = 1 \; \varepsilon_6^{ij} = \sqrt{\epsilon_6^{ii}\epsilon_6^{jj}} \; (2.21)$$

where ε_{ij} is the potential parameter [73] (well depth) of unlike-pair interactions, ε_{ii} and ε_{jj} are the potential energy parameters (well depth) of like-pair interactions. This equation was written regarding the work of adhesion between two phases (i.e. W_{sl}) and work of cohesion of the two phases (i.e. W_{ss} and W_{ll}).

$$W_{sl=} = \sqrt{W_{ss} W_{ll}} \; (2.22)$$

Putting the relevant values, i.e. $W_{ss}=2\gamma_{sv}$, $W_{ll}= 2\gamma_{LV}$ and $W_{sl}=\gamma_{LV}+\gamma_{sv}-\gamma_{sL}$ in equation 22 and rearranging the final relation of Berthelot gives:

$$\gamma_{sl} = \gamma_{sv} + \gamma_{lv} - 2\sqrt{\gamma_{sv}\gamma_{lv}} = \left(\sqrt{\gamma_{sv}} - \sqrt{\gamma_{lv}}\right)^2 \; \gamma_{sl} \; (2.23)$$

Combing with Young equation

$$cos\theta = 1 + 2\sqrt{\frac{\gamma_{sv}}{\gamma_{lv}}} \quad (2.24)$$

The geometric mean combining rule overestimates the strength of the unlike-pair interaction, for this reason, a different strategy is used to recompensate this overestimation.
Li propose a modified combined rule

$$\varepsilon_{ij} = \sqrt{\varepsilon_{ii}\varepsilon_{jj}}\, e^{-\alpha(\varepsilon_{ii}-\varepsilon\varepsilon_{jj})^2} \qquad (2.25)$$

Therefore, rearrange equation one we can obtain

$$Cos\theta = 1 + 2\sqrt{\frac{\gamma_{sv}}{\gamma_{lv}}}e^{-\beta(\gamma_{sv}-\gamma_{lv})^2} \quad (2.26)$$

Thus, the solid surface tension can be determined to know the experimental contact angle and liquid surface tension when β is known using an iterative procedure. β is an empirical constant with an average value of 0.0001057 [(m^2mJ^{-1}). [74,73].

2.2.7 Zisman approach

Zisman introduced an empirical method of treating the contact angle data which allows an estimation of γ_{sv} , the surface free energy of the solid [70]. Cosine of contact angle was measure for series of homologous liquids on a solid; the results were plotted against γ_l of the liquids (the Zisman plot).

$$cos\theta = 1 - b(\gamma_l - \gamma_c) \quad (2.27)$$

The critical value γ_c of γ_l below which θ is equal to zero (found by extrapolation if necessary) is considered to be a measure of the surface free energy of the solid. The method is quite long, and it is very important to use a wide number of liquids with different surface tension to obtain a Zisman plot that can give robust results [75]. This empirical methodology has many limitations like the linearity of equation 2.27 and the availability of proper probe liquids [73].

2.2.8 Literature survey on Liquid - Gas-Solid interaction

To study the gas-liquid-solid interaction, it is possible to place a bubble in contact with a surface immersed in water. In this condition, the system liquid-gas - surface is complementary to the sessile drop contact angle.

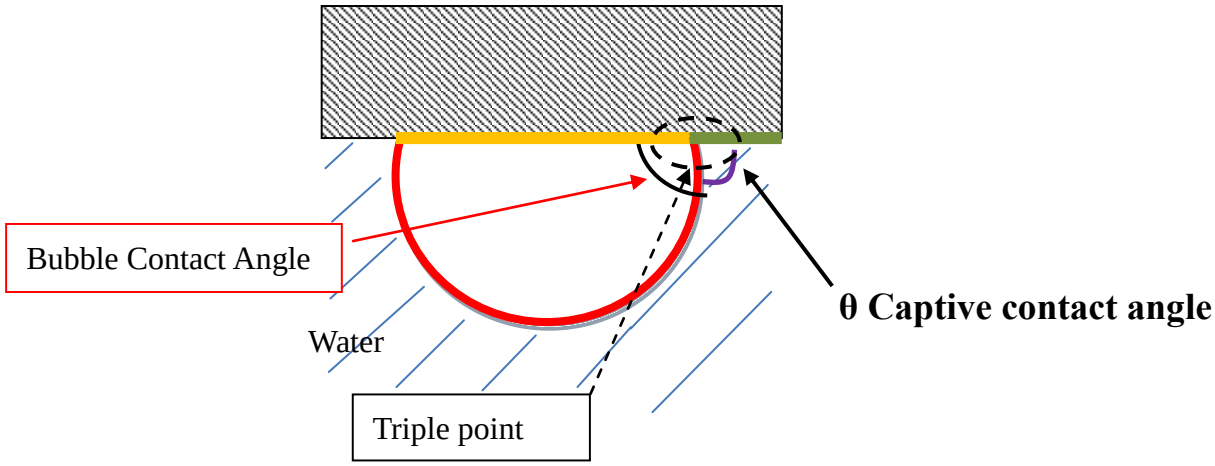

Figure 2.11 Typical step ut of captive bubble contact angle, captive contact angle and bubble contact angle are indicated by arrows

Also captive bubble contact angle there is an equilibrium between the solid-liquid, liquid - vapour, and vapour - solid surface tensions. The contact angle in captive bubble angle set-up usually is the complementary angle of the bubble, this to have a correspondence with the sessile drop contact angle measurement where the angle is measured between the solid-liquid interface and the liquid gas interface Figure 2.11 [76]. This is very useful when a comparison between sessile drop and captive contact angles is necessary. The bubble contact angle measurement is used too, when the interaction of the gas with the surface is studied, or in nanobubbles [77]. Over the definition of the angle, the set-up where a bubble of gas is in contact with a surface immersed in liquid is used to determine the wettability of polymers with a high surface tension, in a contact lens or when the sessile drop contact angle was difficult to determine [78,79]. The thermodynamic theory about the bubble contact angle is less developed than for the sessile contact angle, and the main research work uses bubble contact angle in term of qualitatively drop, as reported by Drielich [78] and a robust theory about the bubble contact angle is still unachieved [80,81,82].

2.2.9 Literature Review on the graphitic materials wettability

Extensive experiments and studies have been conducted on graphitic materials and the reported contact angle are spread on wide range. Eissler and Van Holden in 1962 reported an advancing contact angle of 86.6° and a receding contact angle of 67.5° on the main face of de-ashed natural Ceylon graphite and 71.5° and 60.9° on the edge of graphite leaflets [83]. Fowkes and Harking in

1940 reported contact angle with water in the range of 75° – 95°[84]. Morcos reported a water contact angle (WCA) of 83.9° on pyrolytic graphite and Adamson reported a WCA and exfoliated graphite of 91° [85,86]. Schrader indicated that exfoliate graphite in vacuum shows a contact angle of 42°. Figure 2.12shows the distribution of the values contact angle measured on various kinds of graphitic material as reported in literature. Werder in 2003 observed wide range of contact angle on graphite, and by molecular dynamics simulation Werder estimated the water molecular binding energy when the contact angle is 86° and 42 °, the two extreme cases [82]. Santiso estimated by molecular dynamic calculation a contact angle in the range 66-75° [87]. Li reported a contact angle on the graphitic base material as carbon nanotubes a C.A of 160 ° and 158°. A contact angle less than 50 ° has been observed on graphene deposited on Cu [21]. Cvelbar reported contact angle less than 5 ° when graphite was cleaned with oxygen plasma. Kozbial intensively studied the wetting of HOPG, and in 2014 he show as the fresh graphite is more hydrophilic than aged graphite, in particular, he estimated a value of fresh graphite of 65 ° and values higher than 95° for seven days aged graphite, Figure 2.12 [20]. Wei in 2015 found a linear relationship between the exfoliated graphite contact angle and the ageing time. The initial wetting was estimated by the linear fit and was 61.5° [18]. The linear trend was not recognised in other works, but similar value for new graphite was observed by Li 64.4°. Kozbial recently compared in HOPG with different degrees of mosaicity of graphite and pyrolytic graphite [88]. The static contact angle of the various HOPG was in the range of 62-65°, but the pyrolytic graphite shows a contact angle of 42°; the authors underlined in the work that the static contact angle could be affected by the defects in the graphite structure. Therefore, as we can see by the figure 2.12 and as reveal by the recent works e,g Kozbial the graphite surface is hydrophilic.

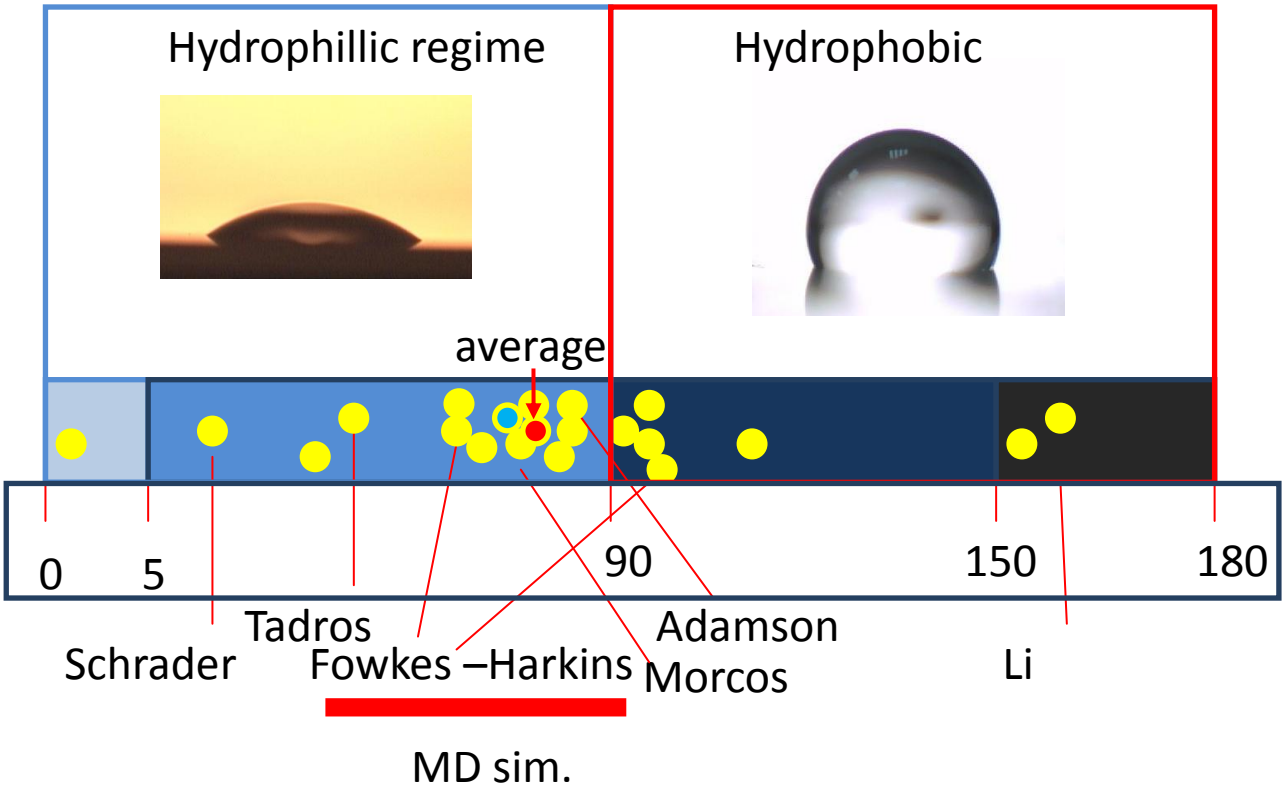

Figure 2.12. Contact angle reported in literature on graphitic materials, and the contact angle estimated by molecular dynamics in literature MD sim (red line)

2.3. Barrier Layers

The surface of materials is exposed every day to a broad range of chemical substances, visible light, UV radiation, heat. The surface is therefore exposed to physical and chemical sources of degradation which can modify the properties of the surface. The modification of a surface can be a problem from the aesthetical point of view, under optical point view as well as the tribomechanical point of view[89]. An example is the corrosion of a surface due to direct attack from chemical compounds like acid on the surface (lemon on marble), the typical galvanic corrosion of bimetallic junctions as well as the differential aeration corrosion [90]. Another kind of degradation mechanism is the degradation induced by UV related to the higher energy compared with the visible light which induces a deterioration of materials as glass wood and polymers [91-94]. Moreover of degradation of the surfaces can be induced by mechanical processes as wear between lubricated and not lubricated materials [95;96] or by mechanical stress accomplished by corrosion [97].

Even if the many kinds of degradation process occur on the surface of a material, an essential part is due to the presence of water in contact with the surface or water in contact with the surface in the presence of gases like oxygen. The typical degradation in the presence of water is due to the partial

solubility of the material with water, due to the process of absorption and hydrolysis of material, ion exchange accomplished in many cases by dissolution and degradation of materials, and the differential aeration corrosion. On metals, the differential aeration corrosion is a significant problem; it occurs when oxygen concentrations vary across a metal surface. The varying concentration of oxygen in water creates an electrochemical cell on the metal surface, and this promotes a corrosion by a galvanic process. This is the typical corrosion that can happens under a water drop. Beside corrosion, typical of metals another degenerative process can occur on the surface of the material exposed to the water as the process of absorption of water in the outer layer of material which by proton exchange or by hydrolysis can degrade the surface. The latter can be encountered on polymers . This kind of degradation is typical of plastic materials and can be mediated by light (UV), water and chemical substances. A simple contact with water can be a source degradation also of a hydrophobic polymer like PDMS [98;99,100]. The surface properties can change due to a morphological rearrangement of the polymer chains. For many applications where the polymer is used as electric insulator or biomedical implant, the modification of the surface should be avoided. The surface can be protected by a layer which acts as a physical barrier against the physical – or chemical source that degrades the surface properties. The barrier coating must protect the surface. The oxide on the metal surface is a typical example of the natural protective barrier, e.g. alumina on aluminium. But not always the natural oxide is efficient enough and therefore a specific barrier must be realised [101]. Barrier coatings can be synthesised using plasma technologies, atomic layer deposition or by electrodeposition, to cite few. Paints and varnishes are also widely used as a barrier against UV degradation, oxidation of surfaces and corrosion of metals [102,4,103]. Recently the researchers were exploring the use of the 2D materials as barriers against the oxidation of metals surface like copper [104,105]. The results were controversial, [106,56] but the use of this new nanotechnology appears really promising for the scientific community in particular for the synthesis of the thinnest protection coating that is actually promising to protect historical manufactures, micro/nanodevices or to protect reactive materials like magnesium [107,17,108,96,103,90].

2.3.1 Literature review on the degradation of surface properties of material induced by water

Water can induce the degradation of materials in many different ways, but the primary is caused by the fact that water is good solvent [109] thanks to its polarity induced by the chemical structure.

Oxygen and Hydrogen have different electronegativities and this induces a partial negative charge on oxygen and a partial positive charge on hydrogen.

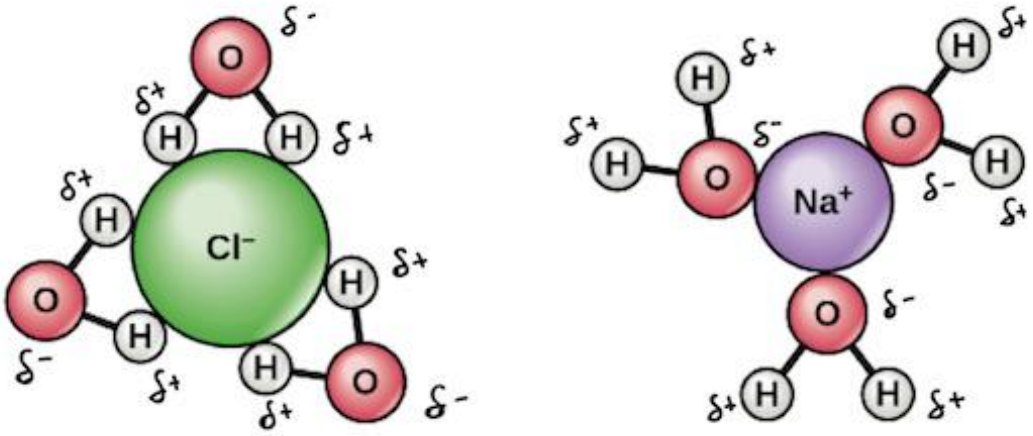

Figure 2.13 Hydration shell of Cl and Na [110]

Due to its polarity, water molecular produces an electrostatic interaction with other polar substances. The partial positive charge of water interacts with a partial negative charge of polar molecules or ions, or vice-versa. In an aqueous environment, the multiple interactions produce a shell around the solute called hydration shell typical of on NaCl solution in water, figure 2.13. The hydration shell allows the molecules to be dispersed in water itself, Figure 2.13 [110]. A similar process can happen on the surface of materials soluble in water as iron hydroxide (0,72gr/100ml), lead oxide (0,0017 gr/ml), lead carbonate (0.00011gr./100ml), germanium oxide, biodegradable polymers or many kinds of semiconductor-like MnO [111,112,113]. Usually, to avoid the degradation of surfaces, the soluble materials are not intentionally used in contact with water, but in certain conditions like exposure to visible light, gases, or simply to the moist air, some metals can produce a soluble compound in water as reported by Thornton for Lead (Pb) surface [114]. Usually, a non-polar substance is not soluble in water, and the surface of non-polar materials are less prone to the permeation of water inside their structure, the case of silicon rubber. Such materials are usually called impermeable. Materials without a polar group are also called dispersive because they show only non-bonding interaction with water (Van der Waals interaction) [115]. For that reason, materials with a dispersive surface are useful to realize impermeable surfaces.

Water induce the degradation of glass materials also through an ionic diffusion and exchange process in a complex chemical and physical change of surface. In this type of corrosion, the water is absorbed on the surface of glass, hydrogen ions diffuse into the glass and exchange with an alkali metal. The produced ions diffuse out of the glass and dissolve in water [116]. The process supports the

dissolution of silicate network structure by water [117]. The initial process, ion diffusion, promotes a local increase in pH from the accumulation of hydroxide ions in the solution near the solid liquid interface, and this increase the corrosion rate [118]. A similar process happens on other materials like polymers and concrete [119,120,121]. On concrete, the water can induce proton exchange to result in corrosion. Water in contact with calcium silicate and calcium silicate hydrate promote the leaching of Ca out of concrete, and this induces a massive change of the mechanical properties [5]. . Water can also degrade insoluble polymers with high thermal and chemical stability as dental resins, PET, PLA and PDMS [120]. The polymer network may absorb water and compounds from the environment. The absorption of the contaminants acts as precursors to a variety of chemical and physical process that produces a degradation of the structure and sometimes compromises the function of the polymeric material. The primary process is the swelling, physical and chemical change in oxygenation and hydrolysis. Degradation by water starts with a forerun phase where water on the surface promotes the migration of polar groups present in the bulk of the material to the most superficial layers, inducing a structural change of the polymer network [122]. PDMS, for instance, is a dispersive surface and hydrophobic material with a water drop contact angle higher than 100° [123;92], which makes it used materials for external electrical insulators of outdoor applications. Bognar 1994[124] observed a substantial increasing of hydrophilicity of the PDMS surface when immersed in water for extended time, 190h; a similar result has been seen obtained by Hillborg 1999 [125], in agreement with Gubansky and Gustavsonn who observed a gain of weighing due to the water sorption in the first 100h of immersion followed by a weight decrease[99] . The reduction of weight has been assigned to hydrolysis effect Figure 2.14 shows the hydrolysis process of siloxane bonds [126].

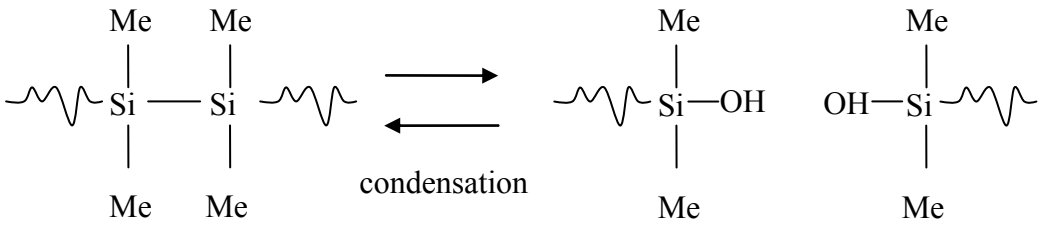

Figure 2.14 Sketch on Hydrolysis and condensation process induced by water in PDMS [98]

The hydrolysis reaction can be accelerated by contamination or by the silica filler and clay dust present in the materials [127,128]. The surface energy of the PDMS is low, less than 20 mJ/m^2. Therefore, dust and contamination are attracted by this favourable energetic conditions, and the

surface of the silicone polymer can be easily contaminated. The formation of OH groups in the presence of water is considered at the origin of the increase of wettability on the surface. In fact, OH groups near the methyl group, thanks to the segmental mobility of the polymer chains, can easily migrate to the surface [129;98]. A similar effect can happen on PET, where the migration of polar groups induced in water produces a modification of the surface topography [130].

Water can also induce the degradation of a metal surface by corrosion. When a metal and an electrolyte are in contact and the electrolyte and metal have a different standard electrode potential an electrochemical cell is spontaneously realised, and the metal can act as anode, and metal ions are removed from the metal surface inducing the degradation of the surface. Corrosion is favourable in the material with the lower red-ox potential. Anyway other phenomena must be considered in corrosion. In fact, Al has a red-ox potential lower than that of Iron, but on aluminium, a layer of alumina oxide is naturally present. Alumina is insulating and shows a high resistance to corrosion; Alumina is a natural passivation layer that acts as a barrier against corrosion.

A particular kind of corrosion is the corrosion due to differential aeration; a typical example is a drop on the surface. In this drop-metal system, there is a different concentration of oxygen diluted in the water near the border of the drop and air and the centre of a water drop. The concentration of oxygen in the water near the drop surface it is higher than in the region in the centre of the drop.

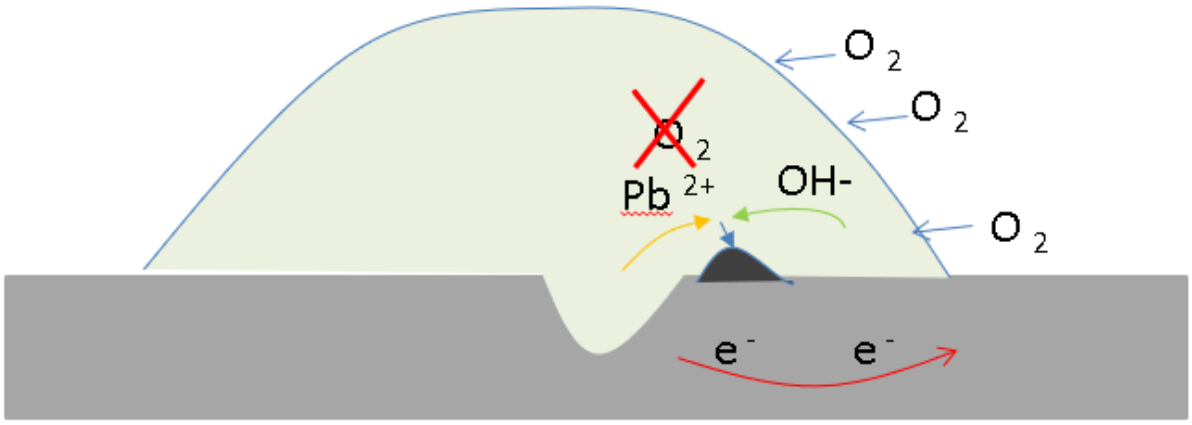

Figure 2.15 Differential aeration corrosion mechanism of a drop on metal surface.

The oxygen-rich region becomes the cathodic part. At the cathode, oxygen takes 2 electrons to form OH^-

$½\ O_2 + H_2 = +2e \rightarrow 2OH^-$

The metal region, poorly oxygenated, becomes anodic, leading to an oxidation of the metal.

$Fe \rightarrow Fe_2^+ + 2e$

The OH and the metal in water produce a metal hydroxide that tends to precipitate in the region between the anode and the cathode as depicted in figure 2.15. This is considered a primary effect on differential aeration corrosion, but other effects must be considered in the acceleration of the corrosion, like the breakdown of passivation, local increase of pH and crevices. De Gruyter in 2000 demonstrated that secondary effect of differential aeriation corrosion is the main source of corrosion, De Gruyter observed in a dedicated electrochemical cell that the polarization of oxygen-starved and oxygen-rich takes place on the electrodes, but it affects only the reduction of the electron acceptor[131]. According to the authors, these corrosion phenomena must be due almost entirely to secondary effects that e.g. local changes of acidity, hydrolysis of metal ions, etc.). In the scientific community, there is still a debate about the understanding of differential aeration corrosion, but the role of local increase of pH can be important in the acceleration of corrosion in differential aeration corrosion [132,133].

2.3.2 Literature review on Barrier layers against degradation of material surface properties induced by water.

In the previous paragraph, we reported a glance on the degradation of surface exposed to different kind of agents and in particular exposed to water. To reduce the effect of degradation by liquids and gases, it is very important to avoid their contact and penetration in the materials. The penetration of substances in the materials is called permeation. The permeation of a liquid and gas in materials is essential to consider in diverse applications ranging from the packaging of food, pharmaceutical and microelectronics for consumers. The permeation of gas and liquid can be described by Fick laws.

$$J = -D(c)\frac{dc}{dx} \quad (2.28)$$

$$\frac{dc}{dt} = \frac{d}{dx}\left[D(c)\frac{dc}{dx}\right] \quad (2.29)$$

where J represents the amount of penetrating liquid/gas moving through a unit area per unit time flux 9, c is concentration, x is the direction of diffusion and D is diffusion coefficient [134].

If there is a linear concentration gradient under steady-state conditions the equation can simplify as follows:

$$J = D\frac{(C_1 - C_2)}{l} \quad (2.30)$$

Where l is the thickness of the film and C_1 and C_2 represent the–concentrations at the two film surface. The equation can also be described in term of partial pressure:

$$J = P\frac{(p_1 - p_2)}{l} \quad (2.31)$$

where p_1 e p_2 are the vapor pressure on either side of the layer. P is the permeability coefficient which is the rate or unit of area at which gas vapor moves through unit thickness of the film under a single unit of the pressure difference. The concentration of gas vapor in material layer surface is related to the solubility coefficient (s) as given in equation:

$$C = Sp \quad (2.32)$$

Permeability is the product of diffusivity and solubility.

$$P = D*S \quad (2.33)$$

In material covered by an impermeable barrier, the flux through the coating and the permeability P in steady conditions depends on the thickness of the coating (d) and by the thickness of material (L). The rate of permeability Q is $\frac{P}{L+d}$ given as:

$$\frac{1}{Q} = \frac{L+d}{P} = \frac{L}{P_s} + \frac{d}{P_c} = \frac{LPc + dPs}{Pc * Ps} \quad (2.34)$$

$$Q = \frac{Pc*Ps}{LPc+dPs} \quad (2.35)$$

Where P_s e P_c is the permeability of the substrate and the permeability of the coating, respectively. By the equation 2.35 we can see that if the barrier permeabilityity is very low, it could have a significant impact on reducing the rate of gas or liquid permeability in the material. An example is the titanium barrier coating on PEEK polymer to reduce gas diffusion [135]. In this condition, the "perfect" impermeable barrier is led by defects like pinholes or scratches. The transport of liquids and gases in an impermeable membrane with defects is determined by the density of the defects and dimension and less by the thickness of the coating.

The Fick diffusion gives an excellent description of diffusion in a simple system, like the behaviour exhibited by a gas and or by water vapour on hydrophobic polymer. However, many polymers depend strongly on concentration. Water, in particular, has a distinctive character that gives rise to certain conditions of non Fickian diffusion. Water exhibits hydrogen bonding, and in hydrophobic polymers without hydrogen bonding sites, clustering of water molecules can occur due to the higher interaction between the water molecules [136,137]. This induces a decrease of the diffusion coefficient of water when water concentration increases. In hydrophilic polymers diffusion coefficients will increase with increasing water concentration due to plasticization effect (reducing of glass temperature of polymer), therefore in many cases more complicated models should be used to describe the diffusion of water. Yano *et al.*[138,136] reported a decrease of 90% in water vapor permeability in polyamide –mica composite with only 3% in the volume of mica. Nielsen explains and modelled the diffusion of the water vapor and gas in the matrix with a filler. Nielsen model is based on the premise that penetrant molecules have an increased diffusion path because of the presence of impermeable filler particles [137]. The filler increases the tortuosity of diffusion path, and this induces a reduction of diffusion through the path, as in figure 2.16. Nielsen takes into account the volume fraction of the filler in the permeation model. Other more detailed models have been proposed by other authors, e.g. Cluster *et al.* and Choudalakis *et al.*, to describe more accurately the diffusion taking into account the aspect ratio of the fillers [139]. All these models, in any cases, are based on in the increase on the path of the diffusing molecules in the matrix. Taking into account this consideration many authors experimented different kinds of nanocomposites to decrease the diffusion of water vapour . In particular, some authors recently proposed graphite nanoplalates, graphene oxide and graphene as fillers with promising results [140].

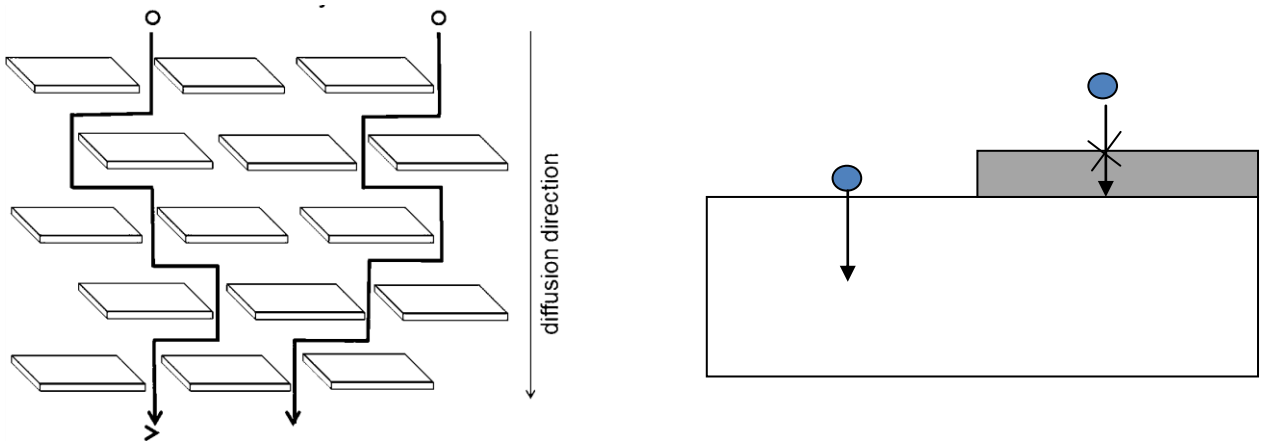

Figure 2.16 Strategy to reduce diffusion of a gas and liquid in materials, using impermeable filler in a matrix and using a coating on the materials [136].

As reported in literature the introduction of nanofillers in a matrix is a way mainly use to reduce the permeation of the substance in a material. However, as indicated by the equation 2.35. Another way to reduce permeation of water is the deposition of a protective layer on the surface of materials that works as a barrier against diffusion (Figure 2.6). Many methods are used to deposit layers against degradation such as paintings, varnishing, deposition of thick and thin coating techniques [89,141]. A low-cost technique is based on the use of varnishes or paints to cover the surface of material while the modern ones require the use of sophisticated apparatus that via physical or chemical process can cover the surface in a conformal mode like plasma depositions, thermal evaporation or atomic layer deposition to protect the surface of metals. Topcuoglu, for instance, developed an acrylic paint to reduce the water vapor permeability [142]. Atomic layer deposition is particularly able to cover the surface of a metal with atomic layers of oxides in a very conformal mode. This allows obtaining an excelled protection of a surface against corrosion [143]. Plasma technologies based on physical vapor deposition (PVD) and chemical vapor deposition (CVD) are widely diffuse in laboratory environments and industrial facilities–Hillborg, for instance, used a plasma treatment to deposit a layer of SiO_2 on PDMS to stabilize the behaviour of polymers against water interaction [98]. Carbon films deposited by PVD and CVD have been used to protect PET and polycarbonate for a biomedical application or to reduce the permeation of gases[8,144]. Unfortunately, all these techniques require vacuum technology or dangerous chemical precursor, that is costly, or they need a specific installation, specialised personnel (UHV) and many cases there are limitations about the volume and geometry of the product. For this reason, an alternative and promising way to protect the surface is the implementation of nanomaterial in the varnishes, paints or inks to obtain a coating

with superior properties [145,102,146].

2.3.3 Literature Review on graphitic material as barrier layer

Graphite, nanographite, graphene nanoplatelets and graphene have been used in many scientific works as a barrier against the permeation of the gases, acid-base corrosion and water adhesion and degradation induced by water [108,147,148]. Rathnayake intercalated nano graphite in polyaniline and used this nanocomposite as anti-corrosion layer of steel and to increase the hydrophobicity of surface [149]. Now the main interest is the synthesis of layers of 2D materials as graphene oxide and graphene because they can be thinnest barrier coating [150]. The number of publications in on graphene as barrier in 2011 was around 433 and 2316 in 2016. This indicates the great interest in the scientific community in this field. The layers of 2D materials flakes, in fact, follow the shape of the surfaces as phyllo dough that work as a barrier against chemical agents. Also, the single layer graphene has been successfully used, by Bimal *et al*., to protect the surface of glasses against water corrosion [151] Sangermano used graphene oxide as a barrier against water vapour in epoxy coating [152]. In 2014 Su *et al.* demonstrated that coatings based on reduced graphene oxide were useful, a flexible barrier against gases permeation and that reduced graphene oxide (RGO)as an excellent barrier against Cl ions[108]. Sun proved as graphene oxide polymer composite coating had an excellent resistance to chlorine ions. Chen *et al.* demonstrated the passivation properties of graphene on Cu and Cu/Ni Alloy [56]. Similarly, results have been predicted by Topsakal *et al.* for aluminium substrate [153]. Schriver observed similar results only in short test, but the experimental work proved that CVD graphene on Cu promoted the corrosion in a long-term test of oxidation [106]. Ya-Ping Hsieh partially overcame this problem passivating the graphene defect using ALD [154]. Mayavan developed a graphene ink to inhibit corrosion on Iron [155]. The main work use graphene and graphene-based material as material to intercalate in a matrix , but many works were also focused on the synthesis of graphene dispersion in different solvents: paraffin oil, toluene, and N,N-dimethylformamide(DMF), to realize inks or paints that can be used to achieve a protective layer of 2D material on a substrate [144,145,146]. The inks based on 2D materials appear very attractive as reported by Mates and Maravayan because of a low-cost, durable method to realise an efficient functional layer that in many cases are also semi-transparent. Even if the synthesis of graphene layer using paints or inks appear at the moment very far from to have the quality obtained by CVD processes, due the presence of defect, edges, holes lack of homogeneity, weak adhesion, it should be attractive to fields where the requirement of barrier layer is occasional or in not harsh environments like in the protection of archeological artifacts [146,153].

References

1. Zhang M, Feng S, Wang L, Zheng Y. Lotus effect in wetting and self-cleaning. *Biotribology*. 2015:1-13. doi:10.1016/j.biotri.2015.08.002.

2. Diéguez L, Winter M a, Pocock KJ, Bremmell KE, Thierry B. Efficient microfluidic negative enrichment of circulating tumor cells in blood using roughened PDMS. *Analyst*. 2015;140(10):3565-3572. doi:10.1039/c4an01768d.

3. Bodas D, Khan-Malek C. Hydrophilization and hydrophobic recovery of PDMS by oxygen plasma and chemical treatment-An SEM investigation. *Sensors Actuators, B Chem*. 2007;123(1):368-373. doi:10.1016/j.snb.2006.08.037.

4. Armelin E, Pla R, Liesa F, Ramis X, Alema C. Corrosion protection with polyaniline and polypyrrole as anticorrosive additives for epoxy paint. 2008;50:721-728. doi:10.1016/j.corsci.2007.10.006.

5. Giraudo N, Weidler PG, Laye F, et al. Corrosion of Concrete by Water-Induced Metal − Proton Exchange. 2016. doi:10.1021/acs.jpcc.6b07347.

6. Bartali R, Lamberti A, Bianco S, et al. Graphene as Barrier to Prevent Volume Increment of Air Bubbles over Silicone Polymer in Aqueous Environment. 2017;I:12865-12872. doi:10.1021/acs.langmuir.7b02915.

7. Li B, Logan BE. Bacterial adhesion to glass and metal-oxide surfaces. *Colloids Surf B Biointerfaces*. 2004;36(2):81-90. doi:10.1016/j.colsurfb.2004.05.006.

8. Favia P, Agostino R. Plasma treatments and plasma deposition of polymers for biomedical applications. *Surf Coat Technol*. 1998;98(1-3):1102-1106. doi:10.1016/S0257-8972(97)00285-5.

9. Sarrica SM. *Paints Types, Components and Applications*. (Nova Science Pubblishers I, ed.). New York; 2011.

10. Pore BV, Rahtu A, Leskelä M, Ritala M, Sajavaara T, Keinonen J. Atomic Layer Deposition of Photocatalytic TiO2 Thin Films from Titanium Tetramethoxide and Water Atomic Layer Deposition of Photocatalytic TiO 2 Thin Films From Titanium Tetramethoxide and Water . 2015;(October). doi:10.1002/cvde.200306289.

11. Bartali R,, Morganti E., Lorenzelli L., et al. Oxygen plasma treatments of polydimethylsiloxane surfaces : effect of the atomic oxygen on capillary fl ow in the microchannels. 2017:1-4. doi:10.1049/mnl.2017.0230.

12. Nowak E, Combes G, Stitt EH, Pacek AW. A comparison of contact angle measurement techniques applied to highly porous catalyst supports. *Powder Technol*. 2013;233:52-64. doi:10.1016/j.powtec.2012.08.032.

13. Joly, T., Tocci, G., Marebia, S., Michadelides A. Strong Coupling between nanofluidic Transport and Interfacial Chemistry: How defectt Reactivity Controls Liquid-Solid Friction through Hydrogen Bonding. *J Phys Chem Lett*. 2016;6((7)):1381-1386.

14. Stalder a. F, Kulik G, Sage D, Barbieri L, Hoffmann P. A snake-based approach to accurate determination of both contact points and contact angles. *Colloids Surfaces A Physicochem Eng Asp*. 2006;286(1-3):92-103. doi:10.1016/j.colsurfa.2006.03.008.

15. Decker EL, Frank B, Suo Y, Garoff S. Physics of contact angle measurement. *Colloids Surfaces A Physicochem Eng Asp*. 1999;156(1-3):177-189. doi:10.1016/S0927-7757(99)00069-2.

16. Sun Y, Xie G, Peng Y, Xia W, Sha J. Stability theories of nanobubbles at solid–liquid interface: A review. *Colloids Surfaces A Physicochem Eng Asp*. 2016;495:176-186. doi:10.1016/j.colsurfa.2016.01.050.

17. Nine J, Cole MA, Tran DNH, Losic D. Graphene : a multipurpose material for protective coatings. *J Mater Chem A Mater energy Sustain*. 2015;3:12580-12602. doi:10.1039/C5TA01010A.

18. Wei Y, Jia CQ. Intrinsic wettability of graphitic carbon. *Carbon N Y*. 2015;87:10-17. doi:10.1016/j.carbon.2015.02.019.

19. Rico V, López C, Borrás A, Espinós JP, González-Elipe AR. Effect of visible light on the water contact angles on illuminated oxide semiconductors other than TiO2. *Sol Energy Mater Sol Cells*. 2006;90(17):2944-2949. doi:10.1016/j.solmat.2006.05.005.

20. Kozbial A, Li Z, Sun J, et al. Understanding the intrinsic water wettability of graphite. *Carbon N Y*. 2014;74:218-225. doi:10.1016/j.carbon.2014.03.025.

21. Li Z, Wang Y, Kozbial A, et al. Effect of airborne contaminants on the wettability of supported graphene and graphite. *Nat Mater*. 2013;12(10):925-931. doi:10.1038/nmat3709.

22. Kim D, Pugno NM, Ryu S. Wetting theory for small droplets on textured solid surfaces. *Sci Rep*. 2016;6(November):37813. doi:10.1038/srep37813.

23. Nier AO, Gulbransen E. Variations in the Relative Abundance of the Carbon Isotopes. *J Am Chem Soc*. 1939;61:697-698. doi:10.1038/1691051a0.

24. Mezzi A, Kaciulis S. Surface investigation of carbon films: From diamond to graphite. *Surf Interface Anal*. 2010;42(6-7):1082-1084. doi:10.1002/sia.3348.

25. Díaz J, Paolicelli G, Ferrer S, Comin F. Separation of the. *Phys Rev B*. 1996;54(11):8064-8069. doi:10.1103/PhysRevB.54.8064.

26. Messina G, Santangelo S. *Carbon The Future Materia for Advanced Technology Applications*. (Springer, ed.). Germany; :2006.

27. Robertson J. Diamond-like amorphous carbon. *Mater Sci Eng R Reports*. 2002;37(4-6):129-281. doi:10.1016/S0927-796X(02)00005-0.

28. Bross H. From Graphite to Graphene: The Confinement of the Fermi Surface to the Line KH. *ISRN Condens Matter Phys*. 2013;2013.

29. Richter A, Ries R, Smith R, Henkel M, Wolf B. Nanoindentation of diamond, graphite and fullerene films. *Diam Relat Mater*. 2000;9(2):170-184. doi:10.1016/S0925-9635(00)00188-6.

30. Cai M, Thorpe D, Adamson DH, Schniepp HC. Methods of graphite exfoliation. *J Mater Chem*. 2012;(November):24992-25002. doi:10.1039/c2jm34517j.

31. Jeloaica L, Sidis V. DFT investigation of the adsorption of atomic hydrogen on a cluster-model graphite surface. *Chem Phys Lett*. 1999;300(1-2):157-162. doi:10.1016/S0009-2614(98)01337-2.

32. Ashraf A, Wu Y, Wang MC, Aluru NR, Dastgheib S a, Nam S. Spectroscopic investigation of the wettability of multilayer graphene using highly ordered pyrolytic graphite as a model material. *Langmuir*. 2014;30(43):12827-12836. doi:10.1021/la503089k.

33. Orimo S, Majer G, Fukunaga T, Züttel A, Schlapbach L, Fujii H. Hydrogen in the mechanically prepared nanostructured graphite. *Appl Phys Lett*. 1999;75(20):3093. doi:10.1063/1.125241.

34. Stankovich S, Piner RD, Chen X, Wu N, Nguyen T, Ruoff RS. Stable aqueous dispersions of graphitic nanoplatelets via the reduction of exfoliated graphite oxide in the presence of poly (sodium. 2006:155-158. doi:10.1039/b512799h.

35. Lebedev SG. Nanographite Films for Solid State Electronic Applications. 2013;2013(Cvd).

36. Blomquist N, Engstr??m AC, Hummelg??rd M, Andres B, Forsberg S, Olin H. Large-scale production of nanographite by tube-shear exfoliation in water. *PLoS One*. 2016;11(4):1-11. doi:10.1371/journal.pone.0154686.

37. Chen Q, Wang X, Wang Z, Liu Y, You T. Preparation of water-soluble nanographite and its application in water-based cutting fluid. *Nanoscale Res Lett*. 2013;8(1):52. doi:10.1186/1556-276X-8-52.

38. Chung DDL. A review of exfoliated graphite. *J Mater Sci*. 2016;51(1):554-568. doi:10.1007/s10853-015-9284-6.

39. Shen J, Hu Y, Li C, Qin C, Ye M. Synthesis of Amphiphilic Graphene Nanoplatelets. 2009;4(1):82-85. doi:10.1002/smll.200800988.

40. Han J, Zhang LL, Lee S, et al. Generation of B - Doped Graphene Nanoplatelets Using a Solution Process and Their Supercapacitor Applications. 2013;(1):19-26. doi:10.1021/nn3034309.

41. Chatterjee S, Wang JW, Kuo WS, et al. Mechanical reinforcement and thermal conductivity in expanded graphene nanoplatelets reinforced epoxy composites. 2012;531:6-10. doi:10.1016/j.cplett.2012.02.006.

42. Jafri RI, Rajalakshmi N, Ramaprabhu S. Nitrogen doped graphene nanoplatelets as catalyst support for oxygen reduction reaction in proton exchange membrane fuel cell. 2010:7114-7117. doi:10.1039/c0jm00467g.

43. Shao Y, Zhang S, Wang C, et al. Highly durable graphene nanoplatelets supported Pt nanocatalysts for oxygen reduction. *J Power Sources*. 2010;195(15):4600-4605. doi:10.1016/j.jpowsour.2010.02.044.

44. Labroo P, Cui Y. Analytica Chimica Acta Graphene nano-ink biosensor arrays on a microfluidic paper for multiplexed detection of metabolites. *Anal Chim Acta*. 2014;813:90-96. doi:10.1016/j.aca.2014.01.024.

45. Geim AK, Novoselov KS. The rise of graphene. *Nat Mater*. 2007;6(3):183-191.

46. Chen H, Filleter T, Chambers BA, et al. electron spectroscopy Accurate thickness measurement of graphene.

47. Castro Neto AH., Peres NMR., Novoselov KS., Geim AK., Guinea F. The electronic properties of graphene. *Rev Mod Phys*. 2009;81(1):109-162. doi:10.1103/RevModPhys.81.109.

48. Zhang Y, Pan C. Measurements of mechanical properties and number of layers of graphene from nano-indentation. *Diam Relat Mater*. 2012;24:1-5. doi:10.1016/j.diamond.2012.01.033.

49. Varykhalov A, Sanchez-Barriga J, Shikin AM, et al. Electronic and magnetic properties of quasifreestanding graphene on Ni. *Phys Rev Lett*. 2008;101(15):1-4. doi:10.1103/PhysRevLett.101.157601.

50. Lin Y. Controllable graphene N-doping with ammonia plasma. 2017;(May). doi:10.1063/1.3368697.

51. Van Nguyen C, Bartali R, Crema L, Speranza G. Effect of glass surface treatments on the deposition of highly transparent reduced graphene oxide films by dropcasting method. *Colloids Surfaces A Physicochem Eng Asp*. 2016;498:231-238. doi:10.1016/j.colsurfa.2016.03.051.

52. Royal THE, Academy S, Sciences OF. Graphene: Scientific background on the Nobel Prize in Physics 2010. *R Swedish Acad Sci*. 2010;50005(October):0-10. doi:10.1038/news.2010.620.

53. Novoselov KS. Nobel Lecture: Graphene: Materials in the Flatland. *Rev Mod Phys*. 2011;83(3):837-849. doi:10.1103/RevModPhys.83.837.

54. Tiwari A. *Innovative Graphene Technologies; Developments and Characterisation Volume1*. shawbury; 2013.

55. Zhang Y, Tan Y, Stormer HL, Kim P. Experimental observation of the quantum Hall effect and Berry ' s phase in graphene. 2005;438(November):201-204. doi:10.1038/nature04235.

56. Chen S, Brown L, Levendorf M, et al. Oxidation Resistance of Graphene- Coated Cu and Cu / Ni Alloy. 2011;(2):1321-1327.

57. Wang Y-J, Li H-X, Ji L, et al. Superior tribological properties of an amorphous carbon film with a graphite-like structure. *Chinese Phys B*. 2012;21(1):016101. doi:10.1088/1674-1056/21/1/016101.

58. Laidani N, Bartali R, Gottardi G, Anderle M, Chuste G, Bellachioma C. Production and characterization of thin a-C:(H) films for gas permeation barrier functionality against He, CO(2), N(2), O(2) and H(2)O. *J Phys Condens Matter*. 2006;18(26):5945-5959. doi:10.1088/0953-8984/18/26/014.

59. Ferrari AC, Robertson J. Interpretation of Raman spectra of disordered and amorphous carbon. *Phys Rev B*. 2000;61(20):14095-14107. doi:10.1103/PhysRevB.61.14095.

60. Gottardi G, Laidani N, Bartali R, et al. Amorphous carbon films PACVD in CH 4 – CO 2 under pulsed and continuous substrate bias conditions. 2005;14:1031-1035. doi:10.1016/j.diamond.2004.10.016.

61. Yoshida M, Tanaka T, Watanabe S, Shinohara M, Lee JW, Takagi T. Improvement of oxygen barrier of PET film with diamond-like carbon film by plasma-source ion implantation. *Surf Coatings Technol*. 2003;174-175:1033-1037. doi:10.1016/S0257-8972.

62. Bouhenguel M, Kouachi S, Bouchemma a. Calculation of the contact angle of a spherical surface with a bubble in flotation. *Desalination*. 2009;245(1-3):44-49. doi:10.1016/j.desal.2008.07.009.

63. Rankl M, Laib S, Seeger S. Surface tension properties of surface-coatings for application in biodiagnostics determined by contact angle measurements. *Colloids Surfaces B Biointerfaces*. 2003;30(3):177-186. doi:10.1016/S0927-7765(03)00085-7.

64. Gezer PG, Brodsky S, Hsiao A, Liu GL, Kokini JL. Modification of the hydrophilic/hydrophobic characteristic of zein film surfaces by contact with oxygen plasma treated PDMS and oleic acid content. *Colloids Surfaces B Biointerfaces*. 2015;135(August 2016):433-440. doi:10.1016/j.colsurfb.2015.07.006.

65. Della Volpe C, Maniglio D, Brugnara M, Siboni S, Morra M. The solid surface free energy calculation. *J Colloid Interface Sci*. 2004;271(2):434-453. doi:10.1016/j.jcis.2003.09.049.

66. Wolf D, Yip S. *Materials Interfaces Atomic Level Structure and Properties*. (Hall C&, ed.). Camnridge; 1992.

67. Nouri M, Abdollah-Zadeh A, Malek F. Effect of Welding Parameters on Dilution and Weld Bead Geometry in Cladding. *J Mater Sci Technol*. 2007;23(6).

68. Schrader ME. Work of Adhesion of a Sessile Drop to a Clean Surface 1. *J colloid Interface*. 1999;213:602-605.

69. Schrader ME. Work of Adhesion of a Sessile Drop to a Clean Surface 1. *J Colloid Interface Sci*. 1999;(213):602-605.

70. Mittal, K. L. *Contact Angle, Wettability and Adhesion*. (VSP, ed.). Utrech , Netherlands; 1993.

71. Volpe CD, Siboni S. Some Reflections on Acid–Base Solid Surface Free Energy Theories. *J Colloid Interface Sci*. 1997;195(1):121-136. doi:10.1006/jcis.1997.5124.

72. Van Oss CJ, Chaudhury MK, Good RJ. Interfacial Lifshitz-van der Waals and polar interactions in macroscopic systems. *Chem Rev*. 1988;88(6):927-941. doi:10.1021/cr00088a006.

73. Siboni S, Della Volpe C, Maniglio D, Brugnara M. The solid surface free energy calculation; II. The limits of the Zisman and of the "equation-of-state" approaches. *J Colloid Interface Sci*. 2004;271(2):454-472. doi:10.1016/j.jcis.2003.09.050.

74. Gindl M, Sinn G, Gindl W, Reiterer A, Tschegg S. A comparison of different methods to calculate the surface free energy of wood using contact angle measurements. *Colloids Surfaces A Physicochem Eng Asp*. 2001;181(1-3):279-287. doi:10.1016/S0927-7757(00)00795-0.

75. Zhu R, Cui S, Wang X. Theoretical foundation of Zisman's empirical equation for wetting of liquids on solid surfaces. *Eur J Phys*. 2010;31(2):251-256. doi:10.1088/0143-0807/31/2/001.

76. Drelich J, Miller JD, GooD R. The Effect of Drop (Bubble) Size on Advancing and Receding Contact Angles for Heterogeneous and Rough Solid Surfaces as Observed with Sessile-Drop and Captive-Bubble Techniques. *J Colloid Interface Sci*. 1996;50(179):37-50.

77. Maiolo D, Federici S, Ravelli L, Depero LE, Hamad-Schifferli K, Bergese P. Nanomechanics of surface DNA switches probed by captive contact angle. *J Colloid Interface Sci*. 2013;402:334-339. doi:10.1016/j.jcis.2013.03.069.

78. Read M.L., Morgan P.B., Kelly J.M., Codina C.M.Dynamic Contact Angle. 26(July 2011). *J. Biomaterials applications* (26) pag 85 doi:10.1177/0885328210363505.

79. Maldonado-codina C, Morgan PB. In vitro water wettability of silicone hydrogel contact lenses determined using the sessile drop and captive bubble techniques. 2007:14-16. doi:10.1002/jbm.a.

80. Brussieux C, Viers P, Roustan H, Rakib M. Controlled electrochemical gas bubble release from electrodes entirely and partially covered with hydrophobic materials. *Electrochim Acta*. 2011;56(20):7194-7201. doi:10.1016/j.electacta.2011.04.104.

81. Liao Q, Zhu X, Zheng X, Ding Y. Visualization study on the dynamics of CO2 bubbles in anode channels and performance of a DMFC. *J Power Sources*. 2007;171(2):644-651. doi:10.1016/j.jpowsour.2007.06.257.

82. Werder T, Walther JH, Jaffe RL, et al. On the Water - Carbon Interaction for Use in Molecular Dynamics Simulations of Graphite and Carbon Nanotubes. 2003:1345-1352.

83. Of S. Naphthalene as measured.

84. Fowkes , FM , Harkins, WD. J.Am.Chem.Soc. *JAmChem Soc*. 1940;62:3377-3386.

85. Adamson, AW GA. *Physical Chemistry of Surfaces*. 6th ed. (John Wiley & sons I, ed.).; 1997:Chapt. 6th.

86. Morcos I. Surface tension of stress aneealed pyrolytic graphite. *J Chem Phys*. 1972;57:1801-1802.

87. Santiso EE, Herdes C, Müller EA. On the Calculation of Solid-Fluid Contact Angles from Molecular Dynamics. 2013:3734-3745. doi:10.3390/e15093734.

88. Kozbial A, Trouba C, Liu H, Li L. Characterization of the Intrinsic Water Wettability of Graphite Using Contact Angle Measurements : Effect of Defects on Static and Dynamic Contact Angles. *Langmuir*. 2017;33:959-967. doi:10.1021/acs.langmuir.6b04193.

89. Silman H, Isserlis G, Averill ì, A. F. *Protective and Decorative Coatings for Metals*. (Ltd FP, ed.). Teddington, England; 1978.

90. Turri S. *Vernici Materiali Tecnologie Proprietà*. 4th ed. (Ambrosiana CE, ed.). Milano; 2011.

91. Montazer M, Seifollahzadeh S. Enhanced Self-cleaning , Antibacterial and UV Protection Properties of Nano TiO 2 Treated Textile through Enzymatic Pretreatment. 2011:877-883. doi:10.1111/j.1751-1097.2011.00917.x.

92. Berdichevsky Y, Khandurina J, Guttman A, Lo YH. UV/ozone modification of poly(dimethylsiloxane) microfluidic channels. *Sensors Actuators, B Chem*. 2004;97(2-3):402-408. doi:10.1016/j.snb.2003.09.022.

93. Hillborg H, Tomczak N, Ola A, Scho H, Vancso GJ. Nanoscale Hydrophobic Recovery : A Chemical Force Microscopy Study of UV / Ozone-Treated Cross-Linked Poly (dimethylsiloxane). 2004;(3):785-794.

94. Schwanninger M, Steiner M, Zobl H. Y ellowing and IR-changes of spruce wood as result of UV-irradiation. 2003;69:97-105.

95. Mellor, B. G. *Surface Coatings for Pretection against Wear*. (Woodhead Publishing Limited, ed.). Cambridge; 2006.

96. Uysal M, Akbulut H, Tokur M, Algül H, Çetinkaya T. Structural and sliding wear properties of Ag/Graphene/WC hybrid nanocomposites produced by electroless co-deposition. *J Alloys Compd*. 2016;654:185-195. doi:10.1016/j.jallcom.2015.08.264.

97. Giraudo N., Weildler P.G.m Laye F., Schwotzer M., Lahann J., Woll C., Thissen P., J. Physical Chemistry C, 2016, 120, 22455-22459

98. Hillborg H, Ankner JF, Gedde UW, Smith GD, Yasuda HK, Wikstro K. Crosslinked polydimethylsiloxane exposed to oxygen plasma studied by neutron reflectometry and other surface specific techniques. *Polymer (Guildf)*. 2000;41:6851-6863.

99. Gustavsson TG, Gubanski SM. Hydratization of the PDMS Backbone During Water Immersion Test. *IEEE-CEIDP*. 1998:269-272.

100. Bhattacharya S, Datta A, Berg JM, Gangopadhyay S. Studies on surface wettability of poly(dimethyl) siloxane (PDMS) and glass under oxygen-plasma treatment and correlation with bond strength. *J Microelectromechanical Syst*. 2005;14(3):590-597. doi:10.1109/JMEMS.2005.844746.

101. Vincent LD. *The Protective Coating User's Handbook*. Houston,Texas: Nace International; :2004.

102. Sathiyanarayanan S, Muthukrishnan S, Venkatachari G, Trivedi DC. Corrosion protection of steel by polyaniline (PANI) pigmented paint coating. 2005;53:297-301. doi:10.1016/j.porgcoat.2005.03.007.

103. Brock T, Groteklaes M, Mischke;P. *European Coating Handbook*. Hannover , Germany: Vincenz Verlag; 2000.

104. Petucci J, LeBlond C, Karimi M, Vidali G. Diffusion, adsorption, and desorption of molecular hydrogen on graphene and in graphite. *J Chem Phys*. 2013;139(4):044706. doi:10.1063/1.4813919.

105. Lee Y-H, Takashima K, Kwon D. Micromechanical analysis on residual stress-induced nanoindentation depth shifts in DLC films. *Scr Mater*. 2004;50(9):1193-1198. doi:10.1016/j.scriptamat.2004.02.009.

106. Schriver M, Regan W, Gannett WJ, Zaniewski AM, Crommie MF, Zettl A. Graphene as a long-term metal oxidation barrier: worse than nothing. *ACS Nano*. 2013;7(7):5763-5768. doi:10.1021/nn4014356.

107. Grosjean M, Zidoune M, Roue L, Huot J. Hydrogen production via hydrolysis reaction from ball-milled Mg-based materials. *Int J Hydrogen Energy*. 2006;31(1):109-119. doi:10.1016/j.ijhydene.2005.01.001.

108. Su Y, Kravets VG, Wong SL, Waters J, Geim a K, Nair RR. Impermeable barrier films and protective coatings based on reduced graphene oxide. *Nat Commun*. 2014;5:4843. doi:10.1038/ncomms5843.

109. Li C, Chen L, Chen L. Organic chemistry in water. 2006. doi:10.1039/b507207g.

110. Water. *Biology (Basel)*. https://cnx.org/contents/GFy_h8cu@9.85:pPjfgsd4@9/Water.

111. Mckeon BBB, Furukawa J, Fenstermacher S. Advanced Lead – Acid Batteries and the Development of Grid-Scale Energy Storage Systems. 2014;102(6):951-963.

112. Vroman J., Tighzert L., Biodegradable polymer. Materials 2009.2,307-344

113. Hang Y, Wang Y, Rong L, Jun H, Gui H, Li C. Applied Catalysis B : Environmental Water-soluble inorganic photocatalyst for overall water splitting. *"Applied Catal B, Environ*. 2017;209:247-252. doi:10.1016/j.apcatb.2017.03.001.

114. J.Thornton, Radiu R.,Brush S. *Lead The Facts*., 2001,RSB, ISBN:0-9542496-0-7

115. Restolho J, Mata JL, Saramago B. On the interfacial behavior of ionic liquids: surface tensions and contact angles. *J Colloid Interface Sci*. 2009;340(1):82-86. doi:10.1016/j.jcis.2009.08.013.

116. Hench LL, Clark DE. Journal of Non-Crystalline Solids 28 (1978) 83-105 © North-tlolland Publishing Company PHYSICAL CHEMISTRY OF GLASS SURFACES L.L. HENCH and D.E. CLARK. 1978;28:83-105.

117. Alloteau F, Lehuédé P, Majérus O, Charpentier T, Caurant D, Biron I. New insight into atmospheric alteration of alkali-lime silicate glasses. *Corros Sci*. 2017;122(November 2016):12-25. doi:10.1016/j.corsci.2017.03.025.

118. Králík V, Němeček J. Comparison of nanoindentation techniques for local mechanical quantification of aluminium alloy. *Mater Sci Eng A*. 2014;618:118-128. doi:10.1016/j.msea.2014.08.036.

119. Hermenau M, Riede M, Leo K, Gevorgyan SA, Krebs FC, Norrman K. Solar Energy Materials & Solar Cells Water and oxygen induced degradation of small molecule organic solar cells. *Sol Energy Mater Sol Cells*. 2011;95(5):1268-1277. doi:10.1016/j.solmat.2011.01.001.

120. Ferracane JL. Hygroscopic and hydrolytic effects in dental polymer networks. 2006:211-222. doi:10.1016/j.dental.2005.05.005.

121. Petersson L, Meier P, Kornmann X, Hillborg H. Effect of surface cleanliness of aluminium substrates on silicone rubber adhesion. *J Phys D Appl Phys*. 2011;44:034011. doi:10.1088/0022-3727/44/3/034011.

122. Technology P, Engineering HV. Hydrophobicity recovery of polydimethylsiloxane after exposure to corona discharges. 1998;39(10):1991-1998.

123. Stanton MM, Ducker RE, MacDonald JC, Lambert CR, McGimpsey WG. Super-hydrophobic, highly adhesive, polydimethylsiloxane (PDMS) surfaces. *J Colloid Interface Sci*. 2012;367(1):502-508. doi:10.1016/j.jcis.2011.07.053.

124. Tóth A, Bertóti I, Blazsó M, ánhegyi GB, Bognar A SP. Oxidative damage and recovery of silicone rubber surfaces. I. X-ray photoelectron spectroscopic study. 1994;52:1293. *J Appl Polym Sci*. 1994;53:1293.

125. Hillborg H, Gedde UW. Hydrophobicity Changes in Silicon Rubbers. *IEEE Trans Dielectr Electr Insul*. 1999;6(5):703.

126. Barch R, H-J W. On the Evaluation of Influences on the Hydrophobicity of Silicone Rubber Surfaces. *10 inter Sympho HV Eng , Montr Canada, pp 13-16, 1997*. 1997:13-16.

127. Vondracek P, Gent AN. Slow Decompositin of Silicon Rubber. *J Appl Polym Sci,*. 7:99-105.

128. Xu S, Lehmann RG, Miller JR, Chandra G. Degradation of Polydimethylsiloxanes (Silicones) as Influenced by Clay Minerals. 1998;32(9):1199-1206.

129. Thomas DK. No TitleNetwork Scission Processes in peroxide Cured Methylvnyl Silicone Rubber. *Polymer (Guildf)*. 1966;Vol.7:pp. 99-105.

130. Dinelli F, Assender HE, Kirov K, Kolosov O V. Surface morphology and crystallinity of biaxially stretched PET films on the nanoscale. 2000;41:4285-4289.

131. De Grutyer J, Mertens SF., Temmenrman E. Corrosion due to differential aeration reconsidered. *J Electroanal Chem*. 2001;506:61-62.

132. Lia X, Guib F, Hongbo Congb, C. S. Brossiab, and G. S. Frankela Z. Examination of Mechanisms for Liquid-Air-Interface Corrosion of Steel in High Level Radioactive Waste Simulants. *J Electrochem Soc*. 2013;160(11):521-530.

133. Xiaoji, LiaF., GuibHongboCongb, C.S.Brossiab, G.S.Frankela. Evaluation of Nitrate and Nitrite Reduction Kinetics Related to Liquid-Air-Interface Corrosion. *Electrochim Acta*. 117(20):299.

134. Lieberman MA, Lichtenberg AJ. *Principles of Plasma Discharges and Materials Processing*. 2nd ed. (Sons JW&, ed.). Jonh Wiley & Sons; 2005.

135. Amanat N, Nicoll AF, Ruys AJ, Mckenzie DR, James NL. Gas permeability reduction in PEEK film: Comparison of tetrahedral amorphous carbon and titanium nanofilm coatings. *J Memb Sci*. 2011. doi:10.1016/j.memsci.2011.05.019.

136. Tan B, Thomas NL. A review of the water barrier properties of polymer / clay and polymer / graphene nanocomposites. *J Memb Sci*. 2016;514:595-612. doi:10.1016/j.memsci.2016.05.026.

137. L.E N. Models for the Permeability of Filled Polymer Systems. *J Macromol A*. 1966.

138. Yano K, Usuki A, Okada A. Synthesis and Properties of Polyimide-Clay Hybrid Films. 2000;(November 1996):2289-2294.

139. Choudalakis G, Gotsis AD. Permeability of polymer / clay nanocomposites : A review. *Eur Polym J*. 2009;45(4):967-984. doi:10.1016/j.eurpolymj.2009.01.027.

140. Tseng I, Liao Y, Chiang J, Tsai M. Transparent polyimide / graphene oxide nanocomposite with improved moisture barrier property. *Mater Chem Phys*. 2012;136(1):247-253. doi:10.1016/j.matchemphys.2012.06.061.

141. Diebold U. The surface science of titanium dioxide. *Surf Sci Rep*. 2003;48(5-8):53-229.

142. Topcuoglu O, Altinkaya SA, Devrim B. Characterization of waterborne acrylic based paint films and measurement of their water vapor permeabilities. 2006;56:269-278. doi:10.1016/j.porgcoat.2006.02.003.

143. Hoivik ND, Elam JW, Linderman RJ, Bright VM, George SM, Lee YC. Atomic layer deposited protective coatings for micro-electromechanical systems $. 2003;103:100-108.

144. Massoudim R., King AD. Effect of Pressure on the Surface Tension of water adsorption of low molecular weight gases on Water at 25 °. *J Phys Chem*. 1974;78((22)):2262-2266.

145. Bayer T, Selyanchyn R, Fujikawa S, Sasaki K, Lyth SM. Spray-painted graphene oxide membrane fuel cells. *J Memb Sci*. 2017;541(April):347-357. doi:10.1016/j.memsci.2017.07.012.

146. Zhong Y, Zhen Z, Zhu H. FlatChem Graphene : Fundamental research and potential applications Solution phase methods. *FlatChem*. 2017;4:20-32. doi:10.1016/j.flatc.2017.06.008.

147. Liu H, Xu Q, Yan C, Qiao Y. Electrochimica Acta Corrosion behavior of a positive graphite electrode in vanadium redox flow battery. *Electrochim Acta*. 2011;56(24):8783-8790. doi:10.1016/j.electacta.2011.07.083.

148. Rafiee J, Rafiee M a, Yu Z-Z, Koratkar N. Superhydrophobic to superhydrophilic wetting control in graphene films. *Adv Mater*. 2010;22(19):2151-2154. doi:10.1002/adma.200903696.

149. Rathnayake RMNM, Mantilaka MMMGPG, Hara M, et al. Applied Surface Science Graphite intercalated polyaniline composite with superior anticorrosive and hydrophobic properties , as protective coating material on steel surfaces. *Appl Surf Sci*. 2017;410:445-453. doi:10.1016/j.apsusc.2017.03.119.

150. Wang B, Cunning B V., Park S-Y, Huang M, Kim J-Y, Ruoff RS. Graphene Coatings as Barrier Layers to. *ACS Nano*. 2016;10:9797-9800. doi:10.1021/acsnano.6b04363.

151. Singh BP, Jena BK, Bhattacharjee S, Besra L. Development of oxidation and corrosion resistance hydrophobic graphene oxide-polymer composite coating on copper. *Surf Coatings Technol*. 2013;232:475-481. doi:10.1016/j.surfcoat.2013.06.004.

152. Sangermano M, Periolatto M, Signore V, Spena PR. Progress in Organic Coatings Improvement of the water-vapor barrier properties of an uv-cured epoxy coating containing

graphite oxide nanoplatelets. *Prog Org Coatings*. 2017;103:152-155. doi:10.1016/j.porgcoat.2016.10.032.

153. Topsakal M. Graphene coatings : An efficient protection from oxidation. 2012;155445:1-7. doi:10.1103/PhysRevB.85.155445.

154. Hsieh Y, Hofmann M, Chang K, Jhu JG, Li Y, Chen KY. Supplementary Material Complete Corrosion Inhibition through Graphene Defect Passivation. :1-10.

155. Mayavan S, Siva T, Sathiyanarayanan S. Graphene ink as a corrosion inhibiting blanket for Iron in aggressive chloride environment. *RSC Adv*. 2013;3(47):24868-24871.

3. Materials and Methods

3.1 Contact angle of liquid on surface

3.1.1 Sessile Drop Contact angle (SCA)

The contact angle measurement is a versatile technique which produces reliable data, for these reasons, the measurement of the contact angle is one of the most used techniques to study the interaction of a liquid and a solid. Precise amounts of liquids and a dedicated software were used. The software, Drop Analysis, uses algorithms of image processing based on the polynomial fit of the drop profile. The software is programmed in Java and was designed by A.F Stalder, Biomedical Imaging Group, Ecole Polytechnique Fédérale de Lusanne (EPFL),[1]. The process to evaluate the contact angle need two steps. The first step is the determination of the profile of the droplet using a cubic B-spline function. The operator only needs to define the border of the initial drop with fifteen points (red and blue profiles figure 3.1). The second step is the optimisation of the profile by using the method of the directional components of the light gradient. The calculation is iterated 3000 times, then the best profile is obtained and the tangent at the triple point is calculated.

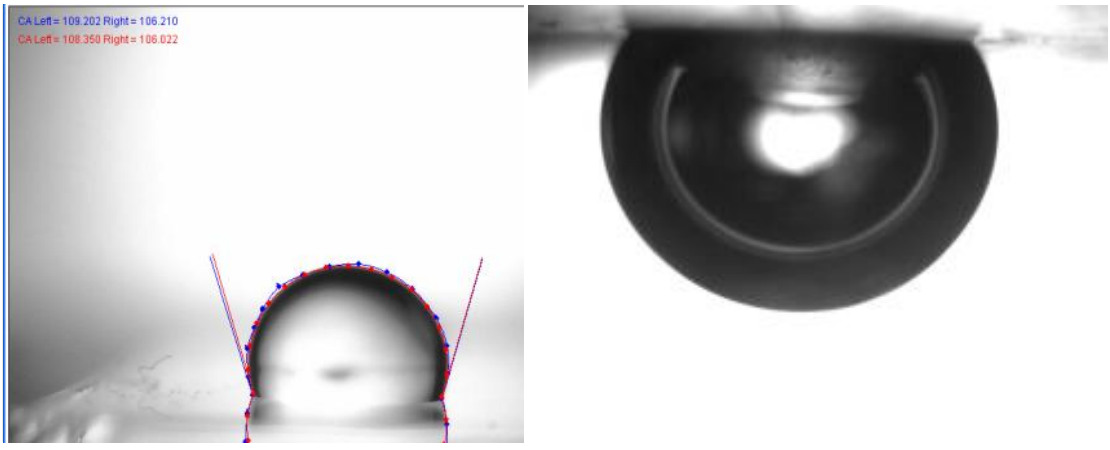

Figure 3.1 Water drop on PDMS and estimation of contact angle using Drop analysis software, blue line is the setting profile, and redline is final profile after 3000 interactions

The drop image was acquired using a C-MOS camera provided with an optical system with microlens. The image magnification is 50X and the image resolution 640*1280 pixel. The camera

can take photographs and capture video 640 * 480 at 60 frames per second. The focal length of the optical system is fixed, then the focus is made placing the micro camera on an adjustable slit with a precision micrometre, resolution of ±1 micron. The fixed optical system has the great advantage that all the images are captured on the same optical plane and with the same depth of field, improving the systematic approach to measurement. The focus in this type of instrument is slower than the traditional optical method and requires a precise pre-calibration before starting the measurements. Moreover, the volume of the drops measurable is limited, in our case from 0.5µl to 10 µl. Figure 3.2 shows the diagram of the home-made equipment used to determine the contact angle. The system consists of a sample holder with the vertical movement of precision (+ / - 1 micron). The illumination consists of a white light LED with a light diffuser. A continuously emitted cold light is chosen, so the sample is not heated by the light source, and fluctuations of the image brightness are avoided. To have a uniform light beam between the illuminator LEDs and the sample holder, there is a light diffuser. The drops of water are placed on the sample in two ways:

- Hamilton syringes 10µl and 5 µl
- micropipette Socorex Acura 825 0.5 µl - 2 µl

The acquisition is via USB cable, and the data are acquired from a computer with Pentium III 1GHz Software was released with the camera, U-eye.

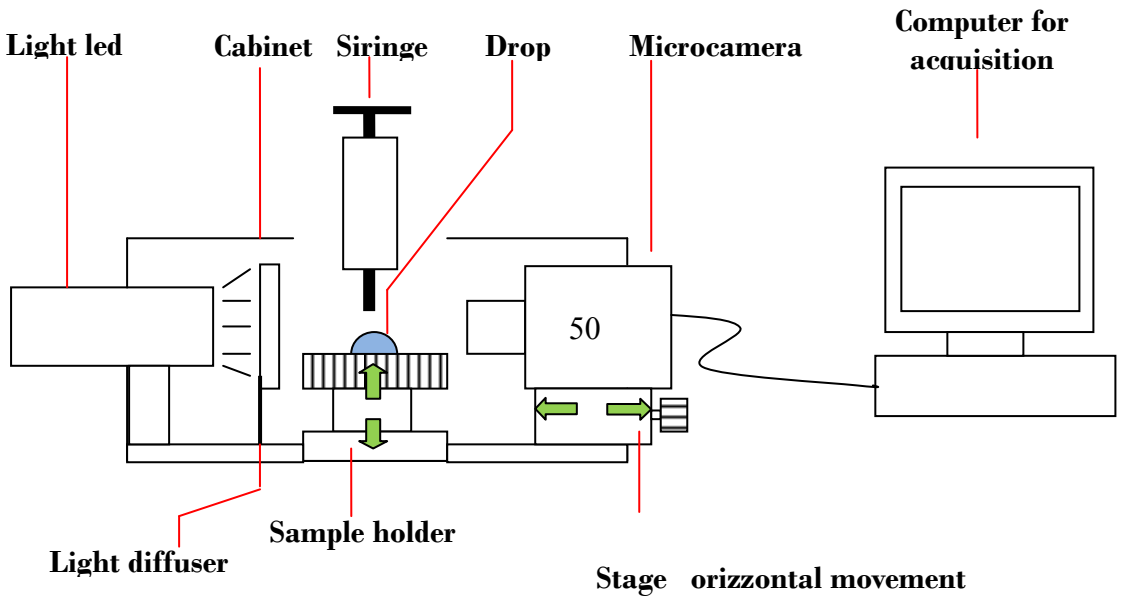

Figure 3.2 Sketch of sessile drop contact angle measurement set-up.

Through the instrument and image processing with Drop Snake software, it is possible to determine

the contact angle geometrical dimensions, the inclination and the volume of the drop [1]. The measuring range of the instrument is from 2-3° to 180° with a resolution of ± 2°.

3.1.2 Captive Contact Angle (CCA)-Bubble

The captive contact angle was measured using the set up reported in Figure 3.3. The cell of the captive contact angle is composed of a plastic cuvette (1.5cm × 1.5 cm) filled with deionized water. The needle of a microsyringe is inserted in a microfore present on one side of the cuvette. The tip shape of the needle is flat and was modified using silicon carbide sandpaper 1200. The shape of the tip was modified to obtain in a repeatable mode bubbles with dimensions of 1mm. The sample is held with bi-adhesive tape on a polyethylene raft. Argon, air, nitrogen, hydrogen and helium were inserted into the cell using a syringe.

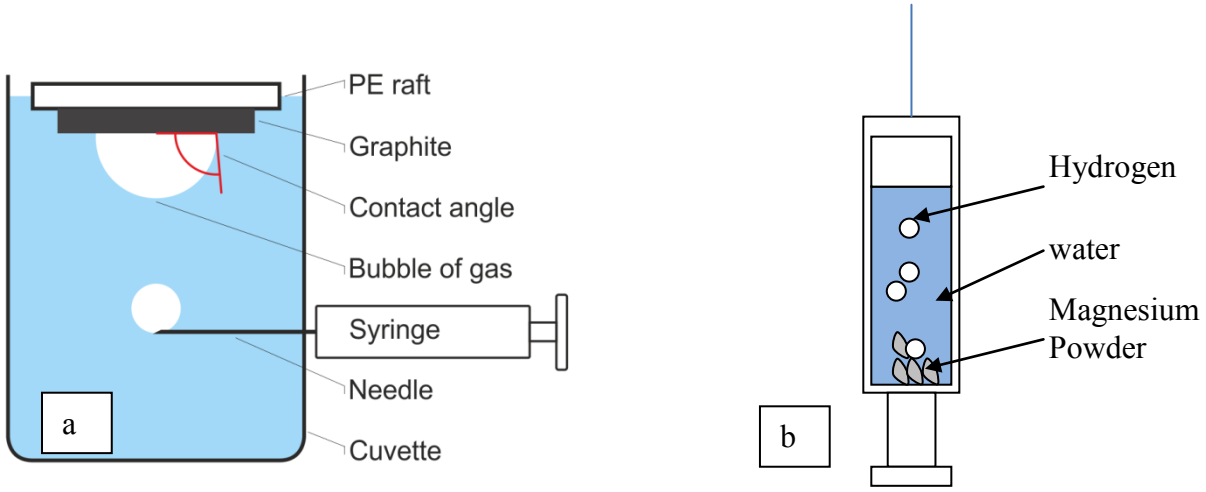

Figure 3.3. Captive bubble method, set up used for air, He, H_2, Ar and N_2 gases (a) and set up for hydrogen (b).

The gases have to be collected in a balloon filled with various gases He, Air, Ar N2. The syringe was filled and emptied five times to reduce as much as possible the percentage of contaminants. For hydrogen, due to its high explosivity, we developed a hydrogen microgenerator to produce H2 by reaction of Mg with water giving MgOH and pure hydrogen[2]. Mg powder (99.99% purity provided by Sigma Aldrich) was immersed in water and the produced H_2 loaded into a syringe, see Figure 3.3b. The hydrogen bubbles, in the captive bubble cell, are inserted with 1 ml of hydrogen in the

syringe.

3.1.3 Time evolution of Contact Angle (T.C.A)

To understand the reactivity of a liquid with a surface, we studied the temporal evolution of the liquid drop contact angle. This was developed using coated silicon as substrate and buffered hydrofluoridic acid (BHF 7:1 dilute in water) as a reactive solution. We used BHF instead of HF because etches rate of HF on is too quickly. The silicon was covered by the inert material (OIRTM674 photoresist from Fujifilm Electronic Materials) and by the following ceramic layers that can be etched by BHF [3]:

- SiOx films grown from tetraethylorthosilicate (TEOS) precursor in a low-pressure chemical vapour deposition (LPCVD) chamber;
- Silicon nitride (SiNx) films grown via PECVD;
- Silicon oxynitride (SiONx) films grown via PECVD. as titanium nitrate. We used a positive OIRTM674 photoresist from Fujifilm Electronic

TEOS was annealed in an N_2 ambient for 90 min at a temperature of 1050 °C. The materials composition, their growth or deposition conditions are detailed below:

1) TEOS oxide – LPCVD deposition from tetraethylorthosilicate Si(OC2H5)4 at 710 ◦C for 138 min, thickness of 1010 nm;
2) 4. SiNx – PECVD deposition at 300 ◦C from a mixture of nitrogen (N2, 3200 sccm), silane (SiH4, 40 sccm) and ammonia (NH3, 40 sccm) gases using an alternation between the high and low plasma frequencies (duty cycle of 13.56 MHz for 50 s and 308 kHz for 10 s), 437 nm;
3) 5. SiONx – PECVD deposition at 300 ◦C from a mixture of nitrous oxide (N2O, 100 sccm), nitrogen (N2, 17,150 sccm), silane (SiH4, 50 sccm) and ammonia (NH3, 65 sccm) gases using low frequency (380 kHz) plasma, 478 nm.

The time evolution of BHF contact angle was acquired with contact angle instrument using a video, and the video frames were extracted in the temporal range between 27ms until 1000 ms. We used this time scaling because the BHF react in a fast mode with the various kind of surfaces. Only BHF

on OIR showed a stable behaviour in this timescale. OIR, in fact, is a dispersive surface, with a surface tension of 40mJ. Therefore it does not react with the BHF. BHF drops on SiONx Teos, and SiN layer showed a fast variation of the contact angle because BHF reacted with materials and induced the fast etching of the surface.

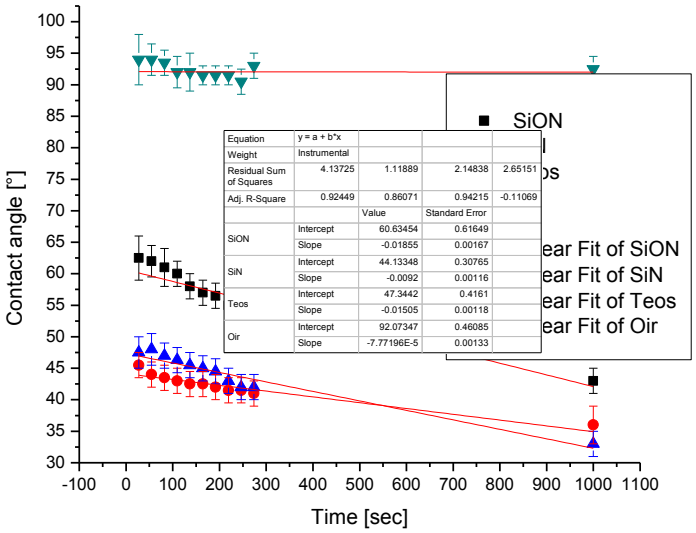

Figure 3.4 Variation of contact angle as function of time

As reported in figure 3.4. the decrease of the contact angle appeared monotonically, and the trend can be fitted by linear fit:

$$Contact\ Angle = \ a + b(time) \qquad (3.1)$$

Where a is intercept and b is the slope of the fit are, reported in Table 3.1. The intercept gives the intrinsic interaction of the liquid with the surface without any reaction, and b indicates the velocity of variation contact angle that is due to the velocity of reaction between BHF and materials surface. The value of intercepts and slopes estimated on the surfaces are reported in Table 3.1

Table 3.1 Fitting parameters in time evolution BHF C.A on OIR, SiON, SiN, and TEOS

	slope	**er**	**Intercept °/ms**	**er**
OIR	-0.0000772	0.00013	92	0.5
SiON	-0.01855	0.00167	60.6	0.62
SIN	-0.0092	0.00116	44.1	0.31
TEOS	-0.0151	0.00152	46.7	0.52

The OIR show a negligible slope value, $-7.7*10^{-5}$ °/ms and an intercept of 92°. The fastest variation was observed on SiON -0.01855 °/msec and on TEOS-0.015 °/msec while the SiN showed a slope of only -0.0092 °/msec. The TEOS and SION, in fact, are also the materials that usually show the highest etching rate with BHF (86 and 46 nm /min respectively) and SIN is the materials with lowest etching rate (26 nm/min).[3].

The time evolution contact angle is a semi-quantitative method to estimate the reactive interaction of liquid on the surface. This methodology was used to estimate the reactivity on lead surface see chapter 6.

3.1.4 Sessile Contact angle in controlled atmosphere

The solid-liquid interaction has also been studied in a controlled atmosphere. In the related experiments, the sessile drop contact angle measurement instrument was inserted in a glove bag. Inside of the glove bag were inserted all the necessary tools: microsyringe, liquids, electrical connection, light, and an oxygen sensor (Crowcon), figure 3.5. The glow bag was filled and emptied at least five times, or until the percentage of oxygen is less than 2%; this value is the detection limit of the oxygen sensor.

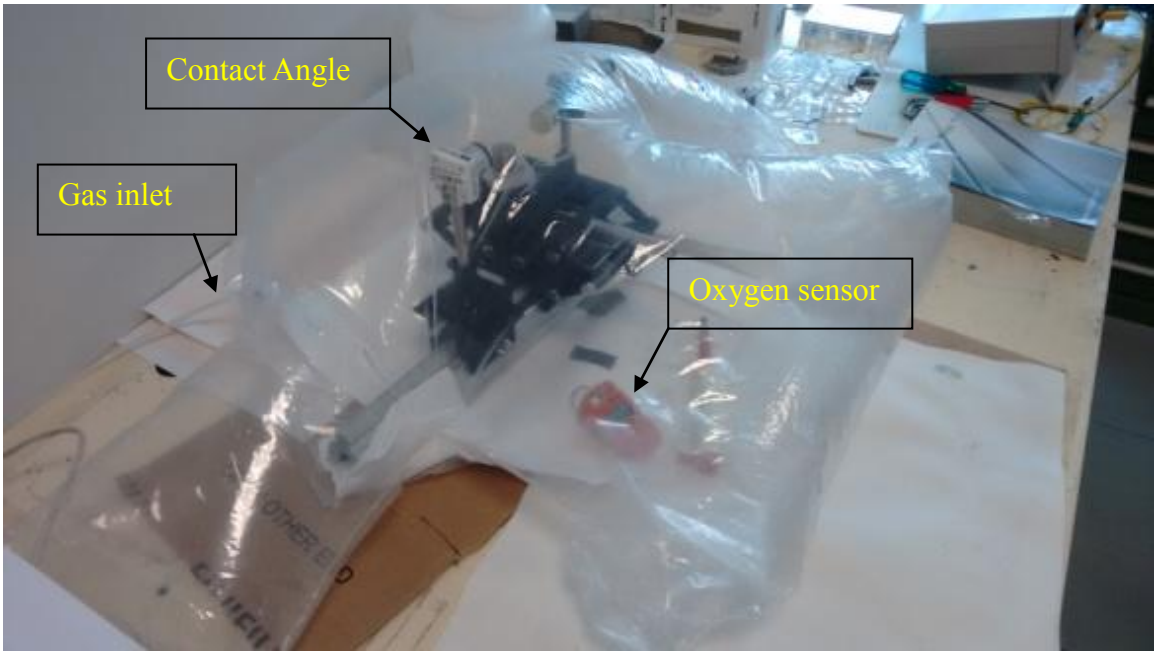

Figure 3.5 Sessile drop contact angle measurement set-up in the glove bag filled with argon.

The sessile drop contact angle was conducted using argon, helium, nitrogen gas with a nominal purity of 99.9990% (N50). The oxygen and hydrogen were not used due to their explosivity.

3.2 Surface characterisation

3.2.1 X-ray photoelectron emission spectroscopy (XPS)

In the surface science field, it is essential to know the surface chemical properties of material. One of the most important techniques to determine the surface chemical properties is the X-Ray Photoelectron Spectroscopy, more commonly known as electron spectroscopy for chemical analysis (ESCA). In Esca analysis, a sample is irradiated by monoenergetic soft x-rays and the electron emitted by the photoelectric effect is analyzed in energy. MgKα x-rays (1253.6 eV) or AlK_{α} (1486.6 eV) are usually used. These photons have limited penetrating power solid, of the order of 1-*10 micrometres. They interact with atoms in this surface regions by the photoelectric effect, causing electrons to be emitted. The emitted electrons have a kinetic energy given by:

$$KE = h\nu - BE - \phi_s \qquad (3.2)$$

where $h\nu$ is the energy of the photon, BE is the binding energy of the atomic orbital from which the electron originated and ϕ_s ids the spectrometer work functions [4].
The binding energy may be regarded as an ionization energy of the atom for the shell involved. If we consider a single electron interaction the binding energy of the electron is equal to the orbital energy E with a negative sign:

$$E_B = Ef_{initia\,(n-1)} - E_{initial(n)}E = -\varepsilon \qquad (3.3)$$

This approximation does not take into accounts the effect of surrounding electrons due to the positive hole created by the ejected photoelectron[5]. This approximation of the photoemission effect implies that the rearrangement of surrounding electrons around the atom is neglected. The electronic configuration is influenced profoundly by the chemical bonding, the electronegativity and oxidation state of the neighbouring atoms can change the electronic configuration, with the appearance of BE shift or modifications in the line shape of the peaks. Although the core level binding energies of a given element are sufficiently unique to allow the precise identification, they

are not a fixed value. Information from these shifts provides, using curve fittings, a semi-quantitative method for chemical analysis. The instrumental resolution is critical to assign the chemical state of atomic species accurately. For instance, the Carbon-Carbon bond shows a C1s peak at a binding energy at 284.5eV while the carbon-oxygen single bonded shows a component C1s at 286.5eV and carbon-oxygen double bonded C=O show C1s components at 289 eV [6,7,8,9]. Peak width is due to the instrumental resolution and the lifetime of the positive core hole created by photoemission process [10]. The instruments used in this work were high-resolution XPS, Kratos Ultra and Scienta Esca 300, with have an energy resolution of 0.3 eV, figure 3.6

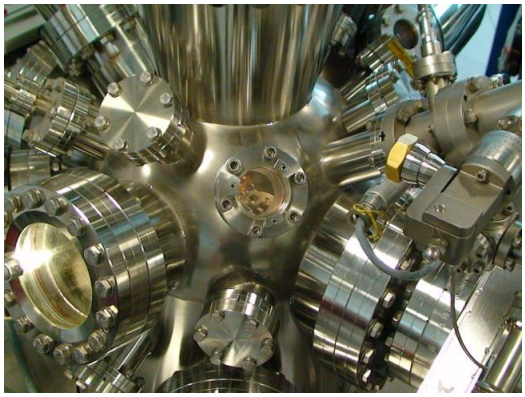

Figure 3.6 Picture of XPS Scientia Esca 300

By XPS analysis, chemical species on the surface like Oxygen, Nitrogen can be easily detected, and with an accurate calibration, a semiquantitative estimation of the surface chemical composition and semiquantitative estimation of different kinds of bonding can be done[11,12,13].The semiquantitative estimation of the amount of the bonds can be done deconvolving the shape of XPS peaks in components. In this work we used R-Studio as software, that is an open source software which was adapted to XPS elaboration data by Speranza G. and Canteri R. The peak background subtraction was performed by using a Shirley function and the Gaussian curves were used to fit multi-component peaks, except for C1s in sp^2C-sp^2C bondings, for which a (Doniach-Sunjic) function was applied for the peak fitting. The element quantification was done taking into account the area of each peak component corrected by a sensitivity factor for each element.

3.2.2 Raman Spectroscopy (RS)

When the material interacts with photons, the photons can be scattered in resonant and in a non-resonant mode. When the photon is dispersed in a non-resonant manner, it can scatter with the

matter in an elastic or in a non-elastic way. The elastic scattering is known as Scattering Rayleigh, while the non-elastic interaction is known as Raman.In the Raman scattering, therefore, there is a release or gain of energy during the scattering process [14,15]. Raman effect is widely used to study carbon materials and in particular graphene-based material. In the Raman analysis, the materials are illuminated by monochromatic light (laser), and the shift in the energy of photons can be detected by a monochromator and by a detector. Different chemical bonds show different vibrations modes that can promote different Raman scattering, and therefore a different spectrum, e.g., of C-H bond is different from a C-O bond, see Table 3.2.

Table 3.2

Functional group	**Region (cm^{-1})**
=) C-H	3000-3100
C=O	1690-1820
C=N	1610-1680
v) C=C	1500-1900

For graphitic material, several Raman modes can be identified: the D band (~1350 cm-1), G band (~1580 cm-1) and the 2D band (~2700 cm-1). The G band is the only band coming from a first-order Raman scattering process in graphene [16].

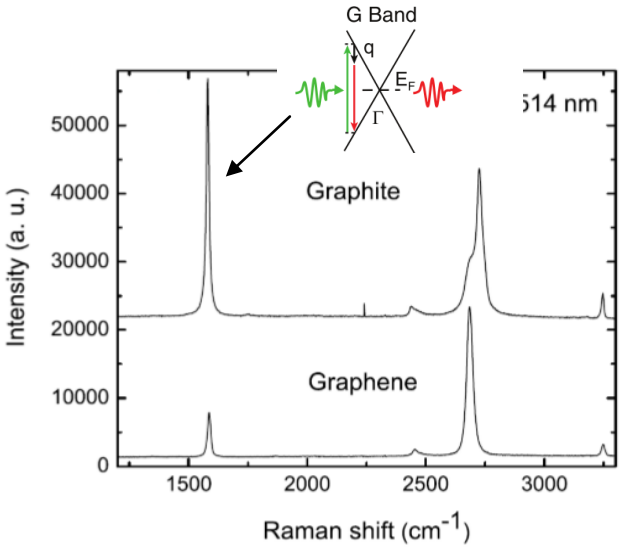

Figure 3.7 Raman spectra of graphite and graphene [17,18], G band transition is indicated by the arrow.

On the other hand, the D band and 2D band originate from a second-order process, involving one ITO (in-plane transverse optical) and one defect for the D band or two iTO phonons in the case of a 2D band.[17] The 2D band is approximately twice the D band frequency and does not require any defect for its activation[19]. Also, the D band production involves two scattering processes: one elastic scattering induced by intrinsic defects in the crystal and one inelastic scattering through emitting a photon, as shown in figure 3.7. Unlike the D band which needs intrinsic defect for its activation, the 2D band consists of two inelastic scattering processes and results in two photons formation. Although the G band frequency is sensitive to many external factors, such as doping level, strain, its integrated intensity IG is more resistant to these environmental factors and often remains constant under the same laser excitation frequency , figure3.8. Due to this robustness, IG is often used as a reference to which intensities of other peaks (like D band) are compared [18,20]. For example, we use the ID/IG ratio to evaluate the defect density on graphene surface after the plasma treatment.

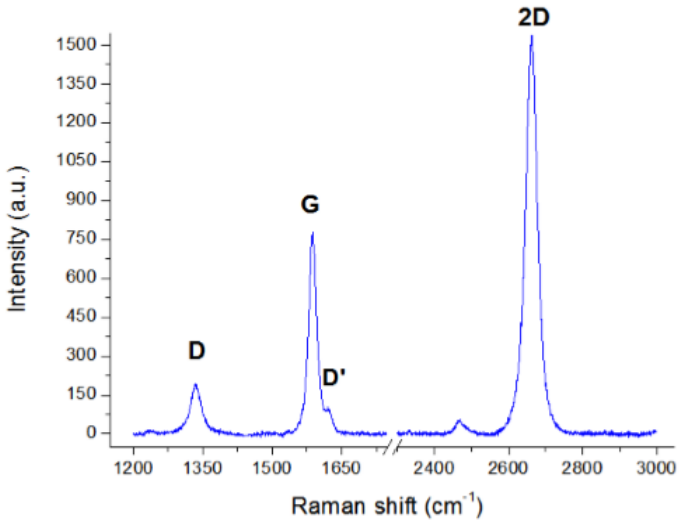

Figure 3.8 Raman spectra on multilayer of graphene, D D' and 2D peak are present. The Raman process for D and the 2D peaks is depicted on the graph.[18]

In addition to the three main peaks, the D' peak is observable, it is like the double resonance in D, but the process happens in intra-valley. This mechanism is also related to another weak defect and involves an iLO phonon mode near the Γ point. The intensity ratio of 2D and G peaks. I2D/IG is used to determine the number of basal layers in graphene-based materials qualitatively. The typical

value I2D/IG of a single layer of graphene is 2, while for the double layer it is 1, for few-layer 0.8 and multilayer <0.5. The instruments used in this work are a) Micro Raman Aramis Horiba Jobib Yvon , equipped with a laser with a laser at 532 nm (2.33 eV energy) and b) Olympus IX71 Raman instrument with Nd: YAG laser with a wavelength of 532 nm (NL202, Ekspla) as the excitation source and equipped with AFM microscope.

Figure 3.9 MicroRaman Aramis Horiba Jobin Yovon

3.3.3 X-ray Diffraction (XRD)

XRD is based on the elastic scattering of x-rays from structures having long-range order. Atoms and molecules that compose substances are commonly arranged at a distance ranging from 0.1 to 0.5 nm. When irradiated with a parallel beam of monochromatic X-rays having a wavelength approximately equivalent to the inter-atomic or intermolecular distance, the atomic lattice of the sample operate as a three-dimensional grating, and the X-rays are diffracted from the crystal lattice at specific angles according to the Bragg law. It provides information on structure, phases, preferred crystal orientations and other structural parameters such as crystallite size, crystallinity, strain and crystal defects.

If the sample is a crystal, X-rays are diffracted only in directions verifying the Bragg condition:

$$2dsin\theta = n\lambda \qquad (3.4)$$

where d is the distance between crystal planes, 2θ the Bragg angle, n an integer, and λ the wavelength of the X-rays. Each crystal has its signature: the position of the peaks depends on the crystal symmetry and the size of the elementary cell of the lattice. Crystalline phases present in a sample can be identified by comparison with x-ray diffraction curves compiled in standard

databases .The shape of each Bragg peak results from a convolution of the crystallite size, of the experimental resolution function and internal stress. If we assume that stress is weak and if the resolution of the setup is good enough, the size can be calculated from the full width at half maximum (FWHM) of the peak with Scherrer's equation 3.5[21]:

$$Size = \frac{0.9\lambda}{(with) * cos\theta} \qquad (3.5)$$

where (width) = $((FWHM)^2-(GW)^2)^{1/2}$, in radian, and GW is the diffractometer broadening.
X-ray diffractometer used in this project was equipped with *Cu* K_α radiation at an incident angle of 3 in steps of 0.02° (Italstructures APD2000), Figure 3.10

Figure 3.10 XRD APD 2000

3.3.4 Optical microscopy (O.M.)

The optical microscope is used to obtain information by light transmission through or reflected from the surface of the material. Reflected light microscopy is a widely used technique to study the interaction of compounds and multiphase carbon materials. Magnified images up to 1000x are available, permitting examination of the structure with a dimension of the order of one micron. Polarised light is used to study the interference colours generated due to the orientation of the

graphitic lamella. The yellow, blue, purple colour is useful to determine the orientation. Yellow blue is due to prismatic edges exposed to the light. Purple indicates the basal plane surface perpendicular to the light [22]. The purple colour indicates isotropic surface, and the colour does not change during the rotating of the specimen. The glassy carbon shows an isotropic purple colour, but usually, the purple is darker the for lamellar graphite. Optical microscopy can thus be used to evaluate the density the dimension and size of a constituent of defects and the porosity. Moreover, it can be employed to determine the presence of graphite, graphene as a single layer and multilayers thanks the adsorption of the light[22].

3.3.5 Scanning electron microscopy (SEM)

Scanning electron microscopy (SEM) is used primarily for the study of the surface topography of solids. It provides a depth of focus more significant than an optical microscope, the resolving power of SEM can be less than 3nm that is 3000 higher of an optical microscope. SEM operates by focusing an electron beam passing through an evacuated column equipped with an electrostatic lens onto the specimen surface [14]. The electron beam is rastered over the surface, and the inelastic scattered secondary electrons are collected by sensors like scintillator counters, and the signal can be modulated to increase or reduce the contrast difference in secondary emission result from changes in surface topography.When materials are bombarded by high-energy electrons (10 Kev = characteristic electron beam), X-ray fluorescence radiation is produced. It is possible to obtain X-ray spectra directly on the area as seen by electron beam by incorporating energy or wavelength dispersive spectrometer directly into the instrument.

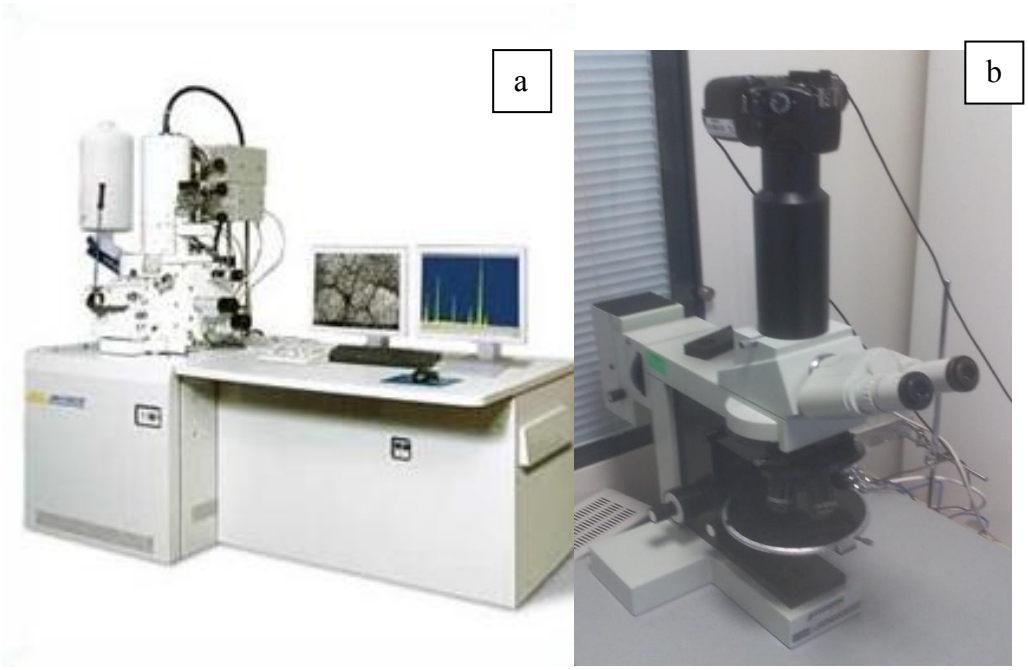

Figure 3.11 Picture of SEM Jeol JSM7401F (a) and Optical Microscope Jena SJ1000 (b).

In this work, Joel JSM 7401F was used. This instrument is equipped with cold field emission source, with Secondary Electron detectors (SE) and Backscattered Electron Detectors (BSE) both "in lens" and "in chamber", offers a nominal resolution of 0,8nm at 30kV and 1,5 nm at 1kV. A sample holder bias reduces the efficient beam energy and enhances the resolution at low tension (0.1 kV), thus improving performances while charging effects are minimized.

3.4 Surface modification of graphitic materials

3.4.1 Plasma Discharge

The history of the 19th century to the plasma starts with W. Crookes, who defined the plasma as a state of the ionized gas. The term was coined by I. Plasma Langmuir in 1929 to denote the area of the glow discharge in mercury vapour.[23] The name derives from the Greek plasmas and indicates something moldable. In any gas with a temperature higher of absolute zero some ionised atoms are present. The charged particles strongly influence the properties of the gas only if their concentrations are such that the space charge created by it restricts the motion of gas particles. When the concentration of ion-electron increase this limitation becomes more essential and the

interactions of a charged particle, positive and negative, results in the keeping of neutrality within a macroscopic volume comparable with the volume of the gas this kind of gas is called plasma [24]. Due to the mobility of the charges in plasmas coulomb forces dominate, and this implies that a particle interacts with all the other particles of the system. In the highly ionised gas then the kinetic theory of gases is no longer valid, particularly at low pressures where the effects of the electromagnetic forces are much stronger than the effects due to the collisions of the particle. There are different methods, such as an increase in temperature or the application of electromagnetic fields to activate a plasma discharge. The latter method is mainly used in the apparatus for research, and it consists of applying a potential difference between two electrodes. The applied potential can be continuous (DC discharge) or alternating, with frequencies ranging from radio frequency (RF discharge) to Microwave (Microwave discharge).[25]. In general, in the plasma, the density of the ions (Ni) is equal to the electron density (ne) to keep the global neutrality. The electrons play a vital role because electrons are the source of the ionisation and excitation of neutral atoms. Ions, on the other hand, play a fundamental role in the chemical reactions that occur in the plasma discharge. The relationship between the concentration of ions (ni) and the total concentration constituted by ions, electrons and neutral atoms is called the degree of ionization and is denoted by α, Table 3.3. The degree of ionization varied as a function of the application, for instance in the deposition process the degree of ionization is 10^{-6} while in the electron cyclotron resonance α is 10.000-time higher

Table 3.3 In the table below we can see how α varies in some important applications of plasma [26]

Type	Pressure (torr)	Ion density (cm^{-3})	Ionization degree
Deposition/etching Treatment	<10	$<10^{10}$	10^{-6}
Reactive ion Etching	10^{-2} /10^{-1}	10^{10}	$>10^{-6}$
Magnetron sputtering	10^{-3}	10^{11}	10^{-6}/10^{-2}
Electron cyclotron resonance	$<10^{-4}$/10^{-2}	10^{12}	$<10^{-1}$

In a first approximation in the plasma discharge, there are two types of systems: the first composed of only heavy species, ions and neutral, the second due to electrons.[27] In a generation of plasma by radio frequency electrons gain energy fast from the electric field and they collide with heavy species if the energy is high enough they can energise the plasma via excitation and ionisation

collisions. The two systems, heavy particles and electrons, can be described by specific temperatures. The condition of thermodynamic equilibrium is given by:

$$Tg = Ti = Te \quad (3.6)$$

Where Tg is gas temperature, Ti ion Temperature and Te is electron temperature. The plasma that satisfies the condition of thermodynamic equilibrium is called in local thermodynamic equilibrium (LTE thermodynamic local equilibrium), while those who do not meet are called non –LTE. Usually, in the plasma where the temperature of the atoms is much less than the electron temperature is defined cold plasma, and this kind of plasma is typically used for the surface treatment. In the low-pressure plasma (less than 100 Torr) the temperature of the electrons is higher than that of the gaseous system (Te is of the order of magnitude of 10^4 K), figure 3.12.
The energy transferred during neutral electron collisions is small, due to the small mass of the electron, but electron instead of neutral are continuously accelerated by an electric field, so the electron continues to increase their kinetic energy and therefore temperature. The electron starts to transfer the energy to neutral when they have enough energy to promote an inelastic collision, like ionization. The high temperature does not cause structural problems since at low pressures there is a low electron density which also has a low ability to conduct heat to the species heavy, so low amount of heat is transferred to the particles and the objects with which the plasma is in contact.

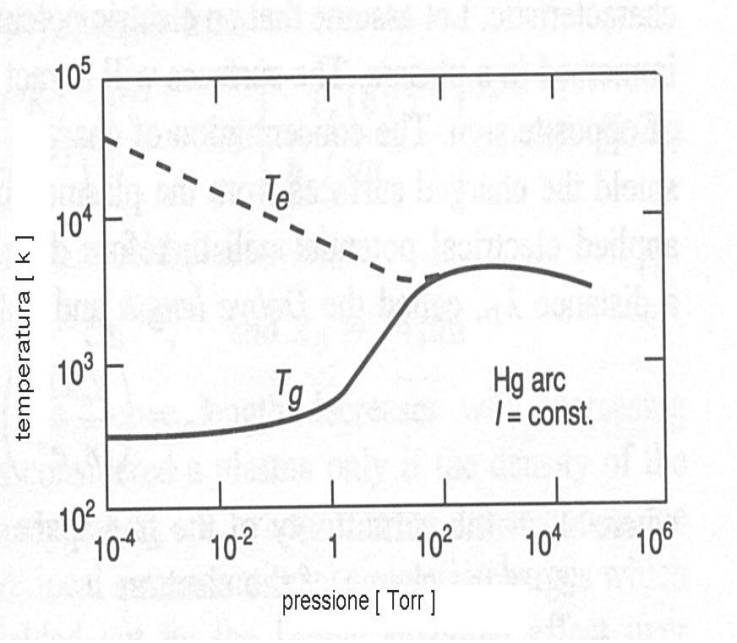

Figure 3.12 Temperature of the gas Tg and electron Temperature Te in Hg discharge.

3.4.2 Plasma Treatment

The plasma discharge can interact with matter, and this induces three main phenomena:
a) the energetic species present in the plasma discharge bombard the matter and this induces the erosion of surface (sputtering).
b) modification of the first surface layers of a material by grafting or substituting functional groups (Plasma treatment)
c) ablation of material produced by reactions that occur between the surface and the active species generated by the plasma (Plasma Etching).

The surface treatment with plasmas is very interesting for the soft and low melting point materials like polymers. The low temperature of the cold plasma, in fact, avoids the degradation of the bulk and allows a selective functionalization of the most superficial layers. There is, therefore, no addition of material (deposition) or subtraction (etching) of material but only modification of the surface. The modification of the surface occurs via two processes a) grafting of chemical groups b) crosslinking of the polymer chains (casing).
In grafting processes, functional groups are attached to some chemical species on the surface while in the crosslinking, a long polymer chain are attached at certain points to one another, Figure 3.13.

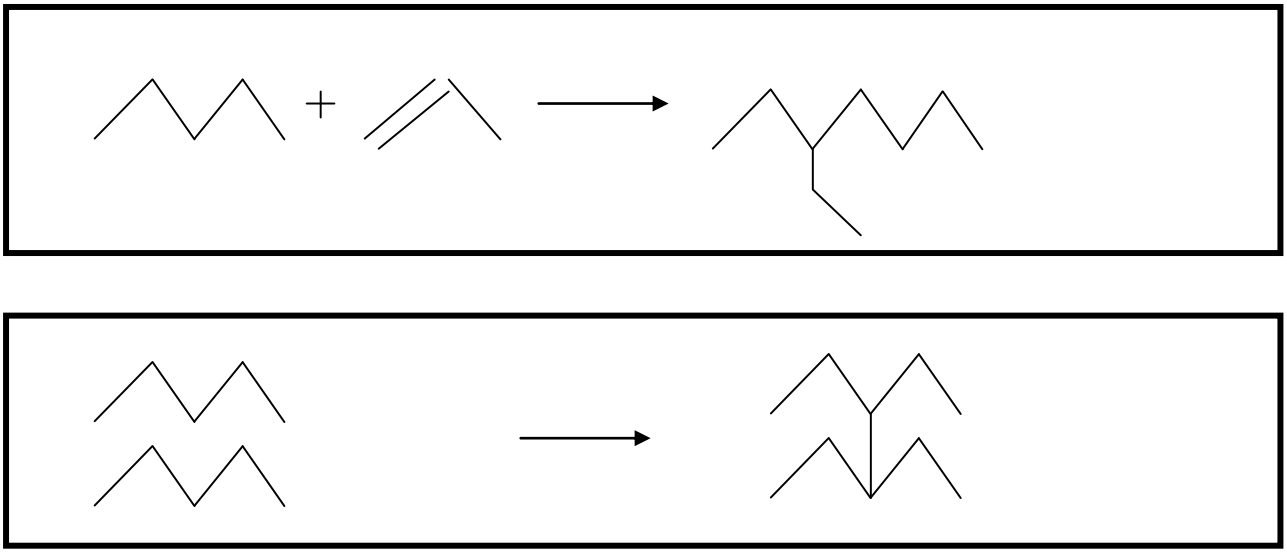

Figure 3.13 Process of Grafting and crosslinking of the polymers both are activated by physical and chemical processes of the plasma.

The plasma treatment of surfaces is many cases forerun by the removing of the atoms from the surface (etching), Figure 3.14. The etching are usually induced by reactive species produced in a plasma discharge, like atomic oxygen [28,29].

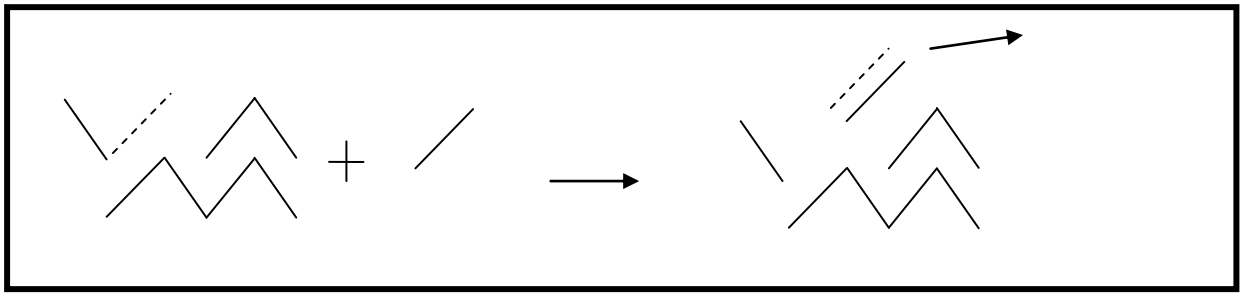

Figure 3.14 Sketch of etching process on the surface.

The local etching of surface structure produces vacancies or dangling bonds that are very prone to react with other chemical species present in the plasma discharge.

3.4.3 Chemical and physical processes in plasma discharge

In plasmas at low temperature and low pressure, the system is, usually, excited with alternative electrical power in radio – frequency range. The energy transferred to the system is mainly acquired by the electrons that have a high mobility. The electrons within the plasma that have gained energy can trigger a whole series of processes including ions or molecules excitation, ionization or dissociation. The product of these processes is a medium in which there are at a relatively high concentration of electrons, ions, ionized molecules, dissociated molecules, atoms and molecules metastable excited states. In this medium, the reactions can occur in the plasma (homogeneous reactions) or between the plasma and the material surface (heterogeneous reaction). Among the principal homogeneous reactions their a) excitation, b) dissociative attachment, c) dissociation and d) Ionization.

In excitation, the impact of an electron, with sufficient energy, with heavy species leads to the production of excited states of atoms or molecules like:

$$e + A \rightarrow e + A^* \quad (3.7)$$

$$e + A_2 \rightarrow e + A_2^* \quad (3.8)$$

$$e + AB \rightarrow e + AB^* \quad (3.9)$$

After excitation of vibrational, rotational or electronic states the species (atoms or molecules) returns to the ground state by emitting energy in the form of electromagnetic radiation in producing UV rays, visible light, or IR and this is a typical source of light in the discharge.

The dissociative attack occurs in electronegative gases; electrons at low power (few eV), can be attached to the molecules of the gas, leading to the formation of an excited state, electronically repulsive and producing negative ions:

$$e + AB \rightarrow A + B^- \quad (3.10)$$

An example is given by the oxygen dissociative attachment:

$$e + O_2 \rightarrow e + 2O \rightarrow O + O^- \quad (3.11)$$

The atomic oxygen formed by dissociative attachment is particularly reactive with the organic species and usually leads to the formation of CO_2, CO, and H_2O.

This type of reaction is very important in many processes including the stripping of the photo-resist and clearing in plasma [30].

Dissociation occurs by an inelastic collision between energetic electrons and molecules as:

$$e + AB \rightarrow e + A + B \quad (3.12)$$

It is typical of H_2 plasma if the electron strikes with enough energy (8.8 eV).

Ionization is due to the electron impact with a heavy species that. as a result, produces a positive ion and releases another electron. Ionization requires more energy than the above processes, with activation energies of the order of 7-15 eV (for O_2, the first ionization potential is 12eV [29]. The ionization process is a fundamental process to maintain the plasma discharge. In the heterogeneous reactions, electrons play an essential role; in fact electrons have a higher mobility than ions (me << mi), then every surface in contact with the plasma is surrounded by a layer of negative charges. At steady state, it generates a potential difference with the plasma that leads to the repulsion of the electrons and the attraction of the positive ions. This potential triggers ion bombardment of the solid surface. In all plasmas, the heterogeneous chemical reactions and the ion bombardment can occur simultaneously on the substrate. Therefore we have continuously a chemical and physical interaction of plasma with the surface. The main reactions that can occur on the surface are a) adsorption b) recombination and the formation of compounds and c) sputtering. The absorption when the molecules and radicals from the plasma are in contact with the surface exposed to the

plasma, they can be adsorbed at the surface:

$S + M_g \rightarrow M_s$ *(3.13)*

Where g and s respectively indicate species in the gas phase and solid-phase.

In recombination, atoms and radicals of the plasma can react with species adsorbed on the surface forming a compound as follows:

S- A + A -> S + A2S (3.14)

A is an atom adsorbed on the surface. During the recombination energy of the particles participating in the reaction is usually released as heat on the surface.

The surface exposed to the plasma is always at a negative potential relative to the plasma[31]; The potential difference that develops between the surface and the plasma accelerates positive ions toward the surface of the material. The accelerated ion penetrates the material, to a depth of 3-4 atomic layers, release its momentum, atoms moved by the impact of ions, provide in turn the amount of motion to the first neighbours including surface atoms that are projected outwards, this process is called sputtering. In any plasma ion bombardment and the chemical reaction of active species coexist [32]. In general, if the process has a high concentration of active species the chemical erosion of the surface leads to the process of etching. If the process is dominated by the ion bombardment, the sputtering process is favoured [33]. An interesting case is obtained in the presence of a relatively low energy ion bombardment but with sufficient species to activate the surface. In this case, a physical modification of surface and the treatment of the surface occur. In the latter condition, there is only the modification of outer material, with grafting of functional groups (such as NH2, - COOH, -F, -OH) or by making the cross-linking of the polymer chains [34-35]. In argon and oxygen plasma, argon ions initiate the physical degradation of the surface, and O_2 present in the plasma reacts with the materials generating a wide variety of functional groups CO, CO, OC = O, COO [36,12,37,30].

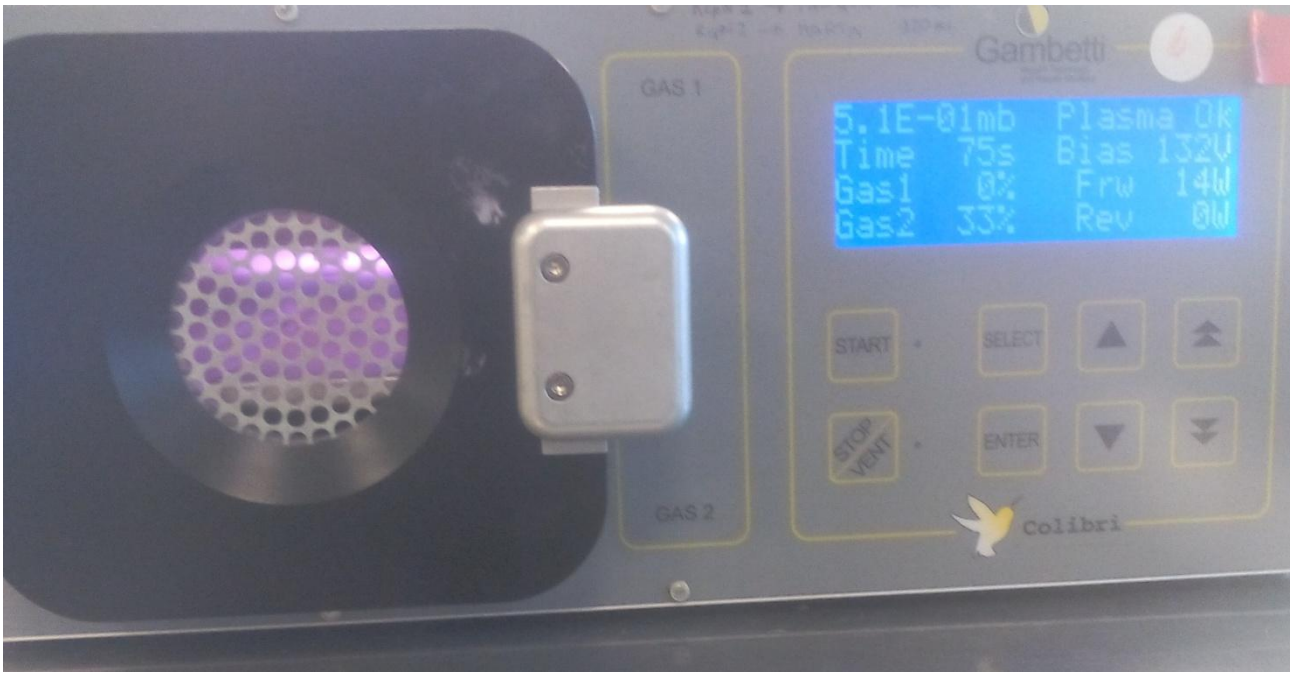

Figure 3.15 Air plasma discharge in Plasma Reactor Colibri

To treat the surfaces, we used a Low-pressure plasma reactor to treat the surface of graphite materials. The Plasma Reactor (Colibri by Gambetti Milano) is equipped with RF generator to activate the plasma at low pressure (1 to 0.01 bar). The system is controlled by a microprocessor. The gas used to treat graphitic materials was Oxygen (N50 purity), and the sample was treated at room temperature. In figure 3.15 is reported a picture of the plasma reactor used in the experiment, the plasma discharge is visible inside the reactor. The RF power was 15 watts, and the base pressure was 0.01mbar, while the processes pressure was 0.4 mbar. The gas line and the chamber were purged with oxygen gas for 180 s before the treatment. The time of plasma treatment started from 5 seconds to 600 seconds, but main experiments were conducted in the range of 5-240 seconds.

3.5.1 Deposition methods of graphitic based materials

To realize the graphitic layer, various methods were explored. The most user-friendly way was the synthesis of the layers using inks based on graphene powder. For this reason, we exploited the field of graphene inks to realize protective film. Moreover, we studied the barrier effect of a single layer of graphene. The single layer of graphene was deposited using transfer technology (these samples were provided by Politecnico di Torino, Italy). In the following paragraph, the description of the mechanical exfoliation and the deposition method used in the project is given. Moreover, the procedure to synthesize the graphitic ink is reported.

3.5.2 Deposition of graphite coating by Meyer road

The deposition of solutions with Meyer rod is a variant of blade deposition, as a doctor blade, casting knife, coating blade. In this type of deposition, a rod with a coil is realized in metal, the liquid or ink is placed on the coil of the Meyer rod, and the rod is rolled on the surface. In this way, the liquid suspension is spread and compressed on the surface. The wire spiral limits the lateral spread of the solutions and guides the fluids to an internal spiral, leading the liquid in the bottom part of the rod. Usually, the thickness is not influenced by the viscosity of the solution or by the density of materials but by the diameter of the wire for coatings with the thickness higher than 10 microns. For films with thickness less than 10 microns, the control of the thickness is difficult, and the wire releases patterns of the surface, reducing the homogeneity of the coating. [38] In our set- up, a plastic spacer in place between Meyer rod and substrate. In this case, the thickness can also be controlled by the thickness of spacer and moreover allow strong reduction of wire traces on the surface. The liquid undergoes a hydrodynamic compression that is more homogeneous than the mechanical compression induced by the wire edges. Figure 3.16 shows the Meyer rod with a polymer tape used as a spacer on the silicon substrate.

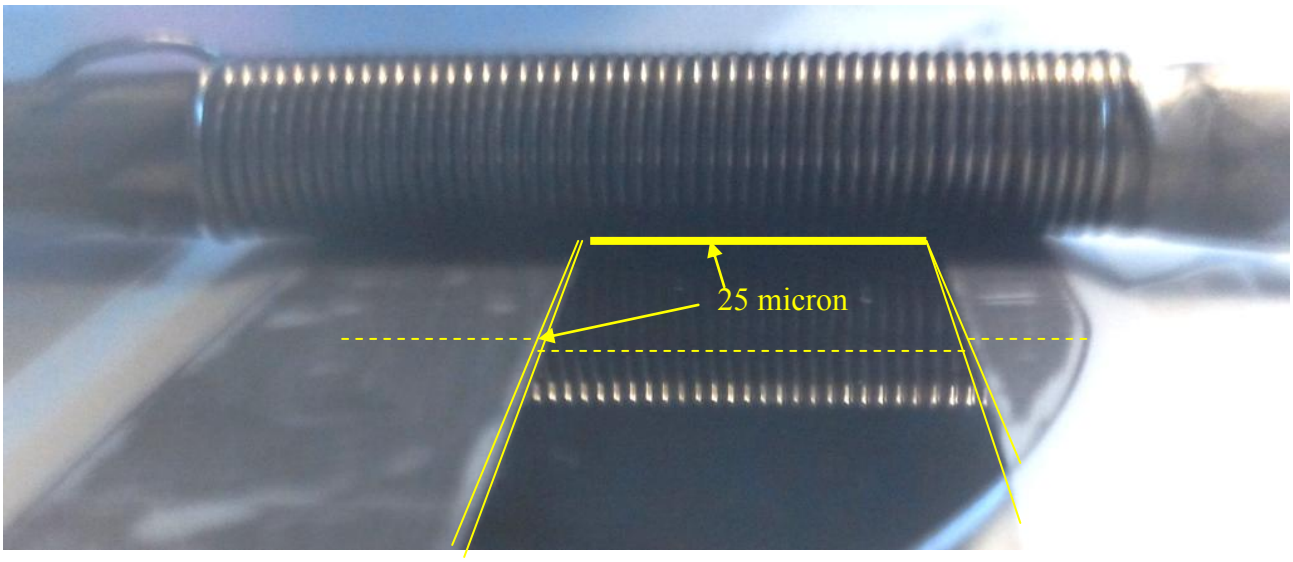

Figure 3.16 Picture of Meyer rood on silicon 100 substrate.

3.5.3 Deposition of graphite coating by drop casting

Drop casting technique is one of the most straightforward techniques to deposit coatings. For this reason, it can be used in a wide range of application such deposition of optical layers or conductive

layers. The method consisted of a deposition of a drop of the solution of a defined volume on the surface, the drop naturally spread on the surface, and by the evaporation of the solvents, a thin layer of materials is deposited on the surface of materials. The coating deposited with this technique can reach thickness less than 100 microns.

3.5.4Transfer of a single layer of graphene

Layers based on nanographite and multilayered graphene were tested as barrier as well as a single layer of graphene. The single layer of graphene transferred on polymer was provided by Prof. Lamberti of Politecnico di Torino, Italy. The single layer of graphene was synthesized using thermal chemical vapor deposition, CVD, using metal foils. This method offers high-quality graphene material and on an industrial scale. The process to deposit graphene on a metal require elevated temperatures and only a few metals are suitable for the growth of graphene, as Cu and Ni. Due to this reason, to cover a polymer with a graphene layer, a transfer procedure was necessary. The transfer procedure required the removing of the underlying metallic substrates to free the graphene layer. The polymer used in this work was PDMS. PDMS membranes were prepared by mixing the polymer base and the curing agent (Sylgard 184, Dow Corning) with 10:1 mixing ratio (oligomer: curing agent) and degassing in low vacuum for one h. The mixture was then poured into 2 cm×1 cm 1x1 mm PMMA moulds (fabricated by milling machine) and cured in a convection oven following two different thermal treatments. One set of samples was cured for 1 hour at 60°C (bare PDMS sample) while another set was cured for 30 min at 60°C. This soft curing step was performed to allow a partial crosslinking of the material, that produces a smooth hardening of the membrane. As already reported by Lamberti et al.[39], this strategy allows facilitating the subsequent bonding of the PDMS membrane with other surfaces, permitting the later graphene transfer. The growth of single-layer graphene is performed using a cold-wall Chemical Vapor Deposition (CVD) system. The synthesis procedure is carried out on high-quality copper foils and foresees the catalytic decomposition of carbon precursor (CH_4) in a high-temperature deposition process (1000 °C) in the reactive H_2/Ar atmosphere (Ar/H_2/CH_4 partial pressure: 80:10:10). The growth process can guarantee the controlled formation of single-layer graphene with reduced defectiveness. The graphene/Cu substrate is transferred to the partially reticulated PDMS surface, obtaining an excellent adhesion between the elastomeric substrate and the G/Cu film during the final reticulation procedure performed for other 30 min at 60°C. Cu layer is then removed in acidic $FeCl_3$ solution in water (2.25 M for 1 h).

3.5.5 Mechanical exfoliation of graphite

The graphites substrates preparation is fundamental to work in systematic mode on liquid-solid and gas-solid interaction. The substrate was prepared by mechanical exfoliation using a scotch tape with an adhesion force of 25gr/cm^2. Graphite was provided by Goodfellow; the thickness was 5 mm and the purity 99,99 %. The effect of some exfoliation procedures on the homogeneity of surface and structure was studied. The XRD was used to verify the structural modification on HOPG substrate during the exfoliation process. The HOPG was mounted on XRD sample holder using bi-adhesive scotch tape was with an adhesion force of 178 gr /cm. Graphite usually present a preferred direction of exfoliation, and not always it is easy to identify the best direction of peeling on HOPG. For that reason and to obtain a systematic method, the peel off procedure was applied in two orthogonal directions, Figure 3.17

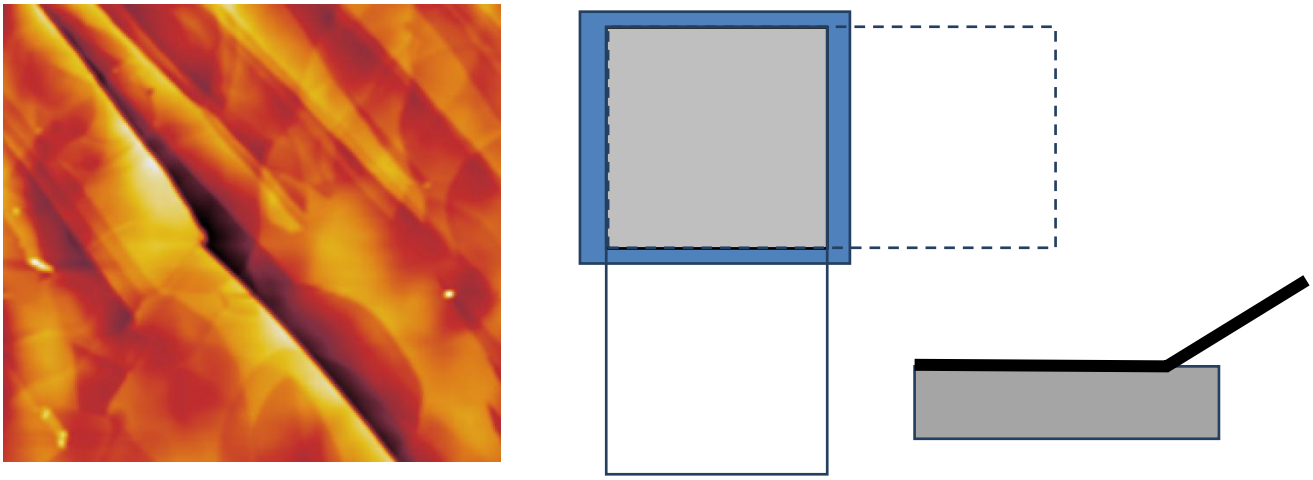

Figure 3.17 Surface Morphology of Exfoliated graphene by AFM, exfoliation procedure.

The thickness of the first layer of graphite after the exfoliation was 14 microns and the surface appeared optically flat, but at the micro-nanoscale, there were many small steps. The reference layer after other two exfoliations became thinner, around 9 microns thick. Applying the procedure again, the thickness of graphite became of 6,5 microns. The thickness of HOPG decreased with increasing the numbers of the peel off steps, Figure 3.18. Unfortunately, it was quite natural that after thirty exfoliations, some pieces of graphite are entirely removed by the scotch tape. For our experiments, it was crucial that surfaces of graphite be without holes, in particular for CCA measurements.

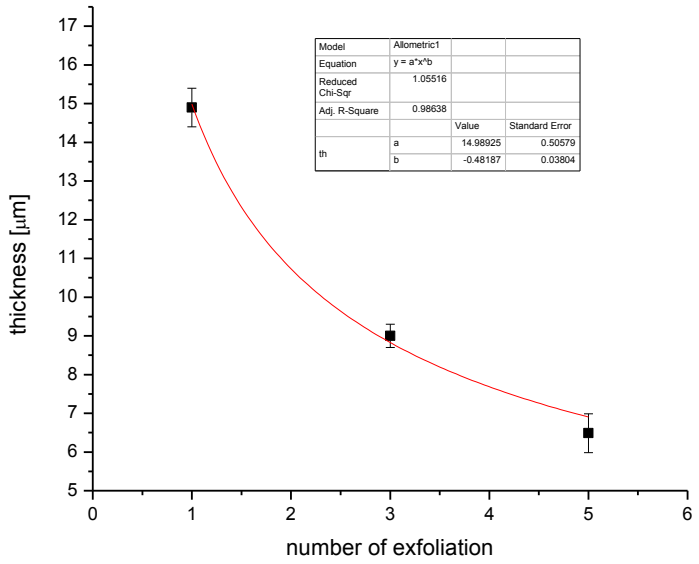

Figure 3.18 Thickness variation of HOPG graphite after different exfoliation

Therefore, the cover percentage of HOPG layer tended to be reduced. This should be avoided to obtain a quite large and homogeneous surface for the various experiments and measurements such as the liquid contact angle measurements and plasma treatment.

3.5.6 Preparation of Graphite substrates

In many experiments or characterization, such as the plasma treatment or XPS respectively, it was essential to avoid the presence of contaminations. Therefore, graphite must be transferred using the adhesive polymer to a clean substrate like silicon. To transfer the layer of HOPG, the adhesive tape needed to be removed in a clean and soft mode. The transfer procedure was based on immersion of graphite in acetone for 4h to separate the tape and graphite. The free-standing layer of graphite was cleaned with pure acetone (1h time) and two times in isopropanol (1 h). A substrate is immersed in a becher, graphite was placed with a tweezer (in solution) on the substrate. Then the substrate and the graphite were removed and dried in nitrogen

3.5.7 Synthesis of suspensions (inks) using Graphitic Materials

To cover the surfaces with graphene, different techniques are available: thermal CVD, transfer of graphene, PVD but one of most interesting methods is the deposition of coating using inks based on graphite materials. The inks are interesting because they do not need vacuum equipment, can be used on any substrates and large areas using automatic systems such as printers.

The graphitic inks are based on suspensions of a graphitic material in a solvent. Many solvents can be used, but one of most used solvent is N-dimethylformamide (DMF). Unfortunately, this type of solvent is toxic and mutagen. For this reason, in many cases instead of pure graphene, the researchers use reduced graphene or graphene oxide, which are materials easier to disperse in common polar solvents like water. In this work, we realized dispersions using a different graphene-based powders and various solvents. We studied first the suspensions using reduced graphene in a broad variety of solvents. The application of inks based on nanographite and treated nanographite and mixtures of graphene and graphene oxide were explored to realize barrier layers after having identified the best solvent regarding availability, toxicity and cost. Figure 3.19 shows the dispersion properties of nanographite and treated nano graphite in water.

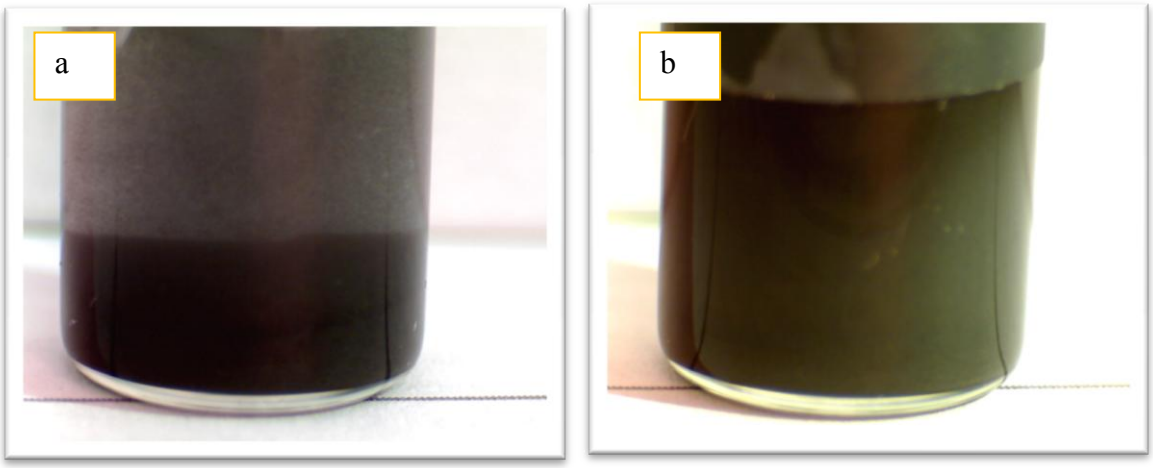

Figure 3.19 Suspensions based on isopropyl alcohol and hydrophobic nano graphite 60nm (a) and graphene 1h after the sonication.

3.5.8 Preparation of inks based on reduced graphene oxide using different solvents

Reduced graphene oxide (RGO) powder was dispersed in different organic solvents: ethanol

(ET), ethylene glycol (EG), 2-propanol, and N, N-dimethylformamide (DMF) with 0.4 mg/ml by ultrasonication for 1h. Water used for the ultrasound bath was repeatedly changed to avoid the temperature increase due to the long sonication time. Immediately after the sonication treatment, the RGO suspensions appeared black and well dispersed. Stability of the suspensions was checked controlling the presence of flocculation after 3 – 24 - 48 hours. Suspension goodness was also evaluated through the absence/presence of clustered RGO in the deposited films observed with the optical microscope. In our experiments, 0.04ml of RGO dispersion was utilized for each drop-cast deposition. After complete drying of the suspension, successive depositions were performed to increase the amount of RGO deposited on the glass substrates. A total amount of 0.04ml, 0.08ml, 0.16ml, 0.32ml, 0.48ml were used to produce films with increasing thickness.

3.5.9 Preparation of inks based on 2-propanol and nanographite

2-propanol is a suitable solvent regarding cost, toxicity and in term of stability to deposit graphitic suspensions on the surface of nanographite. The graphene with a nominal thickness of 60 nm and provided by Graphene Supermarket, were distributed on Petri dish of 2'' diameter and were inserted in the plasma reactor. The graphene nanoplatelets were exposed to oxygen atmosphere for the same time as for graphite. The Petri dish was always loaded with the same amount of graphene nanoplatelets, 40 mg. After the plasma treatment, the same amount of graphene was loaded in vials (1.5 mg) and the bottle was loaded with 50 ml of 2-propanol. The vials were hand shaken for 1 minute and loaded in the ultrasonic bath for 10 minutes at 24°C.

3.5.10 Preparation of inks based on Graphene and graphene oxides mixture

We also explored the feasibility of synthetizing nanocomposite layers of graphene and graphene oxide, with the aim to combine the properties of both materials, regarding synthesis and surface protective properties. Therefore, a series of graphene inks were realised combining graphene and graphene oxide. The powder was dissolved in isopropanol alcohol. Isopropanol was chosen because of its non-toxicity. The amount of powder dispersed in water was kept constant, 3mg, but the composition of graphene oxide in graphene ink varied from 0 wt.% to 100 wt.%. The graphene and graphene oxide was provided by Prof. Tavares (INRS, Varennes, Canada). The powder was dissolved in 5 ml of isopropanol (Sigma Aldrich 99.9%). The suspension was hand shaken for 1-

minute and then mixed using the ultrasonic bath for 10 minutes at 24°C.

References

1. Stalder a. F, Kulik G, Sage D, Barbieri L, Hoffmann P. A snake-based approach to accurate determination of both contact points and contact angles. *Colloids Surfaces A Physicochem Eng Asp*. 2006;286(1-3):92-103. doi:10.1016/j.colsurfa.2006.03.008.

2. Kojima Y, Suzuki K, Kawai Y. Hydrogen generation by hydrolysis reaction of magnesium hydride. 2004;9(2):2227-2229.

3. Ghulinyan M, Bernard M, Bartali R, Pucker G. Applied Surface Science Formation of Mach angle profiles during wet etching of silica and silicon nitride materials. 2015;359:679-686.

4. Wanger C.D., Riggs W.N, Davis L.E,. *Handbook of X-Ray Photoelectron Spectroscopy*. Perkin-Elmer Corporation, Physical Electronics Division; 1979.

5. Minati L. Surface Engineering for Microsensisng.

6. Crist BV, Crist BV. A Review of XPS Data-Banks. 2007;1:1-52.

7. Kozbial A, Trouba C, Liu H, Li L. Characterization of the Intrinsic Water Wettability of Graphite Using Contact Angle Measurements : Effect of Defects on Static and Dynamic Contact Angles. *Langmuir*. 2017;33:959-967. doi:10.1021/acs.langmuir.6b04193.

8. Raj R, Maroo SC, Wang EN. Wettability of Graphene. 2013. doi:10.1021/nl304647t.

9. Wei Y, Jia CQ. Intrinsic wettability of graphitic carbon. *Carbon N Y*. 2015;87:10-17. doi:10.1016/j.carbon.2015.02.019.

10. Minati L, Speranza G, Bernagozzi I, et al. Investigation on the Electronic and Optical Properties of Short Oxidized Multiwalled Carbon Nanotubes. 2010:11068-11073.

11. Vassallo E, Cremona A, Ghezzi F, Ricci D. Characterization by optical emission spectroscopy of an oxygen plasma used for improving PET wettability. *Vacuum*. 2010;84(7):902-906. doi:10.1016/j.vacuum.2009.12.008.

12. Hillborg H, Ankner JF, Gedde UW, Smith GD, Yasuda HK, Wikstro K. Crosslinked polydimethylsiloxane exposed to oxygen plasma studied by neutron reflectometry and other surface specific techniques. *Polymer (Guildf)*. 2000;41:6851-6863.

13. Baker MA, Gilmore R, Lenardi C, Gissler W. XPS investigation of preferential sputtering of S from MoS 2 and determination of MoS x stoichiometry from Mo and S peak positions. 1999:255-262.

14. Bubert H, Jenett H. *Surface and Thin Film Analysis*. 1st ed. Weinheim: Wiley -VCH Verlag GmbH; 2002.

15. Long DA. Raman Spectroscopy.

16. Malard LM, Pimenta MA, Dresselhaus G, Dresselhaus MS. Raman Spectroscopy in Graphene. *Phys Rep*. 2015;473(5-6):51-87. doi:10.1016/j.physrep.2009.02.003.

17. Beams R, Canc LG, Novotny L. Raman characterization of defects and dopants in graphene. 2015;27. doi:10.1088/0953-8984/27/8/083002.

18. Ferrari AC, Meyer JC, Scardaci V, et al. Raman spectrum of graphene and graphene layers. *Phys Rev Lett*. 2006;97(18).

19. Ashraf A, Wu Y, Wang MC, Aluru NR, Dastgheib S a, Nam S. Spectroscopic investigation of the wettability of multilayer graphene using highly ordered pyrolytic graphite as a model material. *Langmuir*. 2014;30(43):12827-12836. doi:10.1021/la503089k.

20. Ferrari AC, Robertson J. Interpretation of Raman spectra of disordered and amorphous carbon. *Phys Rev B*. 2000;61(20):14095-14107. doi:10.1103/PhysRevB.61.14095.

21. Kojima Y, Suzuki K, Fukumoto K, et al. Hydrogen generation using sodium borohydride solution and metal catalyst coated on metal oxide. 2002;27:1029-1034.

22. Savage G. *Carbon-Carbon Composites*. 1st ed. (Hall C&, ed.). Cambridge; 1993.

23. Lieberman MA, Lichtenberg AJ. *Principles of Plasma Discharges and Materials Processing*. 2nd ed. (Sons JW&, ed.). Jonh Wiley & Sons; 2005.

24. Grill A. *Cold Plasmas Materials Fabrication:From Fundamentals to Applications*. (Press W-I, ed.).; 1994.

25. Richard A. *Reactive Plasmas*. First Edit. (SFV, ed.). Paris, France

26. Sacharov. *Fondamenti Di Fisica Dei Plasmi*. (MIR, ed.). Moscow; 1983.

27. Kogelschatz U, Eliasson B, Member S, Kogelschatz U. Nonequilibrium Volume Plasma Chemical Processing. 2015;(September). doi:10.1109/27.125031.

28. Gezer PG, Brodsky S, Hsiao A, Liu GL, Kokini JL. Modification of the hydrophilic/hydrophobic characteristic of zein film surfaces by contact with oxygen plasma treated PDMS and oleic acid content. *Colloids Surfaces B Biointerfaces*. 2015;135(August 2016):433-440. doi:10.1016/j.colsurfb.2015.07.006.

29. Herman IP, Laboratories B, Technologies L, Hill M. Characterization of transformer coupled oxygen plasmas by trace rare gases – optical emission spectroscopy and Langmuir probe analysis. 2000;9:116-127.

30. Vesel A, Mozetic M, Zalar A. XPS study of oxygen plasma activated PET. *Vacuum*. 2007;82(2):248-251. doi:10.1016/j.vacuum.2007.07.021.

31. Kelly PJ, Arnell RD. Magnetron sputtering : a review of recent developments and applications. 2000;56:159-172.

32. Gottardi G, Laidani N, Micheli V, Bartali R, Anderle M. Effects of oxygen concentration in the Ar / O 2 plasma on the bulk structure and surface properties of RF reactively sputtered zirconia thin films. 2008;202:2332-2337. doi:10.1016/j.surfcoat.2007.08.052.

33. Poberaj I, Zalar A, Kosec L, Spaic S. Formation of functional groups on graphite during oxygen plasma treatment. 2006;253:1861-1865. doi:10.1016/j.apsusc.2006.03.028.

34. Jokinen V, Suvanto P, Franssila S. Oxygen and Nitrogen Plasma Hydrophilization and Hydrophobic Recovery of Polymers. *Biomicrofluidics*. 2012;6(1). doi:10.1063/1.3673251.

35. Siow KS, Britcher L, Kumar S, Griesser HJ. Plasma Methods for the Generation of Chemically Reactive Surfaces for Biomolecule Immobilization and Cell Colonization - A Review. 2006:392-418. doi:10.1002/ppap.200600021.

36. Walther F, Davydosvskaya P, Zurcher S, et al. Stability of the hydrophilic behavior of oxygen plasma activated SU-8. *J Micromechanics Microengineering*. 2007;17:524-531. doi:10.1088/0960-1317/17/3/015.

37. Kim KS, Lee KH, Cho K, Park CE. Surface modification of polysulfone ultrafiltration membrane by oxygen plasma treatment. *J Memb Sci*. 2002;199:135-145.

38. Turri S. *Vernici Materiali Tecnologie Proprietà*. 4th ed. (Ambrosiana CE, ed.). Milano; 2011.

39. Lamberti A, Torino P, Marasso SL, Torino P. PDMS membranes with tunable gas permeability for microfluidic applications RSC Advances COMMUNICATION . *RSC Adv*. 2014;4(November):61415-61419. doi:10.1039/C4RA12934B.

4. Liquid and gas interaction with graphitic materials.

4.1 Introduction: Liquid-carbon interaction and gas-carbon interaction

The liquid-carbon interaction and gas-carbon interaction play a significant role in many fields such as surface physics, electrochemistry, chemical industry, battery technology, nanoconfined liquids, gas sensing, permeation and also in noncovalent functionalization of graphene [1,2]. The recent literature is mainly focused on the study of water-graphite or water-graphene interaction [3,4,5]. This great interest in intrinsic water wetting on the graphite-based material has been led by the interesting results observed by various researchers on a surface covered by a single layer of graphite, graphene. Some authors considered the graphene layer "water transparent", and this means that the material covered by a single layer of graphene does not change its wetting properties[6]. Even if water transparency of graphene is under discussion, interest in surface properties of hydrophobic/hydrophilic surfaces has been reignited by the discovery of the graphene and other 2D materials. This topic requires rigour understanding of surface properties, the interaction of molecules and phases with these solid surfaces. Despite considerable progress in this area, many controversial issues remain unresolved. It is noteworthy that interaction of bubble with the surface of nanomaterials immersed in liquid media belongs to the very underexplored field. Due to this great interest, many researchers studied the intrinsic properties of graphene and the properties of parent structure of graphene, graphite[7], Surprisingly also the intrinsic wettability of graphite, which is a dispersive material (able to induce only a Van der Walls interaction), is still under debate due to the great incongruence of the results reported in literature.[8,9]. For this reason, many papers are dedicated to graphite water interaction. Unfortunately, few papers report on the interaction of graphite and functionalized graphite with other liquids or with gasses [10,11,12]. The interaction of gas bubbles with surface immersed in liquid media is of interest in many fields such as nano/microfluidics, membrane technology, biomedical devices(e.g. embolism) as well as in protective surface [13,14,15]. Moreover, the interaction of gasses with the matter in liquid media is important in self-cleaning surfaces based on superhydrophobicity phenomena. On the superhydrophobic surfaces, in fact, the nano and micro corrugation of surface promotes the trapping of air bubbles beneath the water droplets, and this induces the highly hydrophobic character of surfaces [16,17]. Due to the importance of the liquid-gas-solid interaction in graphite materials, which have non-polar surfaces, in this chapter we investigate the interactions of graphite with a) various

kinds of solvents, b) with different gases: air, N_2, Ar, He, H_2. Moreover, c) and the effect of adding polar groups on the surface was explored.

In the first part of the chapter, the surface chemistry and the morphology of exfoliated graphite studied using X-ray photoelectron spectroscopy (XPS) and atomic force microscopy (AFM) and the interaction of graphite with water are reported. The time evolution of wetting on graphitic materials and the substrate effect have been explored. Moreover, the interaction with various kinds of liquids (water, isopropanol, ethanol, glycerol) has been studied. We determined the surface tension and surface properties of HOPG using sessile contact angle measurements (applying the Owens-Wendt, Zisman approaches, by Van Oss Chaudhry Good method and through the work of adhesion determination) [18,19,20]. A comparison between the results will be discussed considering the surface chemistry and morphology of the surfaces. In the second part, the results of the study the interaction of various monoatomic and diatomic gasses with HOPG in the presence of water. We explored the interaction of graphite with the gases when the surface is immersed in the water media using the captive bubble method (in a liquid-gas-solid system). We compared the experimental results with the results obtained with molecular dynamics simulations. We analyzed the data considering the polarizability of the gasses and the potential well depth in gas-gas interaction and gas-solid interactions evaluated by density functional theory and by the data reported in the literature. Finally, we studied the effect of the addition of polar groups on a graphite surface. In particular, the effect of oxygen functional groups grafted on HOPG surface was explored

4.1.2 Survey on carbon materials wettability

In chapter 2.4, we reported the broad range of the contact angle values reported in the literature, underlining that graphite now is considered more hydrophilic than expected. The carbon materials could also show a wide variety of wetting values as a function of the nature of the carbon termination (C-C or C-H) on a surface of sp^2 carbon, the degree of hybridisation(sp^2/sp^3) or the morphology. To have a broad glance on the wetting properties of the carbon-based surfaces, we measured the contact angle on different types of carbon films. We compared polymer-like carbon films deposited by chemical vapour deposition and amorphous carbon deposited by PVD as a single layer and as bi-layer (with a layer of polymer carbon and a layer of amorphous carbon)[21]. Polymer like carbon showed a contact angle of 50° and the amorphous carbon 70°. The coating with bi-layer structure showed a contact angle of 72° comparable with amorphous carbon that is the external layer of the coating. We also measured the contact angle of amorphous carbon layers deposited with different hydrogen contents in Ar gas, that was the gas used as a main gas during the deposition of

the amorphous film by plasma sputtering. We measured the contact angle on carbon films deposited with 3.3%, 8.3% and16.6 % of hydrogen in Argon flux used in plasma sputtering (the thickness of the coating varied from 200 nm to 100nm). The addition of hydrogen promoted the synthesis of films with the higher contact angle, figure 4.1. Hydrogen, in fact, promotes the formation of a more hydrophobic layer thanks to its passivation effect, figure 4.1[22]. Besides the carbon film, we measured the wetting properties of diamond nanocrystalline coatings deposited by microwave plasma enhanced chemical vapour deposition (MWPECVD). We measured a wettability of 75° when the film was deposited at 650 C° and 65° when the coating was deposited at 900°C (samples were provided by CNR Lecce, dr. Cicala)[23]. The variation of the contact angle values was induced by the change of surface morphology due to the increase of temperature, Figure 4.1shows the water contact angle value of carbon coatings measured in our laboratory, compared with the range of values reported in the literature for diamond (sp^3 C) and graphite (sp^2 C)[24].

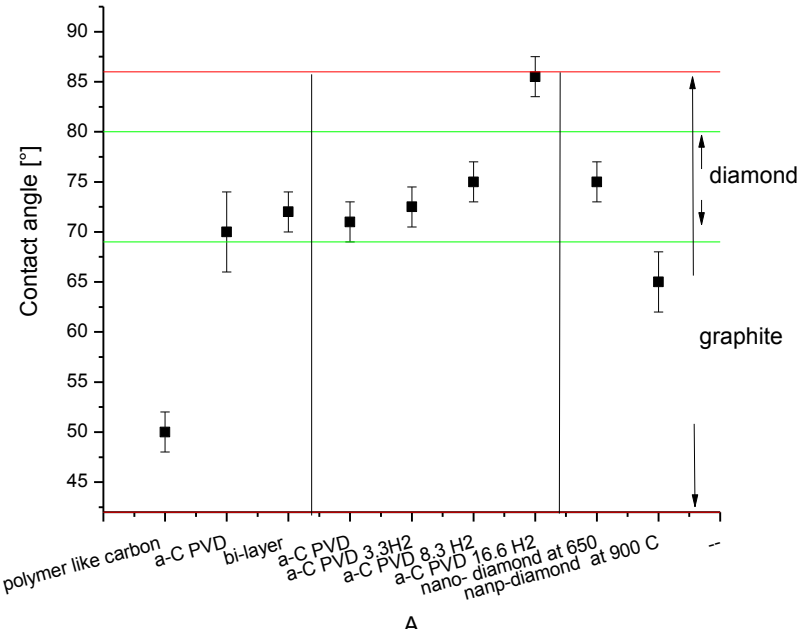

Figure 4.1. Contact angle values of polymer-like carbon, amorphous carbon films deposited by chemical vapor deposition (CVD) physical vapor deposition (PVD) and nano-crystalline diamond films. "H_2" indicates the percentage of hydrogen in Ar/H_2 gas mixture used during the deposition of the amorphous carbon film. The green line illustrates the range of contact angle values reported in literature and the red line indicates the values reported in literature for various kinds of graphite (see chapter 2)

We can see that in general the non-graphitic carbon films show a broad range of contact angle values and it is quite difficult to find a direct correlation with the kind of hybridisation. Moreover, as observed in the bi-layer structure, the outermost layer leads the wetting. Therefore, also small

variation in the preparation can sensibly modify the wetting, as found on carbon film deposited using hydrogen as a gas process. These results and results of reported literature, (see chapter 2) show that carbon-based materials show a broad wetting behaviour. Therefore, it is crucial to work with carbon surface synthesized in a controlled mode to obtain a reliable estimation of wettability on carbon films. Even if graphite is a well-structured material, many factors as defects, contamination and cleaning treatments can affect the contact angle. For this reason, the fresh HOPG surface appears the excellent option to describe the intrinsic properties of a carbon film with sp^2 hybridization. The best method to obtain a fresh surface is the exfoliation of highly oriented pyrolytic graphite (HOPG) [25].

4.1.3 Structural properties of exfoliated Graphite

In Chapter 3.2.1, we reported the methodology to obtain layers of exfoliated graphite. In this paragraph, we report the structure of graphite as a function of the exfoliation number. The structure of bulk graphite and the exfoliated graphite was studied by X-ray Diffraction (XRD). The diffraction patterns of bulk HOPG under examination are displayed in Figure 4.2. The graphite exhibited peaks at 26,54°, 54,6°,87°, due to the (002) ,(004) and (006) plane reflections, figure 4.2.

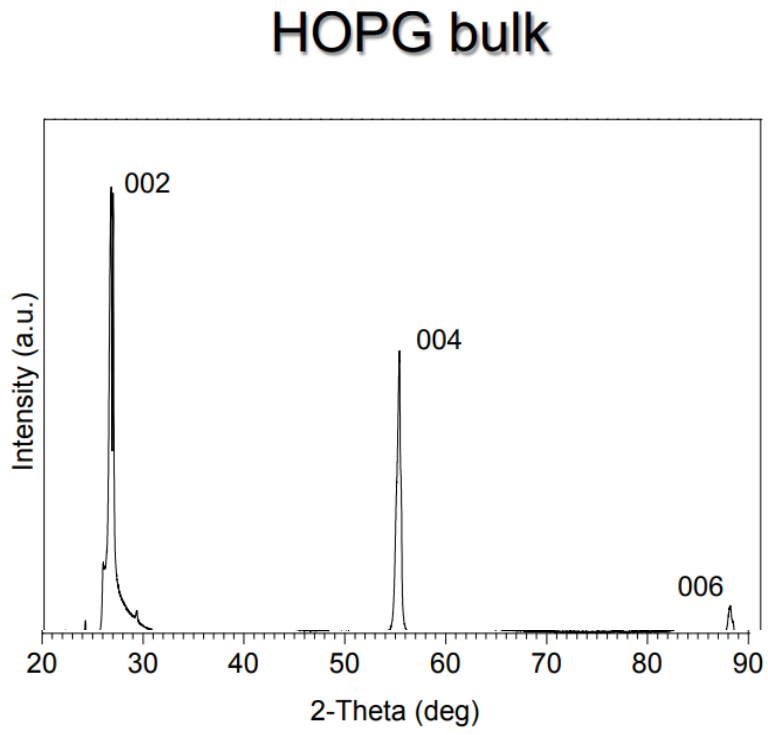

Figure 4.2 XRD pattern of HOPG graphite

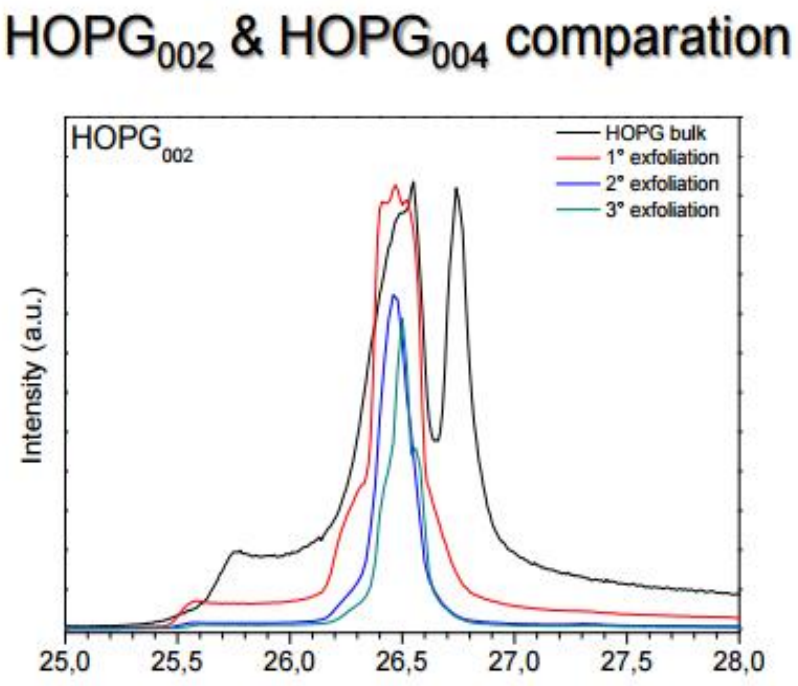

Figure 4.3 Comparison of XRD spectra of graphite and exfoliated graphite for the 002-reflection related peak

The most intense peak is the double peak at 2θ=26.542° and at 2θ =26.8° of HOPG [26], The double peaks corresponds to the (002) reflection of graphite, in particular, the peak at 26.54° indicates an interplanar distance d of 0.3356 nm. The full-width at half maximum of the peak at 26.542° (FWHM002) is of 0.2493°. The spectrum for the exfoliated graphite shows only a sharp peak of 26.5° losing the double structure observed for bulk graphite. In the spectrum figure 4.3 and the FWHM of the peak (002), the exfoliated graphite shows a small increase in the calculated interlayer distance, d spacing 0.3365 nm and a slight decrease of the FWHM002 (0.22°). The crystallite size calculated for the bulk and the exfoliated HOPG samples were 45 nm and 51 nm, respectively. The d002 peak became sharper and narrower with the second and third exfoliation, indicating a progressive improvement of ordering of the HOPG structure, 4.3. Even if the exfoliation process appeared beneficial from a structural point of view, we observed that more than 80% of the samples prepared using 3 and 5 exfoliations of graphite showed the formation of visible defects as holes and fractures. A homogeneous surface is necessary to obtain a reliable evaluation of a sessile contact angle and a captive gas bubble contact angle in liquid media, to avoid as much as possible the influence of substrate (holes) in the final contact angle (i.e. Cassie Baxter effect). In the bubble

contact angle measurement set up, in fact, the placing of the bubble on sample surface is not so well controllable as in the sessile contact angle meausurement one, the use of a homogeneous surface over 1cm^2 is necessary to obtain a proper evaluation of the captive bubble contact angle Taking into account the need of obtaining large areas and fresh homogeneous surfaces, the best compromise to realize in a controlled mode HOPG samples is the single exfoliation. We mention moreover that the homogeneity of the surface is crucial also to transfer the graphite layer successfully to another substrate like silicon.

4.1.4 Surface properties of mechanical exfoliated HOPG

The surface of exfoliated graphite was in general smooth because the average roughness was less than 0.5 nm in an area of 5 µm × 5 µm as measured by AFM, and less than 500 nm on 1 mm scan measured by profilometry. However, certain regions were more rough, for instance, the region showed in the optical image in 4.4. The surface consisted primarily of two planes (I and II) which were separated by consecutive terrace like structures composed of several layers of HOPG, 4 a. The step height of the terrace-like structures was 500 nm. Using an optical microscope and AFM, we evaluated the morphology of the HOPG surface in the micro- and nanoscale inside the planes, such as region I and II (Figure 4.4b). Also inside the flat region, there were steps and corrugations with nanoscale sizes, the main steps showed a height of 150 nm, but there were also some nano-steps, with thicknesses in the range of 1-20 nm (c).

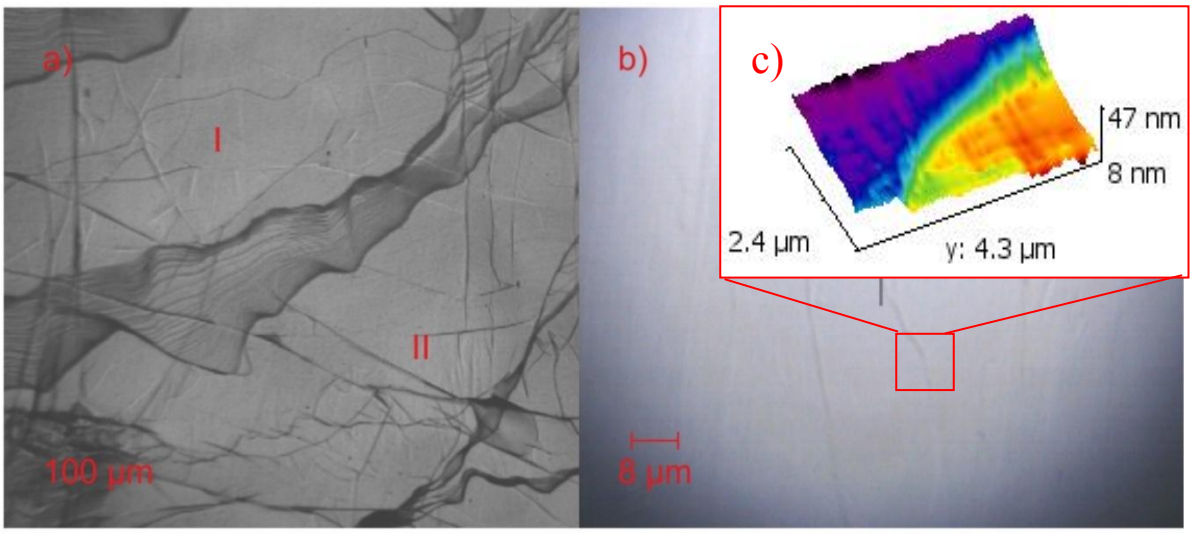

Figure 4.4 Optical microscopy of exfoliated HOPG in millimeter range which reveals terrace-like structure (a); optical microscope image in the range of microns (b); and 3D AFM image of a nanostep (c).

To study the surface chemical properties, the surface of exfoliated graphite was analyzed by XPS. XPS Survey spectrum of HOPG revealed the dominant presence of carbon (98.5 %) and a minor component of oxygen (1.5 at. %) Figure 4.5(a); and C1s line fit with components at 284.70, 285.4, 285.86, 286.48 and 286.90 eV Figure 4.5(b).

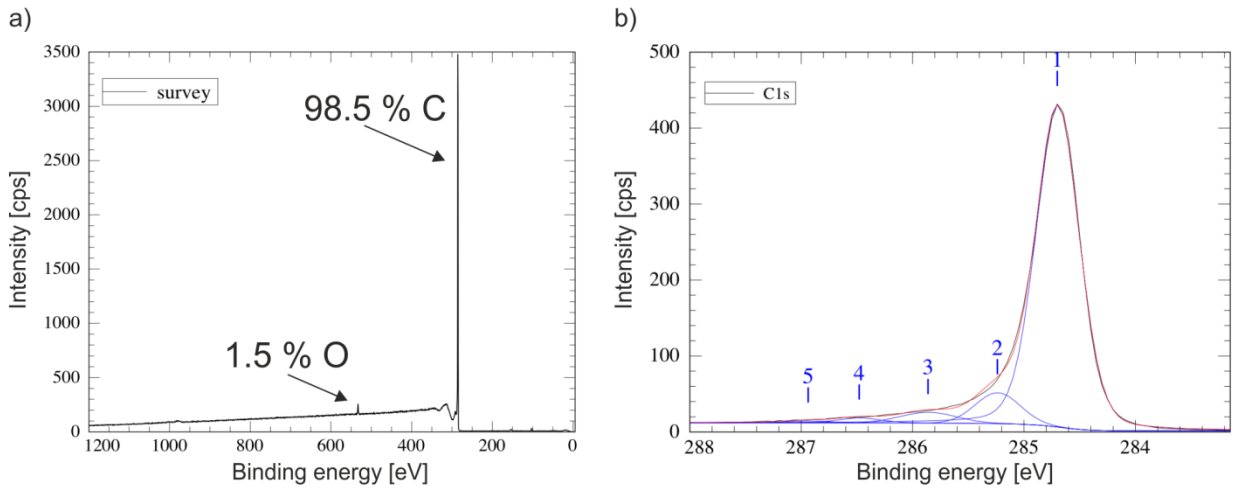

Figure 4.5 XPS Survey spectrum of HOPG revealed the dominant presence of carbon (98.5 %) and a minor component of oxygen (1.5 at. %) (a); C1s line fit with components at 284.70, 285.4, 285.86, 286.48 and 286.90 eV (b).

Figure 4.5b shows the peaks fitting of the carbon C1s core lines. The peak has two components at 284.7 eV and 285.4 eV. The major component at 284.7 (1) is related to C=C bonds in graphite. The 285.4 eV peak is ascribed to C-H bonds in hydrocarbons usually due to airborne contamination (2). The components at 285.8 (3), 286.5 (4), 286.9 (5) eV are the components related to the carbon bonded to oxygen, the sum of these elements concentration is 5.41 at. % relatively to carbon. The C=C bonds represent 87 at. % of the signal; the airborne contamination amounts to 8 at. % and the graphite carbon bonds with oxygen and OH to around 5at.%.

4.2. Solid-gas-liquid interaction on exfoliated graphite

4.2.1 Time evolution of wettability of graphite

Using sessile contact angle measurements, we studied the variation of sessile contact angle (CA) as the function of the time after exfoliation. We observed in Figure 4.6 trend of water CA similar to the trends reported in the literature[4]. We found an increase in the contact angle (CA) in the first 2

minutes and then a stabilisation of the CA values. The increase in the CA can be attributed to adsorption of the airborne contamination [5]. Similarly, the test on the bubble contact angle as the function of the time of exposition to the air has been conducted (Figure 4.6 black dots). The air bubble contact angle appeared in the time more stable than for the sessile drop measurements. This is probably due to the immersion process in the water that keeps clean the surface due to the flotation of hydrophobic contaminants and due to the fact that the transport phenomena in condensed media are significantly slower than in the gas phase, which slows down transport of contaminants to the surface and may contribute to rather stable CA during our measurements. The lowest contact angle on exfoliated graphite was 57°, less than the value reported by Kozbial and similar to the value reported by Wei [9,5], this probably because the surface of HOPG showed on a large scale many basal plane edges as indicated in 4a, between the plane I and plane II. As reported by Wei, edges of graphite are more hydrophilic (43° CA) due to the presence of oxygen on the edges. This was confirmed by XPS that detected a small amounts of oxygen on HOPG surface [9]. In Figure 4.7 we reported the AFM image of exfoliated graphite after 6 minutes and the aged graphite (3 months) The surface shows some steps but the surface of graphite face appears flat, and the contact angle was 79°.

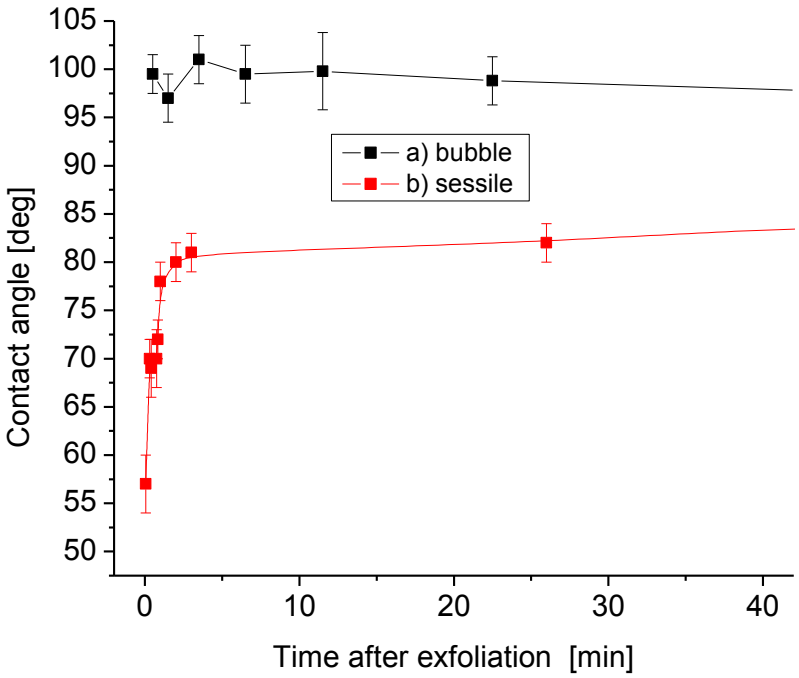

Figure 4.6 Variation of drop contact angle (red) and bubble contact angle (black) as function of time after exfoliation.

The surface of an aged graphite (3months) show steps, but the surface of graphite is not flat. On the graphite surface, there are many small dots due to the accumulation of airborne contamination (Figure 4.7 b. The contact angle of this sample was 91°.

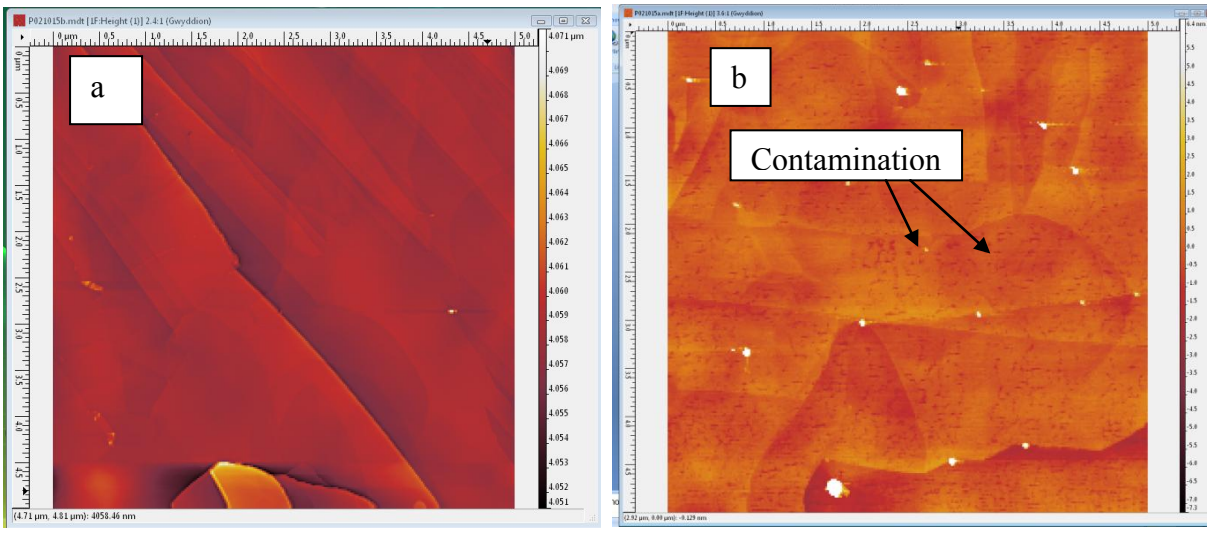

Figure 4.7 AFM image of graphite exfoliated after some minutes (a) and after 3 months.

The results corroborate the observation of Kozbial [25], indicating clearly that the increase of contact angle is due to the airborne contamination of the surface. As we observed in the experiment, the fresh graphite is more hydrophilic than expected (contact angle in the range between 56-64°) but we also observed that the partially contaminated graphite, as indicated by Kozbial, showed a contact angle in the range 80 -85° and the aged graphite a contact angle of 91.5°. Comparable results have been observed by Pittsburgh group (Li et al. [4]).

4.2.2 Wetting of multilayer graphene and single layer graphene

To understand the influence of substrate on wettability on graphitic material, the contact angle of graphene, multilayer graphene and graphite have been compared. We compare the measurements obtained on HOPG, that is a virtual infinite stack of 2D sp^2 layers, with the contact angle measured on the multilayer of graphene (Gr/Ni multilayer), and C.A of a single layer of graphene (Gr/Ni). Graphene and graphene multilayers have been deposited on Nickel substrate. Graphene films were grown by chemical vapor deposition (CVD). It is a commercial sample obtained from Graphene Laboratories Inc. NY, United States (Graphene Supermarket). The investigation started with sequential cleaning procedure with acetone and isopropyl alcohol in an ultrasonic bath for 30 minutes followed by heat treatment at 430°C in argon flux to remove the residual impurities.

The single layer graphene on Ni substrate induced a significant variation of the surface energy with respect to bare Ni producing increases of water contact angle (CA). 4.8. Bare Ni substrate showed lowest CA while aged graphite resulted in the highest value. Note that the presence of airborne contaminants upon exposure to ambient conditions [4] and the presence of native nickel oxide lead to final contact angle values on bare Ni surface (54.4 ± 6.4°). The measurements of CA carried out on the different samples, are reported in figure 4.8.

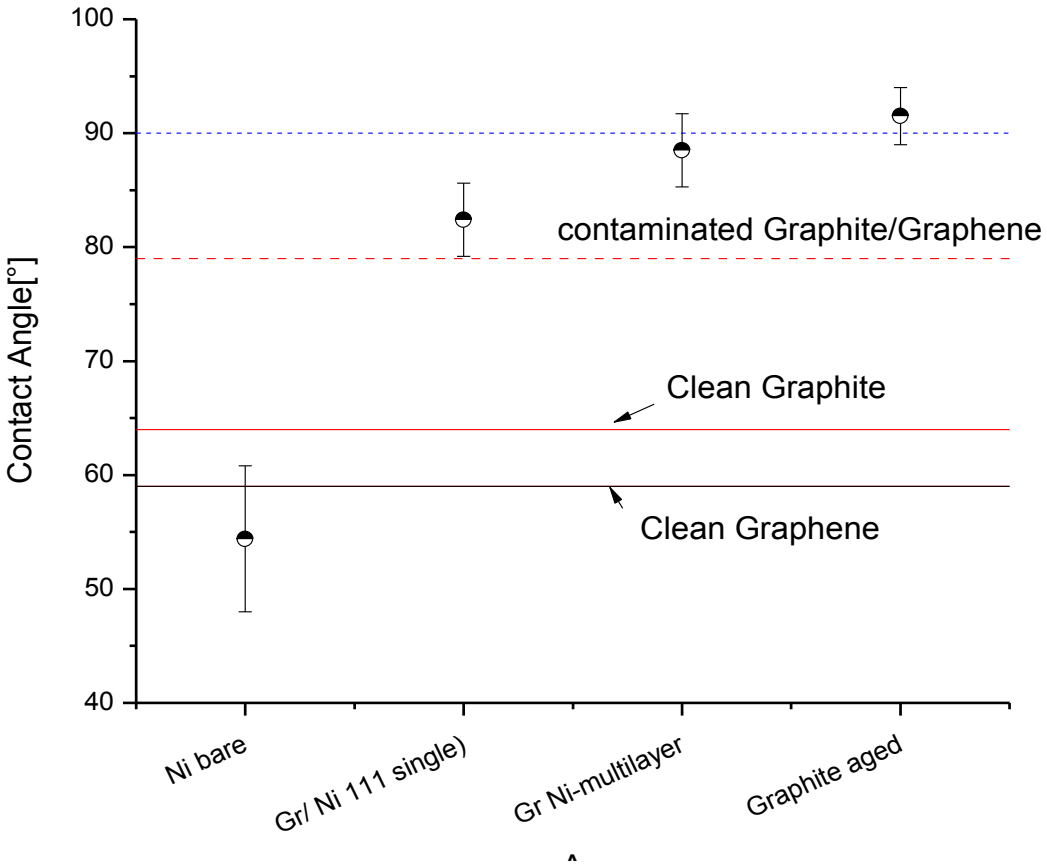

Figure 4.8 :Water contact angle on Nickel, single layer graphene on Nickel, multilayer graphene on Nickel and Graphite.

One layer of graphene over Ni crystal enhanced the WCA from 54,4°± 6.4° (Ni) to 82.4° ± 3.2° to (Gr/Ni). Multilayered graphene showed a WCA of 88.5± 3.2°, that is a value similar to C.A of exfoliated graphite. The roughness (Ra) of the nickel substrate was equal to 0.31 nm, on graphene/Ni it was of 0.41, on multilayer Ra was equal to 2 nm and on graphite 0.27nm. A direct correlation between roughness and wetting was not observed, indicating that WCA was in this experiment primarily influenced by the chemical nature of the surfaces. Figure 4.9, shows the variation of the work of adhesion (WA) between water and different samples, evaluated using

contact angle measurements and applying the Young-Dupre equation. The bare Ni metal showed the highest WA 115 mN/m relatively to 1 layer graphene Gr/Ni(111), multilayer graphene on Ni and graphite, ~82 mN/m, 74.7 mN/m and 73.2 mN/m respectively Figure 4.9. These results indicate that less energy is required to separate water droplet from Gr/Ni sample, even using a single layer of graphene. The range of contact angle values of Nickel surface covered by graphene is in the typical range of values for aged graphitic materials. Therefore, we can reasonably expect that the final contact angle is given primarily by the of graphene surface properties and airborne contamination. Similarly, Li showed weaker substrate dependence for CVD produced graphene on Ni and Cu substrate using WCA values than the effect of airborne impurities [4]. Therefore our results do not support the wetting transparency theory in standard experimental conditions (in air and with timescale of hours), indicating independence of contact angle of the layer of graphene; wettability followed the phenomenon of layer number independence as it shows close resemblance between the WCA for N = 1L, 4-7 L and ∞ for HOPG [27].

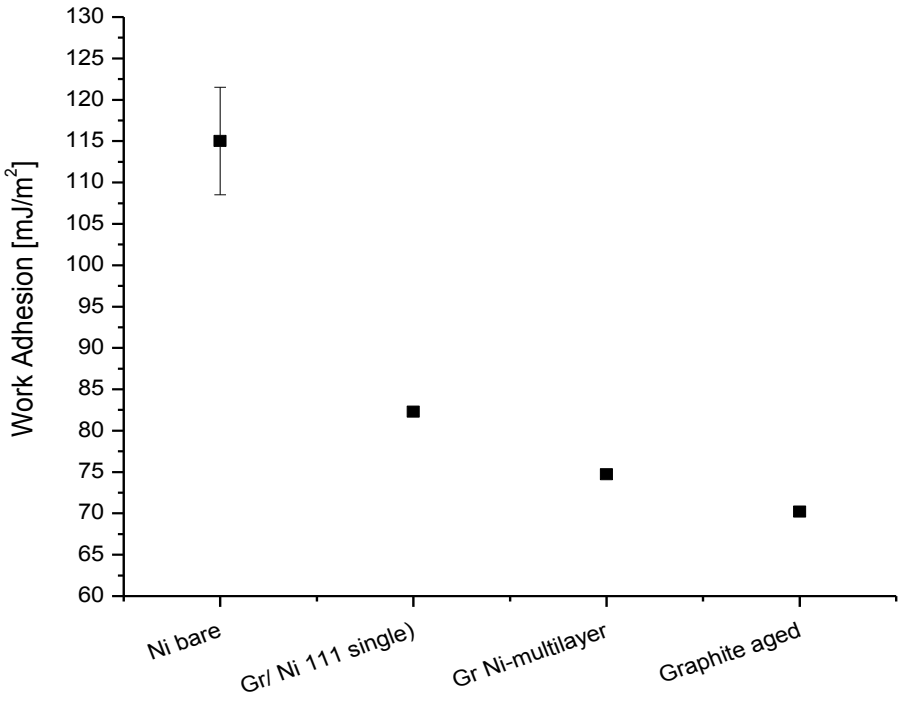

Figure 4.9 Work Adhesion on Ni, on single-layer graphene, multilayer graphene on Ni and graphite.

4.2.3 Interaction of graphite with various solvents

As observed in the previous paragraphs the hydrocarbons from airborne contamination can influence the solid-liquid interaction. To work with quite clean and stable surfaces a typical time scale to measure the HOPG properties after exfoliation was 3 minutes. This is a good compromise to (a) reduce the influence of the contamination which induces a sensible variation of the CA in the first 2 minutes and (b) have enough time to handle the samples for measurements, analysis or surface treatments, (such as bubble measurements, XPS, plasma treatments). On the exfoliated graphite, we studied the wetting behavior and determined the work of adhesion with the different liquids and solvents typically used to disperse graphitic materiasl in solutions or of typical use as probe to determine the surface properties, such as formamide, liquid paraffin, ethanol, 2-propanol, diiodomethane, glycerol, ethylene glycol[28] . Water/ethanol solutions with different molar fractions of ethanol in water were also tested. For surface tension of water/ ethanol mixtures, we used the value reported in the literature by Khattab et al.[29]. Using the large variety of liquids, we measured for each solvent the r contact angle and the work adhesion. Moreover, we used this large variety of liquids as a probe to estimate the surface tension of HOPG by applying all of an empirical method (Zisman plot), chemical approaches (Owens-Wendt, Van Oss-Chaundry, Good) and a thermodynamic approach (Kwon-Neumann)[18,3]. The liquids contact angles on HOPG surface are reported in Figure 4.10. Water showed a contact angle of 78°, in good agreement with the value reported in the literature.[6]. Alcohols such as 2-propanol and ethanol showed the lowest contact angle, around 5°, due to their low surface tension (see Table 4.1). Diiodomethane showed a contact angle less than 10° even if its surface tension is quite high (50.8 mJ/m^2).

Table 4.1 Surface tension of water and water-ethanol solutions [29]

	Surface Tension
	mJ/m^2
Water only	72.8
Water 1.3 mol.% mol ethanol	63
Water 2.2% mol ethanol	60
Water 3.3% mol ethanol	53
Water 7.3% mol ethanol	43

This indicates that the chemical nature of a liquid in terms of its polar and dispersive components is crucial for wetting the surface of exfoliated graphite (see Table 4.2). Figure 4.11 shows the work of adhesion of the liquids with HOPG surface. The isopropanol and ethanol showed the lowest work adhesion, 42-45 mJ/m^2. The formamide and diiodomethane, the liquids with the highest dispersive component, showed the highest work of adhesion, >100mJ/m^2, while water demonstrated a work adhesion of only 87.5 mJ/m^2. It should be noted that alcohols showed a value of the work of adhesion half of that of water, but the surface tension of the alcohols are four times lower than that of water, this is because in alcohols the dispersive components are higher than polar components.

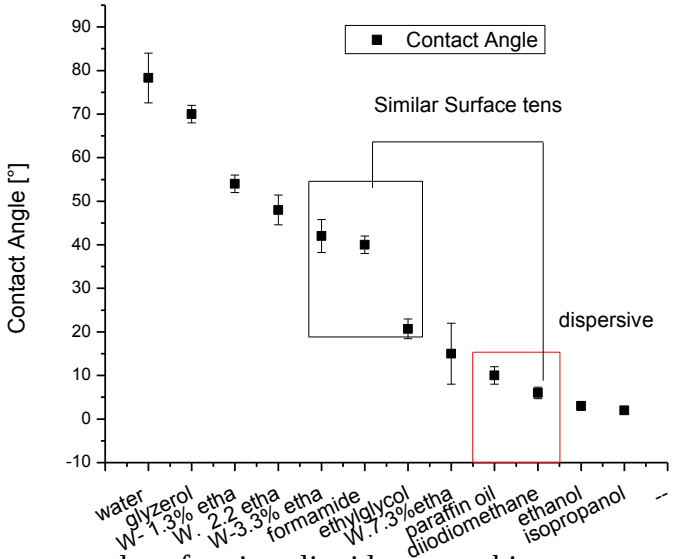

Figure 4.10 Contact angles of various liquids on graphite

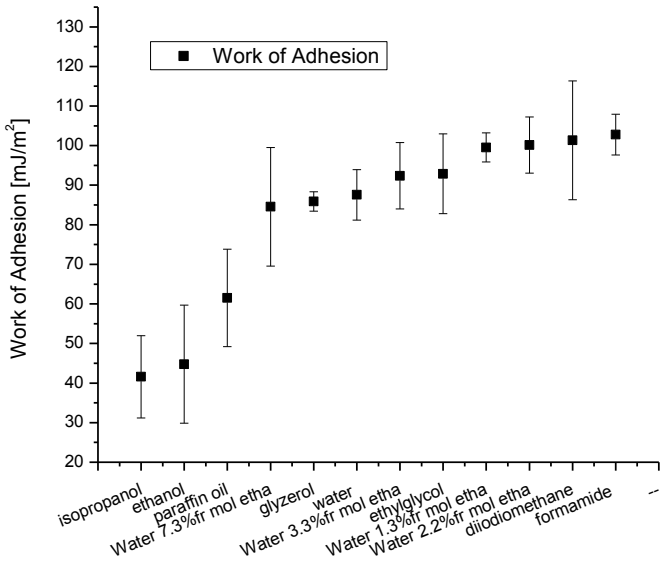

Figure 4.11 Work of adhesion on graphite OF various kinds of liquids**.**

Table 4.2 Total surface tension γ_l, dispersive components γ_l^d and polar components γ_l^p of the liquids, used to measure the surface tension of graphite.[30,29,]

Liquids	γ_l mJ/m^2	γ_l^d mJ/m^2	γ_l^p mJ/m^2
Water	72.8	21.8	51
Glycerol	64	34	30
Ethylene glycol	48	29	19
Formamide	58	39	19
Diiodomethane	50.8	50.8	≈0
Paraffin liq	31	31	≈0
Ethanol	21.4	18.8	2.6
2-propanol	20.93	12	8.3

The water-ethanol mixtures with molar fractions of ethanol up to 3.3 % showed a quite high work of adhesion even if the estimate surface tension is quite low, 53mJ/m^2. In Table 4.2 are reported the dispersive and polar components of ethanol and water. We can see that ethanol has a surface tension lower than water, but the dispersive component in the ethanol is higher than in water, and as demonstrated by the diiodomethane, the dispersive components are crucial to improve interaction with graphite surface. The contact angles reported in figure 4.10 show that many liquids such as water have a quite wide standard deviation of the data. This is probably due to the relatively wide distribution in the surface roughness that can increase the dispersion of the contact angle values on macro-scale which can be explained by the Wenzel mechanism.

The surface energy estimation using contact angle measurements can be done using four approaches: a) Zisman approach, b) Owens-Wendt, c) Van Oss, Chaundry, Good and d) using Neumann thermodynamic considerations (see chapter 2). Numerous controversies concerning the correctness of the different methods are reported in the literature; the best strategy to obtain a reasonable evaluation of surface tension of materials is the comparison between the different methods to obtain complete information on surface properties [30,31,5].

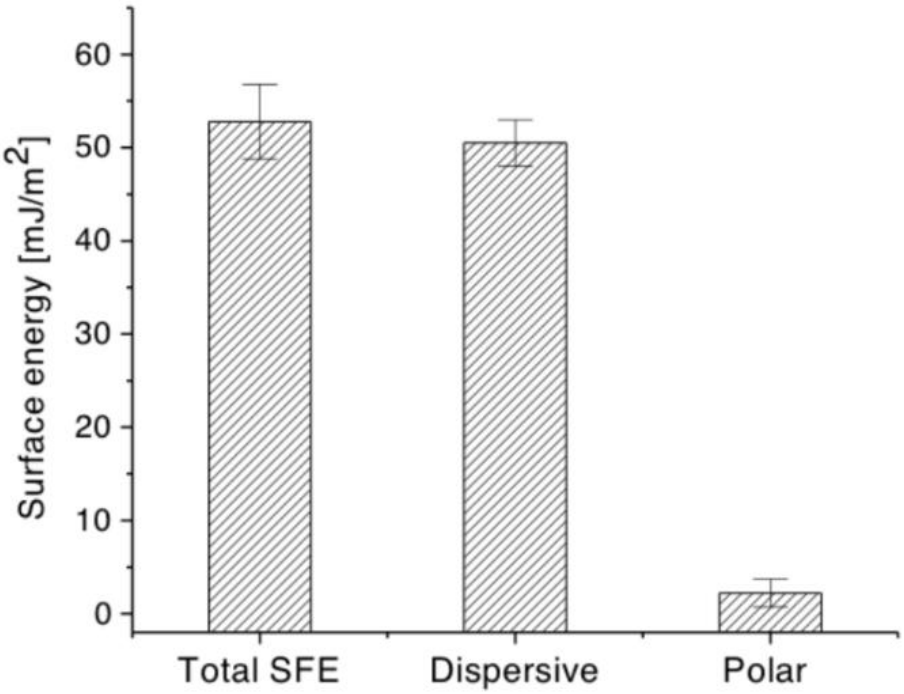

Figure 4.12: Total surface free energy (SFE) and dispersive and polar components for HOPG estimated with the Owens-Wendt method (a)

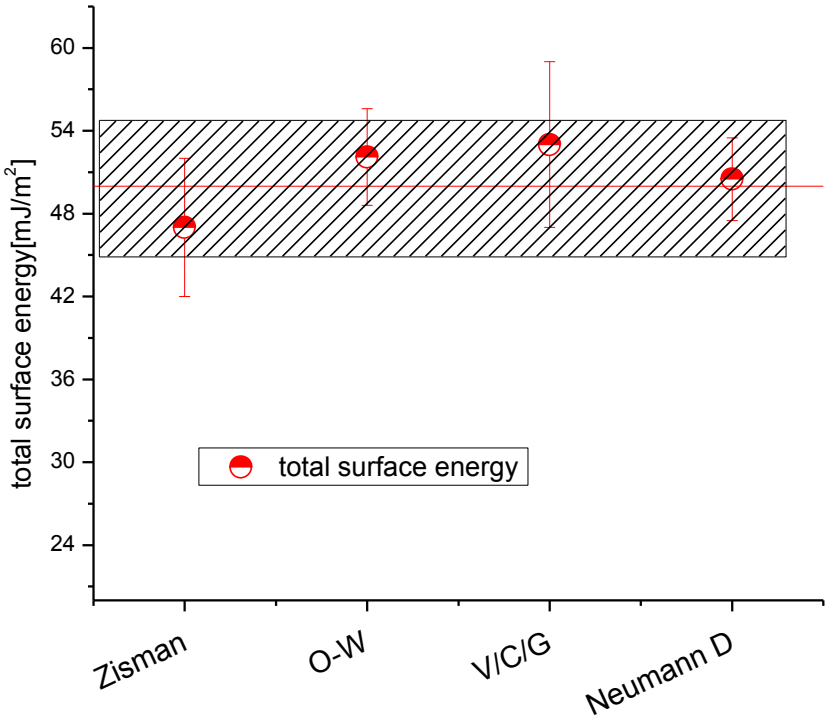

Figure 4.13 Total surface energy estimated using different methods.

Using the Zisman plot, the Owens-Wendt method, the acid-base approach (Van Oss, Good, Chaundry) and the equation of state (Neumann) we determined the total surface energy of graphite. For the Zisman plot we use the liquids with different surface tension as water, diodiomethane, ethyl glycol, formamide, paraffin oil, ethanol, 2 propanol. For the Neumann approach, we used diiodomethane which showed the lowest contact angle. The results are reports in Figure 4.13. All the methods even if based on different theoretical and empirical backgrounds gave a comparable surface tension in the range between 45-54 mJ/m2. This value is similar to the value reported by Good *et al.* one graphite and coal[8]. By the Owens-Wendt we also estimated the dispersive components (due to London interaction) and the polar components of the surface. The dispersive component was equal to 50.2 mJ/m2 and the polar component to 2.2 mJ/m2, Figure 4.12. This indicates that more of 95,8 % of graphite interaction is due to London interaction, in agreement with theoretical calculations of graphene models, and only a small amount of interaction with HOPG is due to the polar component (4.2 %). As indicated by XPS analysis, the polar component is due to the presence of the small amount of oxidized carbon at the surface (5 %), see figure 4.5. The surface of graphite showed a high dispersive component, and this explains the positive interaction of HOPG with non-polar liquids such as diiodomethane or paraffin oil and the weak interaction with water. The results were corroborated by the high work of adhesion of diiodomethane and formamide, which were the liquids with the largest dispersive surface tension, figure 4.11. Therefore, chemical nature regarding polarity and dispersive interaction plays a significant role in the liquid-HOPG interaction. This effect is well reported in the literature, and some works have also revealed that it can be more pronounced on the nanoscale, in particular in nanofluidics.[32].

4.2.4 Interaction of flat HOPG with the various gasses

Considering the non-polar character of HOPG, we immersed the exfoliated graphite in water, and we tested the interaction of gasses with HOPG using the captive bubble method. The surface tension between the liquid and the gasses can be affected by the nature of the gas and by the pressure inside the bubble. To estimate the pressure inside the bubble, we used the Young-Laplace equation 4.1:

$$\Delta p = \frac{2\gamma}{r} \qquad (4.1)$$

Where Δp is the the overpressure, γ is the surface tension of the liquid, and r the redius of bubble.

The average radius of the bubbles was around 1 mm, and therefore, we estimated an internal bubble pressure of ≈1.002 atm. With Massoudi's equation, we estimated the effect of the pressure on liquid-gas surface tension for the different gasses used in the experiment [33]. For all gasses, we estimated a surface tension of water around 72.8 mJ/m^2 and the expected reduction of the surface tension induced by the internal pressure of the bubble is less than 0.4 %. Therefore, taking into account the estimation of the influence of pressure and the kind of gas on the surface tension, we can consider in a first approximation negligible the effect of these two parameters in water-gas surface tension. Taking into account the fact that the water-graphite interaction is identical for all the samples, the variation of the bubble contact angle indicates the affinity of the gases to HOPG surface.

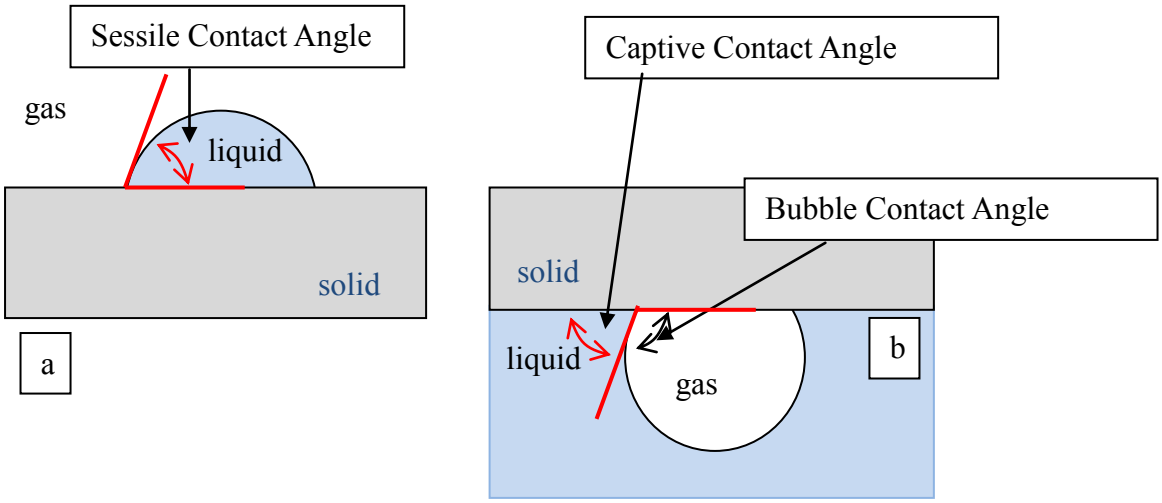

Figure 4.14 Sketch of the sessile contact angle (a) and captive contact angle and bubble contact angle (b)

Therefore the contact angles values shown in Figure 4.16a are the contact angles between the graphite-gas interface and gas-liquid interface instead of the complementary contact angle typically used for the air-bubble (captive contact angle) [34], see Figure 4.14.

Due to the weak interaction of the gas with a particular surface, attention was given to the airborne contamination. To better understand the amount of airborne contamination, in the estimation of captive bubble contact angle we arranged a specific experiment. We measured a bubble contact angle on exfoliated graphite, and immediately after that we analyzed it with XPS. This procedure was used to reduce as much as possible airborne contamination. In Figure 4.15 we report the XPS spectra. The carbon peak is well defined, and the main components observed in this sample are located at binding energies as in the following, with the relative concentration of C in such bonding:

Peak #1: 284.5 eV due to C-C bond, 93.8 at. %

Peak #2: 285.2eVdue to airborne contamination ≈ 0.5at%

Peak #3 : 286.5 eV due C-O-O. 0.73 at %

Peak #4 : 290.5 eV π to π* transition 3.9 at%

The component due to airborne contamination is less than 1at.%. Therefore, we could reasonably expect that the weight of contaminations in the bubble contact angle on just exfoliated graphite, fresh, is negligible. To understand the interaction of graphite with the monoatomic and diatomic gases when it is immersed in water, we conducted the bubble contact angle measurements using helium, hydrogen, argon, nitrogen and air.

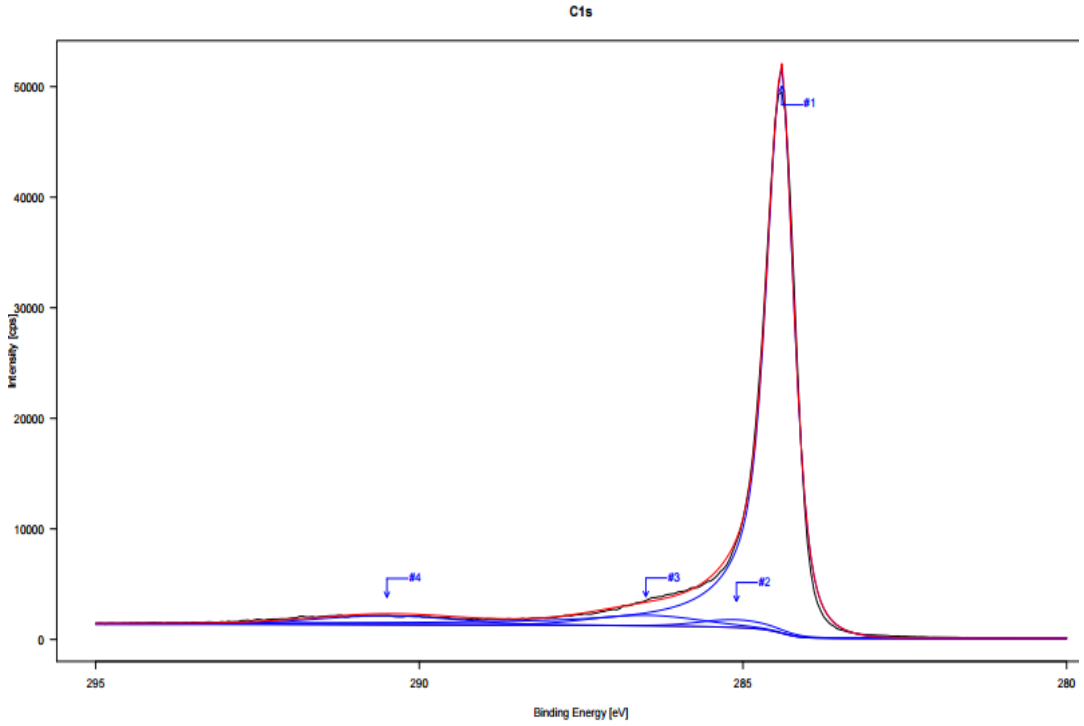

Figure 4.15. XPS spectra of C1s core line of graphite just after the estimation of bubble contact angle

Figure 4.16a shows a bubble contact angle of the various kinds of gases. The gasphillic behaviour of HOPG surface with hydrogen and helium has been recognized (C.A. less than 90°) meanwhile gasphobic interactions. (C.A. higher than 90°) with the air, nitrogen and argon. Using Young-Dupré equation, we estimated the work of adhesion of the gasses. Hydrogen and helium showed the highest value of work of adhesion, > 77 mJ/m^2. Even if the surface is relatively fresh, the experimental contact angle can be easily affected by the airborne contaminations or by the roughness of the surface in micro/nanoscale [25,35]. The bubble contact angle was less prone to be affected by contamination, contrarily to the sessile drop contact angle experiments. We observed, in fact, that the bubble contact angle was constant at different times after the exfoliation procedure (Figure 4.6). However, even if the bubble contact angle was more stable than sessile contact angle,

we cannot exclude a) the presence of airborne contaminants adsorbed on the surface and b) the influence of surface roughness in the final bubble contact angle. To overcome this problem and other issues related to the surface roughness on micro/nanoscale, the molecular dynamic simulations (computer simulation) on an ideal surface, i.e., flat and without contamination have been conducted (the simulation has been conducted by the group of Michal Otyepka University of Olomouc) (Figure 4.16c). Using molecular dynamics (MD) atoms and molecules are allowed to interact for a fixed period, giving a view of the dynamic evolution of the system. The molecular dynamics simulations of noble gasses nanobubbles on graphene were carried out using the GROMACS 4.5. Software package,46 Graphene was represented by a periodic model with dimensions of 92 Å × 92 Å. The *z*-dimension of the box was set to ~100 Å. Carbons in graphene were simulated as uncharged Lennard-Jones spheres with parameters proposed by Cheng and Steele,[36]. Argon and helium parameters were taken from literature [37,38]. The initial configurations consisted of 1,567 gas molecules, which were randomly distributed within the simulating box. The equations of motion were integrated with the time step of 2 fs. The electrostatics was treated using the particle mesh Ewald (PME) method. The cutoff distance for vdW interactions and real space cutoff scheme for PME was set to 10 Å. The system was slowly thermalized from 10 to 300 K and equilibrated at the final temperature (300 K) using the NpT ensemble (pressure, temperature, and N were kept constant). The V-rescale thermostat was used to maintain the desired temperature. The constant pressure (1 bar) was fixed with the Berendsen barostat. Then the simulation was switched to the canonical (NVT) ensemble, whereby last 100 ns of the production run was used for subsequent analysis (the trajectory was recorded every 20 ps. The bonds involving hydrogen (water model) were constrained using LINCS algorithm. Snapshots were rendered with the software PyMOL, [39]. We have chosen two extreme cases identified by experiments, i.e., the argon and helium gas. Obtained values of contact angles 73.2º, 80.0º for helium and argon, respectively, match the order obtained from experimental measurements. However, the estimations from MD differ in absolute values of the C.A. It may be explained in part by the: a) size of the studied bubbles (radii amounted to ~40 nm), b) by difference in the surface morphology (no steps) and c) in part by the fact, that the classical force field methods neglect the polarization effects, that may be necessary in such cases involving graphene, and it would require further analysis. Nevertheless, the result of MD simulations confirms that the variation of the bubble contact angle on HOPG is due to the nature of the gas.

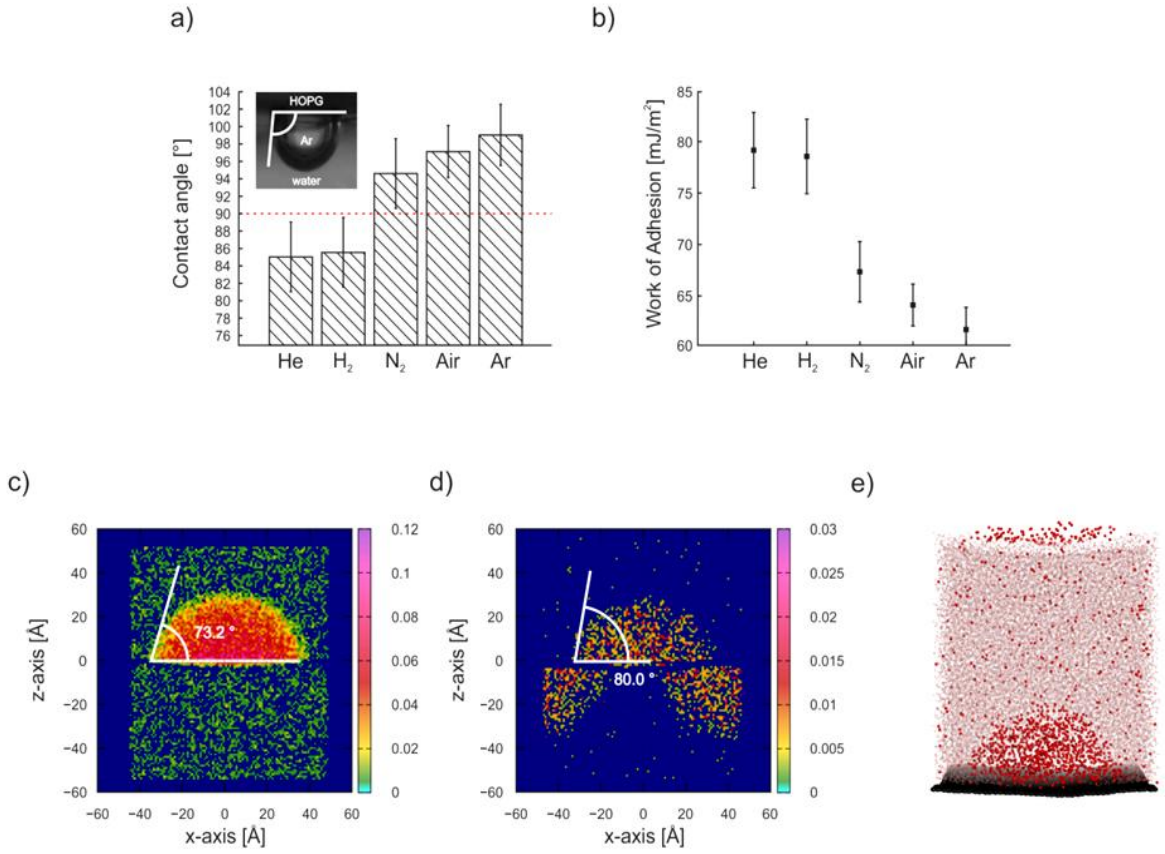

Figure 4.16 Contact angles of gas bubbles with graphite and a picture of contact angle measurement on argon bubble, (a) Work of adhesion of the gasses estimated by Young-Dupré equation from the contact angles (b), contact angles of helium (c) and argon (d) calculated on the basis of MD; resulting values were averaged over the production run. A snapshot of a typical MD simulation system (e).

4.2.5 Water wetting of flat HOPG in different atmospheres

As reported in the previous paragraph the gasses can show a different interaction with graphite when graphite is immersed in water. Therefore we reasonably expected that the contact angle of the water could change in the presence of gasses that are different from the air when the surface is graphite-based material, (or highly dispersive surfaces with Van der Walls interaction). This variation can be observable if the rate of airborne contamination air is quite low. We arranged an experimental setup which consists of a contact angle instrument inserted in a transparent plastic bag (glove bag), Figure 4.17. We performed the drop contact angle directly in a controlled atmosphere (Ar, He). After the measurement in the controlled atmosphere on the same sample, we measured

the contact angle in air. The result has been reported in Figure 4.17 as the ratio of contact angle measured inside the glove bag (controlled atmosphere) and the value measured in air. We observed slight changes of the ratio of contact angle on graphite as a function of the gas, Figure 4.17.

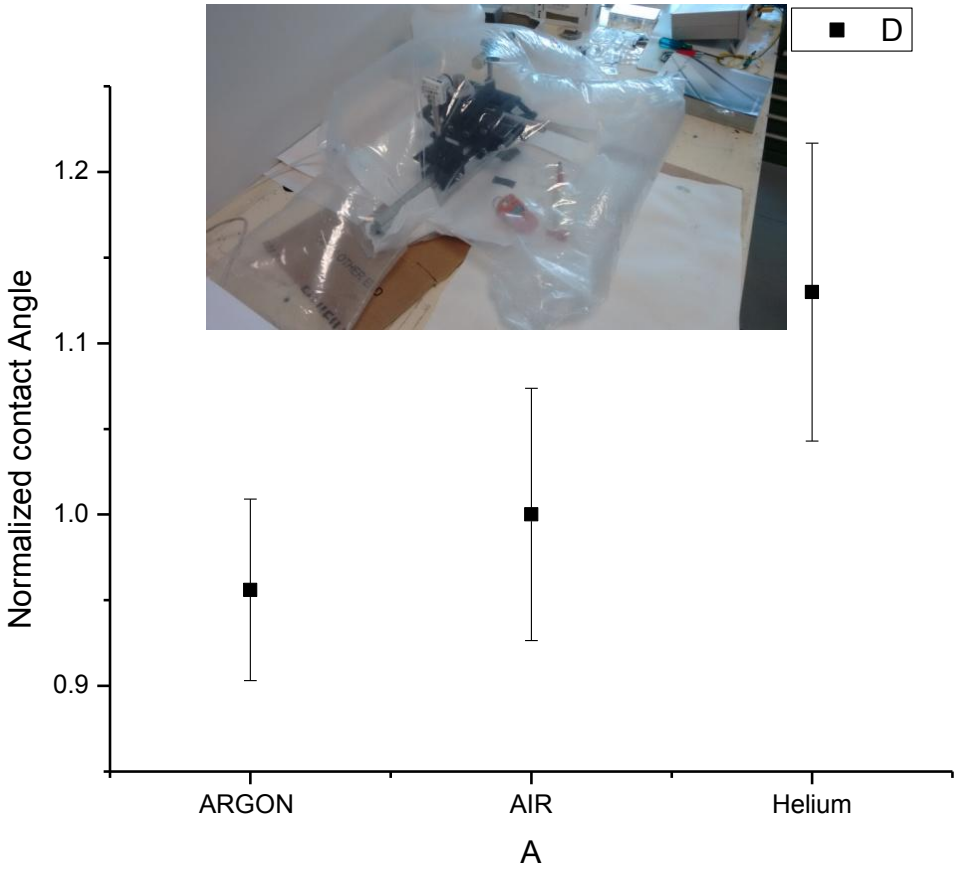

Figure 4.17 Picture of the instrument inside a glove bag filled by Ar and ratio between the contact angle measured in the glove bag using Ar, Air, or Helium and the contact angle measured outside of the glove box (indicated as "normalized contact angle").

Figure 4.17 shows the variation of the normalised contact angle (ratio between the contact angle measured in the glove bag using Ar, Air, or Helium and the contact angle measured outside of the glove box) on exfoliated graphite for the different gases atmosphere. Even if we cannot claim that a significative variation is present because the trend is almost comparable to the intrinsic measurements error. The final error on the sessile contact angle is due to the combination of intrinsic error of the instrument, around 2-4%, to an irregularity of morphology on the surface and, as observed in the previous sections, to airborne contamination. The role of airborne contaminations is the most difficult source of error to control [9], and we cannot entirely exclude that the trend

observed in Figure 4.17 is due only to the different nature of the of the used gas. In any case, the airborne contamination can influence the contact angle also in non-air atmosphere. On the other hand, from the trend showed in Figure 4.17 it appears that each kind of gasses shows a specific interaction with HOPG surface. Unfortunately, the error associated to the measurements is large and only comparing helium and argon we can appreciate a significative difference.

4.2.6. Water wetting on non-flat graphite in different atmospheres

As observed in the previous paragraph the difference between the sessile contact angles measured in the controlled atmosphere using Helium and Argon was weak. Therefore, we tried to reduce the water/graphite interaction and to increase the gas-graphite interaction increasing the roughness and inducing the Cassie Baxter effect. The method that we used was based on the physical modification of the morphology by introducing microcavities on the surface to promote gas trapping between the water drop and graphite (Cassie Baxter effect). [41]. Many techniques can be used to focussed ion beam, micro-nanofabrication, mechanical modification, plasma etching. [43,44]. To create the Cassie Baxter effect of graphite, we tested different techniques as plasma techniques, mechanical modification using sandpaper and dry dip coating using nanographite. The plasma technique (argon and oxygen plasma) and mechanical modification of surface using sandpaper gave a slight increase in the contact angle. The best method to increase the contact inducing a Cassie Baxter effect was dry dip coating. In dry dip coating, we used nanographite powder with a chemical composition like graphite, but with a structure based on flakes with a diameter of 1 micron and thickness of 60nm. In order to deposit a nanographite coating on the surface, we used a dip coater. On the dip coater, we attach graphite scotch tape, and the tape was gently immersed in a becher containing nano-graphite flakes. After 10 s, the tape has been removed. The graphite surface sample coated with nanographite flakes showed a wide range of micro- and nanocavities on the surface. Figure 4.18 reported the SEM image of exfoliated graphite and the image of surface realised using graphite nanoplates and dry dip coating. The graphite appears flat with some steps due to exfoliation of basal steps. The surface based on nano graphite shows a corrugated surface, many flakes are vertical oriented, (thickness 60-10nm) Between the flakes many cavities are present, and on the flakes nano steps due the graphite basal are present.

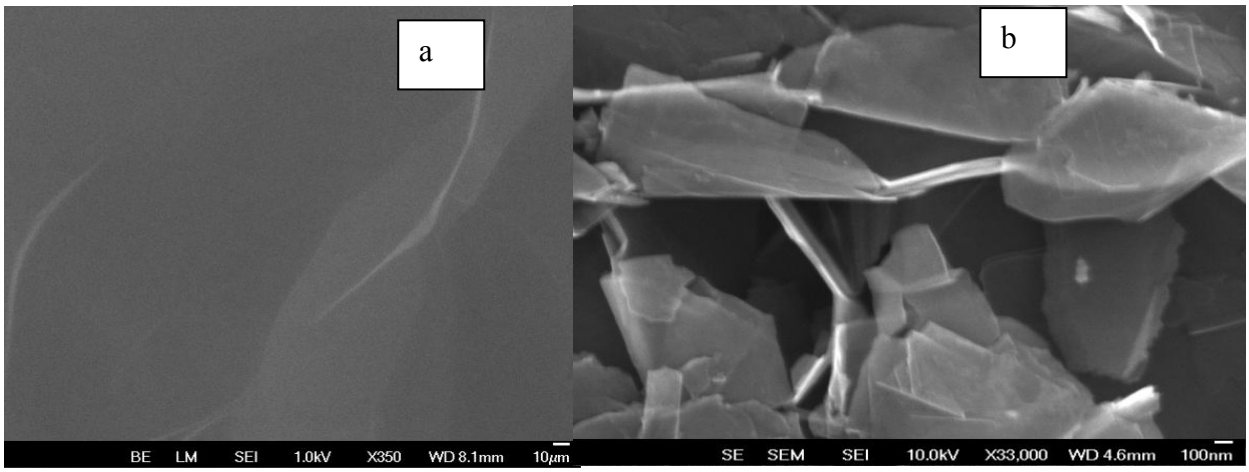

Figure 4.18 Surface morphology of exfoliated graphite (a) and graphite nanoplates deposited by dry-dip coating on the exfoliated graphite (b).

The surface, therefore, shows a structure with nano micro and macro defects. Using XPS, we estimate the chemical composition of both surfaces. Table 4.3 report the chemical atomic composition of the samples. Only carbon and Oxygen has been detected. On graphite, we detected 98.2 at. % of carbon and a small percentage of oxygen 1.8 at.%.

Table 4.3. The surface chemical composition-of HOPG and graphite nanoplates estimated by XPS.

Atomic percentage by XPS	**Carbon at%**	**Oxygen at %**
HOPG	98.2	1.8
Graphite nanoplates	97,6	2.4

The nanographite surface shows a similar composition even if the oxygen content is slightly higher 2.4 at. %. This is expected due to the different method of production of the two materials and probably to the larger amount of graphite edges, more prone to oxidation.

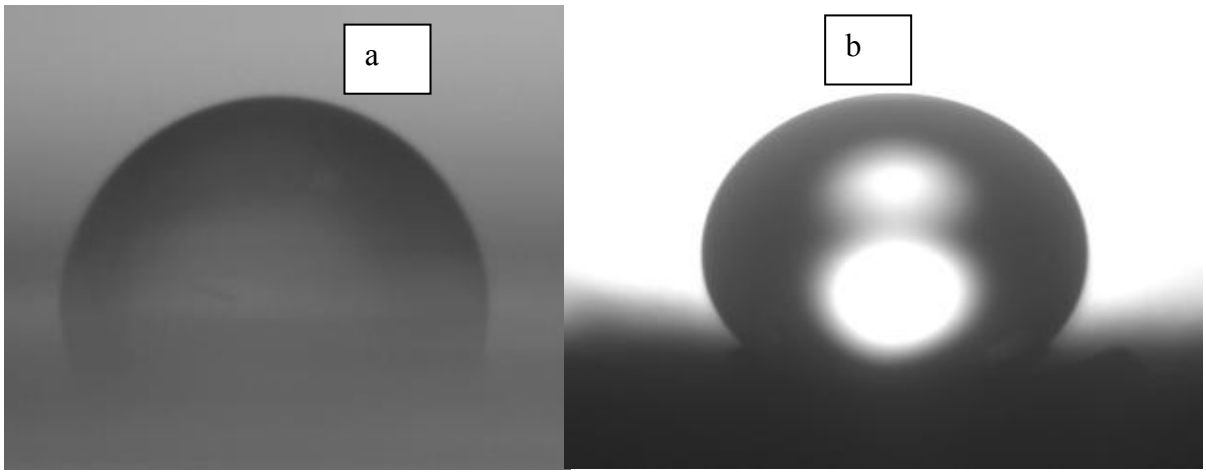

Figure 4.19 Water contact angle on exfoliated graphite (a) and on nanographite (b)

Figure 4.19 shows the wetting of exfoliated graphite (aged 1 day) and porous nanosize (aged 1 day too). The contact angle on graphite, in agreement with previous results, was 89°, on the nanoporous graphite surface obtained by coating by nanograohite flakes, the contact angle was 133°. The surface of the nano-graphite, even if more oxidized than the original graphite surface, showed a higher contact angle. This is due to the Cassie-Baxter effect. In fact, in the Casse-Baxter wetting mode, the gas becomes trapped beneath the water drop. Therefore, the surface becomes more heterogeneous by the fact that there is a zone where water is in contact with carbon and a zone in contact with air (that is virtually fully hydrophobic). Due this air entrapping we observed a significant increase of contact angle, and the surface became strong hydrophobic, (Figure 4.20).

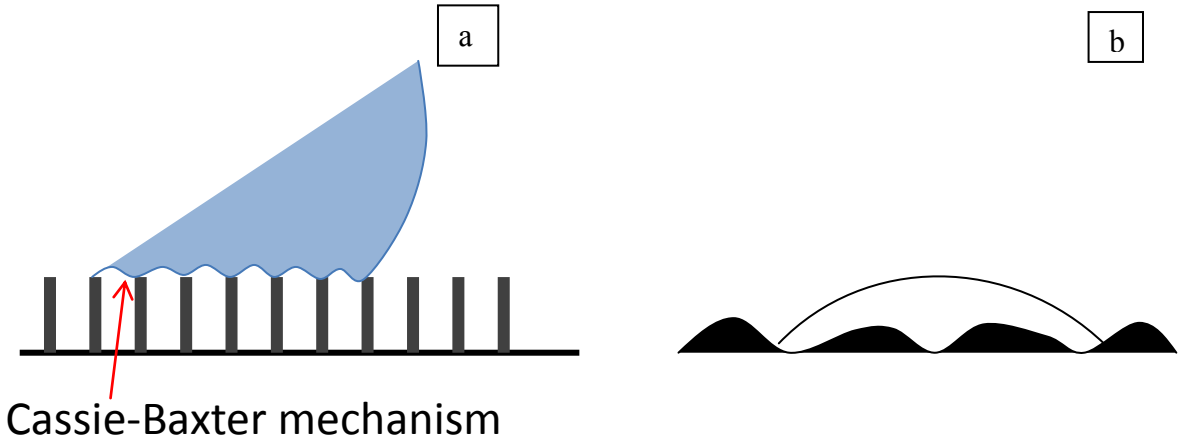

Figure 4.20 Sketch of Cassie Baxter wetting mode (a) and Wenzel wetting mode (b)

In the previous chapter, we observed that there was a small variation of wettability when we used different kinds of monoatomic and diatomic gasses when the surface is immersed in water. *Mutatis*

mutandis we could reasonably expect that the sessile contact angle of water can change in the presence of gasses that are different from the air when the surface is graphitic, (or a highly dispersive surface with Van der Walls interaction). To verify this hypothesis, we measured the sessile contact angle in a controlled atmosphere. The experimental setup consists of a C.A measurement instrument placed in a glove bag. The glove bag was filled with Argon and Helium. The glove bag was filled and emptied ten times. Inside a portable oxygen sensor was inserted. The level of oxygen detected in the glove bag was less 2%.

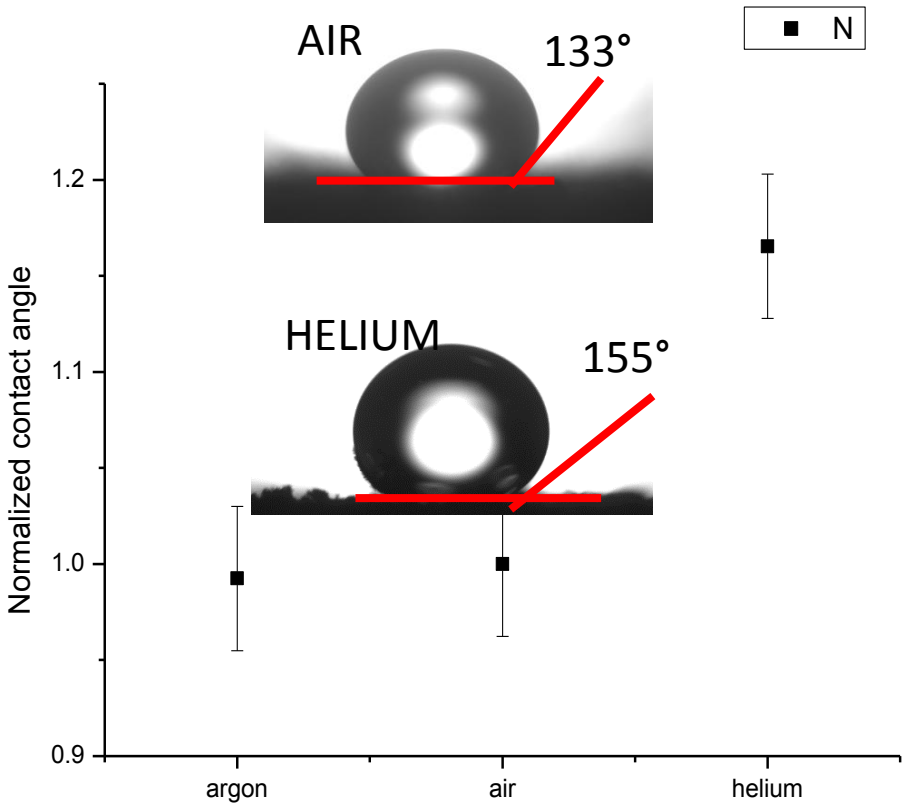

Figure 4.21 . Image of sessile contact angle on graphite nanoplates in air and in helium and ratio of contact angle in argon, air and helium atmosphere normalized to the contact angle on the same surface measured after glove bag experiment.

To reduce as much as possible the source of error, after the measurement in a controlled atmosphere, the instrument and the sample were removed from the glove bag, and after 3 minutes the contact angle was measured on the same surface. The obtained results on argon and helium have been normalised to the contact angle measured in the air on the same sample. Figure 4.21 shows the drop of water on nano graphite in a different environment. In helium atmosphere, we measured a

contact angle of 155° and in the air a contact angle of 133°. In Figure 4.21 we reported the normalized contact angle of the surface with the different gasses. We observed that in helium the contact angle is sensibly higher than in air and in argon. The results appear in agreement with the results reported in the previous section, using bubble contact angle. In fact, we observed that in the bubble contact angle measurements, the angle in helium was lower than in air. It should be taken into consideration that the bubble contact angle is the angle between the surface-gas interface and the gas-liquid interface. This angle is the complementary angle of the standard contact angle between the solid-liquid and liquid-gas interfaces. Therefore, the increase of the drop contact angle means a reduction of the interaction of water with graphene and an increase of interaction of the gas with graphite, as observed with the bubble contact angle. It is interesting to note that this phenomenon is more evident on the nano-graphite surface, thanks to the reduction, proportionally, of the interaction water/graphite interaction and to the increase of the gas/graphite interaction by Cassie Baxter effect.

4.2.7 Polarizability and behaviour of the gas on the HOPG surface

Since sessile drop analyses demonstrated that graphite surface had a non-polar behaviour, we could also expect that the interaction between gas and graphite is mainly due to London interactions. In the dispersive interaction, polarizability plays a significant role, and this is also demonstrated by the correlation between polarizability of the gas and the contact angle reported in Figure 4.22. The gasses, in fact, with low polarizability such as helium and hydrogen (1.4 - 5.4 a.u.) show a positive interaction with exfoliated HOPG while the molecules with high polarizability show a repulsive interaction with HOPG see Table 4.4. The transition from gasphilic to gasphobic regime regarding polarizability happened, in these samples, around 7–10 a.u. That is the typical range of polarizability of aromatic carbon bonds reported in the literature (7–10).[45]

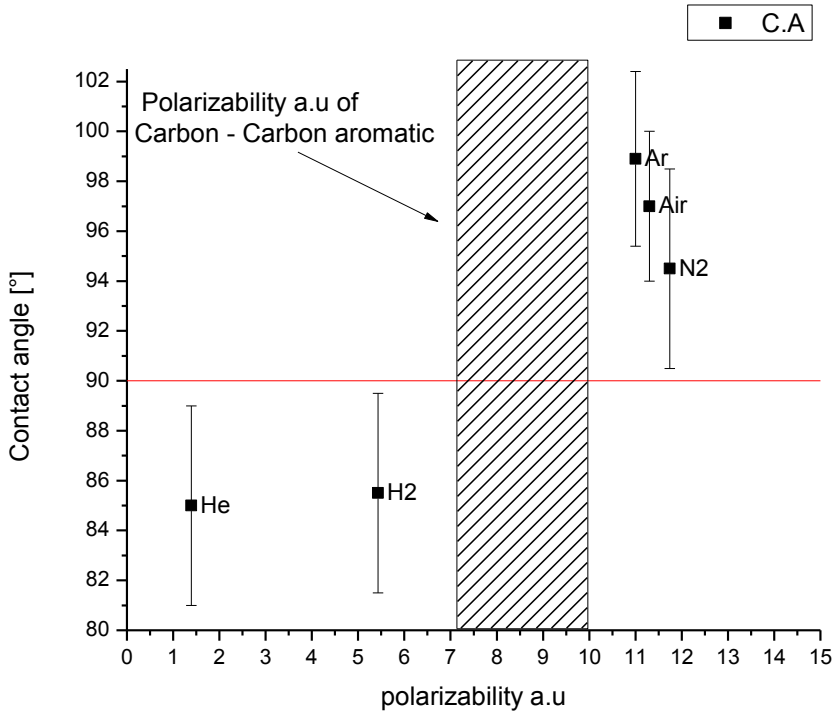

Figure 4.22. Bubble contact angle as a function of gas polarizability (atomic unit), on exfoliated graphite.

Therefore, when the polarizability of the gas is higher than the polarizability of the surface, the contact angle of the bubble tends to increase, and the work of adhesion tends to decrease, Figure 4.16b. This indicates that under a phenomenological point of view, in a system composed of a bubble in contact with a solid surface, there is a dynamic equilibrium between the gas-solid interaction at the interface (bubble–solid) and gas–gas interaction presents in "bulk" of the bubble. The higher is the gas–gas interaction the lower is the gas adhesion on the surface.

Usually, the gas-solid interaction is stronger than the gas–gas interaction (cf. Table 4.4). For instance, the N_2–HOPG interaction potential is 166 meV while N_2–N_2 interaction potential is only 17 meV. If we define χ as the ratio between gas-HOPG and gas-gas potentials.

$$\chi = \frac{Gas{-}HOPG\ (well\ depth\ potential)}{Gas{-}Gas\ (well\ depth\ potential)} \quad (4.2)$$

We can observe that N_2–graphite interaction is ~7 times higher of N_2–N_2 interaction. Table 4. shows the values gas-HOPG (gsw) and gas–gas potential well depth (ggw) reported in the literature. Anyway, to have a systematic evaluation on a flat clean HOPG surface at 300K and a 1atm, gsw

and ggw have been calculated by Density functional theory, vdW-DF functional (the calculation has been performed by M. Otyepka University of Olumuc) calculations were performed using the projector-augmented wave method in the Vienna Ab initio Simulation Package (VASP)[81]. Optimized van der Waals functional optB86b-vdW functional[38,84] was used in all calculations, which provided a balanced description of structural and adsorption properties[46,47]. In addition, possible effect of many-body dispersion interaction was considered by using the many-body dispersion energy method (MBD@rsSCS) introduced by Tkatchenko et al [48] because the many-body terms can affect the binding energy of noble gas atoms on graphene [49]. The (0001) surface of graphite was modelled using a slab of 3×3 elementary cells with a thickness of two layers (36 carbon atoms in total). The two-layer system is denoted as graphite since it mimics the behaviour of a real graphite substrate due to weak interaction among layers. The 6×6×1 k-point grid was used to sample the Brillouin zone. The periodically repeated slabs were separated by 17 Å of vacuum. The energy cutoff for the plane-wave expansion was set to 400 eV. The He and Ar atoms were placed into the hollow positions (the centre of hexagonal ring). It should be noted that other adsorption positions (top of C atom, bond between two carbon atoms) are almost isoenergetic [50] The H_2 and N_2 were positioned so that their center of mass lied in the hollow position. The minimum of the energy was found by force-relaxation, i.e., the atomic forces were fully relaxed using conjugate gradient algorithm. For the calculation of dimer potential well depth, the species were placed into a cubic supercell having the length of 22 Å in each direction. The energy cutoff for the plane-wave expansion was increased to 600 eV. We used T-shaped dimer geometry for both H_2 and N_2 molecule, which is the ground-state geometry of the dimer according to earlier calculations [51,52] The calculated potential well depths are generally in agreement with other theoretical calculations. For the N_2 dimer, energy values of 17 meV and 14 meV were obtained using the optB86b-vdW and MBD@rsSCS functional, respectively. Accurate ab-initio calculations at the MP4 and CCSD(T) levels provided the values in the range 7–16 meV [47,83], depending on the method and the basis set used. The well depth of argon dimer agrees well to the coupled cluster singles and doubles and perturbative triples – CCSD(T) – value of 11.5 meV [53,83] as well as to the experimental value of 12.4 meV. The only slight exception is the well depth of He on graphite. In that case, both optB86b-vdW and MBD functional predict the potential well too deep (42 meV and 56 meV, respectively), whereas previous calculations reported the values in the range of 12-20 meV [see Ref.[47,54]]

Table 4.4 Data of static polarizability in atomic units (a.u.) and potential well depth (meV) and χ used in this work, estimated by vdW-DF and experimental values reported in the literature.[55,56,57 54;58]

Gas	Polarizability α_0 (a.u.)	Potential well depth[1] (meV) Gas–Graphite. vdW-DF	Potential well depth[1] (meV) Gas–Gas vdW-DF	χ Ratio Gas–Graphite/ Gas–Gas vdW-DF	Potential well depth (meV) Gas–Graphite	Potential well depth (meV) Gas–Gas	χ Ratio Gas–Graphite / Gas–Gas	Kinetic Molecular Radius (pm)
He	1.38	42 (56)	1 (4)*	~42	16.2	0.88	18.4	260
H_2	5.43	65 (79)	5 (9)	13.0	51.7	3.1	16.7	289
Ar	11.07	141 (113)	14 (13)	10.1	96	10.7	8.9	344
N_2	11.74	166 (126)	17 (14)	7.2	104	7.89	13.1	346
Air	11.2[2]	172**	20**	8.6	101.2	8.26[2]	12.2[2]	350

1) All values were calculated by optB86b-vdW functional. The values calculated by MBD@rsSCS functional are in parentheses.

2) Estimated as a function of molar fraction of N_2 and O_2, by Refs.[57,59]

*** lower than the convergence precision, in literature the value amounts to 0.95 meV[60]**

**** estimated as the weighted average 78 % of N_2, 21 % of O_2 (potential well depth for gas-graphite is 198 meV and for gas-gas is 10 meV) and 1 % of Ar.**

The most elaborate study calculated the He–graphene interaction via the method of increments by evaluating two- and three-body dispersion terms at CCSD(T) level[61] and obtained 17.7 meV at the distance of 3.2 Å. However, they did not consider other distances, so the minimum of the binding energy lied presumably deeper. The binding of the He dimer was very weak (1 meV using the optB86b-vdW functional and five meV using MBD@rsSCS), despite overbinding for He on graphite. Comparing optB86b-vdW functional to its many body counterpart MBD@rsSCS, one can observe that the functional yield very similar values, except for the interaction of N_2 and Ar with graphite, in which case the MDB functional provided significantly lower values of the well depth. The lower values of the interaction energy were caused by the long-range many-body effects, which brought a negative contribution to the well depth (-13 and -11 meV for N_2 and Ar, respectively).

This finding is analogical to the effect many-body terms observed in the previous study by Ambrosetti and Silvestrelli.[62] Nevertheless, both our theoretical calculations indicated that the group of gas composed of helium and hydrogen had the lowest contact angle and showed the highest χ value. Meanwhile, the group of gas composed by Ar, Air and N_2 that had the highest contact angle, has the lowest χ ratio. This indicates that the equilibrium of interaction in the bubble of gas in contact with a surface immersed in a liquid is tuned by the χ ratio.

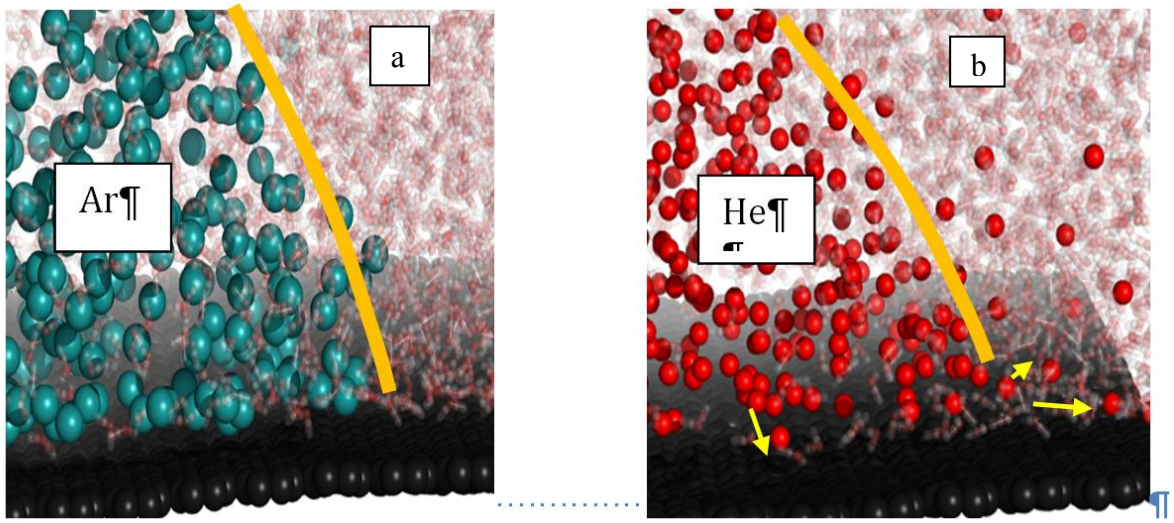

Figure 4.23 Argon (a) on, and He (b)bubbles on graphite, the yellow arrow indicates the higher tendency of He to be spread on the surface

.

The work of adhesion that is calculated by equation Young Dupre equation using the surface tension of water and the bubble contact angle of the gasses gives a semiquantitative indication of gas adhesion with HOPG in water. The work of adhesion of He and H_2 was higher by ~14 mJ/m^2 than the work of adhesion of Ar indicating that the work of adhesion lowered when the χ ratio decreased. This finding was corroborated by theoretical calculations because the estimated works of adhesion (from gas-graphite potential well depth, Table 4.4) of H_2 was by ~26 mJ/m^2 higher than the work of adhesion of Ar (by MD). For H_2 and He the weaker gas–gas interaction the relative good interaction of HOPG leads to the high χ ratio; this promotes a higher spread of this kind the gas on HOPG surface, Figure 4.23.

We can suggest that some gasses such He and H_2 fit better-corrugated potentials present on HOPG surface due to the geometrical dimensions of the molecules. This is corroborated by the kinetic molecular radius of the molecules, reported in Table 4.. Helium and hydrogen show a small

radius 260 and 285 pm respectively. The typical radius of a ring of graphite is 240 pm. The dimension of He and H_2 can help solid-ordering of the gas molecules at the graphite surface that is reflected in the high gas affinity of He and H_2 with graphite. We remark that χ indicates that in thermodynamics properties estimation the gas-gas interaction should be explicated. Therefore, the equation giving the work of adhesion equation needs further improvement to be correctly applied to the gas–surface interaction estimation of carbon-based materials immersed in liquid. Although these results were obtained only on HOPG surface which is perfectly oriented, the findings may provide new insight into interfacial phenomena, which may have an impact on a broad range of fundamental studies and applications in particular in gas storage and on the self-cleaning surfaces.

4.3.1 Effect of Surface Modification on wetting properties of graphite.

In this section, the results of a study of the effect of graphite surface modification on its wetting properties will be presented:

4.3.2 Surface oxidation of Graphite

To modify/oxidize in a controlled mode the surface of materials, one of the most efficient methods is the cold plasma treatment. In the cold plasma treatment, reactive chemical species are created in the plasma discharge. The volatile reactive species in the gas phase are free to penetrate in micro- and nano-steps and asperities and they can react with the side which is not exposed directly to the plasma discharge. For this reason, the cold plasma treatment is used to activate also structures with a complex geometry like micro-nano structures as well as porous structures. [63,64,65]. Moreover, low-pressure plasmas have been widely studied to modify the liquid-solid interaction on carbon-based surfaces. Plasmas have many advantages such as low power consumption, control of the surface modification and low temperature of the process that reduces the probability to degrade the temperature sensitive surfaces [63]. Different kinds of plasmas has been used to modify the surface of materials. Jokinen *et al.* used oxygen and nitrogen plasmas to efficiently reduce the water contact angle on various polymers including hydrophobic polymers as PDMS [66,67]. Argon plasma at 100W was successfully used by Pinto to improve the wetting properties of materials for bio-applications [68]. Results reported in the literature indicate that low-pressure plasma, in particular, oxygen plasmas, is an efficient tool to activate polymer surfaces [64,65]. In our work, the HOPG were treated by ŧadiofrequency oxygen plasma. (Instrument Colibri Gambetti, Binasco Milano). The pressure was kept at 0.4 bar, electrical power at 15 W, while the time of treatment was varied from 10s to

240 s. The optical emission spectroscopy was used to identify the main chemical species present in the plasma discharge, in a non-invasive manner. Optical emission spectra were acquired using an optical fibre connected to the monochromator and photomultiplier. We acquired the signal from plasma in the region near the HOPG surface (spot diameter 4cm). The signal was acquired from 400 nm to 850 nm wavelength.

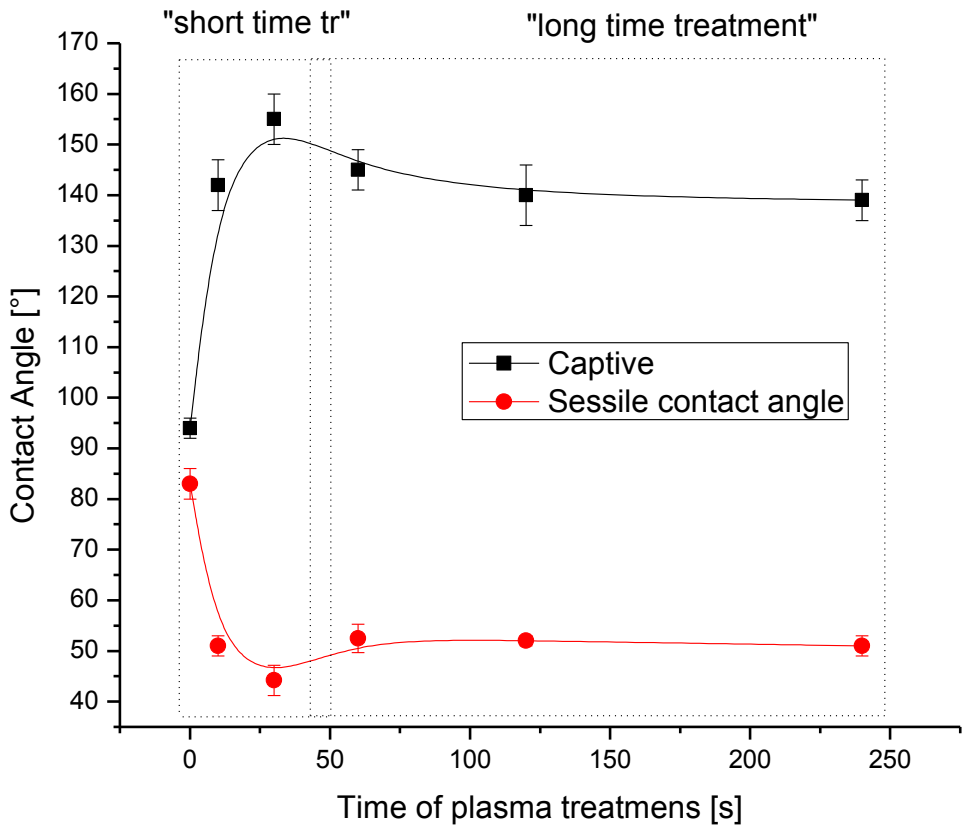

Figure 4.24 Sessile water contact angle on graphite and captive contact angle on treated graphite.

The optical emission spectroscopy of the plasma showed the presence of the line of atomic oxygen (777.4 nm) and the bands of O_2^+ species (500-700)[69]. Moreover, the H_α and H_β lines at 656.3 and 486.1 nm were detected, more probably due to the presence of water on the wall of the plasma reactor[7071]. Atomic oxygen is strongly reactive species that can easily react with carbon species from graphite. This is confirmed by results reported in figure 4.24 that shows the variation of contact angle on graphite and the change of bubble contact angle. We can observe that the short plasma treatment increase the wettability because the contact is less of 60 deg. A minimum value of the water contact angle with a treatment at 30 sec was reached (45°). Using longer treatment times,

hereafter “long-time treatment”, we observed a slight increase of the sessile contact angle. A similar trend is reflected, on air bubble contact angle. The “short time treatment” showed an increase of bubble contact angle from 94° to 155°. After 30 seconds of treatment, the bubble contact angle increased to 145°and using a treatment of 60 seconds to 155°. The increase of the air bubble contact angle after the “short time treatment”, is due to the increase of the interaction on water/graphite, this led to the increase of the bubble contact angle. After the 60 second of treatment, a reduction of bubble contact angle was observed. The behaviour of the sessile contact angle is complementary to the captive bubble contact angle. Therefore, if we consider a rigid geometrical correlation between the sessile contact angle and the captive bubble contact angle, we could expect that their sum should be equal to 180°. Figure 4.25 reports the sum of the two contact angles. We can observe that for pristine HOPG the sum of sessile and bubble contact angle was 180°, the treated samples sample showed instead a sum higher than 180°.

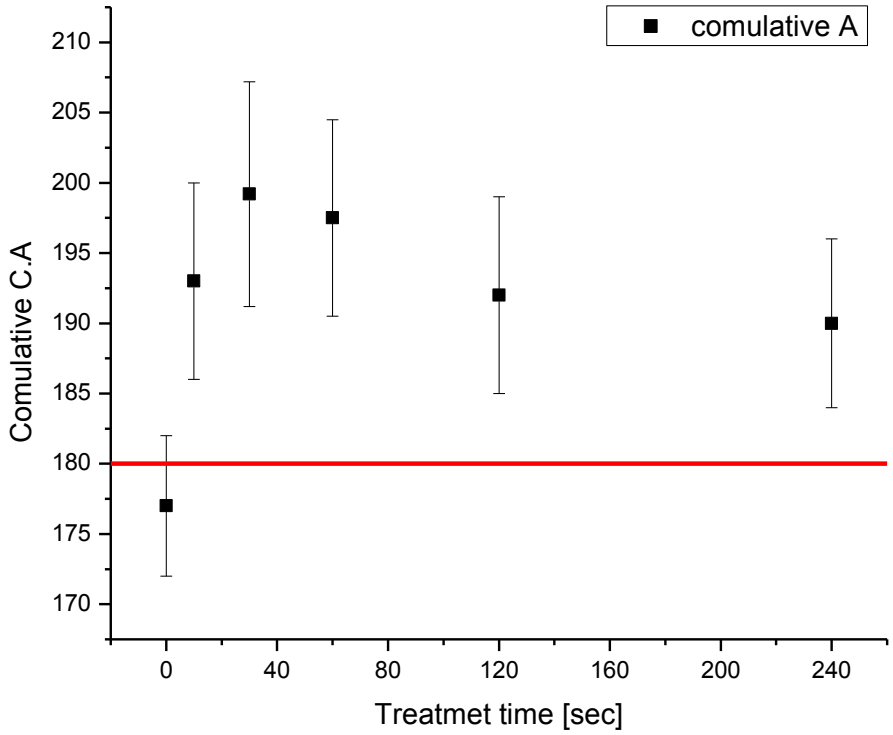

Figure 4.25. Sum of sessile contact angle and captive contact angle as a function of treatment *time.*

This indicates that water interacts in different manners in function of the experimental set-up (when the surface is totally immersed in water and when a water drop is on the surface). Using Raman spectroscopy analysis, we observed that for the untreated HOPG only the 1G e 2D peaks are

present, figure 4.26. G peak appears very sharp. The G peak is at 1589cm^{-1}, and the 2D peak is at 2690cm^{-1} as in the typical Raman spectrum of HOPG [72,73]. The treatment did not produce a shift of the peaks of G and 2D peak. The peak 1D, typically due to the defects was not present on HOPG. Only the samples treated with oxygen plasma at the time of treatment longer than the 60s showed the presence of a 1D peak Figure 4.26. The 1D peak is associated with the presence of defects in the lattice of graphite, like the removing of the atom from the lattice [74]. The G band is the only band coming from a first-order Raman scattering process in graphene, after absorbing a photon from the laser radiation, the electron on graphene surface undergoes an inelastic scattering and releases a G band phonon. Sample environment does not so much influence 1G, and for this reason is a good reference peak to study the evolution of peak 1D 2D.

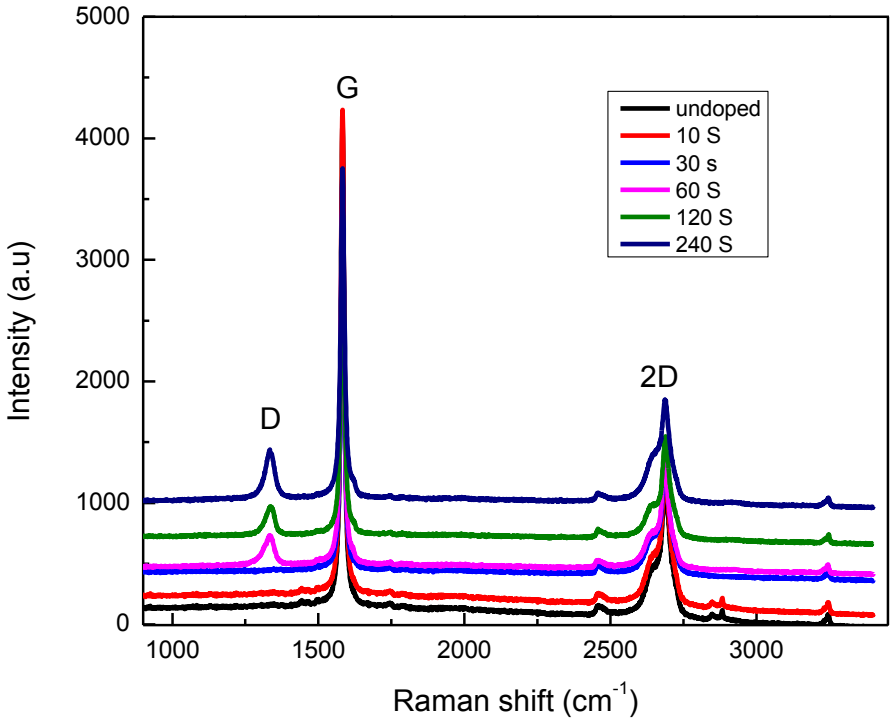

Figure 4.26 Raman spectroscopy of graphite treated with oxygen plasma.

The intensity ratio of 2D peak to G peak is reported in Figure 4.28. The value of the ratio was 0.27 for HOPG and increased monotonically up to 0.5 when HOPG has been exposed to a plasma for 240s [75]. In figure 4.28 we report the intensity ratio of peak 1D to 1G, 1D/G, as a function of the time of exposure to the plasma treatment. The surface exposed to the plasma for more than 30s showed a higher 1D/2G ratio, 0.20. The 1D peak is detected, indicating the formation of a structural

defect in the honeycomb structure of HOPG graphite. After 180s, the 1D/G intensity ratio remained constant, also indicating probably a stabilization in the formation of the structural defects in graphite lattice. From the 1D/1G ratio value we could expect that defects produced by "long time" oxygen plasma is round holes with a border with armchair hedge shape, because of the ratio is around 0.3 [76].We cannot exclude that the presence of another kind of structural defect on HOPG and the surfaces exposed to the plasma for 10 and 30 sec, like a hole with a perfect zig-zag profile, charged impurities The contribution to the 1D peak of borders with zig-zag profile, in fact, is less than armchair profile [76]. In any case using SEM and AFM on exfoliated graphite, borders of basal plane of graphite was detected, Figure 4.27, but the distance between two basal borders was in many cases higher than 15 microns. Therefore, the border to border distance is always greater than lateral resolution of Raman spectroscopy (200-500nm), and the probability of detecting an edge of the basal plane is rare. We can consider the weight of the border of basal plane negligible. In the Raman spectra we didn't observe a significant shift of the G peak nor broadening bordering of the 2D peak.

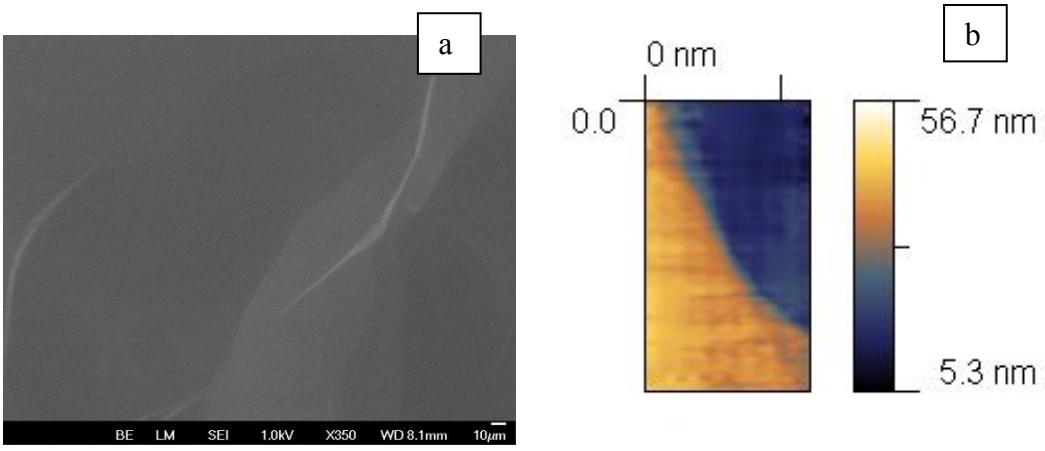

Figure 4.27 SEM image of exfoliated graphite (a), and topography map by AFM of the border of the basal plane on HOPG surface, thickness around 25 nm (b).

Apparently, there is no increase in the strain of the lattice structure. However, the ratio of intensity 2D on G intensity increase with the time of treatment, Figure 4.28a. The 2D band is the second order of the D band, sometimes referred to as an overtone of the D band. It is the result of a two-phonon lattice vibrational process, but unlike the D band, it does not need to be activated by proximity to a defect.

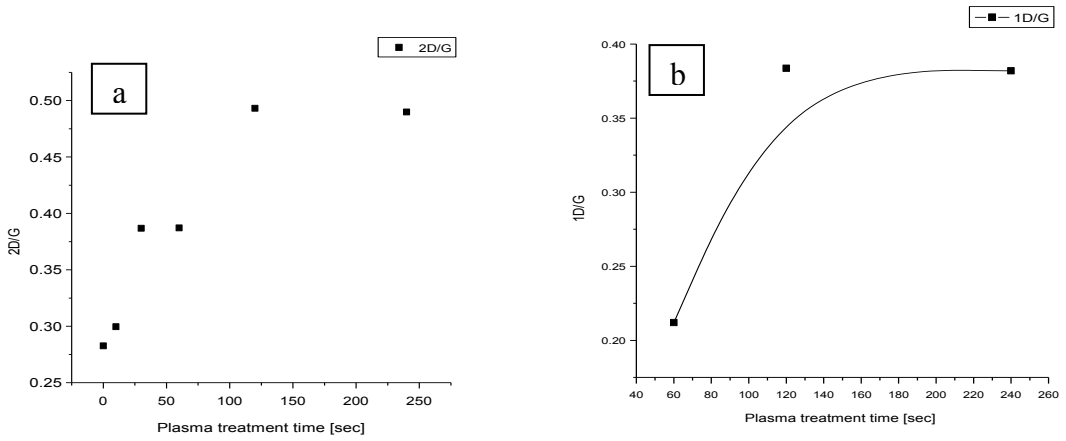

Figure 4.28 Ratio I_{2D}/I_G (a) and ratio of I_{1D}/I_G on graphite and treated graphite (b).

As a result, the 2D band is always a strong band in graphene even when there is no D band present, and it does not represent defects. This band is also used to determine graphene layer thickness. There is a linear increase in G band intensity as the number of graphene layers increases, collected with 532 nm excitation. The ratio I2D/IG for high quality (defect-free) single layer graphene is to be equal to 2. This ratio, lack of a D band and a sharp symmetric 2D are often used as a confirmation for a high-quality defect-free graphene sample. The absence of 1D peak (defects) and low ratio I2D/IG 0.2 on graphite indicate that the surface is without defect ad it is composed of several layers of graphene as expect of graphite, but the quality of ordering of surface should be low [77,78]. The plasma oxygen introduced defects in materials but as indicated by the I2D/IG intensity ratio it promoted a more uniform surface, and ordered Bernal structure (A-B) . For the treatment at 180 and 240 sec, the ratio is 0.5 the typical value of well-ordered multilayered graphene surface.
Graphite samples have been mounted on silicon slide (100) to be analysed in the XPS instrument. Carbon-Oxygen and a small signal of silicon (<1%) were detected. Silicon signal and silicon oxide are due to the substrate. Figure 4.29 shows the variation of surface chemical composition, atomic %, of the samples. The carbon percentage react a minimum of 85% when the surface is exposed to the plasma process of 30 for the same treatment the oxygen reach a maximum of 15%.

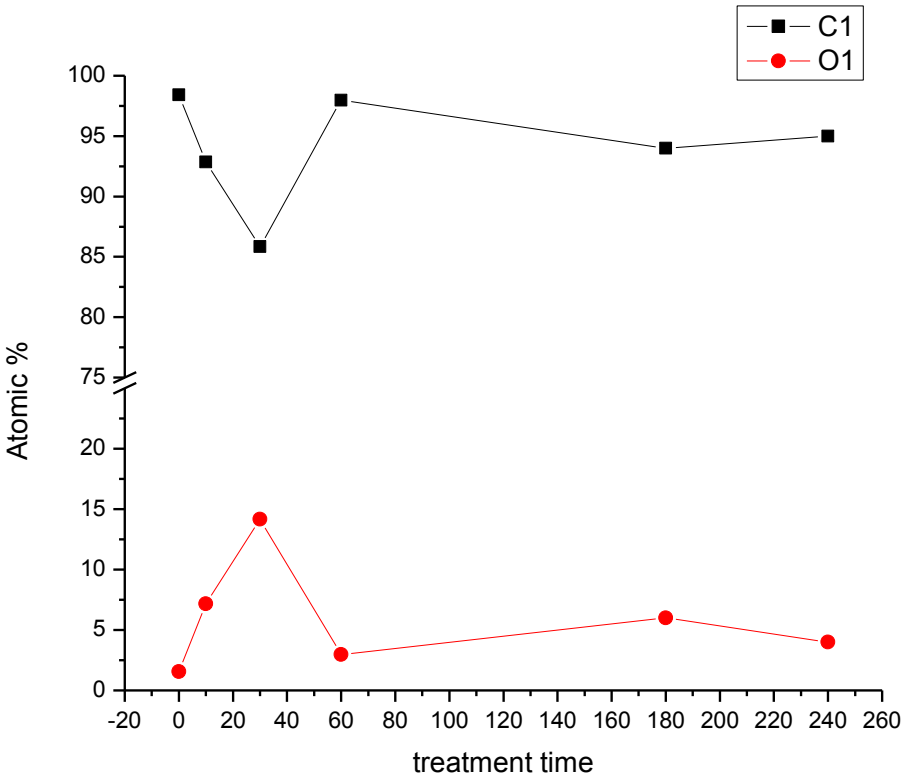

Figure 4.29 Carbon and Oxygen atomic percentage measured by XPS on graphitic samples

In Figure 4.30 we reported the XPS spectrum of C1s core line of the HOPG and sample exposed to the oxygen for 30sec and 240 sec. On the sample treated by oxygen plasma we identify the component due to C-C interaction at 284.5 eV (C#1) the components due to airborne contamination at 285.2 eV(#2) the components attribute to epoxies group C-O, C-OH bonds (286.5 eV #3) the components due to the double bonds of carbon with oxygen, carbonyl C=O (287.5eV #4) the components due carboxyl group to HO-O-C=O and COOH (289.2eV#5) and shake up band due to π-π^*(290.5 eV#6).The kind of carbon-oxygen bonds are depicted in Figure 4.30. The quantification of each component for all sample is reported in Table 4.5. In Figure 4.31 we reported the XPS peak of oxygen O1s core line at between the 525 eV 540 eV, in particular, we reported the comparison of the normalized peak of the HOPG of HOPG treated for 30sec and treated for 240 s with oxygen plasma. The peak of the O1s can be deconvoluted in different components 531.08 is due to double bonding to aromatic carbon denote #1 peak at 532.03 is typically assigned to (C-O oxygen single bonded to aliphatic carbon denoted as #2) the peak at 533.4 e.V assigned to phenolic group (oxygen single bonded to aromatic carbon #3) and 534.7 assigned chemisorbed water #4), Table 4.6 show the percentage of O1s components.

The difference in of C1s core line for the HOPG; HOPG treated at 30 sets, and the 240 s can be easily appreciated Figure 4.30. The shape of core line of HOPG is quite similar to the shape of graphite treated for 240 sec. The shape of C1s of graphite treated for 30 sec show shoulders at higher binding energy > 286.5 eV typical of carbon-oxygen bonding. The short time plasma until 30 seconds promotes the formation of epoxy carbonylic on the carboxylic group; all these functional groups are polar group, and this improve of wettability on a graphite surface. The longer plasma treatment promotes a significative reduction of oxygen bond on HOPG surface, in particular, the formation C-O bond and the component of O1s is 533.1 is strongly dismissed see the comparison of the O1s.

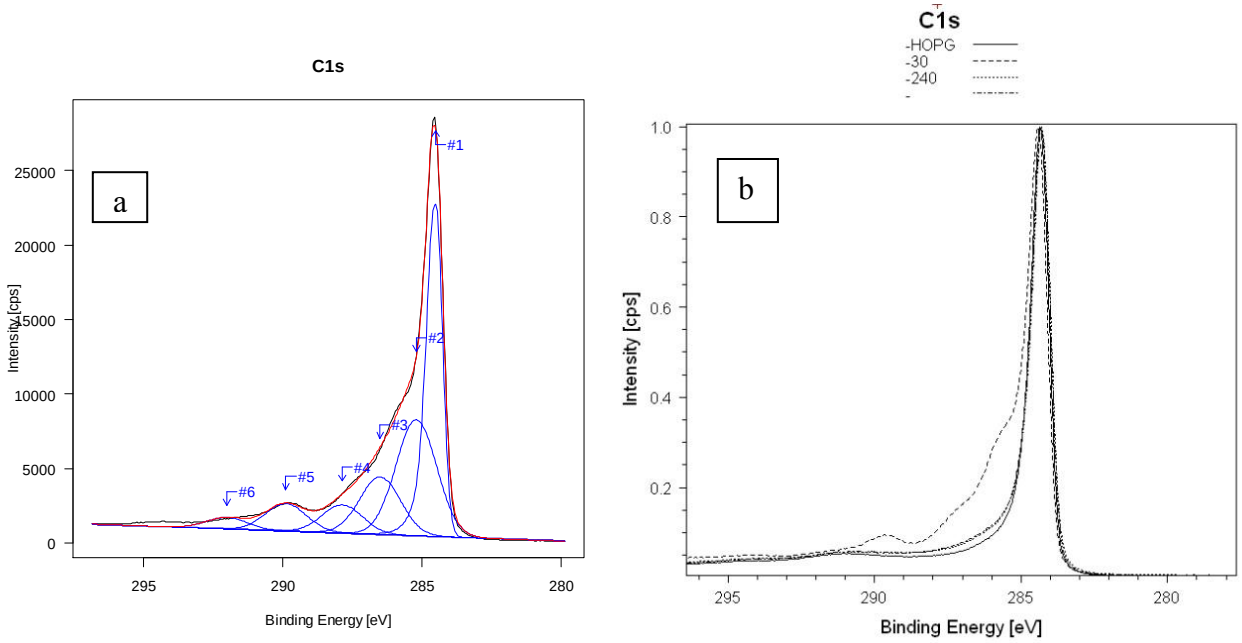

Figure 4.30 C1s core line of graphite (a) and comparison of normalized C1s core line of graphite exposed to plasma for 30sec, 60sec and 240 sec (b)

The same trend was observed in the C1s core line where we observed the increase of C-O components for short time treatment and a significant reduction for longer plasma treatment. The decrease of oxygen polar on the sample treated with longer exposure to the plasma (>60sec) is accomplished by an increase of sessile contact angle.

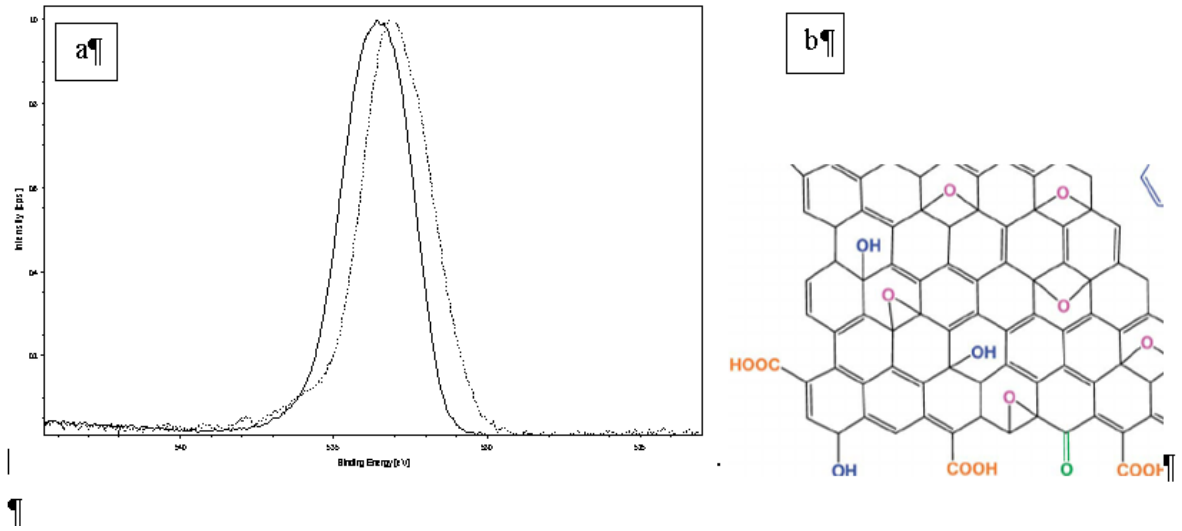

Figure 4.31.Normalized XPS O1s core line of graphite treated with oxygen 30sec (solid line) and treated 240 seconds (dot line) (a), the functional groups on a graphite surface, an epoxy group (purple) carbonylic (green) and carboxylic (orange)(b)[79] .

Table 4.5. The relative percentage of the different components on C1s XPS core line on graphite and treated graphite.

	284.5eV at. %	**285.3eV at%**	**286.5eV at%**	**287.5 at%**	**289.1eV at%**	**291eV at%**
	C-C	Hydrocarbon	C-OH C-O	C=O	COOH	π-π^*
HOPG	61.28	12.58	2	2.45	0	20.4
10 s	58.2	5.6	11.7	4.39	1.46	14.6
30 s	33.18	27.25	13.49	6.62	6.44	2.24
60 s	59.5	10.84	9.2	0	1	17
120 s	56.27	11.82	8.2	1	0	18.
240 s	58.4	10.77	6.73	3.16	0.86	16.01

The short plasma treatments do not induce a defect in the HOPG lattice, On the contrary, the long-time treatment reduces the presence of oxygen in the particular carbonylic carboxylic group while the epoxy group remain on the surface of the material. Raman spectroscopy has detected formation of defect/hole on the surface of HOPG surface.

Table 4.6 Relative atomic concentration of the different components on O1s XPS core line on graphite and treated graphite for different times.

	531.7eV at. %	**532.3eV at%**	**533.4eV at%**	**534.2eV at%**
	C=O	-C-O-	(C-O)-aromatic	Chemisorbed water
HOPG	0.15	0.9	0.18	
10 s	0	1.63	1.65	
30 s	0	0	9.42	0.4
60 s	0.32	0.76	0.57	0.25
120 s	0.58	1.15	1.10	0.54
240 s	0.2	2.53	1.11	

Nakahara[74] observed similar results on graphite exposed to an oxygen plasma but using time of exposure 20 times longer than the time employed in our experiments. Nakahara proposed that the producing of a nanoporous basal plane of graphite is due to the reaction of carbon with oxygen that for long exposure can lead to the formation of C-O and CO_2 molecules which are removed easily to the gas phase and consequently to the removal of carbon atoms from the graphite surface with the creation of pores in the carbon honeycomb basal structure. Our results seem in line with the results of Nakahara. We observed that the transition by C=C to CO_2 is probably mediated by the formation in the early stage of epoxy and carboxylic groups. The result does to explain why the sum of the sessile contact angle and the captive bubble contact angle differ with 180°C for some treatments even if this phenomenon appears to be linked to the oxygen functional groups presence. We can suggest that some zones of the surface where polar functional groups (epoxy, carbonyl, carboxyl group) were grafted had a greater interaction with water in comparison to the remaining zones of the surface of dispersive character. This chemical heterogeneity combined with the nanostructuring of the surface can induce different kinds of the wetting mode in different experimental conditions, For instance, on the same surface, using a drop we could have the Wenzel wetting mode but when it is immersed in water Penetrate wetting mode could become dominant. The latter mode induces a higher hydrophilicity than the Wenzel mode. Therefore, the sum of the contact angle will be greater than expected. Inside the bubble, in fact, the relative humidity is high, and condensation of water

vapour can easily happen. Water condensation can produce micro/nano drops, in particular near the triple point (contact angle), and this can promote a variation of the wetting mode, i.e. from Cassie Baxter mode to Wenzel mode. The condensation of water may more likely happen on the region decorated with polar groups, like epoxy, carbonic and carboxylic groups and the intensity of this effect is proportional to the amount of the polar groups, because these kind of groups are more hydrophilic. The main divergence of the total contact angle with the value of 180° occurred when the HOPG surface is exposed to 30 sec of oxygen plasma that was also the plasma condition that produced the most hydrophilic graphite surface. For this reason, we suggest that there is a correlation between hydrophilicity and the divergence of the sum of the contact angle with 180°, induced by different wetting modes in the two different set-ups that we used to measure the solid-liquid interaction.

In addition, we measured the wettability of different kinds of oxygen-treated materials with 2-propanol. The value of contact angle is reported in Figure 4.32, the contact angle with 2-propanol was always less than 5°, indicating a good interaction of isopropanol with pure graphite, that have a dispersive surface, and with oxidized graphite. Similarly, we observed a captive bubble contact angle >175° when various kinds of graphite surface were immersed in 2-propanol indicating a good interaction of 2-propanol with all kinds of surfaces. This is due to the low surface tension of 2-propanol.[28], A low surface tension, in fact, promotes the liquid spreading onto the graphite surface in any surface condition.

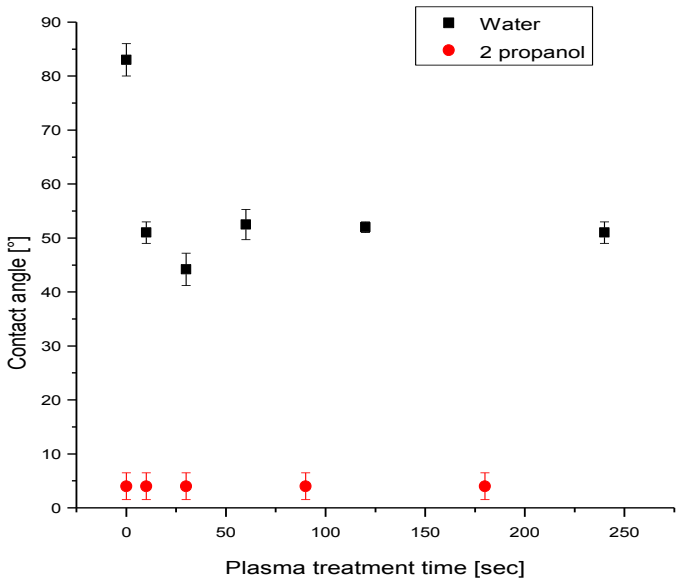

Figure 4.32 Contact Angle of 2-propanol in function of time of treatment (in red) and water (black) on graphite and plasma treated graphite

4.3.3 Effect of oxygen plasma treatment on the solid-liquid interaction of graphite nanoplatelets (60nm) and effect on the stability of suspension using water and 2-propanol.

The capability of liquid to disperse graphitic material to realize a suspension is critical to realised graphitic membranes using the ink technology [80]. Taking into account the experimental results, we tested the effect of oxygen plasma treatment also on the capability of graphene nanoplates to be suspended in a liquid environment (water and isopropanol). The graphene nanoplatelets were distributed on Petri dish of 2" diameter and inserted in the plasma reactor. The graphene nanoplatelets were exposed to oxygen atmosphere using the same timescale used for graphite. The Petri dish was always loaded with the same amount of graphene nanoplatelets, 40 mg. After the plasma treatment the same amount of graphene was loaded in vials (1.5 mg) and the vials were loaded with 50 ml of 2-propanol. The vials were hand shaken for 1 minute, and then, loaded in an ultrasonic bath for 10 minutes at a temperature of 24°C. In figure 4.33 we reported the picture of the inks produced following the above procedure for sample plasma treated for different times, 3 hours after the ultrasonic bath. We can observe that all the suspensions based on water as solvent totally sediment at the bottom of the vials.

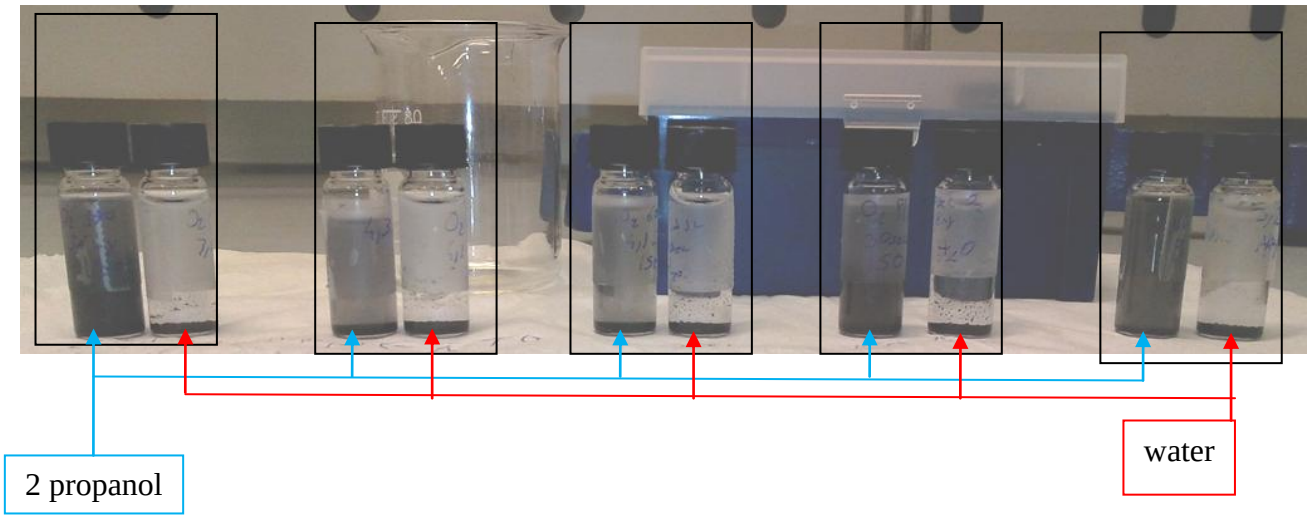

Figure 4.33 .Suspension based on graphite nanoplatelets in water and isopropanol after 3 hours of the ultrasonic bath.

Only the sample treated for the 30s in plasma showed agglomerates of graphene nanoplalates suspended in the liquids, even if the main amount of the materials laid down as a sediment at the bottom of the vials. The ink-based on 2-propanols are in many cases still dispersed in the solvent.

The graphene nanoplates treated for 10, 30sec. The graphene nanoplatelets treated for 60s and 120s are partially segregated down. The 2-propanol showed a lower contact angle on the graphitic surface than water. This indicates that there is a correlation between the wetting properties of the graphitic surface and the ability of a graphitic material to be dispersed in a solvent. The result is corroborated by the results of the plasma treatment where we observed that graphene nanoplatelets treated with "short-term" plasma are dispersed better in the solvent than other of graphene nanoplatelets.

4.4 Conclusion

In this chapter, we performed a detailed studied of the gas-liquid-solid interactions of graphite in a wide range of experimental conditions. The main activity was devoted to the investigation of intrinsic wettability of graphitic materials against water, solvents and with different low molecular weight gases. Moreover, the effect of the addition of oxygen functional group and photoactive materials were also explored. In the first part of the chapter, we observed that wetting of graphite materials in water was sensitive to the physical-chemical properties of the surface. Also on unmodified HOPG surface, a small amount of airborne contamination, the layer structuring (e.g. single, multilayer layer) and the gas environment can perturb the intrinsic wettability behaviour of graphite. Even if part of results were expected, e.g. wetting semi-transparency, other results as the captive bubble contact angle of different gases and intrinsic hydrophilicity of graphite was not predicted. This led to rigorous study the liquid gas-solid interaction. We observed that the HOPG surface had an attractive interaction with bubbles of H_2 and He (gasphilic behaviour) and weaker interaction with air, Ar and N_2 (gasphobic response). The findings show that gasphilic/gasphobic behaviour is related to the polarizability of the gas and of HOPG. Polarizability influences the ratio between the gas–HOPG and gas–gas potential, the χ ratio. A high χ ratio indicates a strong force of interaction at gas-solid interface compared to the effect of gas–gas interaction. Helium shows the lowest contact angle and the highest adhesion with HOPG in relation with the highest value of the χ ratio. Beside the intrinsic properties of HOPG graphite which is a totally dispersive surface, we investigated the effect of adding of polar compounds on the graphite surface. The graphite was modified by oxidizing the surface, creating new functional groups .Oxygen plasma has been used to oxidize the HOPG surface. Polar oxygen-containing groups attached on HOPG surface induced a significant increase of surface hydrophilicity. The results showed that the epoxy, carbonyl and carboxyl groups created on graphite surface are fundamental to improve the hydrophilicity. We

curiously observed that these functional groups on the surface induced different wetting modes when the surface was immersed in water. The latter results and the result about the gas bubbles behaviour clearly indicate that the liquid-gas-interaction on immersed graphite is more complex than the classical approximation.

References

1. Rodriguez-reinoso F. The Role of Carbon Materials in Heterogeneus Catalysis. Carbon 1998;36(3):159-175.

2. Morcos I. Surface tension of stress aneealed pyrolytic graphite. *J Chem Phys*. 1972;57:1801-1802.

3. Zhu R, Cui S, Wang X. Theoretical foundation of Zisman's empirical equation for wetting of liquids on solid surfaces. *Eur J Phys*. 2010;31(2):251-256. doi:10.1088/0143-0807/31/2/001.

4. Li Z, Wang Y, Kozbial A, et al. Effect of airborne contaminants on the wettability of supported graphene and graphite. *Nat Mater*. 2013;12(10):925-931. doi:10.1038/nmat3709.

5. Kozbial A, Trouba C, Liu H, Li L. Characterization of the Intrinsic Water Wettability of Graphite Using Contact Angle Measurements : Effect of Defects on Static and Dynamic Contact Angles. *Langmuir*. 2017;33:959-967. doi:10.1021/acs.langmuir.6b04193.

6. Rafiee J, Mi X, Gullapalli H, et al. Wetting transparency of graphene. *Nat Mater*. 2012;11(3):217-222. doi:10.1038/nmat3228.

7. Ashraf A, Wu Y, Wang MC, Aluru NR, Dastgheib S a, Nam S. Spectroscopic investigation of the wettability of multilayer graphene using highly ordered pyrolytic graphite as a model material. *Langmuir*. 2014;30(43):12827-12836. doi:10.1021/la503089k.

8. Good, R, Srivasta, N, R, Islam, M, Huang H. T. Theory of the Acid-Bae Hydrogen Bonding InteractionsmContact Angles, and the Hysteresis of Wetting:Application to Coal and Graphite Surfaces. *J adhes Sci Technol 1990, 4 1-617*.

9. Wei Y, Jia CQ. Intrinsic wettability of graphitic carbon. *Carbon N Y*. 2015;87:10-17. doi:10.1016/j.carbon.2015.02.019.

10. Traini D, Rogueda P, Young P, Price R. Surface Energy and Interparticle Force Correlation in Model pMDI Formulations. 2005;22(5):816-825. doi:10.1007/s11095-005-2599-2.

11. Koos E, Willenbacher N. Capillary Forces in Suspension Rheology. 2002;13054(1994).

12. Tanvir S, Qiao L. Surface tension of Nanofluid-type fuels containing suspended nanomaterials. 2012:1-10.

13. Brussieux C, Viers P, Roustan H, Rakib M. Controlled electrochemical gas bubble release from electrodes entirely and partially covered with hydrophobic materials. *Electrochim Acta*. 2011;56(20):7194-7201. doi:10.1016/j.electacta.2011.04.104.

14. Pittoni PG, Wang R-J, Yu T-S, Lin S-Y. Occurrence and formation mechanisms of bubbles entrapped into water drops impinging on graphite. *J Taiwan Inst Chem Eng*. 2014;45(6):3062-3068. doi:10.1016/j.jtice.2014.04.021.

15. Watanabe H, Furuyama T, Okazaki K. Enhancing the efficiency of direct carbon fuel cells by bubbling Ar gas in carbon/carbonate slurry. *J Power Sources*. 2015;273:340-350. doi:10.1016/j.jpowsour.2014.09.079.

16. Onda T, Shibuichi S, Satoh N, Tsujii K. Super-Water-Repellent Fractal Surfaces. *Langmuir*. 1996;12(9):2125-2127. doi:10.1021/la950418o.

17. Zhang M, Feng S, Wang L, Zheng Y. Lotus effect in wetting and self-cleaning. *Biotribology*. 2015:1-13. doi:10.1016/j.biotri.2015.08.002.

18. Della Volpe C, Maniglio D, Brugnara M, Siboni S, Morra M. The solid surface free energy calculation. *J Colloid Interface Sci*. 2004;271(2):434-453. doi:10.1016/j.jcis.2003.09.049.

19. Volpe CD, Siboni S. Some Reflections on Acid–Base Solid Surface Free Energy Theories. *J Colloid Interface Sci*. 1997;195(1):121-136. doi:10.1006/jcis.1997.5124.

20. Kabza K, Gestwicki JE, Mcgrath JL. Contact Angle Goniometry as a Tool for Surface Tension Measurements of Solids , Using Zisman Plot Method A Physical Chemistry Experiment. 2000;77(1):63-65.

21. Bartali R, Micheli V, Gottardi G, Vaccari A, Laidani N. Nanoindentation: Unload-to-load work ratio analysis in amorphous carbon films for mechanical properties. *Surf Coatings Technol*. 2010;204(12-13):2073-2076.

22. Williams OA, Jackman RB, Nebel C, et al. Surface conductivity on hydrogen terminated diamond.

23. Cicala G, Magaletti V, Senesi GS, et al. Superior hardness and Young's modulus of low temperature nanocrystalline diamond coatings. *Mater Chem Phys*. 2014;144(3):505-511.

24. Ostrovskaya LY. Studies of diamond and diamond-like film surfaces using XAES , AFM and wetting. 2003;68:219-238.

25. Kozbial A, Li Z, Sun J, et al. Understanding the intrinsic water wettability of graphite. *Carbon N Y*. 2014;74:218-225. doi:10.1016/j.carbon.2014.03.025.

26. Mannan MA, Baba Y, Hirao N, Kida T, Nagano M, Noguchi H. Hexagonal Nano-Crystalline BCN Films Grown on Si (100) Substrate Studied by X-Ray Absorption Spectroscopy. *Mater Sci Appl*. 2013;04(05):11-19. doi:10.4236/msa.2013.45A003.

27. Tripathi M, Awaja F, Paolicelli G, et al. Tribological characteristics of few-layer graphene over Ni grain and interface boundaries. *Nanoscale*. 2016;8(12):6646-6658. doi:10.1039/c5nr06273j.

28. Van Nguyen C, Bartali R, Crema L, Speranza G. Effect of glass surface treatments on the deposition of highly transparent reduced graphene oxide films by dropcasting method. *Colloids Surfaces A Physicochem Eng Asp*. 2016;498:231-238. doi:10.1016/j.colsurfa.2016.03.051.

29. Khattab IS, Bandarkar F, Fakhree MAA, Jouyban A. Density, viscosity, and surface tension of water+ethanol mixtures from 293 to 323K. *Korean J Chem Eng*. 2012;29(6):812-817. doi:10.1007/s11814-011-0239-6.

30. Gindl M, Sinn G, Gindl W, Reiterer A, Tschegg S. A comparison of different methods to calculate the surface free energy of wood using contact angle measurements. *Colloids Surfaces A Physicochem Eng Asp*. 2001;181(1-3):279-287. doi:10.1016/S0927-7757(00)00795-0.

31. Siboni S, Della Volpe C, Maniglio D, Brugnara M. The solid surface free energy calculation; II. The limits of the Zisman and of the "equation-of-state" approaches. *J Colloid Interface Sci*. 2004;271(2):454-472. doi:10.1016/j.jcis.2003.09.050.

32. Joly, T., Tocci, G., Marebia, S., Michadelides A. Strong Coupling between nanofluidic Transport and Interfacial Chemistry: How defectt Reactivity Controls Liquid-Solid Friction through Hydrogen Bonding. *J Phys Chem Lett*. 2016;6((7)):1381-1386.

33. Massoudim R., King AD. Effect of Pressure on the Surface Tension of water adsorption of low molecular weight gases on Water at 25 °. *J Phys Chem*. 1974;78((22)):2262-2266.

34. Baek Y, Kang J, Theato P, Yoon J. Measuring hydrophilicity of RO membranes by contact angles via sessile drop and captive bubble method: A comparative study. *Desalination*. 2012;303(October):23-28. doi:10.1016/j.desal.2012.07.006.

35. Salim M, Amemiya S, Li L, Liu H. Water Protects Graphitic Surface from. 2016. doi:10.1021/acsnano.5b04843.

36. Cheng A, Steele W. Computer simulation of ammonia on graphite. Low temperature structure of monolayer and bilayer films. *J Chem Phys*. 1990;92(6):3858-3866.

37. Martin-Calvo A, Garcia-Perez E, Garcia-Sanchenz A, Bueno-Perez R, Hamad S, Calero S. Effect of air humidity on the removal of carbon tetrachloride from air using Cu-BTC metal-organic framework. *PCCP*. 2011;13(23):11165-11174.

38. Hirschfelder JO, Curtiss CF, Bird RB. *Molecular Theory of Gases and Liquids*. (Wiley, ed.).; 1954.

39. Schrodinger LLC. The PyMOL MolecularGraphicSystem Version 1.8 2015

40. Stanton MM, Ducker RE, MacDonald JC, Lambert CR, McGimpsey WG. Super-hydrophobic, highly adhesive, polydimethylsiloxane (PDMS) surfaces. *J Colloid Interface Sci*. 2012;367(1):502-508. doi:10.1016/j.jcis.2011.07.053.

41. Ghio S, Paternoster G, Bartali R, Belluti P, Boscardin M, M. Pugno N. Fast and large area fabrication of hierarchical bioinspired superhydrophobic silicon surfaces. *J Eur Ceram Soc*. 2016:1-7. doi:10.1016/j.jeurceramsoc.2016.01.041.

42. Antisari MV, Montone A, Jovic N, Piscopiello E, Alvani C, Pilloni L. Low energy pure shear milling: A method for the preparation of graphite nano-sheets. *Scr Mater*. 2006;55(11):1047-1050. doi:10.1016/j.scriptamat.2006.08.002.

43. Orimo S, Majer G, Fukunaga T, Züttel A, Schlapbach L, Fujii H. Hydrogen in the mechanically prepared nanostructured graphite. *Appl Phys Lett*. 1999;75(20):3093. doi:10.1063/1.125241.

44. Paliotta L, De Bellis G, Tamburrano a., et al. Highly conductive multilayer-graphene paper as a flexible lightweight electromagnetic shield. *Carbon N Y*. 2015;89:260-271. doi:10.1016/j.carbon.2015.03.043.

45. Israelachvili JN. *Intermolecular and Surface Forces*. (Press A, ed.).; 1991.

46. Lazar, P.; Karlický, F.; Jurecka, P.; Kocman, M.; Otyepková, E.; Šafářová K. O. Adsorption of small organic molecules on graphene. *J Am Chem Soc*. 2013;135:6372-6377.

47. Lazar P, Martincov J, Otyepka M. Structure , dynamical stability , and electronic properties of phases in TaS 2 from a high-level quantum mechanical calculation. 2015;224104:1-11. doi:10.1103/PhysRevB.92.224104.

48. Tkatchenko, A.; Distasio, R. A.; Car, R.; Scheffler M. Accurate and efficient method for many-body van der Waals interactions. *J Chem Phys*. 2014;140(18):184508.

49. Silvestrelli, P. L.; Ambrosetti A. Including screening in van der Waals corrected density functional theory calculations: The case of atoms and small molecules physisorbed on graphene. *J Chem Phys*. 2014;140(12):124107.

50. Ambrosetti, A.; Silvestrelli PL. Adsorption of rare-gas atoms and water on graphite and graphene by van der waals-corrected density functional theory. *J Phys Chem C*. 2011;115(9):3695-3702.

51. Couronne, O.; Ellinger Y. An ab initio and DFT study of (N2)2 dimers. *Chem Phys Lett*. 1999;306(1-2):71-77.

52. Wada, A.; Kanamori, H.; Iwata S. Ab initio MO studies of van der Waals molecule (N2)2: Potential energy surface and internal motion. *J Chem Phys*. 1998;109(21):9434.

53. Tkatchenko A, Distasio RA, Car R, Scheffler M. Accurate and Efficient Method for Many-Body van der Waals Interactions. 2012;236402(June):1-5. doi:10.1103/PhysRevLett.108.236402.

54. Taylor P, Hohm U, Kerl K. Temperature dependence of mean molecular polarizability of gas molecules. 2006;(November 2011):37-41.

55. Lu Y-H, Yang C-W, Fang C-K, Ko H-C, Hwang I-S. Interface-induced ordering of gas molecules confined in a small space. *Sci Rep*. 2014;4:7189. doi:10.1038/srep07189.

56. Petucci J, LeBlond C, Karimi M, Vidali G. Diffusion, adsorption, and desorption of molecular hydrogen on graphene and in graphite. *J Chem Phys*. 2013;139(4):044706. doi:10.1063/1.4813919.

57. Hohm U. Experimental static dipole–dipole polarizabilities of molecules. *J Mol Struct*. 2013;1054-1055:282-292. doi:10.1016/j.molstruc.2013.10.003.

58. Gengenbach R, Hahn C, Schrader W, Toennies JP. Determination of the H2-H2 potential from absolute integral cross section measurements. *Theor Chim Acta*. 1974;34(3):199-212. doi:10.1007/BF00578417.

59. Patkowski, K.; Cencek, W.; Jeziorska, M.; Jeziorski, B.; Szalewicz K. Accurate pair interaction energies for helium from supermolecular Gaussian geminal calculations. *J Phys Chem A*. 2007;111(31):7611.

60. Schwerdtfeger P. Table of experimental and calculated static dipole polarizabilities for the electronic ground states of the neutral elements (in atomic units).

61. De Lara-Castells, M. a. P.; Stoll, H.; Civalleri, B.; Caus, M.; Voloshina, E.; Mitrushchenkov, A. O.; Pi M. Communication: A combined periodic density functional and incremental wave-function-based approach for the dispersion-accounting time-resolved dynamics of 4He nanodroplets on surfaces: 4He/graphene. *Phys, J Chem*. 2014;141(15):2012.

62. Silvestrelli PL, Ambrosetti A. Van Der Waals-Corrected Density Functional Theory Simulation of Adsorption Processes on Noble-Metal Surfaces : Xe on Ag (111), Au (111), and Cu (111). *J Low Temp Phys*. 2016;185(1):183-197. doi:10.1007/s10909-016-1515-y.

63. Favia P, Agostino R. Plasma treatments and plasma deposition of polymers for biomedical applications. *Surf Coat Technol*. 1998;98(1-3):1102-1106. doi:10.1016/S0257-8972(97)00285-5.

64. Kim KS, Lee KH, Cho K, Park CE. Surface modification of polysulfone ultrafiltration membrane by oxygen plasma treatment. *J Memb Sci*. 2002;199:135-145.

65. Wu GM. Oxygen plasma treatment of high performance fibers for composites. *Mater Chem Phys*. 2004;85:81-87. doi:10.1016/j.matchemphys.2003.12.004.

66. Bartali R, Lorenzelli L, Scarpa M, et al. Super-hydrophilic PDMS and PET surfaces for microfluidic devices . *Adv Sci Technol*. 2013;81:96-100. doi:10.4028/www.scientific.net/AST.81.96.

67. Jokinen V, Suvanto P, Franssila S. Oxygen and Nitrogen Plasma Hydrophilization and Hydrophobic Recovery of Polymers. *Biomicrofluidics*. 2012;6(1). doi:10.1063/1.3673251.

68. Pinto S, Alves P, Matos CM, et al. Colloids and Surfaces B : Biointerfaces Poly (dimethyl siloxane) surface modification by low pressure plasma to improve its characteristics towards biomedical applications. *Colloids Surfaces B Biointerfaces*. 2010;81(1):20-26. doi:10.1016/j.colsurfb.2010.06.014.

69. Safeen K, Micheli V, Bartali R, Gottardi G, Laidani N. Low temperature growth study of nano-crystalline TiO_2 thin films deposited by RF sputtering. *J Phys D Appl Phys*. 2015;48(29):295201. doi:10.1088/0022-3727/48/29/295201.

70. Larijani MM, Le Normand F, Crégut O. An optical emission spectroscopy study of the plasma generated in the DC HF CVD nucleation of diamond. *Appl Surf Sci*. 2007;253(8):4051-4059. doi:10.1016/j.apsusc.2006.09.004.

71. Goujon M, Belmonte T, Henrion G. OES and FTIR diagnostics of HMDSO/O2 SiOx deposition assisted by RF plasma. *Surf Coatings Technol*. 2004;188-189(1-3 SPEC.ISS.):756-761. doi:10.1016/j.surfcoat.2004.07.048.

72. Ferrari AC, Meyer JC, Scardaci V, et al. Raman spectrum of graphene and graphene layers. *Phys Rev Lett*. 2006;97(18).

73. Malard LM, Pimenta MA, Dresselhaus G, Dresselhaus MS. Raman Spectroscopy in Graphene. *Phys Rep*. 2015;473(5-6):51-87. doi:10.1016/j.physrep.2009.02.003.

74. Nakahara M. Modification of pyrolytic graphite surface with plasma irradiation. 28:1327-1333.

75. Zandiatashbar A, Lee G, An SJ, et al. and stiffness of graphene. *Nat Commun*. 2014;5:1-9. doi:10.1038/ncomms4186.

76. Beams R, Canc LG, Novotny L. Raman characterization of defects and dopants in graphene. 2015;27. doi:10.1088/0953-8984/27/8/083002.

77. Ferrari AC, Basko DM. studying the properties of graphene. *Nat Publ Gr*. 2013;8(4):235-246. doi:10.1038/nnano.2013.46.

78. Lattin WC, Utgikar VP. Transition to hydrogen economy in the United States : A 2006 status report. 2007;32:3230-3237. doi:10.1016/j.ijhydene.2007.02.004.

79. Shen J, Hu Y, Li C, Qin C, Ye M. Synthesis of Amphiphilic Graphene Nanoplatelets. 2009;4(1):82-85. doi:10.1002/smll.200800988.

80. Stankovich S, Piner RD, Chen X, Wu N, Nguyen T, Ruoff RS. Stable aqueous dispersions of graphitic nanoplatelets via the reduction of exfoliated graphite oxide in the presence of poly (sodium. 2006:155-158. doi:10.1039/b512799h.

81 . Blöchl, P. E., Projector Augmented-Wave Method. *Phys. Rev. B* **1994,** *50* (24), 17953-17979.

82. Ambrosetti, A.; Reilly, A. M.; DiStasio, R. A.; Tkatchenko, A., Long-range Correlation Energy Calculated from Coupled Atomic Response Functions. *J. Chem. Phys.* **2014,** *140* (18), 18A508.

83. Hilal, R.; Hassan, W. M. I.; Elroby, S. A. K.; Aziz, S. G., Theoretical Investigation of the Dispersion Interaction in Argon Dimer and Trimer. *Procedia Computer Science* **2013,** *18*, 826-834.

84. Klimeš, J.; Bowler, D. R.; Michaelides, A., Van der Waals Density Functionals Applied to Solids. *Phys. Rev. B* **2011,** *83* (19), 195131-195131.

5. Graphene as a barrier against the dynamic evolution of air bubbles in contact with PDMS polymer immersed in water.

5. Introduction

In Chapter 4 the experimental results showed that even if the graphite was impermeable to water a variation of the wetting properties of fresh graphite surface was observed when exposed to the atmosphere. The experimental results indicated that the change during time was due to hydrocarbons from airborne contamination. The airborne contamination is not easy to control in the laboratory environment due to the fact that the different environments show different amounts and different kinds of airborne contamination as indicated by works reported in literature[1]. Anyway, our results and the data reported in literature show that the main variation happens in the first 20 minutes after the exfoliation, after which the surface wettability is stabilized [2,3]. This phenomenon is strongly dismissed when a surface is immersed in water and put in contact with a gas bubble[4]. The graphite surface, in fact, is kept cleaned by water, an amount of airborne contamination is negligible in the volume of the bubble of 1 -2 mm^3. Due to this effect and the stability of the surface structure of graphite, the gas-solid interaction in water remains unvaried for very long time. In this Chapter, we repeat the experiments on another material that shows only dispersive interaction with gas and liquids, the polydimethylsiloxane (PDMS) [5]. PDMS, as graphite, interacts with gases and liquids in a non-bonding manner, but the structure of the PDMS surface is different from the chemical and structural point of view. PDMS, which monomer is $[SiO(CH_3)_2]$, didn't have a lattice structure but only an assembly of polymer chains without strong bonding between the chains. The PDMS is solid but the polymer chains are quite free to flow, and this give to PDMS its viscoelastic behaviour. PDMS, which is a hydrophobic material, is used in many applications where the surface of the materials is in contact with water as in the outdoor electrical insulators, microfluidics, membranes. In many of these requests, PDMS remains for a long time immersed in contact with water and often in contact with air bubbles [6,7]. However, PDMS surface is prone to be unstable and to degradation induced by water, as reported by Hillborg and Gustavsson [8,9].The unstable behaviour of PDMS in contact with water is due to the absorption of water molecules which induces a hydrolysis of the polymer chains causing the surface properties degradation. In this Chapter, we explore the feasibility of a protection solution for PDMS surface using a single layer of graphite, graphene. Graphite, in fact, has a 2D parent system, namely graphene, constituted by a single layer of sp^2-hybridized carbon atoms arranged in six-membered rings in a honeycomb network [10,11,]. Due to this

peculiar structure graphene has been used as the thinnest blanket to protect a surface of materials from the environmental conditions[1,12,13] For this reason, PDMS substrates were coated with graphene and the effect of a graphene layer on gas-surface interaction dynamics. In the first part of the chapter, we will describe the following surface characteristics: chemical properties, wettability and surface tension of PDMS and graphite. In the second part of the Chapter, the study results of the interaction of gas bubbles with PDMS immersed in water will be presented as well as a comparison with graphite. Finally, the interaction of air bubbles with a single layer graphene on PDMS surface (graphene/PDMS) will be described and characterized and the barrier effect of graphene against water investigated.

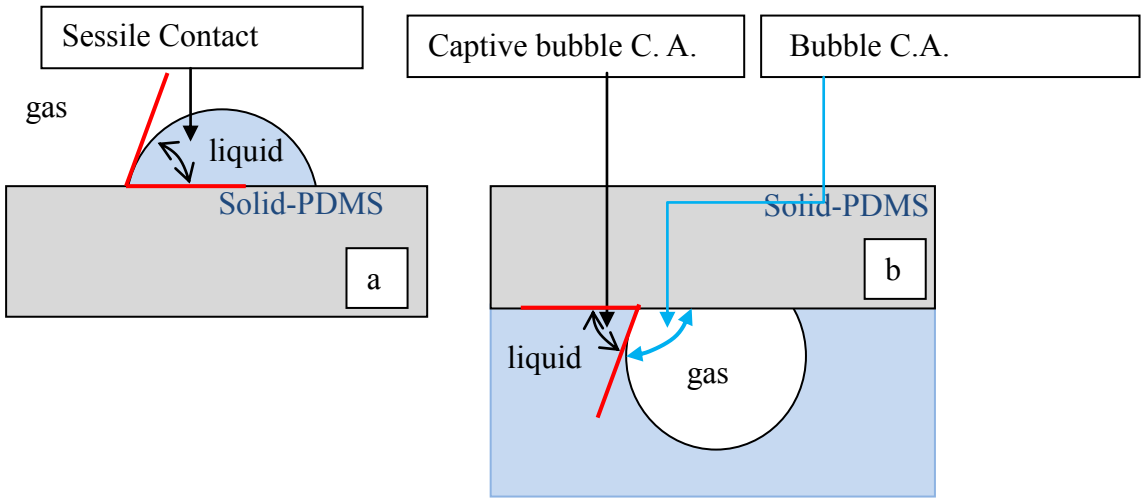

Figure 5.1. Drop and Bubble in contact with a surface a) sessile drop contact angle b) captive bubble contact angle and bubble contact angle.

In this study only air was used as probe gas, therefore to make easier the comparison between the sessile contact angle measurement set-up and the captive bubble contact angle set up , we compare the results obtained considering the angle between the solid-liquid and liquid-gas interfaces that is called captive bubble contact angle, instead of the bubble contact angle, that is the angle between solid-gas interface and gas-liquid interface, figure 5.1 [14,15,16].

5.1.1 Surface chemical properties of Polydimethylsiloxane (PDMS)

The Poly(dimethylsiloxane) surface chemistry has been studied by XPS analysis. In figure 5.2 we

report a large scan survey spectrum acquired on a PDMS sample surface.

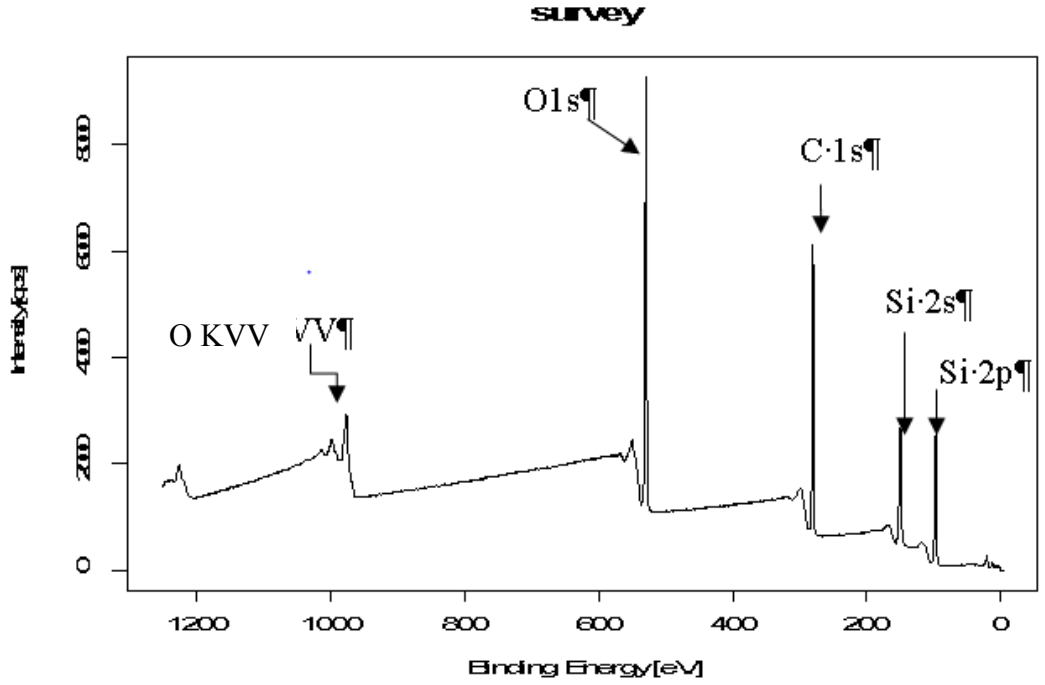

¶

Figure 5.2 XPS survey spectrum for PDMS surface showing the Si2p, Si2s, C1s, O1s and O $_{KVV}$ peaks.

The XPS peak of Si 2p, Si 2s, C1s and O1s at 101.8 eV, 182 eV, 284.38 eV and 532 eV were identified, as well as the O $_{KVV}$ Auger peak [17]. The core line Si2p spectrum is shown in Figure 5.3 For Si 2p three components were necessary to fit the core line, Figure 5.3c, the major intensity one is related to Si bond with two methyl groups [$(CH_3)_2SiO_1$]at 101,87 eV (#1)[18]. The other components are related to Si bond with a methyl group [$(CH_3)SiO$] (#2) at 102.67 eV and the component assigned to silicon bond with oxygen SiO_2(#3) at 103.5 eV. The semi-quantitative analysis results are given in Table 5.1 the major amount of the signal was due to silicon bonded with methyl group as expected for siloxane materials. A small amount of silicon showed bonding with oxygen, 2.89 at. %. This is also confirmed by the presence of 6,46 at.% oxygen bonded with silicon estimated by the O1s core line (at 533.88 eV). The C1s core line can be fitted using three components at 284.38 eV, 285.2 ev and 286.1eV, related to C-Si bond, to C-C and C-O bonds [19] [20211722]. The primary signal of carbon is due to C bonded to silicon. Around 8 at.% of the signal of the carbon is due to the airborne contamination (#2) and almost negligible component is due to C-O bond.

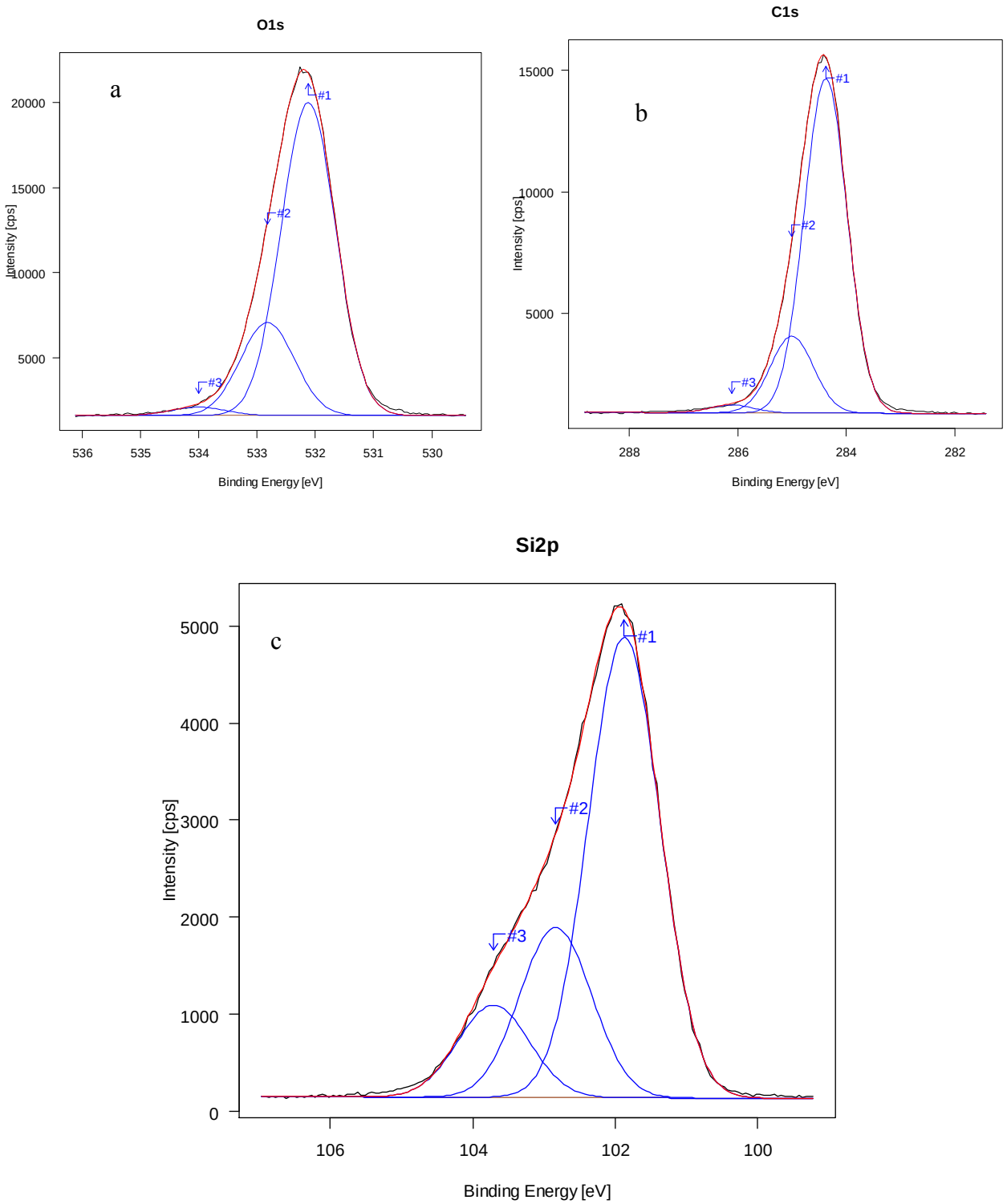

Figure 5.3 XPS core lines with curve fitting of O1s (a), C1s (b)and Si2p (c) on as received PDMS sample .

The core of O1s can be well fitted using the peak #1 due to Si-O-Si bond (532.2 eV), the peak #2

due to SiO_2 (around 533 eV) a small peak #3 due to Carbon bond O-C=O. The surface of PDMS is similar under the chemical point of view to the other flexible siloxane reported in the literature[23].

Table 5.1 XPS Binding energy of C1s, O1s, Si2p and atomic abundances of the elements in the relative chemical bonds for PDMS surface

BE (eV)	Bond	Atomic %	Total %
C1s			48.53
284.38	C-Si	38.74	
285.16	C-C	8.84	
286.01	C-O	0.91	
O1s			28.80
532.1	Si-O-Si	21.76	
532.88	SiO_2	6.46	
534	O-C-O ‖ O	0.59	
Si2p			22.74
101.87	$(CH_3)_3SiO_{1/2}$ $(CH_3)_2SiO_{2/2}$	14.44	
102.84	$CH_3SiO_{3/2}$	5.33	
103.7	$SiO_{4/2}$	2.89	

The surface is covered by an amount of carbon due to hydrocarbons by airborne contamination. On the surface of PDMS, a substantial amount of Silicon bonded only with oxygen is also present.

5.1.2 Effect of the immersion procedure on surface properties of PDMS

The sessile contact angle measured on as received PDMS was between 104° to 110° [24]. To understand the effect of water on the surface properties of this polymer the sample was immersed in water. After soaking, the PDMS showed a contact angle less than 100°. The procedure was repeated various times, and after the soaking procedure, the sample was left to dry in the laboratory conditions (25°C, 25% humidity). The test was conducted for 1300 hours (54days). The C.A results are reported in Figure 5.4a; the blue arrows indicate the transition during the trial before and after

the immersion procedure, the red arrows indicate the effect before and after the drying process.

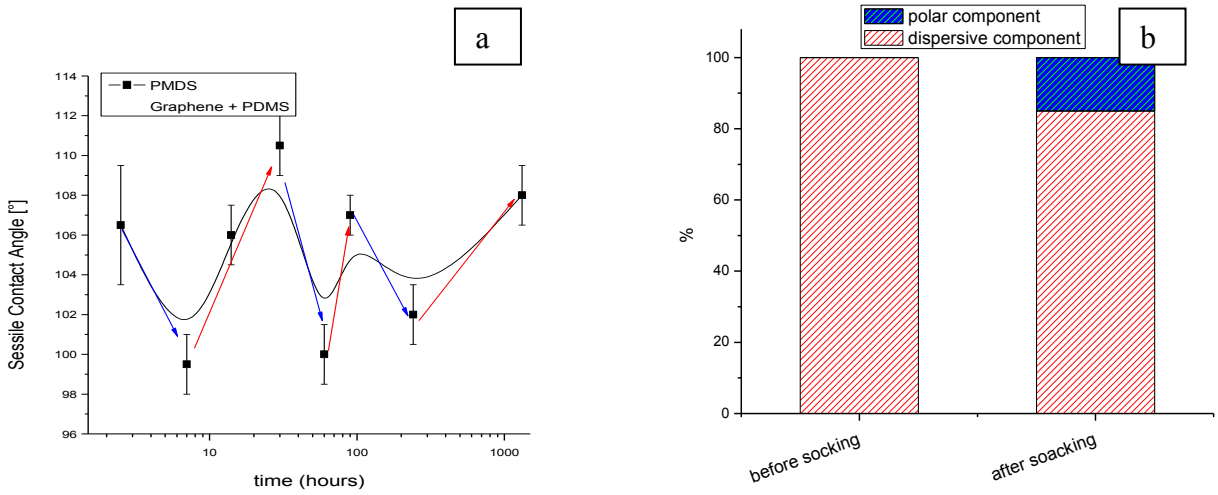

Figure 5.4 Water sessile contact angle on PDMS surface before and after immersion in water (blue arrows) and before and after drying (red arrow) (a) percentage of polar and dispersive components of PDMS before and after the soaking procedure (red is for dispersive components, and blue is the polar components) on PDMS surface (b).

After each cycle of immersion and drying, we observed a substantial variation of contact angle, in , we always detected a reduction of the contact angle after the immersion (from 107° to 100°), and we observed an increase of the contact angle after the drying procedure (from 100° to 107°). To better understand the surface modification during the immersion, we estimated the polar components of the surface of PDMS before and after the immersion/soaking procedure, using Owens – Wendt method (figure 5.4b). The results showed that before the immersion, the surface of PDMS was of dispersive character but after 5h of immersion 10% of the surface showed a polar component. This result are in line with the one reported by Hillbolrg *et al.*, who observed that the immersion of PDMS in water induces the migration of polar group on the surface [8,25,9,26] following a complex pathway as indicated in chapter 2.

5.1.3 Water vapour condensation on PDMS during bubble captive contact angle

We observed in the interior region of the bubble, the formation of dew drops due to the high relative

humidity inside the bubble itself, Figure 5.5a. Using a simple set-up composed of the humidity sensor and a bottle of polyethylene filled at 85% with deionized water, we measured in laboratory condition the increase of moisture, and we calculate the dewing temperature. The trend of the dewing temperature is reported in Figure 5.5b. We observed that after few minutes inside the cell the dew temperature reaches the temperature of the laboratory, due to an increase of the relative humidity (higher than 95%). This means that the condensation of water is possible in lab condition due to high relative humidity. Even if the experimental setup did not exactly replicate the situation inside the bubble in the captive bubble contact angle measurement set up (because the proportion between the gas volume and the contact area is different), it confirms that the dewing condition is reached in short time, few minutes. The dewing point can be moreover influenced by the fluctuation of temperature in the lab (usually around 3°C). We could reasonably expect that in the bubble, due to a smaller volume, this condition can be reached in shorter time and therefore the formation of water drops of condensed water can be promoted by the immersion procedure. The interaction of condensed water drops and PDMS inside the bubble can support the migration of polar groups present on the polymer chain locally.

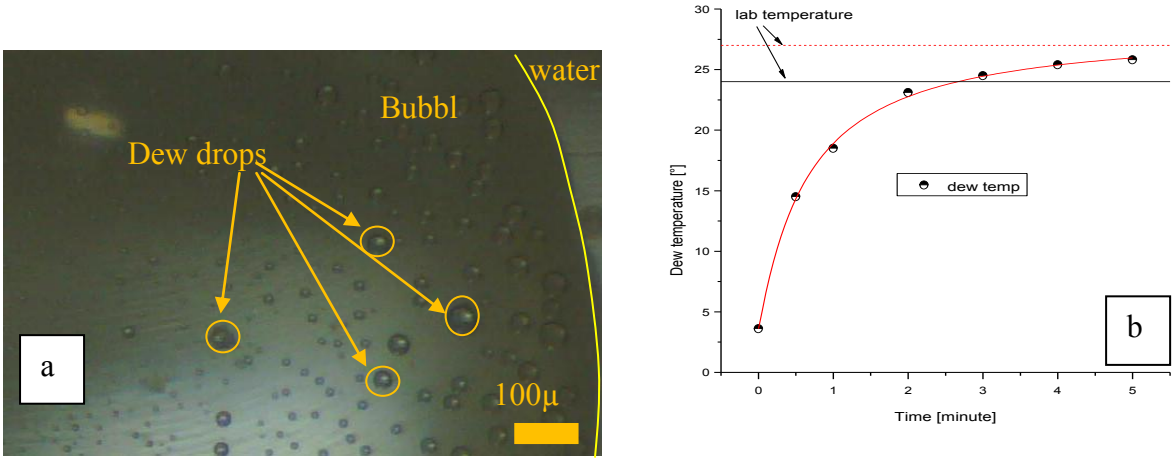

Figure 5.5. Picture of condensed water vapor inside the bubble region during the captive bubble contact angle measurement. The microdrops water vapor were detected thanks to the transparency of PDMS and the micro camera on the top side of the cell measurement (a) Dewing temperature inside the captive simulation experiment as a function of time (b) The data has been well fitted by logistics fit curve (b). The lab temperature range is indicated inside the graph by a black line figure 5.5b.

5.1.4 Morphology of PDMS in water

Since is was not possible to carry out the XPS analysis in a liquid environment, due to the fact that this equipment needs high vacuum technologies that are not compatible with liquid environments, (water evaporates at a pressure less than 24mbar and the breaking the Ultra High Vacuum C conditions do not allow the photoelectron detection). To in-situ study the interaction of water with PDMS, AFM was used. The microscope was implemented with a head dedicated to in liquid measurements performing. The surface of PDMS was analysed before the immersion and after 24 h of immersion in water. Its morphology before and during the immersion can be seen in the images in Figure 5.6. The images show that surface of native PDMS is flat with a roughness of 2 nm and a maximum peak-to-peak height of 49 nm.

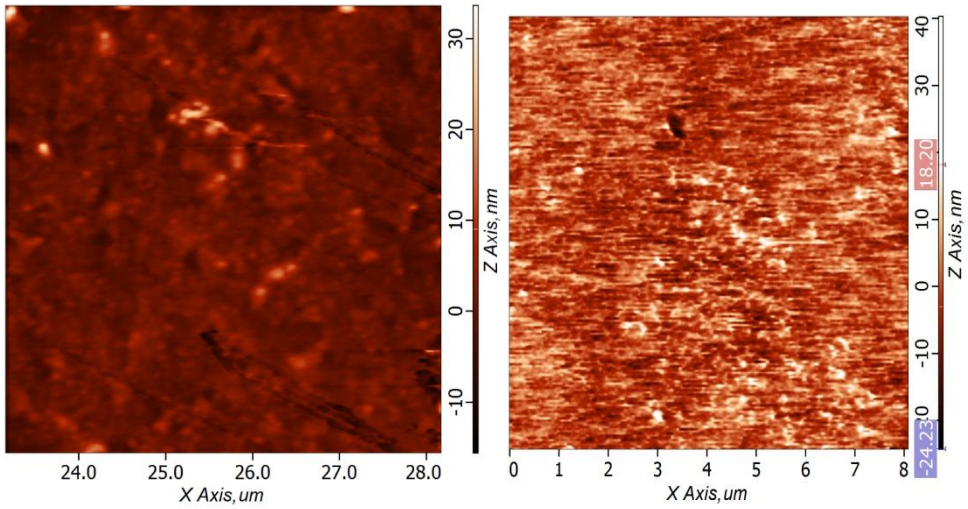

Figure 5.6 AFM images showing the morphology of PDMS surface in air and after 24h immersion in water.

PDMS immersed in water for 24h showed a more corrugated an irregular surface. The average roughness was 6 nm, and the maximum peak-to-peak height 91 nm. The roughness of PDMS immersed in water was three times higher than on the initial sample. Taking into account the observed surface modification, induced by immersion in water, we can reasonably think that water promotes the rearrangement of the polymer chains, and the physical arrangement changes the morphology of PDMS surface ar micro and nanoscale.

5.1.5 Comparison of chemical properties and thermodynamic properties of PDMS surface and graphite surface

The surface chemical properties of exfoliated graphite (EG) and polydimethylsiloxane (PDMS) obtained by XPS analysis are summarized (see Table 5.2). The survey spectra of XPS on EG show, as expected, the presence of carbon and a small amount of oxygen, due to the contamination. The surface chemistry of the PDMS indicates the presence of Carbon, Oxygen and Silicon. The atomic percentage of carbon and oxygen on PDMS is less than the theoretical value (25 and 50%, respectively) while the proportion of silicon is slightly higher than the theoretical one (i.e. 15%). The unbalanced surface stoichiometry is typical of slightly aged PDMS as reported in the literature [27].

Table 5.2. Chemical surface composition as obtained by XPS analysis and surface energy of graphite, PDMS and graphene on to PDMS.

	XPS Atomic percentage %			**Surface Energy (Owens-Wendt) mJ/m^2**		
	Carbon	Oxygen	Silicon	Total	Dispersive components	Polar components
PDMS	53.5 ±0.5	26.86 ±0.3	19.6±0.2	25.8 (±2.5)	25.7 (±2.4)	0.1(±0.1)
Graphite	98.5±0.9	1.5±0.1	-	52.2 (±3)	50.8 (±2.8)	2.2(±0.2)
PDMS+Graphene	54.2±0.4	26.3 0.2	19.4±0.2	33(±2)	32.9(±1.9)	0.1(±0.1)

The surface energy was estimated applying the Owens-Wendt method using water and diiodomethane as liquid probes. We measured an average water contact angle of 80° ± 2° on graphite, a typical value for slightly aged graphite (minutes) [2] and 105°± 2° on PDMS. The diiodomethane, which is a dispersive liquid, showed contact angles lower than 10° on graphite and higher than 60° on PDMS. The total surface energy of graphite was of 52.2 mJ/m^{2,} and more of the 95% of surface energy was due to dispersive components. Only a small component of the surface (4.4%) derived from the polar component; the polar component was probably due to contaminations, as corroborated by the XPS findings. PDMS showed a surface energy of i.e. 25.5 mJ/m^2 , a value lower than that of graphite, as indicated by the contact angle of diiodomethane. Similarly, to graphite, the dispersive components on PDMS constitute more than 99% of the surface energy, and only a negligible percentage of the surface tension was due to a polar behaviour.

5.1.6 Air Bubble contact angle on PDMS and Graphite

The interaction of air bubble with the immersed surfaces in water was studied using captive bubble contact angle measurement (hereafter CCA). The air captive bubble contact angle on graphite was 82° and as already reported this value remained stable with increasing the immersion time [4]. The bubble contact angle stability appears in contrast to that of the sessile drop contact angle as reported in the literature with a, and this is more likely due to the fact that the immersion procedure helps keeping the surface cleaner, due to the reduction of exposure to the airborne contamination [28,29,30].

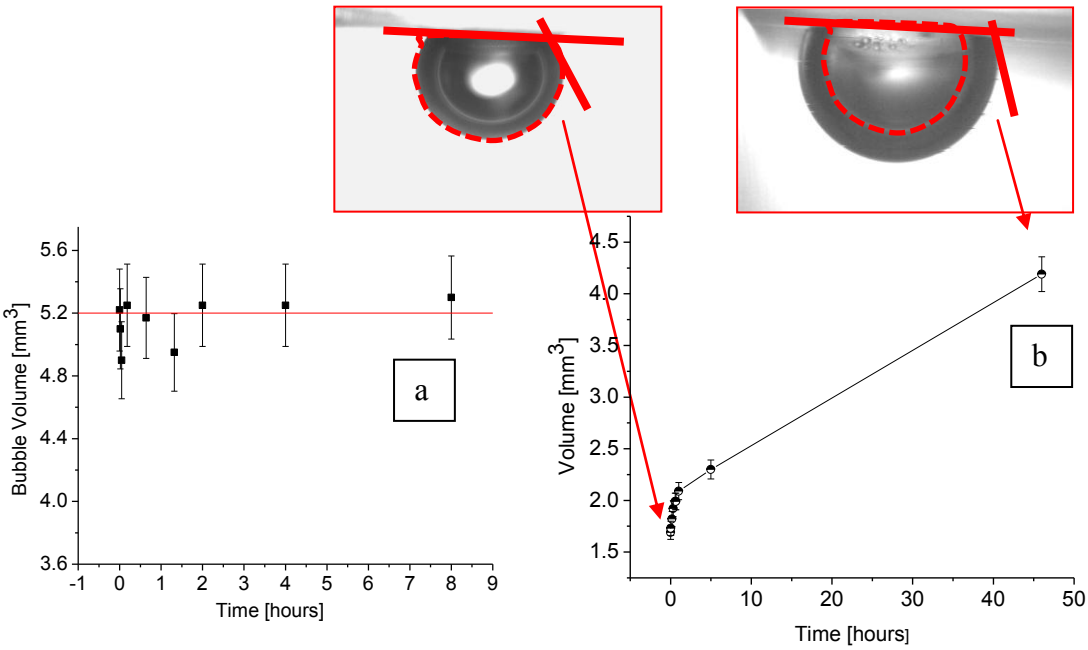

Figure 5.7. Air bubble volume on (a) graphite and (b) PDMS as a function of the immersion time.

. In the same way, estimate the volume of the bubble was estimated. The evaluation of the volume was done using Drop Analysis software. Figure 5.7a shows the air bubble volume on graphite which remained stable during the experiment.

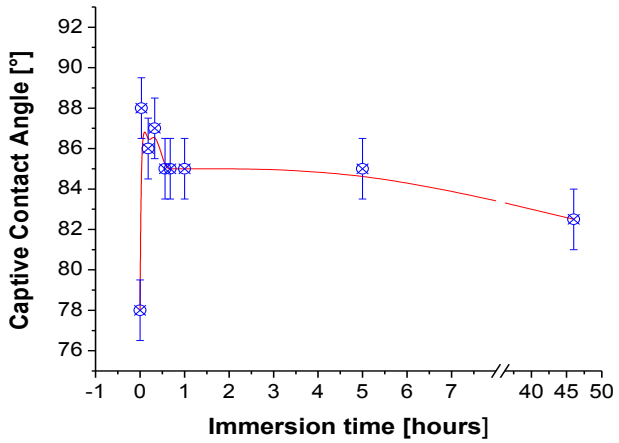

Figure 5.8. Time evolution of Captive bubble contact angle on PDMS during the immersion.

The C.A measurements of captive bubbles were performed on PDMS surface. We observed an increase of captive bubble contact angle from 78° to 88°, an oscillation of contact angle values in the first 0,3 h and after a decrease and finally a stabilisation of the CCA at 83-84°, Figure 5.8. The initial increase of the CCA was probably due to the presence of surface contamination. The reduction in CCA, after initial stage, was expected if we refer to since Hillborg *et al.* [31,32] and Gustavsson *et al.* [9] who also reported such variation of the contact angle after immersion of PDMS in water. The reduction of hydrophobicity on PDMS was related to the formation of polar Si-OH groups due to hydrolysis of PDMS backbone and migration of the polar group at the surface when the polymers are immersed in water. Similarly, Ismail *et al.* [33] revealed centralized oxygen molecule from water can diffuse through methyl terminated PDMS that causes "caging" and "hopping" phenomenon. Surprisingly in our experiment, we also observed an increase of the bubble volume (see Figure 5.7b). The starting volume was 1.69 mm^3 and after 5 h the volume grew up to 2.03 mm^3, i.e. an increase of 21 %. To verify this unexpected result, the immersion time was extended up to 46 h.and we measured a contact angle of 82.5° and a volume of 4.03 mm^3, so an increase of 238%. The inset of the figure 7b shows the images of the bubble at the beginning of the test and after 46 h. The red line in the picture reported in figure 5.7b indicates the original bubble profile. The variation of the bubble volume logically is due to the addition of gas inside the bubble, and this means that there is a source of gas. The source of gas can be endogenous as gas from water and PDMS or exogenous as the air coming by outside of captive bubble cell. Therefore in a first approximation the source can be (a) due to the coalescence of microbubbles/ nanobubbles solved in

water, (b) related to surface phenomena of PDMS and/or (c) related with the gas permeation from the external side of PDMS exposed to the atmosphere to the side exposed to the water. Considering the experimental conditions, the permeation of the gas due to a differential pressure between the external pressure and bubble pressure can be excluded from inside the bubble there is a small positive overpressure. The overpressure inside the bubble was estimated by Young-Laplace equation and was around 40 mbar [34].We cannot ignore the fact that the increase of the bubble volume can be due to the coalescence of microbubbles, but the stability of the bubble volume on graphite surface indicate that the coalescence of micro-nanobubbles in first approximation was negligible. The AFM observation of the surface in the liquid medium, the Owens Wend method based calculations for the samples immersed in water (paragraph 3.1.3 and 3.1.2) and the reported works in literature indicate that PDMS underwent a rearrangement of the polymer chains with a probable migration of polymer chain with polar groups to the surface, i.e. chains with SiO_x groups or polar contaminations (clay or oxidized carbon) .

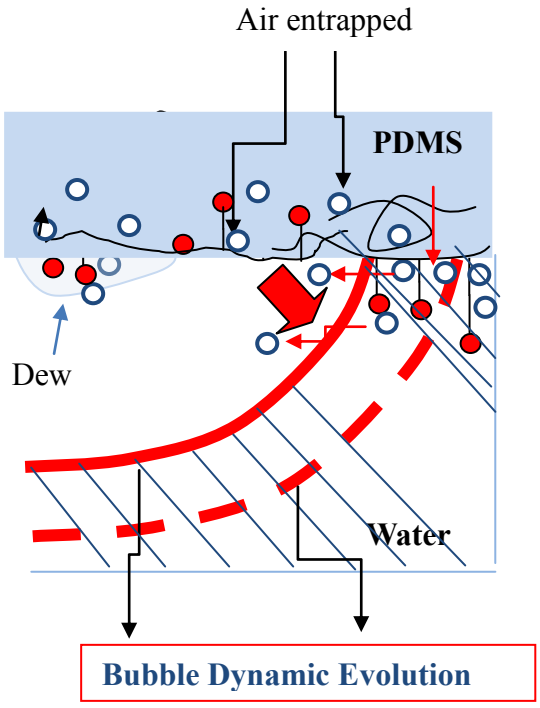

Figure 5.9 Scheme of the possible mechanism of the dynamic evolution of a bubble in contact with PDMS, polar groups (red circles) ,air micro-bubbles (white circles), bubble border (red lines). As a result of the rearrangement surface structure of PDMS in water, act as a continuous source of gas that can inflate the bubble.

We believe that the migration of polymer chains with polar groups in the polymer promotes the rotation and the movement of the polymer chains of PDMS. PDMS has a porous structure, and the air is entrapped in these pores. The rearrangement and movement of polymer chains promote the transport of the air from the polymer volume structure to the PDMS external surface; we cannot ignore the percolation of water inside the first layers of PDMS due to the diffusion process. The percolation of water in the first layers of PDMS can also be a source of hydrolysis of PDMS backbone and can help removing of air from polymer pores [35]. The air molecules that are coming from PDMS structure, due to the geometrical constraint of CCA measurement system, are forced to move on the surface of polymer until they nucleate in a bubble. The sketch of the dynamic evolution of the bubble is illustrated in figure 5.9.

5.2. Transfer of Graphene on PDMS

The evolution of bubble in dynamic bubble evolution (D.B.E) is clear indication that surface of PDMS was not inert to the water and that degradation process of surface started. To verify this hypothesis partially and to protect the PDMS surface that is the source of gas for the D.B.E, we cover the surface using the thinnest material available as a barrier the. single-layer graphene. The graphene should have a double effect on PDMS surface since it has a rigid surface which may a) avoid the dynamic rearrangement of the surface and b) inhibit the interaction of water and polar groups and diffusion of water. In Figure 5.10, the Raman spectra of Graphene coated on Cu and graphene transferred on PDMS is reported. As-deposited graphene on copper foil shows the presence of the G band at ~1580 cm^{-1} (due to the first order inelastic scattering process involving the degenerate iTO and iLO phonons at the G point, E_{2g} mode) and of the 2D band at ~2700 cm^{-1} (related with the second-order zone-boundary phonons)[36]. The D peak at ~1350 cm^{-1}, related to the defectiveness of the hexagonal carbon lattice, is not revealed in the spectrum [37,6]. The described features are superimposed to a luminescent behaviour, related to the metallic supporting substrate. The high intensity ratio between the 2D and G peaks mirrors the high quality of the graphene film [38,39]. Indeed, the transferring of graphene on PDMS by the developed simple procedure does not dramatically affect the quality of the layer.

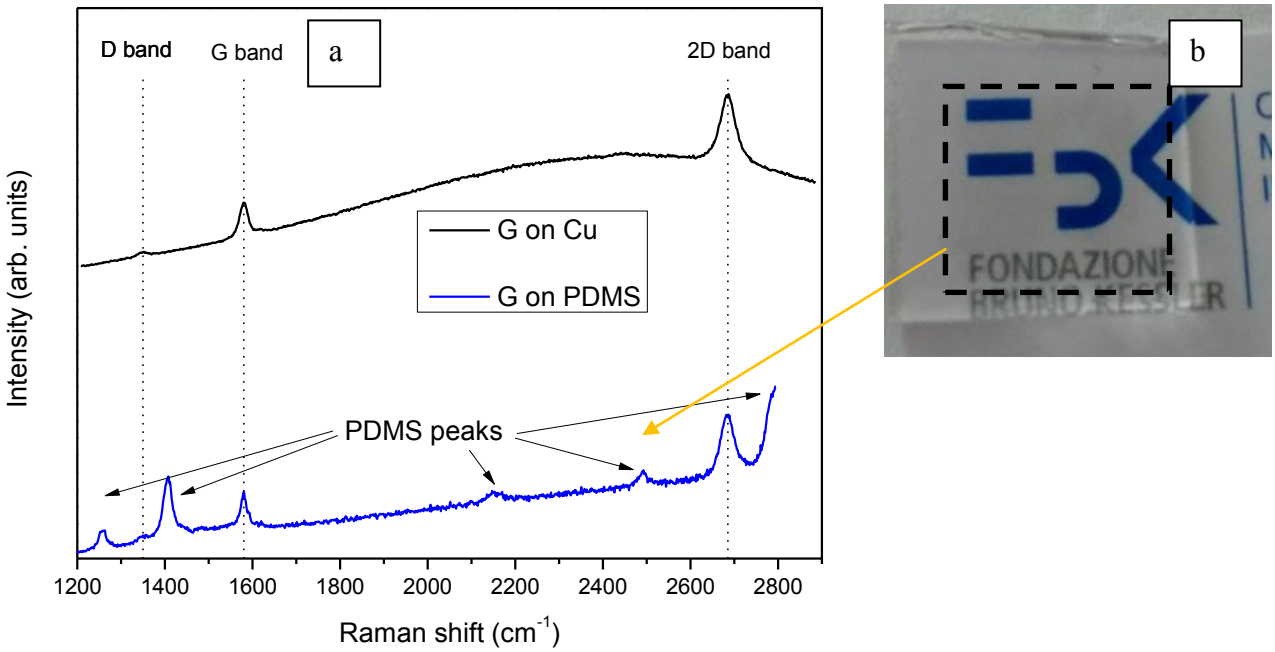

Figure 5.10. Raman spectra of graphene on Cu surface G and 2D peak position are indicated by dotted lines, the blue spectra is the Raman spectra of graphene onto PDMS, the arrows indicate the peaks due to PDMS substrate (a), picture of graphene on PDMS (zone inside the black square), showing that the transparency of PDMS was maintained.

By contact angle measurements, we observed a substantial reduction of the water contact angle on graphene/PDMS, from 107° to less than 100°, a wetting behavior more like that of the graphite surface. The increasing of the surface energy as indicated in Table 5.2, and the presence of the G and 2D peaks in the Raman spectrum confirm that graphene layers covered the surface. It is interesting to observe digital photograph of the graphene / PDMS sample (inset in Figure 5.10b) that the optical transparency of the substrate was preserved, as expected from the low optical absorption of a single layer of graphene.

5.2.1 Barrier effect of graphene layer on PDMS

Figure 5.11a shows the bubble volume normalised to the initial value of PDMS surface and graphene/PDMS in function of the immersion time. The comparison shows that in the system composed by graphene/PDMS the bubble size remained unchanged. The captive bubble contact angle onto graphene/ PDMS surface is reported in Figure 5.11b. We observed an initial increase of from 78° to 87°. Similarly to PDMS, we could aspect that the variation at the early stage of the experiment was due to the contamination [40].

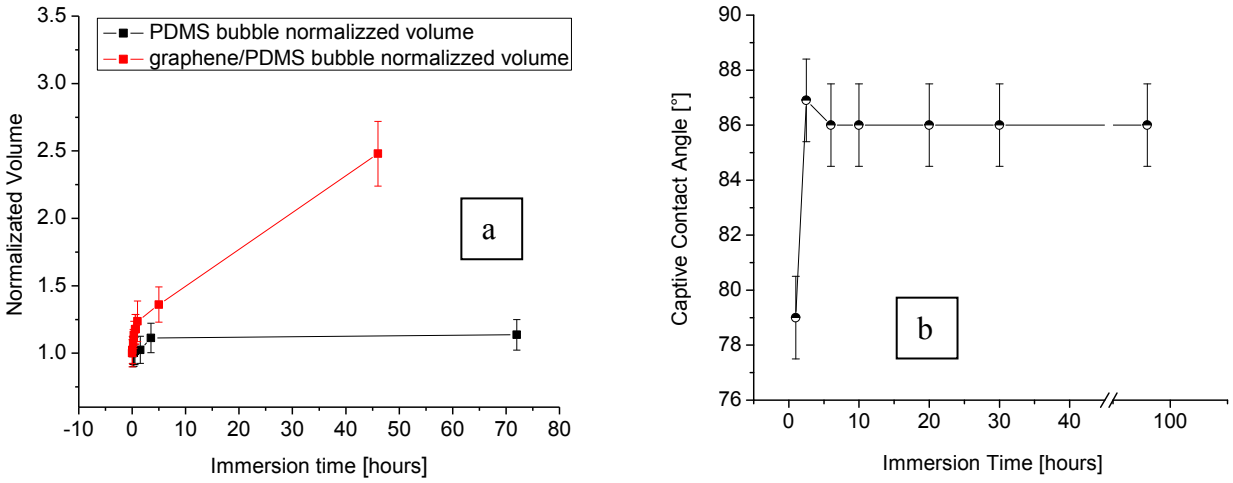

Figure 5.11 Bubble volume normalized to 1 on PDMS surface and on graphene/PDMS (a) and captive bubble contact angle (b) in function of the immersion time.

After the initial stage of the immersion, the of CCA remained unchanged probably because the water cannot permeate through the graphene layer to continuously promote the migration of polar groups. This is supported by the stabilization of bubble contact angle at 86°.

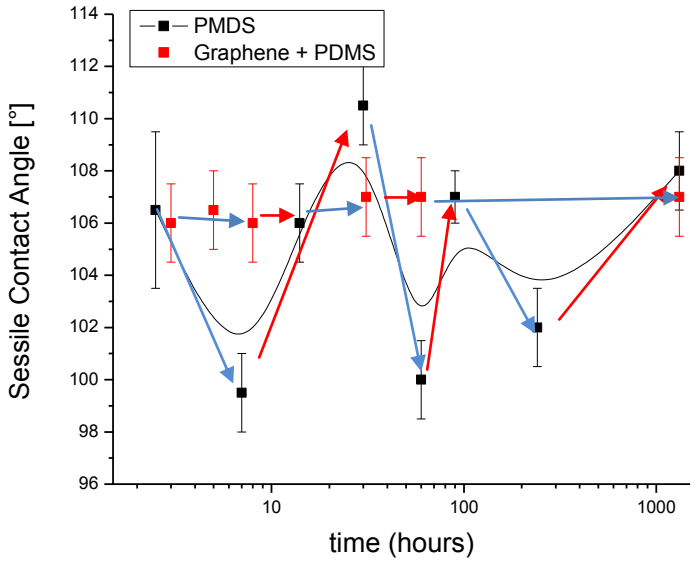

Figure 5.12. Trend of sessile drop contact angle just after the immersion in water and after the drying procedure (red arrows) for PDMS (blue arrow) and Graphene onto PDMS (red symbols). The C.A indicate with red arrows are the point measured after the drying and C.A indicate with (blue arrow) are the value measured just after immersion. The results are reported in a similar timescale.

On the surface of the graphene/PDMS sample, we repeated the immersion and drying procedure, (see paragraph 5.1.2). After each cycle of immersion (blue arrow) and drying (red arrow), the sessile drop contact angle measured has been measured. Figure 5.12 shows the comparison of the results obtained on graphene/ PDMS and PDMS. The graphene/PDMS surface shows a stable value of contact angle, 106°. The surface of PDMS covered by graphene seemed more stable than the surface of pristine PDMS.

5.2.2 Morphology of graphene / PDMS samples during immersion in water.

To better understand the morphological changes of graphene surfaces at the nanoscale in water we characterized the materials using AFM in liquid media. The interface of deionized water with graphene/PDMS morphology was analyzed in the contact mode operation, and live imaging was carried out with samples in water. Figure 5.13 shows AFM image of PDMS (a, b, c) and Gr/PDMS (d, e, f) surfaces in air and in water. In air condition, the roughness (rms) of PDMS and Gr/PDMS was measured as 2.6 ±0.33 nm and 7.9 ± 0.8 nm respectively. The higher roughness of the graphene covered PDMS is related to the presence of corrugation induced by graphene wrinkles, Figure 5.13

(a, d). The graphene wrinkles were in many cases present on the graphene transfered to the polymer from a Cu substrate, and this was due to the fact that graphene have a memory of the shape of the metal substrate surface. The topography of PDMS as observed in paragraph 5.13 gradually changed in water medium with the progression of the immersion time.

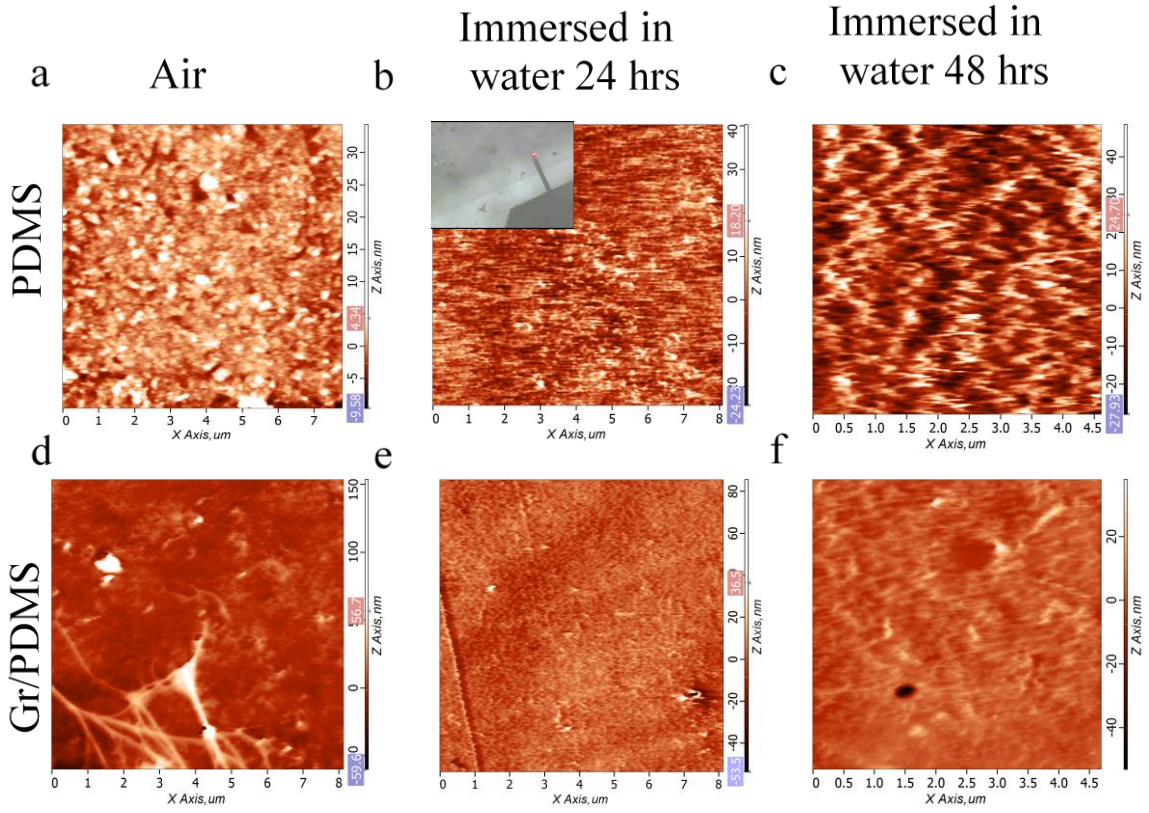

Figure 5.13. AFM topography of PDMS and graphene covered PDMS (Gr/PDMS) in the air and water after 24h and 48 h. Inset is showing the live imaging of the samples immersed in water.

Roughness increased up to 5 times at different time intervals up to 48 h after the immersion, black column figure 5.14. Nevertheless, the topology of the graphene covered PDMS remained unaffected in similar conditions. Figure 5.14 shows the interaction of water molecules at the surface of PDMS which was protected by a graphene layer. A similar phenomenon has been observed by B. Wang *et al.* [1]to protect silica glass surface from corrosion in water through implementation of CVD graphene as a barrier. The roughness of as received graphene was 6nm after 24 hours in water the roughness was around 7 and after 48 hours the roughness was 6nm. The result of the roughness evolution on the surface of the sample immersed in water is reported in figure 5.14. The value reported in the graph are the average value estimate in three different zones of the sample. Figure 5.14 show the stability under morphological point of view of graphene/PDMS immersed in water. This indicate that the effect of rearrangement of surface structure in presence of graphene is negligible.

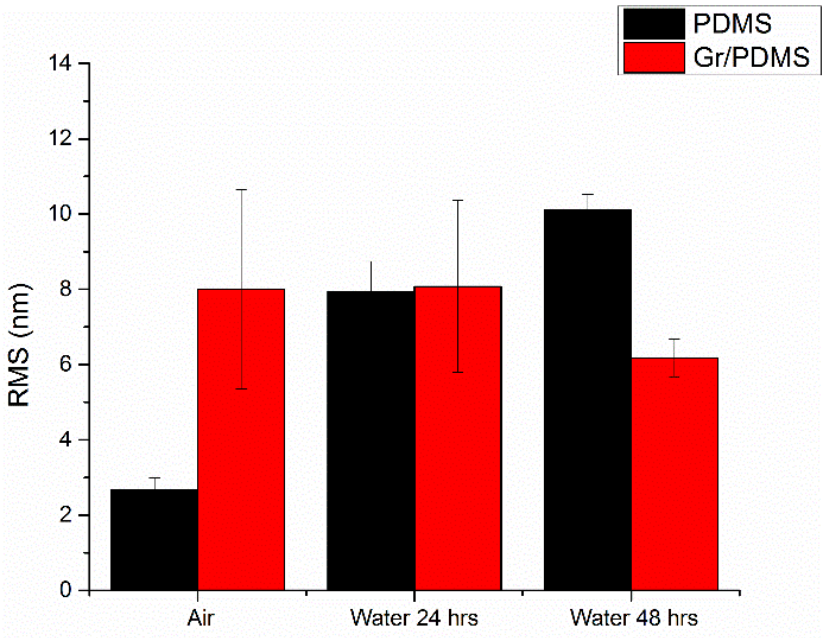

Figure 5.14.Roughness of the PDMS (black columns) and Gr/PDMS (red columns) in air and in water for 24h and 48h. The roughness of PDMS increased for an immersion time in water up to 48h while for graphene covered PDMS it remained unaltered.

5.2.3 Correlation between of surface morphology in water and dynamic evolution of the bubble

In Figure 5.15 we reported for PDMS and graphene/PDMS the variation of the volume of the air bubble with roughness acquired by AFM in liquid media (both parameters were normalised to the initial values). We can observe that there was a correlation between the roughness increase and the dynamic evolution of bubble volume for PDMS (blue symbols figure 5.15). On graphene/PDMS, no significative, a variation of roughness has been observed, and no sensible change of bubble volume has been recognized. The direct relationship between roughness evolution in water and the trend of bubble volume confirm that the dynamic evolution on PDMS is related to rearrangement of surface polymer chains and as well as the diffusion of water in the polymer structure. The graphene layer inhibits almost entirely the interaction of water with PDMS surface and inhibits almost entererly the inflating of air bubble increasing the PDMS surface stability. This behaviour is also in line with previous studies on the permeation properties of single layer graphene as an absolute gas barrier[41].

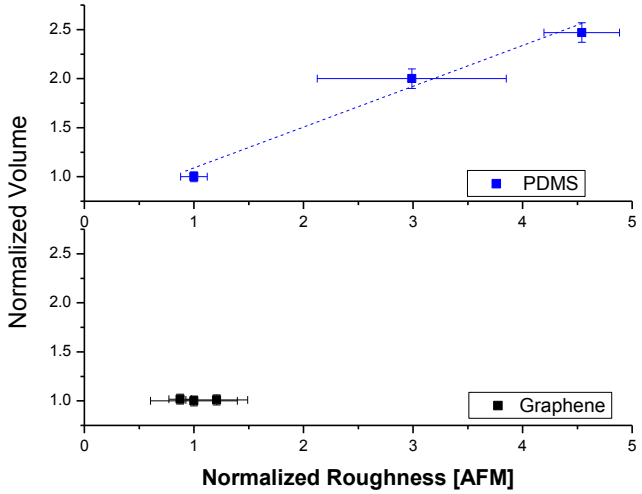

Figure 5.15 Variation of bubble volume normalized to the initial bubble volume as a function of roughness during immersion in water, (roughness estimated using AFM in liquid).The standard deviation is calculated from data for different zones of the sample.

These findings, therefore, indicate that a single layer of graphene on PDMS surface acted as a barrier against the interaction with water. In figure 5.16 we reported with a sketch the difference in behavior on PDMS with without a graphene layer and immersed in water.

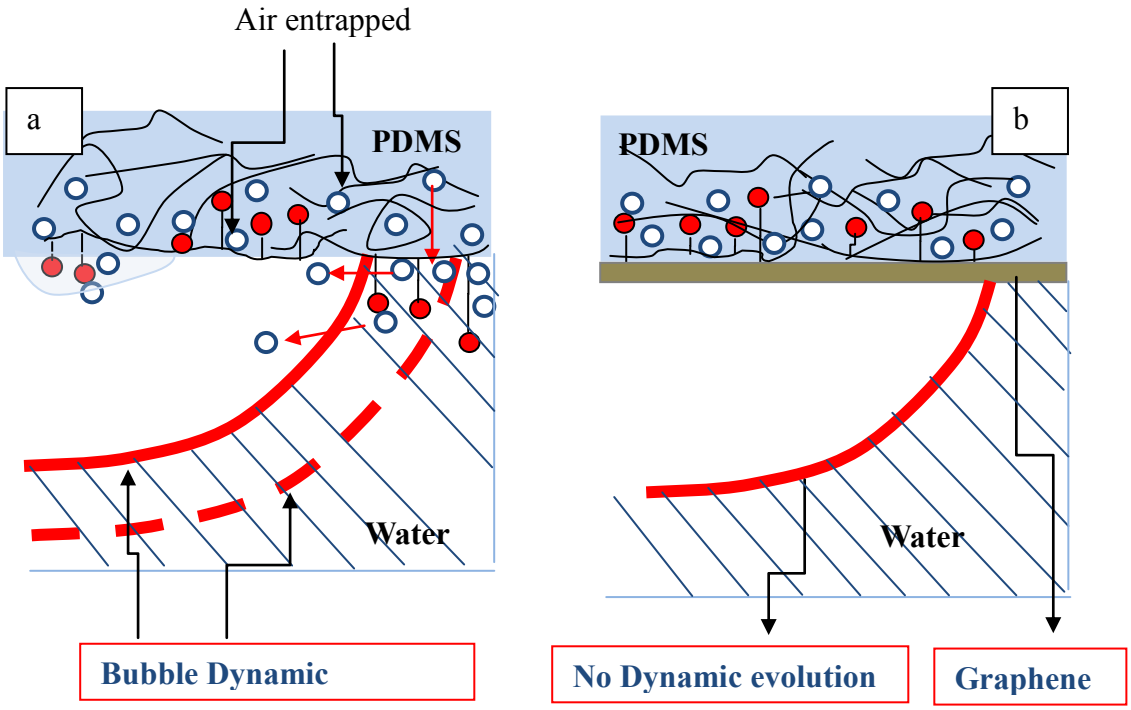

Figure 5.16 Bubble dynamic evolution on PDMS surface (a) and Barrier effect of graphene against water (b)

The inhibition of the water/surface interaction also suppressed the dynamic evolution of air bubbles. In this model, we did not consider the effect of the difference in the wetting modes of the two types of surfaces. We cannot exclude, in fact, that the two kinds of surfaces can show a small difference in liquid-solid interaction due to the prevalence at nanoscale of one different wetting mode like Wenzel mode, Cassie Baxter and Penetrate mode.

5.3 Conclusion

In this chapter, we studied the interaction of water with PDMS surface. We observed, on the basis by AFM analysis in liquid media, the captive bubble and sessile drop contact angle measurements and using the Owens Wendt method that the surface of PDMS is prone to a dynamic modification when interacting with water for extended time. These findings indicate that this response is related to the rearrangement of the polymer structure on the surface due to the migration of polymer chains with the polar group on the surface. The polymer chains rearrangement on the surface induce the degradation of the polymer and the undesired inflation of the air bubble in contact with the material. This phenomenon was not observed in graphite even if, like PDMS, it is a dispersive surface (no-polar interaction). This because graphite has a rigid honeycomb surface that avoids any dynamic evolution of the surface structure with water. For this reason, we used a single layer of graphite, graphene, to protect the PDMS surface. The results showed that the dynamic evolution can be entirely avoided using a graphene layer as an impermeable barrier. Moreover, the optical transparency in the visible of PDMS material was maintained. We remark that even if the positive protective effect of graphene on PDMS surface was demonstrated, the full understanding of the captive contact angle variation and the inflating mechanism of the bubble in contact with the polymer is not reached. We did not consider, for instance, the potential effect of nano/micro corrugations on the captive bubble which can play a significant role in determining the wettability by promoting Wenzel, Cassie Baxter or Penetrate mechanisms[42]. This is corroborated by the fact that captive bubble contact angle is far from the value of the sessile drop contact angle; it is suggested that the spread of the liquid (Penetrate model) and the spread of gas near the triple point have to be considered in order to obtain a more accurate description of the captive bubble contact angle variation[4]. Further work is necessary to better understand the dynamic behaviour of the bubbles.

References

1. Wang B, Cunning B V., Park S-Y, Huang M, Kim J-Y, Ruoff RS. Graphene Coatings as Barrier Layers to. *ACS Nano*. 2016;10:9797-9800. doi:10.1021/acsnano.6b04363.

2. Kozbial A, Li Z, Sun J, et al. Understanding the intrinsic water wettability of graphite. *Carbon N Y*. 2014;74:218-225. doi:10.1016/j.carbon.2014.03.025.

3. Ashraf A, Wu Y, Wang MC, Aluru NR, Dastgheib S a, Nam S. Spectroscopic investigation of the wettability of multilayer graphene using highly ordered pyrolytic graphite as a model material. *Langmuir*. 2014;30(43):12827-12836. doi:10.1021/la503089k.

4. Bartali R, Otyepka M, Pykal M, Lazar P, Micheli V, Gottardi G. Interaction of the Helium, Hydrogen, Air, Argon, and Nitrogen Bubbles with Graphite Surface in Water. *Appl Mater Interfaces*. 2017;9(20):17517-17525. doi:10.1021/acsami.6b16493.

5. Francioso L, De Pascali C, Bartali R, et al. PDMS/kapton interface plasma treatment effects on the polymeric package for a wearable thermoelectric generator. *ACS Appl Mater Interfaces*. 2013;5(14):6586-6590.

6. Lamberti A, Torino P, Marasso SL, Torino P. PDMS membranes with tunable gas permeability for microfluidic applications RSC Advances COMMUNICATION PDMS membranes with tunable gas permeability for micro fl uidic applications †. *RSC Adv*. 2014;4(November):61415-61419. doi:10.1039/C4RA12934B.

7. Liu H-B, Gong H-Q, Ramalingam N, Jiang Y, Dai C-C, Hui KM. Micro air bubble formation and its control during polymerase chain reaction (PCR) in polydimethylsiloxane (PDMS) microreactors. *J Micromechanics Microengineering*. 2007;17(10):2055-2064. doi:10.1088/0960-1317/17/10/018.

8. Hillborg H, Gedde UW. Hydrophobicity Changes in Silicon Rubbers. *IEEE Trans Dielectr Electr Insul*. 1999;6(5):703.

9. Gustavsson TG, Gubanski SM. Hydratization of the PDMS Backbone During Water Immersion Test. *IEEE-CEIDP*. 1998:269-272.

10. Chung DDL. A review of exfoliated graphite. *J Mater Sci*. 2016;51(1):554-568. doi:10.1007/s10853-015-9284-6.

11. Geim AK, Novoselov KS. The rise of graphene. *Nat Mater*. 2007;6(3):183-191.

12. Nine J, Cole MA, Tran DNH, Losic D. Graphene : a multipurpose material for protective coatings. *J Mater Chem A Mater energy Sustain*. 2015;3:12580-12602. doi:10.1039/C5TA01010A.

13. Chen S, Brown L, Levendorf M, et al. Oxidation Resistance of Graphene- Coated Cu and Cu / Ni Alloy. 2011;(2):1321-1327.

14. Sun Y, Xie G, Peng Y, Xia W, Sha J. Stability theories of nanobubbles at solid–liquid interface: A review. *Colloids Surfaces A Physicochem Eng Asp*. 2016;495:176-186. doi:10.1016/j.colsurfa.2016.01.050.

15. Baek Y, Kang J, Theato P, Yoon J. Measuring hydrophilicity of RO membranes by contact angles via sessile drop and captive bubble method: A comparative study. *Desalination*. 2012;303(October):23-28. doi:10.1016/j.desal.2012.07.006.

16. Drelich J, Miller JD, GooD R. The Effect of Drop (Bubble) Size on Advancing and Receding Contact Angles for Heterogeneous and Rough Solid Surfaces as Observed with Sessile-Drop and Captive-Bubble Techniques. *J Colloid Interface Sci*. 1996;50(179):37-50.

17. Crist BV, Crist BV. A Review of XPS Data-Banks. 2007;1:1-52.

18. Hare LO, Parbhoo B, Leadley SR. Development of a methodology for XPS curve-fitting of the Si 2p core level of siloxane materials. 2004;(September):1427-1434. doi:10.1002/sia.1917.

19. Bodas D, Khan-Malek C. Formation of more stable hydrophilic surfaces of PDMS by plasma and chemical treatments. *Microelectron Eng*. 2006;83(4-9):1277-1279. doi:10.1016/j.mee.2006.01.195.

20. Malecha K, Gancarz I, Tylus W. Argon plasma-assisted PDMS–LTCC bonding technique for microsystem applications. *J Micromechanics Microengineering*. 2010;20(November 2014):115006. doi:10.1088/0960-1317/20/11/115006.

21. Vesel A, Mozetic M, Zalar A. XPS study of oxygen plasma activated PET. *Vacuum*. 2007;82(2):248-251. doi:10.1016/j.vacuum.2007.07.021.

22. Mezzi A, Kaciulis S. Surface investigation of carbon films: From diamond to graphite. *Surf Interface Anal*. 2010;42(6-7):1082-1084. doi:10.1002/sia.3348.

23. Schnyder B. UV-irradiation induced modification of PDMS films investigated by XPS and spectroscopic ellipsometry. 2003;535:1067-1071. doi:10.1016/S0039-6028(03)00148-1.

24. Bodas D, Rauch J, Khan-malek C. Surface modification and aging studies of addition-curing silicone rubbers by oxygen plasma. 2008;44:2130-2139. doi:10.1016/j.eurpolymj.2008.04.012.

25. Technology P, Engineering HV. Hydrophobicity recovery of polydimethylsiloxane after exposure to corona discharges. 1998;39(10):1991-1998.

26. Kennan JJ, Peters YA, Swarthout DE, Owen MJ, Namkanisorn A, Chaudhury MK. Effect of saline exposure on the surface and bulk properties of medical grade silicone elastomers. 1996.

27. Baker MA, Gilmore R, Lenardi C, Gissler W. XPS investigation of preferential sputtering of S from MoS 2 and determination of MoS x stoichiometry from Mo and S peak positions. 1999:255-262.

28. Wei Y, Jia CQ. Intrinsic wettability of graphitic carbon. *Carbon N Y*. 2015;87:10-17. doi:10.1016/j.carbon.2015.02.019.

29. Raj R, Maroo SC, Wang EN. Wettability of Graphene. 2013. doi:10.1021/nl304647t.

30. Salim M, Amemiya S, Li L, Liu H. Water Protects Graphitic Surface from. 2016. doi:10.1021/acsnano.5b04843.

31. Petersson L, Meier P, Kornmann X, Hillborg H. Effect of surface cleanliness of aluminium substrates on silicone rubber adhesion. *J Phys D Appl Phys*. 2011;44:034011. doi:10.1088/0022-3727/44/3/034011.

32. Bhattacharya S, Datta A, Berg JM, Gangopadhyay S. Studies on surface wettability of poly(dimethyl) siloxane (PDMS) and glass under oxygen-plasma treatment and correlation with bond strength. *J Microelectromechanical Syst*. 2005;14(3):590-597. doi:10.1109/JMEMS.2005.844746.

33. Ismail AE, Grest GS, Heine DR, Stevens MJ. Interfacial Structure and Dynamics of Siloxane Systems : *Macromolecules*. 2009;42:3186-3194.

34. Nagayama G. Molecular dynamics simulation on bubble formation in a nanochannel Molecular dynamics simulation on bubble formation in a nanochannel. *Int J Heat Mass Transf*. 2006;49(March):4437-4443. doi:10.1016/j.ijheatmasstransfer.2006.04.030.

35. Stanton MM, Ducker RE, MacDonald JC, Lambert CR, McGimpsey WG. Super-hydrophobic, highly adhesive, polydimethylsiloxane (PDMS) surfaces. *J Colloid Interface Sci*. 2012;367(1):502-508. doi:10.1016/j.jcis.2011.07.053.

36. Malard LM, Pimenta MA, Dresselhaus G, Dresselhaus MS. Raman Spectroscopy in Graphene. *Phys Rep*. 2015;473(5-6):51-87. doi:10.1016/j.physrep.2009.02.003.

37. Lamberti a., Quaglio M, Sacco a., Cocuzza M, Pirri CF. Surface energy tailoring of glass by contact printed PDMS. *Appl Surf Sci*. 2012;258(23):9427-9431. doi:10.1016/j.apsusc.2011.12.117.

38. Ferrari AC, Meyer JC, Scardaci V, et al. Raman spectrum of graphene and graphene layers. *Phys Rev Lett*. 2006;97(18).

39. Beams R, Canc LG, Novotny L. Raman characterization of defects and dopants in graphene. 2015;27. doi:10.1088/0953-8984/27/8/083002.

40. Li Z, Wang Y, Kozbial A, et al. Effect of airborne contaminants on the wettability of supported graphene and graphite. *Nat Mater*. 2013;12(10):925-931. doi:10.1038/nmat3709.

41. Koenig SP, Wang L, Pellegrino J, Bunch JS. Selective molecular sieving through porous graphene. *Nat Nanotechnol*. 2012;7(October):728-732. doi:10.1038/nnano.2012.162.

42. Kim D, Pugno NM, Ryu S. Wetting theory for small droplets on textured solid surfaces. *Sci Rep*. 2016;6(November):37813. doi:10.1038/srep37813.

6. Synthesis of Graphene/Graphene oxide membranes as a protective barrier on lead (Pb) surfaces.

6.1 Introduction

In chapter 4, the effect of the surface treatment of graphite and graphene nanoplaletes powder on the solid/liquid interaction was reported. Chapter 5 it was reported that a single layer of graphene can be used successfully as a barrier against the deterioration of surface properties of PDMS induced by water. Unfortunately, the synthesis of a single layer of graphene by thermal CVD and transfer of graphene is limited to a restricted number of substrate materials. Taking into account the result obtained in chapter 4 we tried to realize a protective coating using a simple method based on the use of graphene-based inks. Many techniques, in fact, are available to realize protective coatings like plasma film deposition, evaporation or atomic layers deposition to protect the surface of metals. The atomic layer deposition is able to cover the surface of the metals with consecutive atom layers in a very conformal mode. This allows obtaining an excelled protection of surface against corrosion[1]. Unfortunately, all these techniques require vacuum technology that are costly, and in many cases, there are limitations about the volume and geometry of the products. An alternative straightforward and promising way to protect the surface is the deposition of layers consisting of flakes of 2D materials as graphene oxide and graphene [2]. The layers of 2D materials flakes follow the shape of the surfaces as phyllodough that works as a barrier against chemical agents. In 2014, Su *et al.* reported that coatings based on reduced graphene oxide were useful and flexible barriers permeation of the gases and reduced graphene oxide (RGO) is an excellent barrier against Cl ions [2]. Bimal *et al.* proved that a graphene oxide - polymer composite coating had a very good resistance to chlorine ions [3]. Chen *et al.* showed passivation properties of graphene on Cu and Cu/Ni Alloy [4]. Similarly, results have been predicted by Topsakal *et al.* on Al 111[5]. However Schiver observed similar results only for short tests, but the experimental work proves that CVD graphene on Cu promoted the corrosion in long-term tests of oxidation [6]. Ya-Ping Hsieh partially overcame this problem passivating the graphene defect using ALD [5]. Mayavan developed a graphene ink to inhibit corrosion of Iron [7]. Unfortunately, there is no work that exploits the effect of graphene and graphene-based material as a protective barrier of Lead. Lead (Pb) has been widely used in antiquity, jewellery, water pipe, cult figures or lamps in the buildings. During the Roman era, Pb was used for plumbing systems; during mediaeval the lead was used as roofing material that gave typical white colour, and Padua Dome is a great example.[8]. Nowadays the Pb is widely used in ***i)***

lead acid battery which is a promising solution for energy storage in smart grid solution due to the low cost and improvement of efficiency of the cel[9]l, and ***ii)*** in lead electrode for electro-reduction of carbon dioxide in water solution[10]. Due to the hazardous nature of all lead compounds produced by water corrosion and the negative effect of water corrosion on a visual aspect of artefacts, the protection of the lead surface is needed [11,12,13]. Moreover, the protection of lead surfaces against the formation of dangerous compound can be useful in handling lead products in the daily life and can also be helpful to preserve the aesthetic of the historical artefacts like coins, cult figures [11,14,8]. For this reason, in this chapter, we developed protective membranes deposited on lead using the simple method, based on graphene inks. Different kinds of graphitic suspensions were realised using reduced graphene, graphene oxide. In the first part of the chapter, we will report on the synthesis of graphene suspensions and their use as thin films. In the second part, we report on the estimation of the Pb surface reactivity and in the last section the protective properties of graphene layers on Pb.

6.2 Preparation of graphitic suspensions of graphene-based materials

Two different series of suspensions based on graphitic materials to deposit graphene materials were prepared.

i) For a first set, we studied the effect the different kinds of solvents as a base for realising an ink using reduced graphene powder. The reduce graphene with a low amount of oxygen on the surface (oxygen content between 10-20% of atomic concentration) were used to test the different solvents,

ii) The second set of solutions was produced by mixing graphene and graphene oxide using the best solvent option available to realized the suspensions. (2 propanol). We develop the graphene, graphene oxide and their mixture to explore the synthesis of 2D nanocomposite layer as protective membranes.

6.2.1 Deposition of reduced graphene oxide on glass using dispersion of reduced graphene oxide on 2-propanol, ethanol, ethylene glycol and NNdimethylformamide

Reduced graphene oxide (RGO) contains a few polar groups on surface and a surface that shows only a dispersive character. The reduced graphene oxide has been dispersed in typical organic solvents: used to disperse graphene based material in literature ethanol (ET), ethylene glycol (EG), , and N, N-dimethylformamide (DMF) and in 2-propanol as non-toxic user-friendly option [15,16].Water used for the ultrasound bath was repeatedly changed to avoid a temperature increase due to the extended sonication time. Immediately after sonication, the RGO suspensions appear black and well dispersed. The stability of the suspensions was checked controlling the presence of flocculation after 24h–48 h. The suspension were used to deposit a layer of reduced graphene material on the glass, using drop casting deposition The glass before the deposition has been clean with piranha solution. In our experiments, 0.04 ml of RGO dispersion was utilised for each drop cast deposition. After complete drying of the suspension, successive depositions were performed to increase the amount of RGO deposited on the glass substrates. An amount of 0.04 ml, 0.08 ml, 0.16 ml, 0.32 ml, 0.48 ml of solution were used to produce films with different thicknesses.

Table 6.1 Relative polarity, viscosity, density, surface tension, boiling point and water solubility of the solvents used to prepare the suspensions.

Solvents	Relative Polarity	Viscosity (c.p.)	Density (g/ml)	Surface Tension (dyne/cm)	Boiling Point (°C)	Solubility in Water %
Ethanol	0.654	1.2	0.789	22.32	78.5	100
2-propanol	0.546	2.3	0.785	21.79	82	100
Dymetylformamide	0.386	0.92	0.944	36.72	153	100
Ethylene glycol	0.790	16.9	1.115	48	197	100
water	1.00	1.00	0.998	72.8	100	-

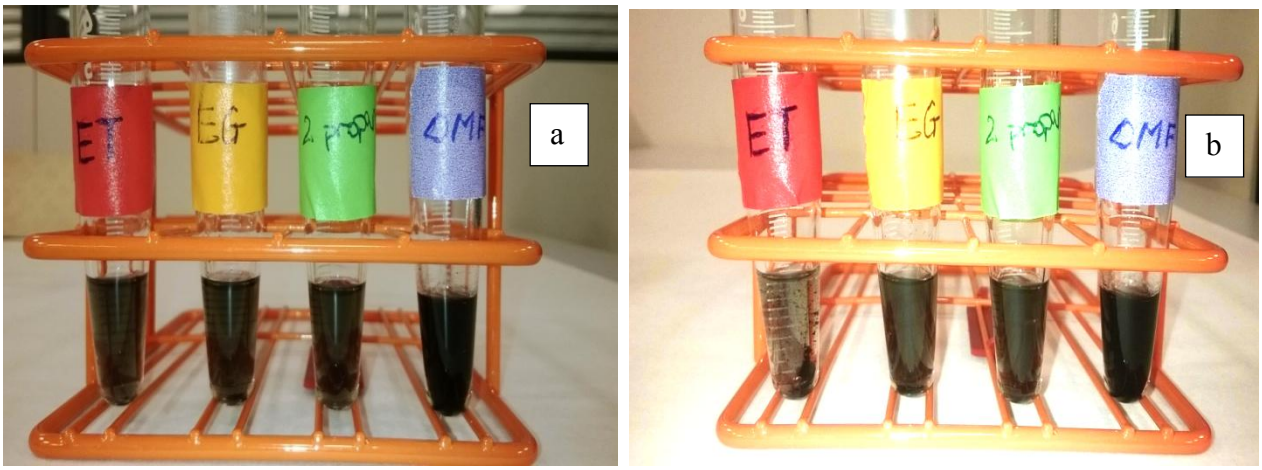

Figure 6.1 Photographs of RGO dispersed in ET, EG, 2-propanol and DMF solvents with 1h sonication (a) Photographs were taken 12 hours after the preparation of the RGO dispersions(b)

Figure 6.1a and 6.1b are pictures of RGO dispersed in ET, EG, 2-propanol and DMF solvents with 1h sonication and 12 h after the preparation, respectively. Figure 6.1b shows that 12 hours after the preparation, the RGO suspensions obtained using ET and EG became lighter due to instability. After 12 hours of preparation, the suspension of RGO in DMF also showed some flakes clusterization and instability. We utilised the just prepared EG and DMF RGO suspensions for the films deposition. These samples were dried at room temperature for 48 h. Both leading to non-uniform RGO films as shown in Figure 6.2. In particular, it was difficult to spread homogeneously the drops on the glass substrate

Figure 6.2 Photographs of: (a) RGO/EG and (b) RGO/DMF depositited onto glass substrates,

We were able to reach an improvement of the homogeneity of the coating with the 2-propanol

solvent which led to a good dispersion of the RGO flakes and stable suspensions; A similar result was obtained on graphite nanoplates treated by oxygen plasma. Using the drop-casting method, the coating appeared still not fully homogeneous, as can be seen in Figure 6.2. However, the homogeneity of RGO film deposited onto the surface of glass substrates using 2-propanol is much higher than that obtained using the other solvents. The better films quality achieved by using the 2-propanol concerning the other solvents can be explained considering the lower surface tension, lower boiling point and viscosity of the 2-propanol relatively to the EG and DMF, as it can be seen in Table 6.1. The marked difference in term of solution stability and coating homogeneity between ethanol and 2-propanol which possess similar characteristics is surprising. As already observed, RGO suspensions in ET were unstable. This may be due to higher surface tension, and balance among the solvent properties (i.e. surface polarity and viscosity) which have to couple to a macro system, graphene flake, which should display a prevalent hydrophobic character. RGO flakes still contain polar functionalities. An oxygen concentration ranging from 10at.% to 20at.% was found on the flakes surface. To measure the residual oxygen concentration on the RGO flakes, XPS analysis was performed on the coating deposited on glass. The elemental abundance of carbon and oxygen, the binding energy of the C1s and O1s core lines and the relative fit components are summarised in Table 6.2. The presence of these oxygen functional groups prevents the flakes to be readily dispersed in apolar solvents such as hexane, cyclohexane or pentane. On the other hand, the presence of a dispersive component makes difficult to suspend the RGO flakes in DMF or EG as already observed. Probably , the 2-propanol show relatively low polarity, enough density and low surface tension, enough to allow coupling with the RGO flakes and maintain them stable in suspension on a time scale of days. The excellent properties of this alcohol as a solvent to disperse graphitic powder were observed in chapter 5. It can be underlined that isopropanol is also a nontoxic solvent, which can simplify the method of deposition of graphene-based materials for various kinds of application-

Table 6.2 Fit component of the C1s and O1s core levels and their bond assignment and elemental composition of reduced graphene oxide deposited on gold obtained by XPS analysis.

Element	**BE (eV)**	**Bond assignment**	**Relative concentration (at. %)**
C1s			**82.3**
	284.4	sp^2C-sp^2C	57.0
	286.2	C-O-C, C-OH	10.0
	287.7	C=O	5.3
	288.9	-O-(C=O)	3.8
	290.8	π→π* shake-up	6.2
O1s			17.7
	531.0	C=O	7.2
	532.9	-C-O-C-	9.7
	534.6	H_2O	0.8

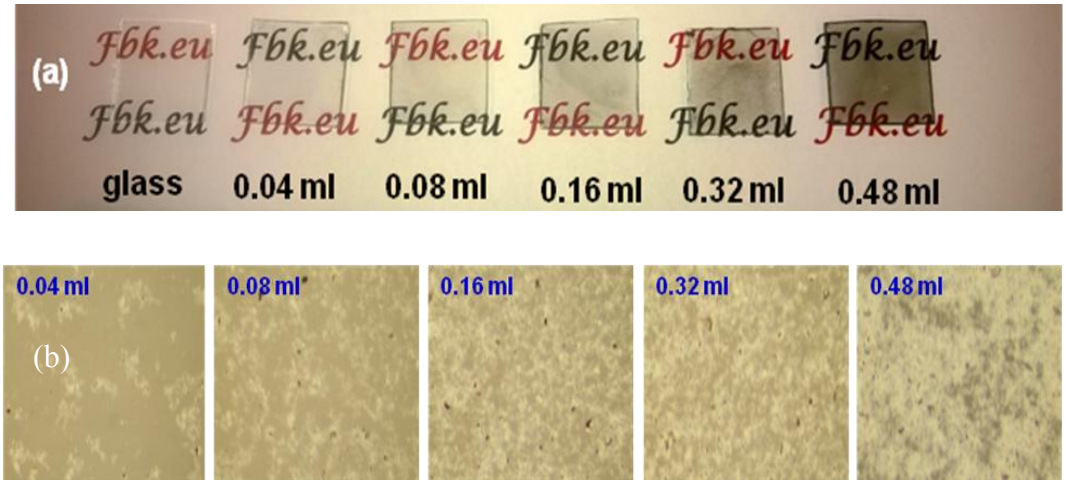

Figure 6.3 Photographs of as-made RGO films on glass substrates. The amount of RGO/2-propanol solvent deposited onto the glass substrates is in the range of 0.04-0.48 ml. The numbers shown in the figure indicate the drops volumes dispersed on the substrates (a). Optical microscope images of RGO films fabricated from 0.4mg/ml RGO suspensions in 2-propanol (b).. The numbers indicate the drops volumes dispersed on the substrates: Optical magnification: 50x.

6.2.2 Graphene and graphene oxides mixed with Isopropanol

In the second set of suspensions based on graphene inks, we realize a nanocomposite ink based on graphene and graphene oxide. The graphene ink was realized mixing graphene and graphene oxide powder provided by Prof. Hang G. and Shuhui Sun, Varenne (Quebec). The GO was synthesized by the modified Hummers method. Graphite powders were oxidized by potassium permanganate in the mixture of concentrated sulfuric acid and nitric acid at 80°C. After ultrasonic and concentration process, the GO was washed with water for several times. Finally, the GO powders were dried at 80 °C for 24 h. Subsequently, graphene can be obtained from GO by explosion–expansion method and thermal reduction at 1050ºC. The GrO shows a typical dimension of the flakes of 1 micron and graphene less than 100 nm. The powder has been dissolved in isopropanol alcohol, a non-toxic solvent to disperse reduced graphene oxide. The weight ratio of graphene oxide to graphene in the inks varied from 0% to 100%.

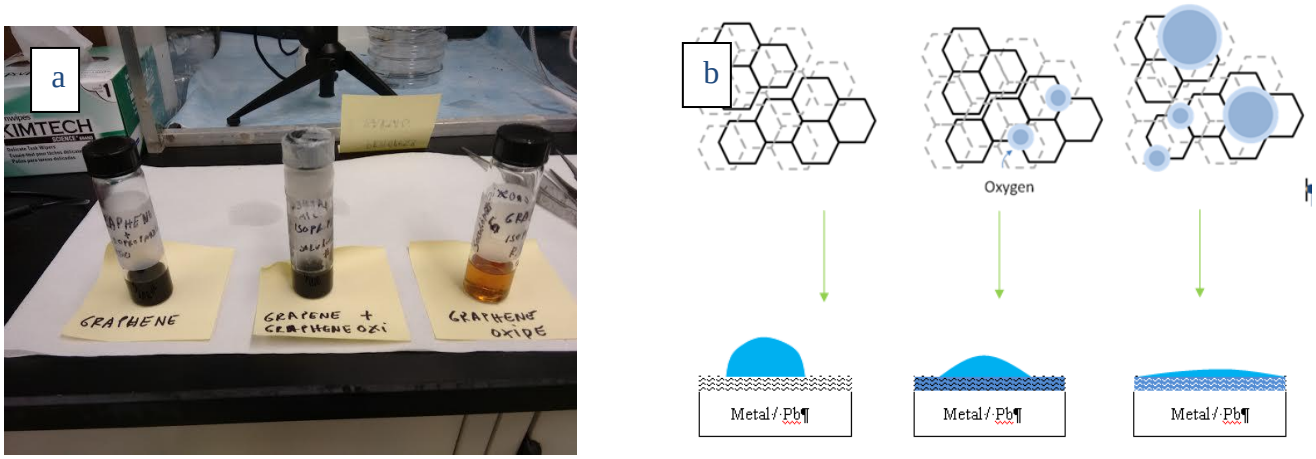

Figure 6.4 Picture of the suspensions realized using graphene and graphene oxide : in the left vials the uspension is based only on Gr, in the central vials the suspension is based on Gr and GrO mixture (0.3% graphene) and in the right vials the uspension is based only on graphene oxide (a) sketch of the nanocomposite coating realized using graphene and graphene oxides (b)

For each suspension, the total mass of materials was kept constant (3 mg) and the materials were dissolved in 5ml of isopropanol. In the inks different percentage of graphene in the total mass of 2D material have been used, 100%, 10%, 3%,0.3% 0% weight %. The complementary percentage of material is of graphene oxides (GO). For clarity the samples in the manuscript are named indicating the percentage of graphene: (Gr); 100% Gr, 10% Gr, 3%Gr,), 0,3 % Gr, 0%Gr.

Figure 6.4shows the suspension based on graphene and graphene oxide. The graphene oxide was

well dissolved in the isopropanol solution, the colour of the solution was amber, we did not observe any sedimentation even after 6 months; figure 6.4. The pure graphene appears well dissolved too, the colour of the graphene suspension was black just after the suspension preparation. After 1 day we observed the sedimentation of graphene in the vials. The nanocomposite inks were realised using 0, 0,3, 3, 10 and 100 wt.% of graphene in graphene oxide weight). The composite ink with 0.3 % of graphene retained the amber colour of the GO while the other inks were black. The ink based on graphene was easy to spread by drop casting on the surface of materials. Unfortunately, as observed in previous experiments, the homogeneity of graphene was inadequate, with agglomeration of the flakes on the surface.

6.2.3 Deposition of/GrO coatings using Meyer road

Figure 6.5a shows the non-uniform deposition using graphene ink by drop casting onto a glass substrate. To improve the homogeneity, a rod was used to spread the graphene flakes onto the substrate surfaces. A Meyer method as used and optimised to deposit coatings based on graphene and graphene oxide inks see material and method. As observed before, by drop casting, the coating was not uniform, and the graphene flakes easily agglomerated. Many disconnected regions of the graphene coating were present on the surface of the substrate. The flakes of graphene were scattered distributed and without a planar orientation. With Meyer rod, the coatings were more homogeneous, and the graphene flakes were more ordered in planar mode Figure 6.5b. We mention that the Meyer rod, has coil on its external surface, for these reasons it tend to leave permanents lines on the coatings [17]. To reduce this effect, we introduced a spacer between the Meyer rod and the substrate (a spacer thickness of 25 microns). This set-up reduces the presence of the grooves in the coating, (see the Material and Methods Chapter). After the deposition, the samples were heated on a hotplate at 60°C for 5 minutes to remove the solvent.

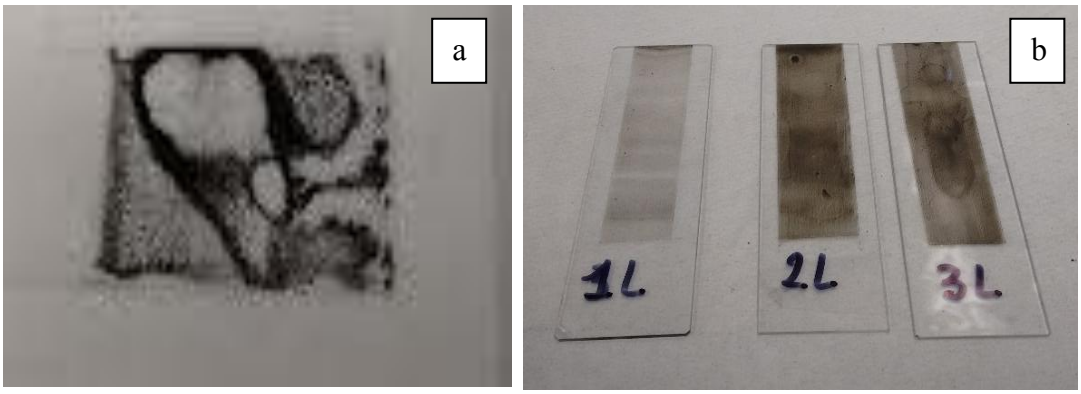

Figure 6.5 Graphene film deposited by drop casting on glass b) film of graphene deposited on glass by Meyer rod, 1L is one layer, 2L is 2 layers anf 3L is a coating realized using 3 consecutive layers.

6.3 Study of lead (Pb) reactivity to water using Sessile Contact Angle time measurements.

In the air and with oxygen dissolved in water as moist air, or in the presence of water drops on the surface, the corrosion of Pb is accelerated. To understand the reactivity of the lead surface towards water drops three methods were combined ; a) XPS analysis b) time evolution of contact angle to study the surface reactivity by the contact of water drops with the lead surface and c) the estimation, using stylus profilometry, of the volume of Pb salts produced by corrosion.

6.3.1 XPS analysis of lead surface exposed to water drops

The surface of lead was first cleaned with acetone and isopropanol. The surface of lead was exposed to a water drop of 2 µl for 30 minutes which led to white stain formation on the surface. By XPS we analysed the surface of the white stain zone (A in Figure 6.6) the unmodified lead surface, (zone B).Table 6.3 atomic concentration of C, O, Pb on lead and white stain on lead estimated by XPS.

Table 6.3. Relative atomic concertation on zone A and zone B by XPS

	Lead **Zone B** **Relative** **Atomic concentration (at. %)**	**Lead/ Water** **Zone A** **Relative** **Atomic concentration (at. %)**
C	49.6	32.2
O	37.1	44.1
Pb	8	12

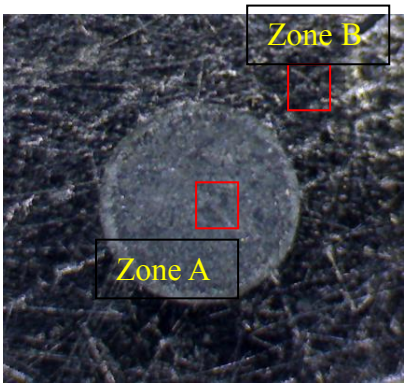

Figure 6.6: Image of white lead stain produced by the contact with a water drop, red square indicates the region analyzed by XPS (zone A is a region inside the white stain and zone B on the lead surface).

On lead, we detected Carbon, Oxygen and Lead signals, 32 at.% was due to C-C interaction (285.5 eV), assigned to airborne contamination (C1s binding energy equal to 285.1 eV)[18]. The other components of the C1s peak are due to C=O and O-C=O (at 287.1 eV and 289.3 eV). This indicates that the main carbon on the surface is due to the contaminations and a small part is bonded to oxygen. The lead signal is relatively low due to the presence of airborne contamination and due to the native lead compounds with oxygen carbon and hydrogen. A small peak of the lead metal has been detected at 136.5 eV, (relative atomic concentration of 1 at.%) amount. The other contribution to the lead signal (15 at.%) is due to lead carbonate at 138.9 eV, and we do not exclude a contribution of lead Oxide PbO_2 (137,5eV). Oxygen represents 37.1 % of the total atomic amount, the main contribution is due to metal oxide at 529 eV, and to bonding with C such as PbCO3 at 532 eV, even if a contribution of oxidized carbon cannot be excluded [19]. The results show that in the lead there is a layer composed lead carbonate lead oxide.

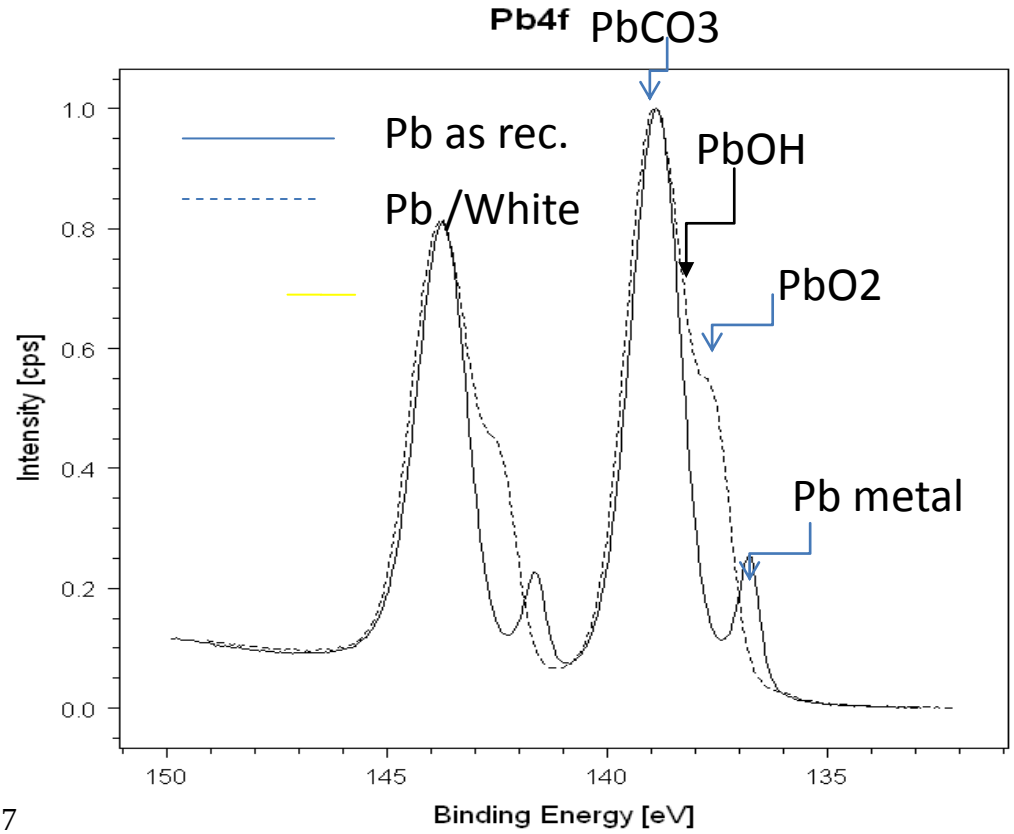

7

Figure 6.7 Pb 4f core line spectra for lead (straight line) and white stain (dotted line).

The relative atomic percentage of lead surface estimated by an XPS survey analysis is reported in

Table 6.3 if we consider that the principal amount of carbon (33 at.%) on the surface is due to airborne contamination, we can in first approximation suppose that the surface is composed of Pb 8 %, C 16% O 37%. The correlation/ relationship among Pb, O, C, and The lead oxide appears to present only in small amount, the fingerprint of Pb4f reported in figure 6.7, indicate that on the surface there is a compound with a form of primarily by lead carbonate and lead metal.

The XPS analysis done on the white stain showed chemical composition different to the pristine lead surface. The relative atomic concentration of carbon, oxygen and Pb is reported in Table 6.3. We observed a reduction of carbon an increase of lead and oxygen. The shape of the Pb4f core line is different from line shape of the pristine lead surface (Figure 6.7). The component due to the Pb metallic state is absent, and the component due to lead hydroxide at 138.2 eV and lead oxides at 137,5 eV became more prominent figure 6.7. Regarding the lineshape of the O1s peak, the component at 529 eV disappeared, and a new one appeared at 528,7 eV. The latter is typical of the hydroxyl group, but it may also arise from adsorbed water on PbO_2 that interacts with vacancies in the lattice [20]. The C1s peak shows a signal increase for the component at 290 eV, typical of HO-C=O functional group, figure 6.8.

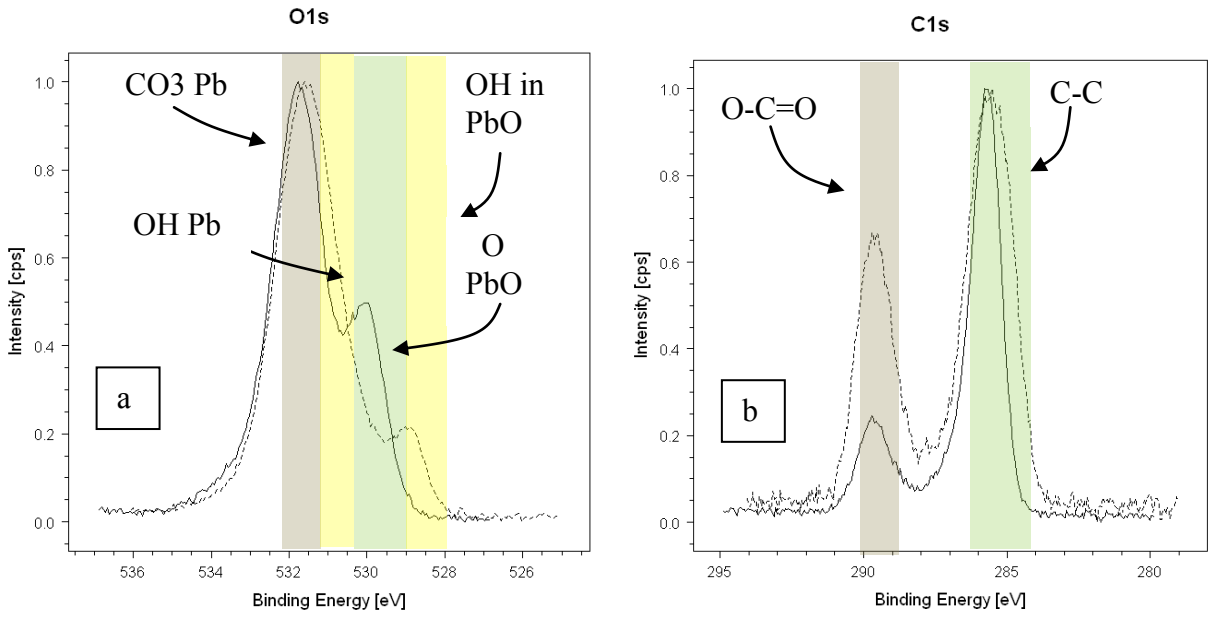

Figure 6.8 XPS O1s (a) and C1s Core line spectra (b) for the Pb surface and the white stain on Pb (dotted line).

The variation of chemical composition indicates a reaction of water with the sample surface, even if the lead surface is considered very stable with water [21]. The fast modification of chemical composition (less than 30 minutes) could be due to the electrochemical corrosion induced by oxygen at air/bubble interface (differential aeration corrosion). Near the water drop edge, in fact,

the concentration of oxygen dissolved in water is higher, than in the bulk of drop. Moreover, this can induce oxygen to act as a cathodic reactant

$$O_2 + 2H_2O + 4e \rightarrow 4(OH) \qquad (6.1)$$

The anodic reaction happens on lead surface

$$Pb \rightarrow Pb^{2+} + 2e \qquad (6.2)$$

These two reactions must occur at the same rate so that an increase in the supply of oxygen assists the cathodic reaction and the corrosion at the anode. The lead ions then react with the hydroxyl ions to form lead hydroxide or with any dissolved carbon dioxide to form lead carbonate and basic lead carbonate[8,12].

The reaction is supported by the XPS analysis where we observed, the absence of any contribution of the Pb metallic state and increase of hydroxide component an oxide component, see figure 6.7a in the chemical composition of the surface of white stain.

6.3.2. Time evolution of water contact angle on lead.

The formation of lead compound (i.e. lead hydroxide lead oxide) due to the interaction with water could induce a variation of the solid-liquid interaction, for this reason, we studied the evolution of water contact angle on Pb surface. The time evolution of contact angle measurement is an interesting method to study the variation of liquid-surface interaction [22]. The variation of water-contact angle as a function of the time, in fact, can change due to a) the surface chemical properties (reaction of water with metal) or b) due to the water evaporation. The liquid evaporation may affect the contact angle value in our particular case where the volume of the drop is only 2 µl. In order to understand the effect of the liquid evaporation on the time evolution of the contact angle, we measured the latter on inert materials with different wettability properties: PDMS (CA of 104°), HDPE (83°), Si (68°), SiO_2 (44°), The measurements were conducted at 21.5C° and with a relative air humidity of 27.5%. We observed that the evaporation rate of water up to 300 sec was low. The variation of the C.A on HDPE is reported in Figure 6.9a. (blue symbols), where a monotonic reduction of the contact angle with increasing time can be observed, due to the evaporation. The evolution of the contact angle as a function of the time in the range between 0 to 300 seconds can be fitted by a linear equation.

$$Contact\ angle(t) = a + b.time \qquad (6.3)$$

The intercept a gives the original contact angle of water with the surface before any effect of evaporation. Tthe slope b indicates the rate of the evaporation and how it can influence the evolution of the contact angle. On inert materials, in our experimental conditions, we observed a value of slope b is always lower than -0.06. PDMS showed the lowest b value, -0.03 and HDPE the highest value, -0.056.

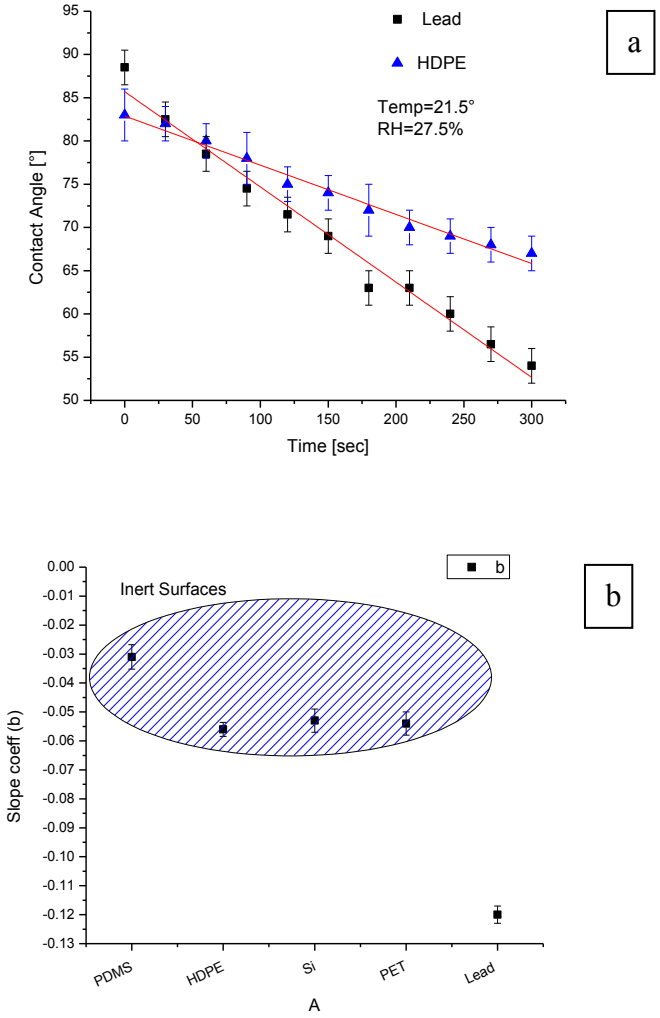

Figure 6.9 Time evolution of contact angle on lead and HDPE in function of time (a) slope of the linear fit of the data for HDPE, silicon, PET and Pb, the blue zone indicates the value range of the slope for inert materials towards water (b).

C. Measurements in function of time were performed on the Pb surface, Figure 6.9a (black

symbols). We can observe that even if the initial contact angle is like that of HDPE, 87°, the evolution of the contact angle is faster than for HDPE the linear fit parameters for Pb are a = 85.7 and b = - 0.12 ± 0.04. The fit, therefore, confirms that for Pb the variation of the contact angle is not influenced only by the evaporation because of the linear fit slope is 2.2 times higher than that for an inert surface. On Pb surface, in fact, as reported in paragraph 6.3., after the water drop evaporation a white stain due to corrosion of surface remained, this rapid change of wetting, therefore, is related to the reaction of the lead surface with water that produced a chemical modification of the surface.

6.3.3 Estimation of volume of the white lead formation using stylus profilometry

The thickness and width of white stain formed onto Pb surface were measured. The measurements were repeated three times, and along three different directions as shown in Figure 6.10. Using a simple–approximation of a cylindric shape of the white stain, its volume was calculated as 0.07 mm^3. The surface of white stain was rougher on the lead surface. The white stains border was not sharp but show shoulder near the white stain border typical for differential aeration corrosion [17].

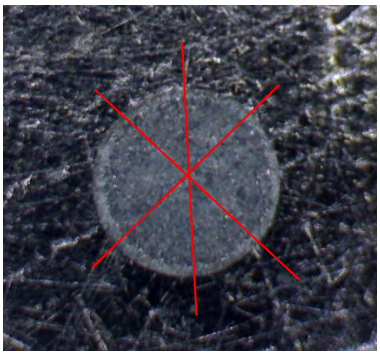

Figure 6.10 Picture of a white stain, the red line indicates the region where the profile of white stain was measured by a stylus profilometer.

6.4 Synthesis of graphene oxide/graphene nanocomposite membranes as barriers against water.

In paragraph 6.3, we observed that the Pb surface was reactive in the presence of a water drop. To inhibit this surface reactivity, Pb surface was coated with a nanocomposite layer deposited using ink developed following the description is given in paragraph 6.2.2 with the aim to obtain a barrier effect. The barrier layer was developed by deposition of material using graphene oxide- and graphene-based inks and also using ink based on the mixture of graphene and graphene oxides. As

reported in 6.2.2 total amount of 2D materials and the amount of solvent (2 propanols) was kept almost constant for all inks. The surface tension of the coating was measured for the different kinds of coatings deposited by the Meyer rod technique, using the Owens-Wendt method (water and paraffin oil employed as probe liquids) [23]. The value of surface free energy (SFE)of the membranes is reported in Figure 6.11. A surface tension value of the 30 mJ/m was found for the graphene coating, attributed entirely to the dispersive component, a typical picture for graphitic materials [24,25]. The graphene oxide-based ink showed a surface tension of 47 mJ/m2 with 50% of it due to the polar component, a typical case of an oxidized surface. The coating with 0.3% of graphene in graphene oxide gave an SFE of 65 mJ/m2, and as for the graphene oxide-based ink, the polar component amounts to 50% of the surface tension, Figure 6.11. The surface tension of the samples with 3% and 10% of graphene in graphene oxides decreased towards the value of pure graphene-based ink. The Pb surface gave a surface tension of 30 mJ/m2 with a relatively small contribution of the polar component,4mJ/m^2.

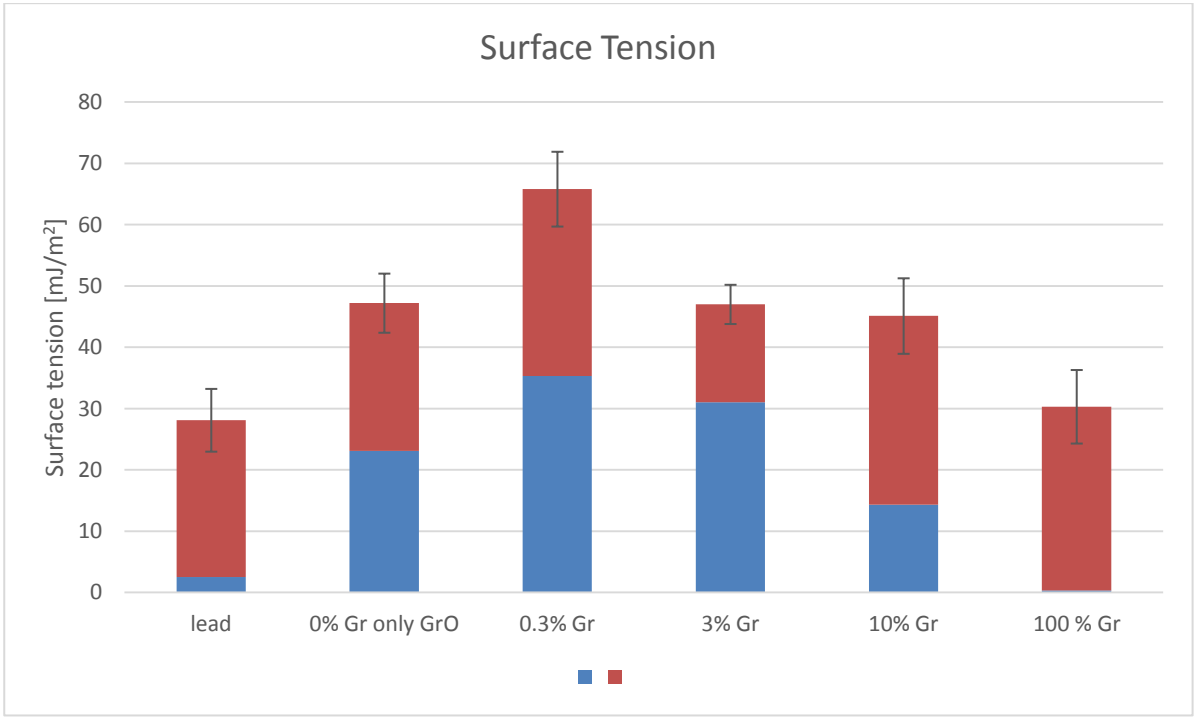

Figure 6.11, Surface tension of the graphene-, graphene oxide- and Gr/GrO nanocomposite- films deposited on Pb, (blue: Polar component, red: dispersive component).

6.4.1 Structure of the nanocomposite coating

To study the morphology of the GrO/Gr nanocomposite films, the films were deposited on a silicon wafer exploiting its flat surface to get information about the intrinsic morphology and structure of the graphene- and graphene oxide-based films which are very thin (20-30nm). Figure 6.12 shows the morphology of nanocomposite films as observed by atomic force microscopy AFM(by Pierini group). The coating deposited with only of graphene oxide (0 %Gr) film appear compact, but the edges of graphene oxide flakes are easily identified, the average roughness is 2.45nm. The width of the flakes is in the range of some microns. The coating based on graphene appears very smooth with some islands (due to the agglomeration of graphene flakes) uniformly distributed on the surface; some large agglomerates were also present on the surface. The average value of roughness is less than 1nm (Figure 6.13.) The samples based on mixtures of Gr/GrO showed a more complex morphology. The surface of Gr/GrO is composed by flakes of graphene oxide covered by small islands of graphene, see blue arrows if AFM image reported in Figure 12(c),(d),(e). On the samples deposited with 0.3% of the graphene, some islands with a dimension around 50 nm diameter are present. In the sample with 10% of Gr, the surface of GrO flakes was covered by graphene island with a diameter of 200 -250 nm. The graphene islands are uniformly distributed on the surface of the sample.

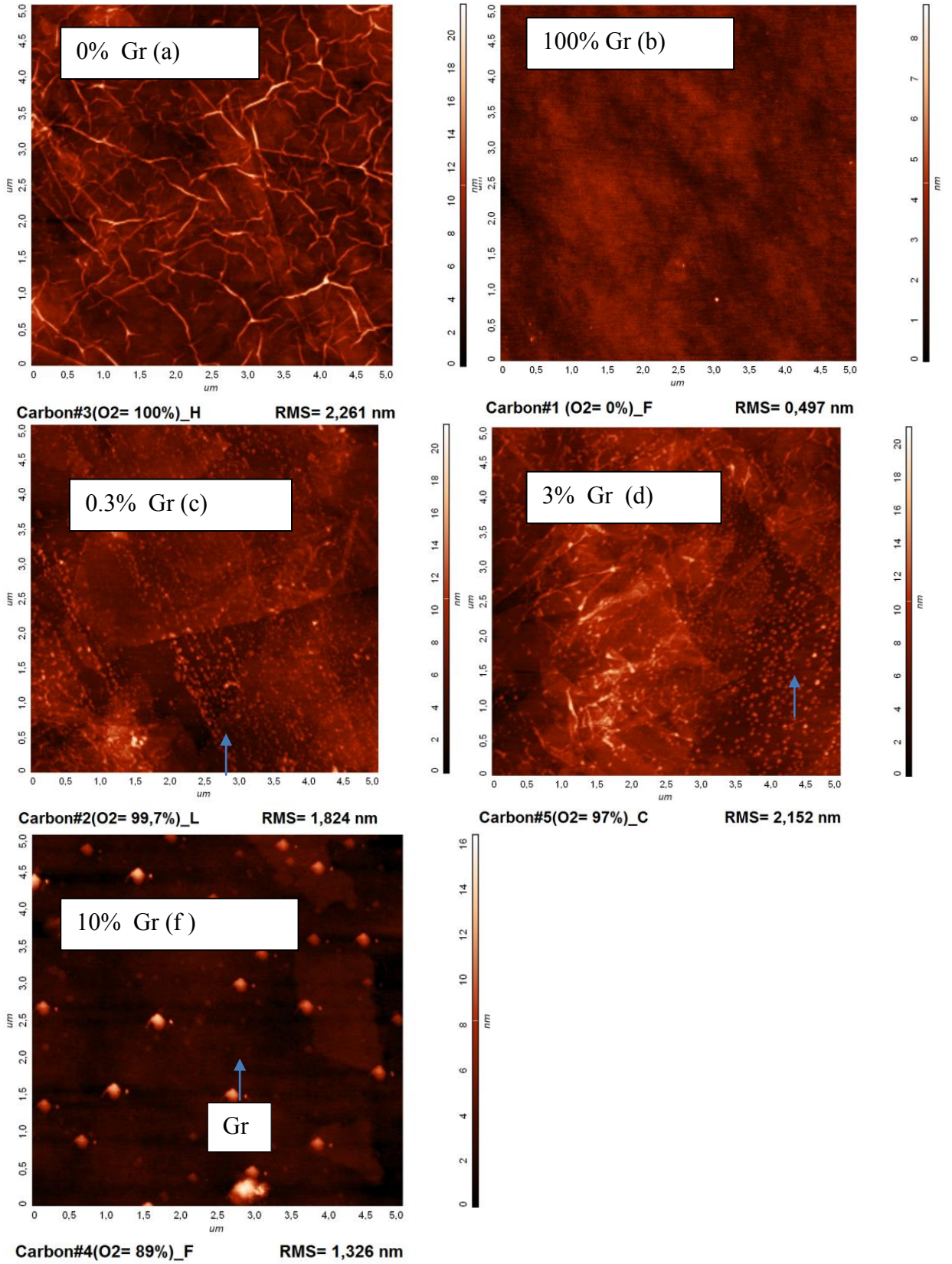

Figure 6.12 Topography images acquired by AFM on the samples realized with graphene-based inks with 0%,100%, 0.3),7% and 10 % of Gr in Gr/GrO mixture (a) flakes. Blue arrows indicate the graphene islands on GrO

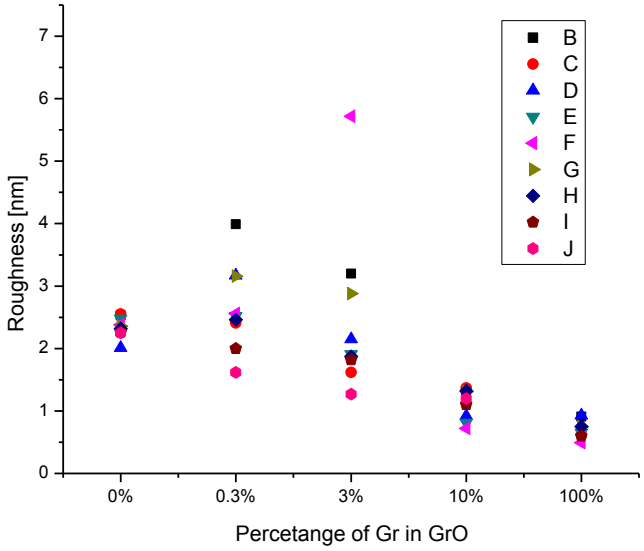

Figure 6.13 Roughness as a function of % Gr in Gr/GrO mixture in the ink(f), roughness has been measured in different places on the surface

Using Raman spectroscopy analysis of all samples, the peaks 1D, 1G and 2D were detected [26] (Raman by Pierini group). Selected spectra are shown in Figure 6.14. The Raman spectrum of Graphene oxide (Gr 0%) film gave a prominent 1D peak; this peak is higher in intensity than peak 1G. Figure 6.14e show the Raman spectra of graphene film (Gr 100%), the 1G peak is the most prominent peak because is higher of the 1D peak. Figure 6.14b show the Raman spectra of the 0,3% Gr sample the spectra appear of this kind of materials appear similar to the sample based on graphene oxide 0% Gr. The Raman spectrum of the sample with 3% and 10% of graphene are reported in figure 6.14 c,d they are similar to the graphene oxide, The Raman analysis has been conducted on the different places of surface and in some places of the coating realized using the mixture of Gr and GrO (0,3% Gr, 3% Gr,10% Gr), we observed some Raman fingerprints of Gr used in our experiment. The 1D/1G intensity ratio of the peak 1D and 1G were calculated for different the samples. Figure 6.14f shows the graph with the evolution of 1D/1G ratio as a function of the concentration of graphene oxide in graphene, the ratio has been measured on different zones of the samples. In the graph, we can observe a general decrease of this ratio when inks with lower GrO concentration, is used to synthesized the coating (green arrow) [27]. This decrease is non-uniform because as we can observe graph of figure 14(f) , in particular on the sample at 10 % of graphene. In latter sample the presence of two kinds Raman structure, one related to graphene oxide (1D/1G higher than 1) and one related to graphene (1D/1G less than 1) is easy to recognize,

this indicate the coating is nanocomposites material composed of the two structure (Gr and GrO). The high intensity of 1D Raman peak indicate that all coating are strongly defected, in particular the coating based on GO.Moreover, Raman reveals that the graphene used in our experiment is a multilayer graphene, because the 2D peak is more smaller thand 1G peak (ratio 2D/1G< 1).

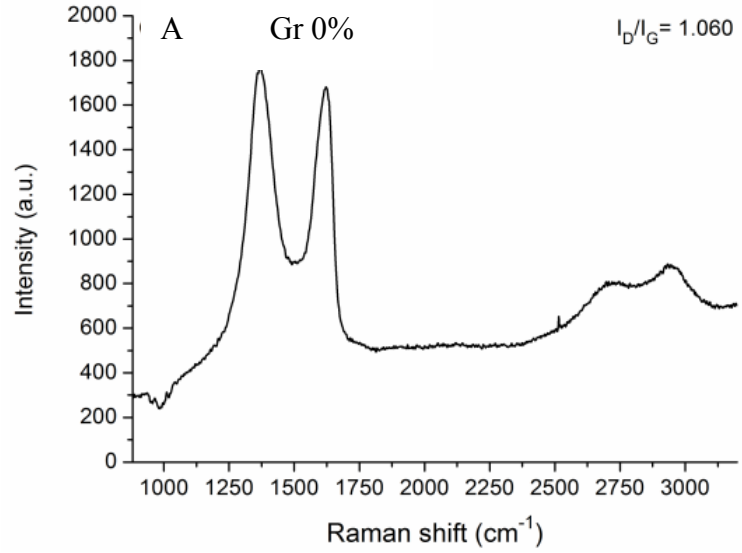

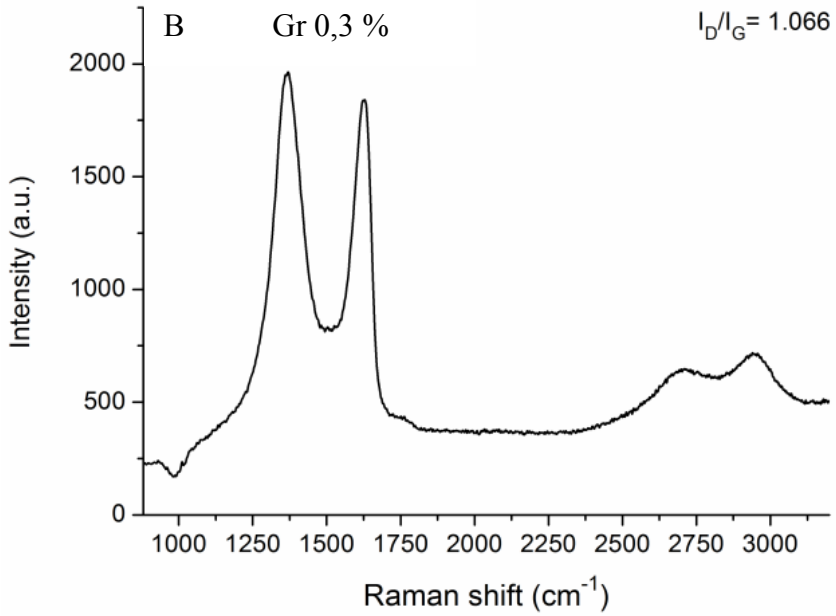

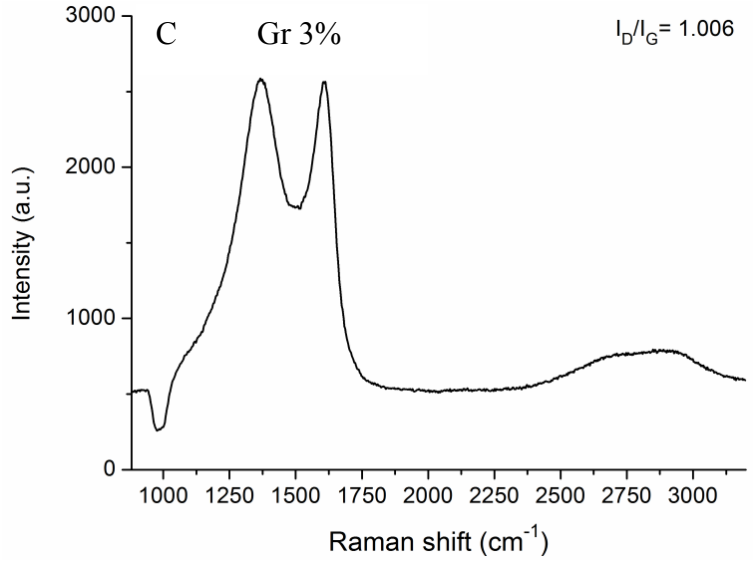
C
Gr 3%
I_D/I_G= 1.006
Intensity (a.u.)
Raman shift (cm^{-1})

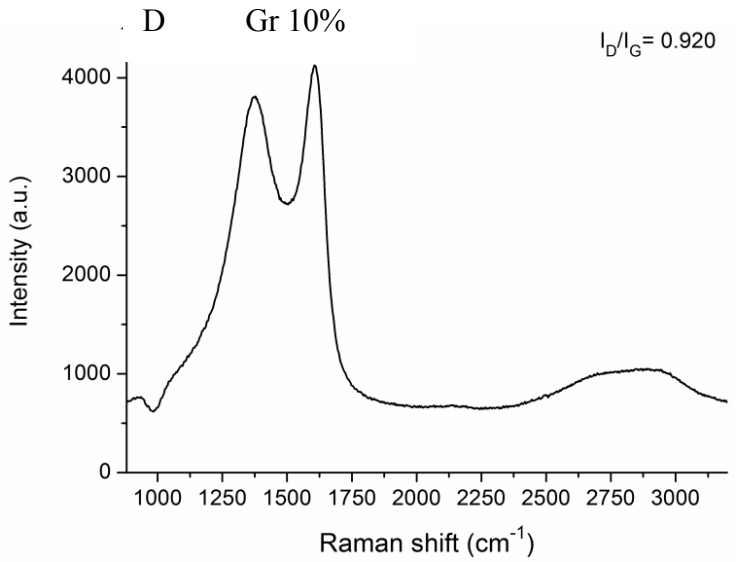
D
Gr 10%
I_D/I_G= 0.920
Intensity (a.u.)
Raman shift (cm^{-1})

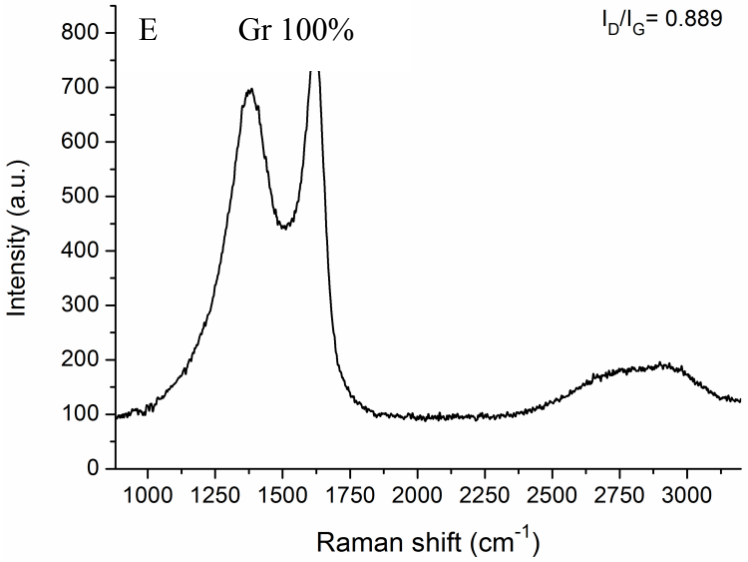
E
Gr 100%
I_D/I_G= 0.889
Intensity (a.u.)
Raman shift (cm^{-1})

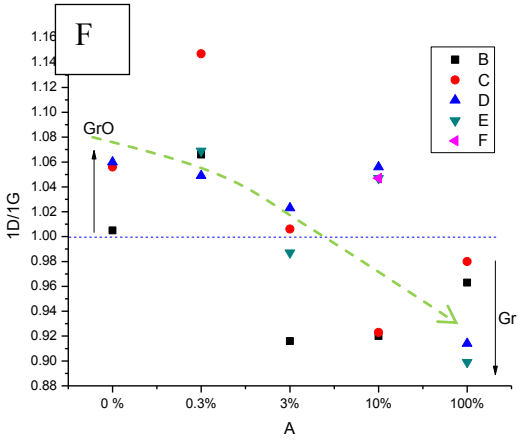

Figure 6.14 spectra of the coating deposited on silicon for the film deposited using with 100% GO(a) 099.7(b) 93(c) 89 %(d) 0%(e) the intensity ratio 1D/1G is reported in the figure. The ratio of 1D/1G Raman peak estimated in differents zone on the sample is reported in the graph (f).

The graphene oxide and reduced graphene films were analysed by XPS. The spectra of C1s are reported in Figure 6.15. On graphene, the peak of the carbon-carbon bond (284.5-285.5 eV) is the most intense. On the graphite oxide films, the peaks related to C=O(287.5) functional group and O-C=O (288.8eV) are the most intense. The semiquantitative analysis of C band on graphene oxide show that the amount of C in C=O functional groups was 44,78. Atomic % and in. C in O-C=O group was 12.3 %. The signal related to C carbon bond C-C and C=C is 42.9.2%.

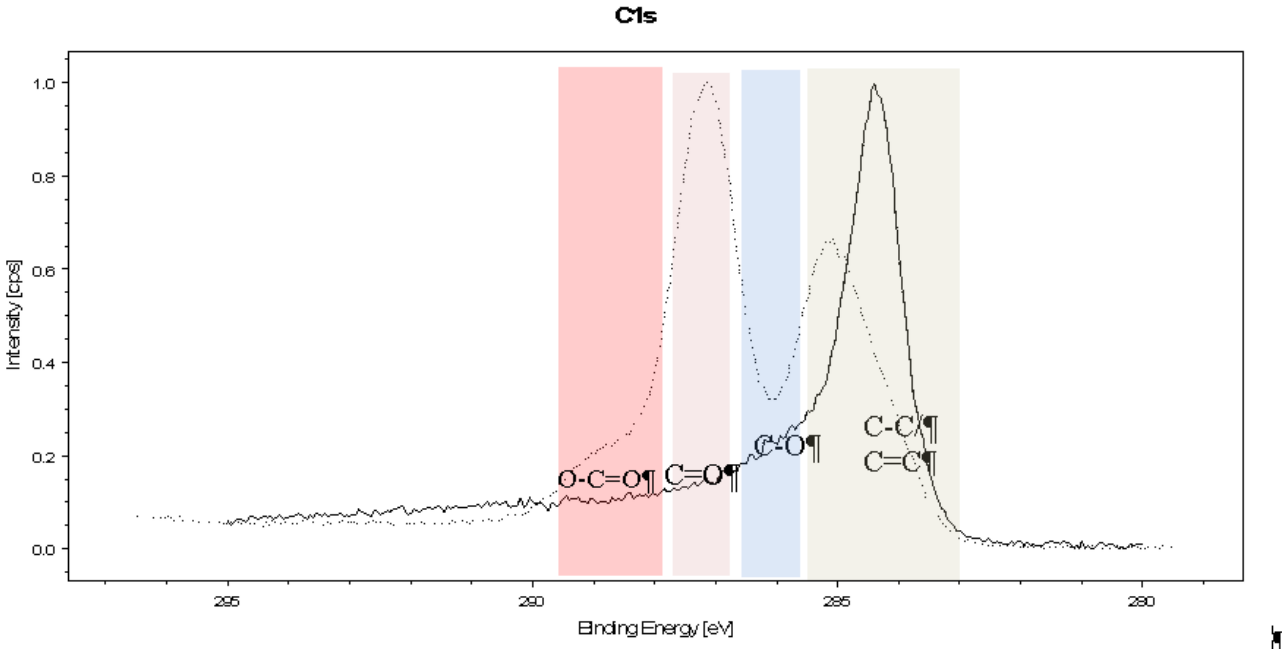

Figure 6.15 XPS C1s core line of graphene oxide (dotted line) and graphene.

The semiquantitative analysis of band related to the carbon of graphene shows the main component at 284.5 eV typical of the C=C bond, the percentage of atomic concentration due to C=C is 77.1% of carbon signal. Moreover, 4.141% is due to the components at 285.2 eV typical of the airborne contamination [28]. A small amount of oxygen bonded to carbon has been detected 10,55 % due to C-O, 4,94% due to O-(C=0) and only 3,9 due to O=C-O. The quantification of the components of carbon for GrO and Gr is reported in Table 6.4.

Table 6.4 XPS quantification of C1s line of graphene and graphene oxide

	Binding Energy	Graphene	Graphene Oxide
	eV	Relative atomic concentration (at.%)	Relative atomic concentration (at.%)
C=C	284.5	77,1	19,6
C-C airborne contamination	285.2	14,1	23.3
C-O	286.5	10.5	0.10
C=O	287.5	-	44.73
-O-(C=O)	288.6	4,9	288.78
O=C-O-C=O-	289.3	3,3	-

The graphene oxide has more of 55% of the surface covered by oxygen functional group. All functional groups detected on carbon are polar and this explains the good dispersion of graphene oxides in the 2-propanol that is a polar solvent.

6.4.2 Morphology of graphene /graphene oxide films on Lead

Pb substrates were coated by the nanocomposites described in Section 6.2.2. To obtain a good homogeneity of the films the Meyer rod method was used. The surface of Pb was macroscopically well covered by the layer of the nanocomposite materials. SEM was used to check the homogeneity of the substrate coverage. Figure 6.16 shows the surface of lead covered by the film realized with graphene oxide and 0,3 wt.% graphene, at 1000 and 19002 magnifications respectively. Both films were homogenous and conformal to the surface.

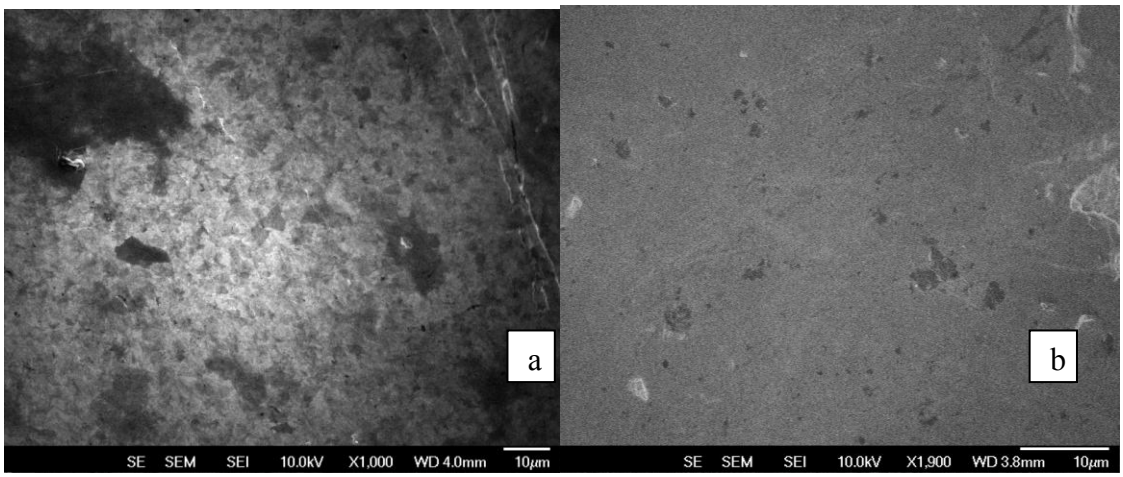

Figure 6.16. Topography by SEM of the samples realised with graphene oxide and 0,3 wt.% graphene, magnification 1000X (a) and 1900X (b).

The image reported in Figure 6.17 was acquired near holes to show the difference between the of the morphology of the film and that of the Pb substrate.

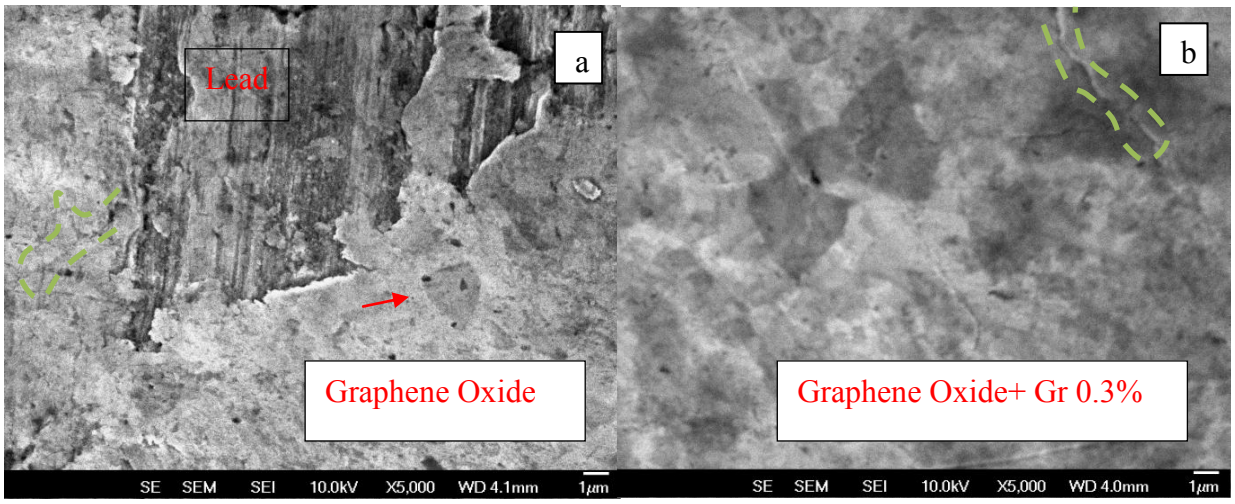

Figure 6.17 Morfology of graphene oxides, and with graphene oxide and 0,3 wt.% graphene with the scale at 1 micron, magnification X5000, green dot line indicates a defect on the surface

The graphene oxide coating (30nm) appeared homogeneous, and some flakes are identified in the SEM image in Figure 6.17 (red arrow). The surface of the coating based on graphene oxide ink with 0,3 wt.% graphene appeared flattened. The graphene flakes were not strongly agglomerate l indicating a good dispersion of graphene flakes in the ink and a suitable preparation of the coatings. Some cracks were observed on the surface of the materials, (green lines) in Figure 6.17, however, the coating appeared compact.

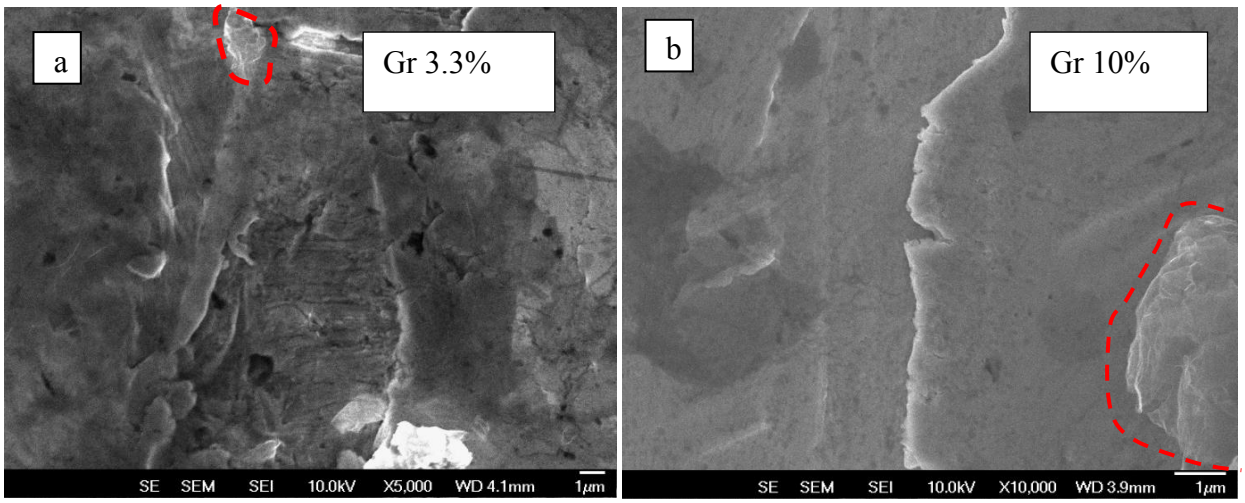

Figure 6.18 Morphology of the lead surface covered by graphene oxide with 3.3 wt.% of graphene and graphene oxide with 10 wt.% of graphene. Red line indicates graphene agglomerates.

Figure 6.18 shows the morphology of the coating synthesised using 5.5 wt.% and 10 wt.% of graphene in the graphene oxide –graphene mixture. The coatings were quite conformal and compact. However, the coating appeared more damaged, with more cracks and agglomerated particles of graphene on the surface (indicated by the red dotted line in Figure 6.18). These defects were more evident in the sample with 10 wt.% of graphene in the mixture.

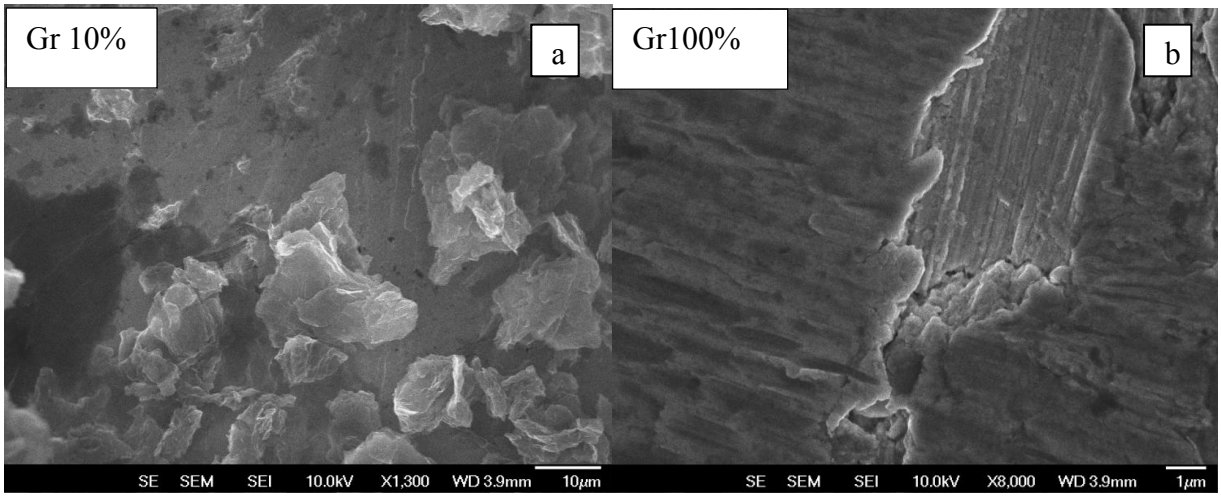

Figure 6.19 Morphology of the lead surface covered by graphene oxide with 10 wt.% of graphene (a) and with 100% of graphene (b).

The membranes prepared using the only graphene, surprisingly, were compact without agglomerates, Figure 6.19. The coating developed with a high concentration of graphene oxide (i.e. the samples with 0 or 0.3 wt.% graphene) or with pure graphene appeared of better quality from the

morphological point of view.

6.4.3 Barrier effect of nanocomposite coating

To test the barrier properties of the coating, the results obtained by the time evolution of contact angle, profilometry, XPS and SEM were compared.

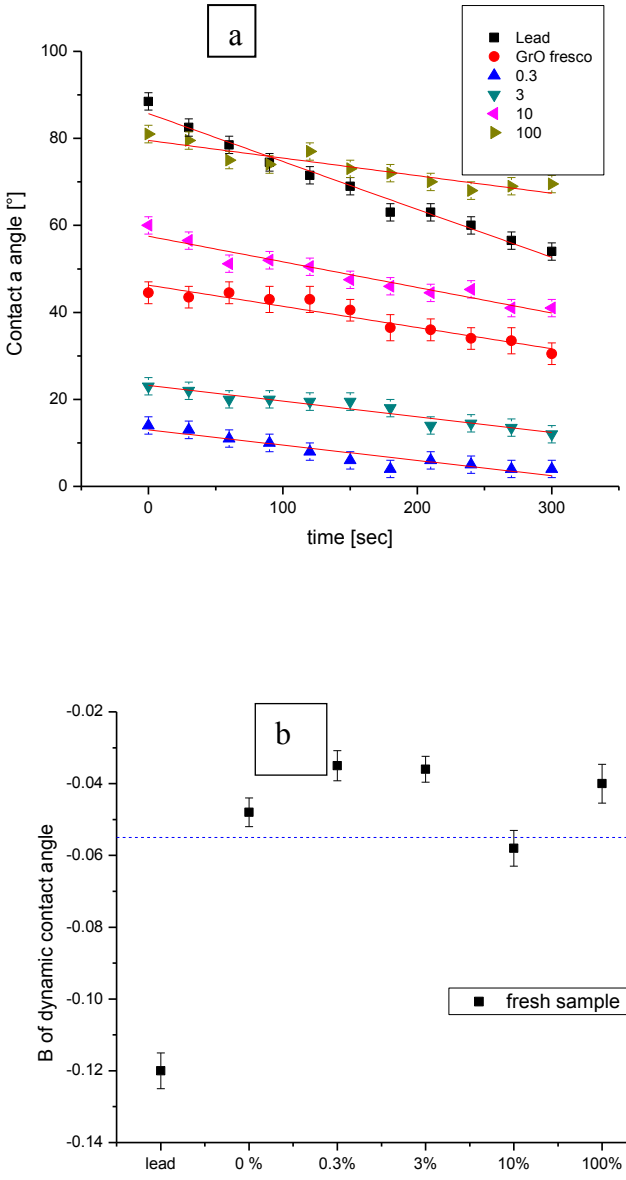

a

Figure 6.20 Time evolution variation of the water contact angle on Pb in function of time (a), the slope of the linear fit of the data in function of the concentration of graphene in the graphene oxide-graphene mixture. (b) .

The contact angle has been measured on a lead surface covered by the GrO/Gr nanocomposite coating. The coating based on graphene oxide showed a starting contact angle value of 44° and the slope of the linear fit of the evolution curve in function of time was -0.048 while for the composite sample with 0.3% of graphene in the mixture we had a contact angle less than 20° and a variation slope of -0.03.while for the other coating realized using 10% of graphene is -0.058. On the layer realized with ink based on 100% of graphene, the slope variation was less than -0.04. This indicates that the reactivity of Pb with water is sharply reduced, even if sample realized with 10% of Gr appeared the less effective. To have a quantitative estimation of reduction of the lead surface, we estimate the average volume of the stain. (see paragraph 6.3.3) The volume of white stain on Pb was 0.07mm^3. The volume of the white stain after the deposition of graphene oxide coating was only 0.025 mm^3, 2.8 times lower than on uncoated Pb. Figure 6.21, shows the volume of white stain on the lead surface and lead covered by graphene and graphene oxides films

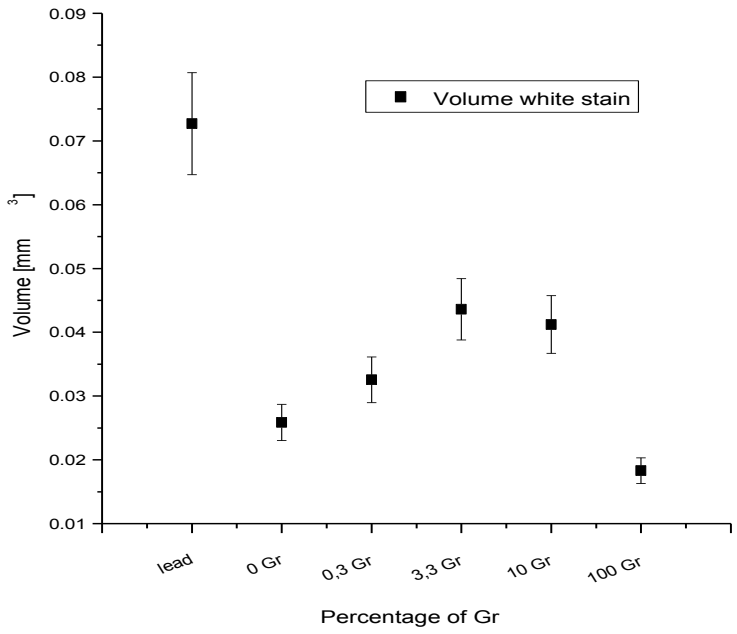

Figure 6.21 Volume of the white stain formed on Pb for samples with increasing graphene concentration in the graphene oxide- used inr the ink preparation, 0% (only GrO), and O,3%,3.3% 10%,100% of graphene (Gr) . For comparison, the volume measured on the uncoated Pb is also shown.

The other coatings based on the mixture of graphene and graphene oxide showed a volume of white stain from 0.03 to 0.045 mm^3, and the volume tends to increase with the increase of graphene in the composition while the coating based only on graphene showed a volume of white stain of 0.018 mm^3 that is the lowest measured value (3.8 times lower than for lead). The results indicate the all

coating show a reduction of the surface reactivity. This can also be appreciated also by optical observation of the sample, figure 6.22, microscope 25 X.

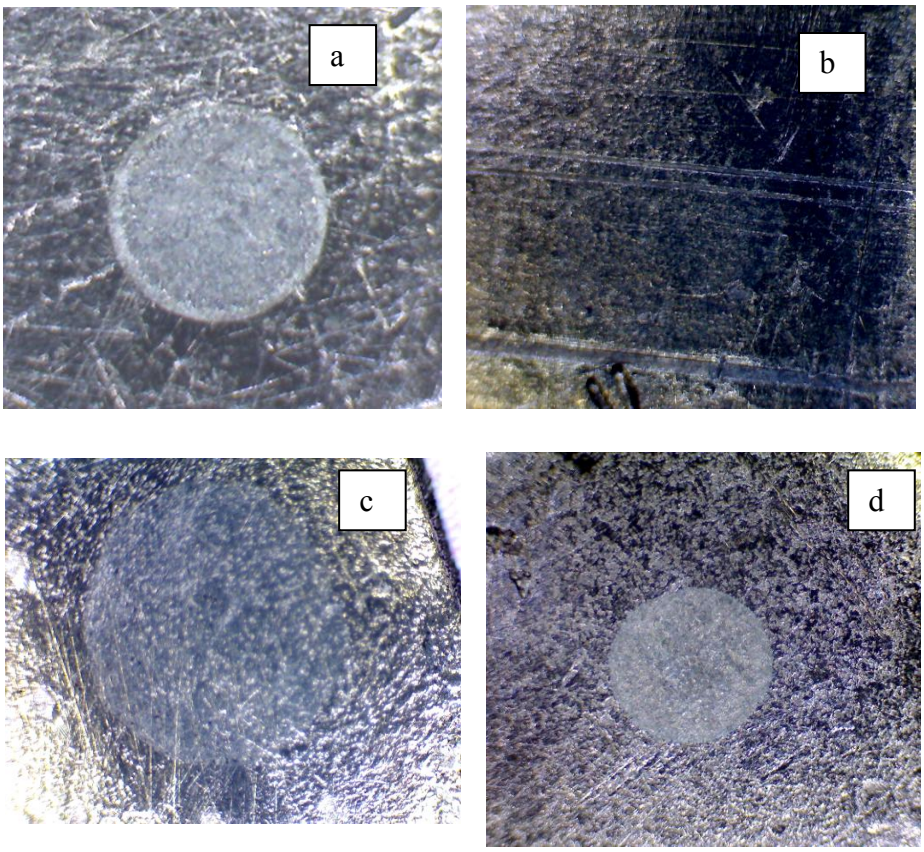

Figure 6.22 Optical image of white stain on lead (a), on GrO on Lead (b), on film deposited with 0.3. % Gr (c) and a film deposited using only Gr (d).

On the sample coated with the graphene oxide, the white stain is almost imperceptible. The white stain on coating with graphene became more evident because the colour of the surface was darker and this improve the optical contrast with the white stain. On graphene, the stain appeared smaller than other samples.

By XPS analysis we studied the chemical properties of the "white stain " for lead and the sample covered by graphene-based films. On the surface of the lead white stain as indicate in the paragraph 6.3.1 Carbon, Oxygen and lead have been detected, this due to the formation of a lead salt, as lead hydroxide, basic lead carbonate. The atomic percentage of Pb on this stain was around 12 at % while O_2 was 44 at % and C was 32 at%. The concentration of lead on the pristine surface was only of 8%, because the surface was covered by large amount of carbon contamination. The increase of Lead signal after the contact of the water in due to the formation of a new layer of Pb salts induced aerial corrosion. For this reason, the signal of Pb by XPS can indicate the superficial salt formation

induced by water lead reaction. We followed the atomic percentage of Lead compounds for the different samples after the interaction of the surface with water drops.

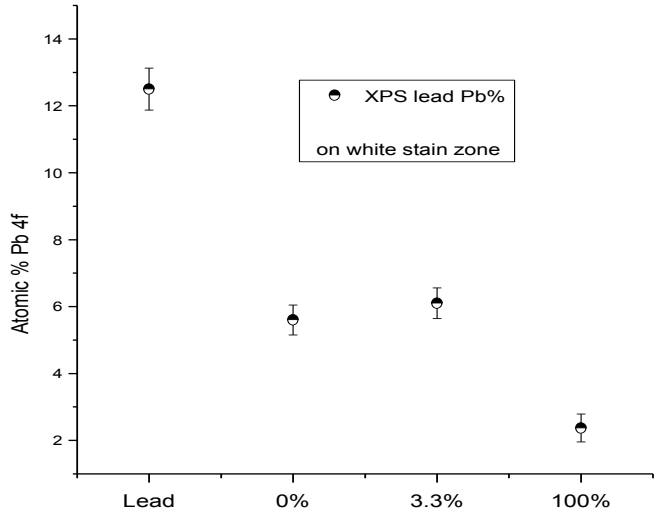

Figure 6.23 Atomic % of Pb estimated by XPS on lead and lead coated with the nanocomposite films, The % reported in the graph are the % of graphene in the graphene-graphene oxide mixture

All sample coated with graphene films showed a lower concentration of lead compounds. The amount values of the lead compounds is reported in figure 6.22. Considering the results of the contact angle measurements in function of time, the profilometry measurements, the optical microscopy observation and the chemical evolution of lead as seen by XPS, it appears that all the coatings were able to significantly reduce the corrosion induced by water on the lead surface. The most efficient coating was the coatings based on pure graphene and pure graphene oxide. The composite coatings made of their mixture, graphene and graphene oxide, appeared less efficient. The loss of protective properties of the coatings is directly related to the amount of the graphene in the mixture.

To understand the role of graphene in the degradation of barrier properties of the films on lead SEM analysis have been conducted. SEM images of the layers based on Gr/GrO mixed composition showed that on the surface there were agglomerates of graphene flakes. The amount and the dimension of the graphene agglomerates increased with the increase of graphene amount in the ink composition. A significant amount of graphene agglomerates were detected on the coating synthesized with 10% graphene in the mixture. Figure 6.23c and figure 6.24 show the surface morphology by SEM image e agglomerate of graphene flakes on the lead surface for the layer

synthetized using dispersion with 3% and 10% of graphene in graphene oxides

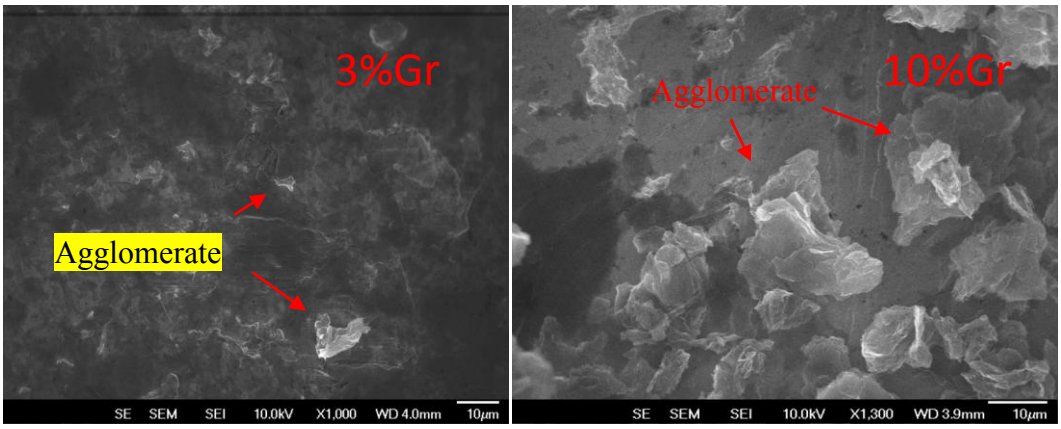

Figure 6.24 SEM images of films realized with 3% of Gr and 10% of graphene in graphene-graphene oxide mixture. The agglomerates are indicated by red arrows.

The SEM images reveal that near the agglomerate there are holes with shape and dimension similar to the graphene agglomerates, yellow line in picture 6.24.

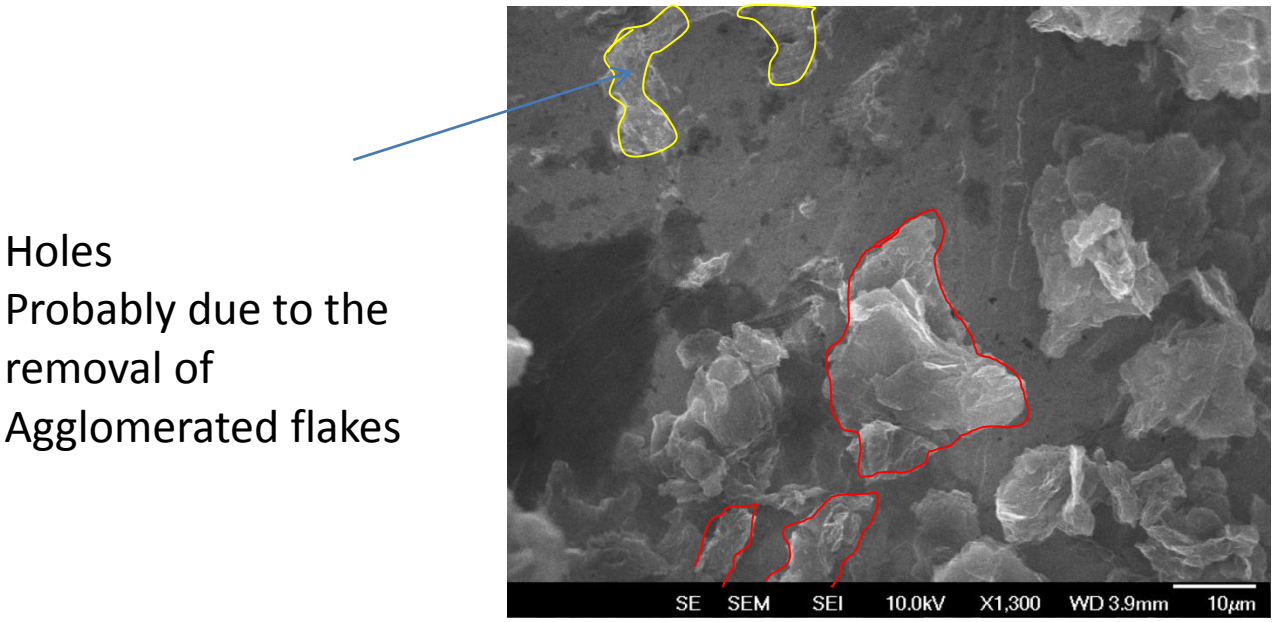

Figurea 6.25 Agglomerates on lead sample coated with ink based on –inks with Gr10%, the red line indicates the agglomerates contour and the yellow ones the uncovered zones (hole) in the coating.

This indicates that the graphene agglomerates are prone to detachment, leaving uncovered regions of the substrate surface easily exposed to water. This can explain the reduction of the protective

properties of the samples realised with a concentration of graphene of 3.3% and 10 % for which graphene was not well dispersed in isopropanol solvent, and the effect of compression due to the Meyer rod was too low to obtain an entirely uniform coating. The inadequate dispersion of the graphene in isopropanol is due to the high polarity of the solution containing graphene oxide. Therefore is a preferential dispersion of GrO in 2 propanol is expected Moreover the introduction of graphene oxides in the solution (ink) probably induced an increase of polarity and the surface tension of the ink-GrO, in fact, showed a polar component of 24 mJ/m. (determined by Owens Wendt method), and a total surface tension of 45 mJ/m (twice that of 2- propanol) The surface tension increase is a limitation factor for the dispersion of the graphene flakes in the solution, as revealed in paragraph 6.2. This factor reduces the capability of 2 -propanol to disperse graphene flakes and induces the coalescence of the graphene flakes to compensate the increase of surface tension. As a result, there is the formation of an agglomerate of flakes of graphene with dimension in the range of 1 to 10 micron. The agglomeration of the graphene flake promotes the formation of pinholes on the surface of the coatings.The pinholes on the surface reduce the barrier properties of the films. This show that, in a counterintuitive manner that the mixture of graphene and graphene oxide do not produce films with barrier properties that have the average barrier properties of these two kinds of materials.

We can remark that even if a high percentage of graphene in graphene oxide ink led a degradation of the structure of the coatings, a small amount of graphene in ink could be used without detrimental effect on the barrier properties and the morphological properties of the coatings.

6.5 Durability test

The capability of the sample to protect the lead surface by water drop corrosion was tested 45 days, and 180 days after the synthesis of and films. The tests were conducted to evaluate the durability of protective properties of the barrier coating based on graphene materials. Figure 6.26(a) shows the variation of the water contact angle on the freshly synthesised coatings with the contact duration with the surface, and Figure 6.26 (b) shows the variation of the water contact angle on the coating surface with water-surface contact duration measured on 180 days aged coatings. We can observe that all the aged coatings showed an increase of the contact angle with increasing the water-surface contact duration.

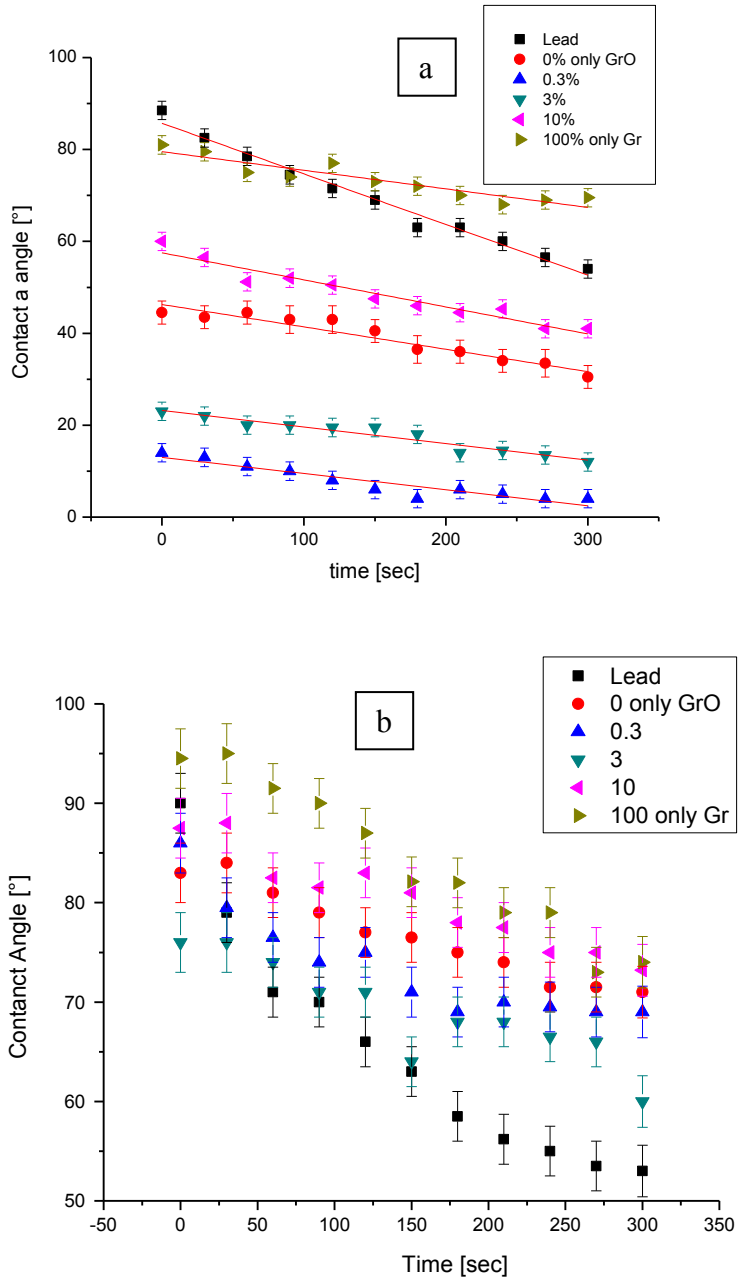

Figure 6.26 Variation of water contact angle on fresh (a) and 180 days aged coatings (b) and linear data fit curves.

In Figure 6.26 we reported the linear data fit slope as determined from the graphs in figure 6.26 for each sample during the durability test. Additional test on 45 days aged coatings was also performed. After 45 days ageing, the coating based on GO showed a slope value like the one estimated on fresh samples. A significant reduction of the slope value was observed only for coatings based on graphene. For all the samples the slope value was less than -0.06, therefore comparable to the value

on an inert surface.

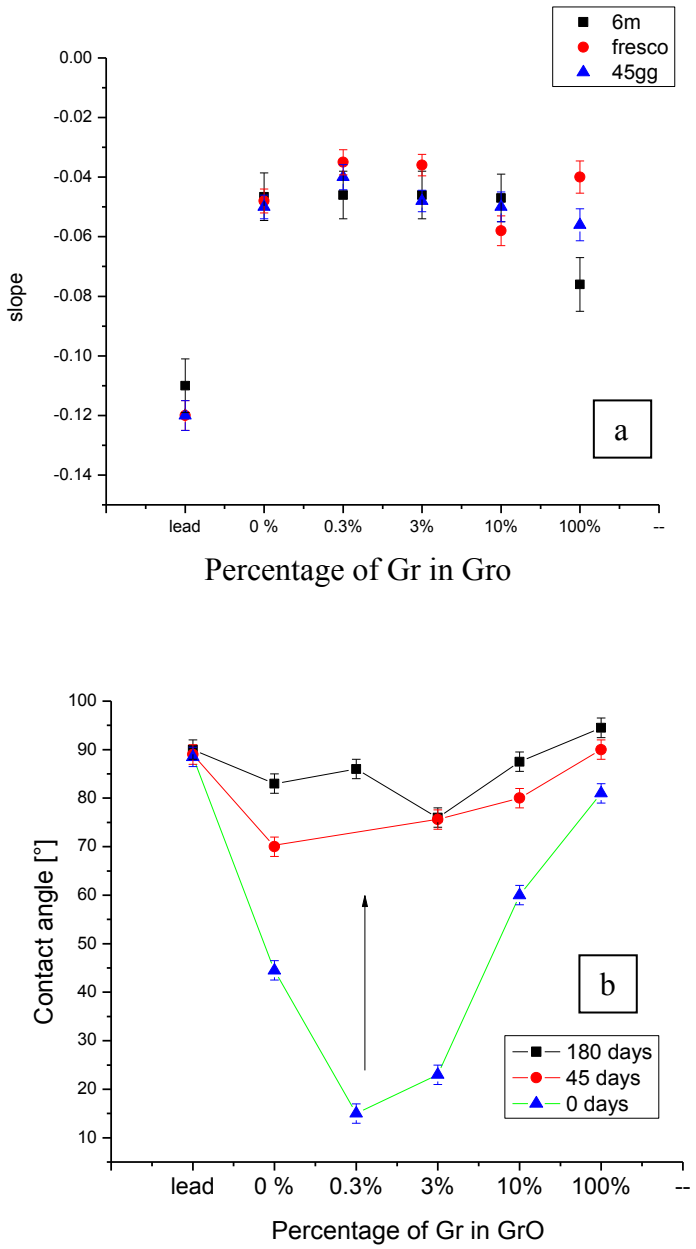

Figure 6.27 Slope of the linear fit of the evolution data of the contact angle with time for fresh, 45 days and 180 days aged coatings.

The slope value of the sample aged for 180 days appeared slightly lower than the one value found in the fresh sample. The most important reduction of the slope value was observed on the graphene-coated lead surface for which it was of -0,076, a value between the one for Pb and that found on an inert surface. This indicates that the reactivity of the surface increased and the coating lost the barrier property against water.

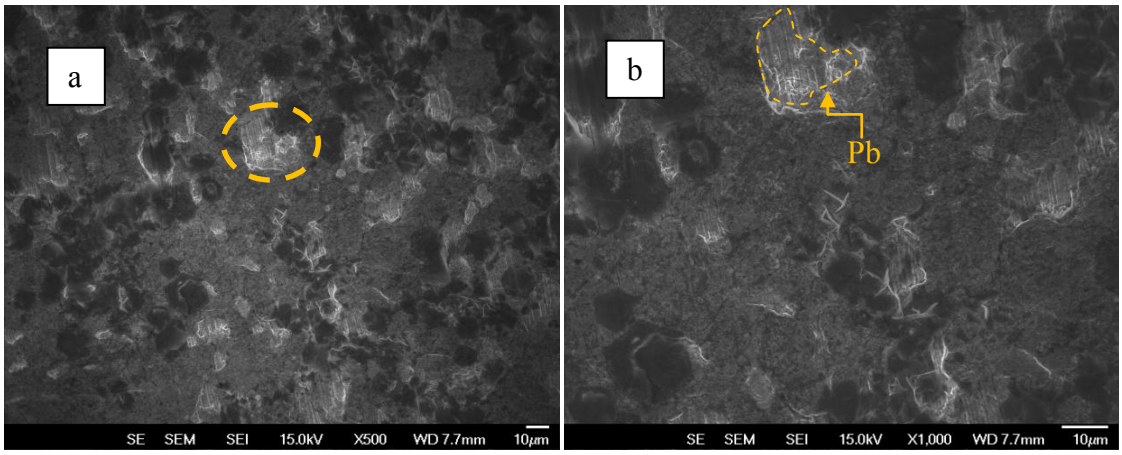

Figure 6.28 SEM images of two different zones of Pb coated with graphene after 180 days ageing, in many zones of the surface the coating was delaminated and Pb substrate exposed (orange circles).

By SEM microscopy we analyzed the graphene morphology on lead after months ageing. In Figure 6.28, in many places of the surface of the graphene coatings were lift out indicating a delamination of the flakes. This indicates that the adhesion of graphene coating was inferior, due more likely to the fact that graphene surface, as graphite surface, shows exclusively a Van der Waals interaction which is weaker than polar interaction [29,30]. The coating with graphene oxide is more stable, probably due to a better adhesion that favours the mechanical stability of the coating. The coating composed of the mixture of GrO and Gr, despite the presence of graphene agglomerates, are more stable and with good protection properties even after 6 months ageing.

6.5.1 Increase of water contact angle due to the ageing of Gr/GrO coatings

In the previous paragraph, we observed that the ageing of the coating also produces an essential increase of the surface wettability. On some samples, we measured the variation of the surface energy using the Owens Wendt method after several days ageing. The polar component of the surface energy for graphene oxide coatings, while typically high, decrease, in contrast with the polar component of the graphene-rich coatings which increased. The final polar-to-dispersive component ratio tended to converge to a narrow range of values, between 0,15 -0,3 after 20 days ageing, Figure 6.29, indicating that the surfaces became more similar and the final contact angle tended to converge to a range between 80° and 94°.

This behaviour indicates that the surface by ageing was covered by airborne contamination,

similarly to graphite as seen in Chapter 4, which can explain the decrease of wetting properties of the surface.

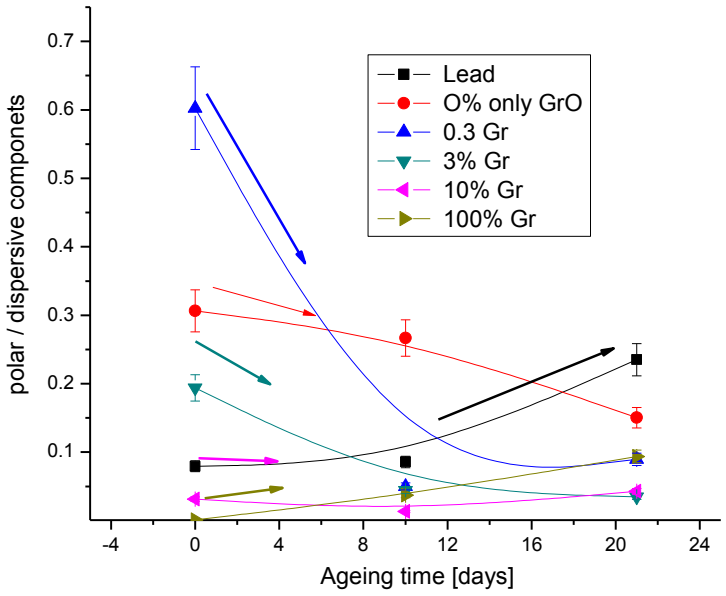

Figure 6.29 Polar to dispersive component ratio for nanocomposite coating as a function of ageing time.

6.6 Conclusion

Protective films based on graphene and graphene oxide deposited on Pb using a simple method based on graphene inks were developed. Various kinds of graphitic suspensions were realised using graphene and graphene oxide. The synthesis of graphene suspensions with different kind of solvents ethanol (ET), ethylene glycol (EG), 2-propanol, and N, N-dimethylformamide (DMF) are reported. We observed that 2-propanol is a suitable solvent to disperse graphene-based materials. Combining 2-propanol with graphene and graphene oxide materials were produced films on Pb surface as a barrier against water corrosion. Surface reactivity of Pb and the protective properties of graphene layers on lead were studied. The results show that all the films were able to significantly reduce corrosion by water drops. The best results on fresh samples were obtained with films realized with graphene and graphene oxide, while the membrane realized as a composition of graphene and graphene oxide showed a defected surface, due to the agglomeration of the graphene flakes. The barrier properties and stability were evaluated for 6 months, and in the case of membrane based on graphene, a reduction ìof such properties was observed. This was due to the delamination of the graphene layer from Pb surface while the films based on graphene oxide were more stable upon ageing, indicating that the layer based on graphene oxide is the best candidate to protect Pb surface against differential aeration corrosion induced by water drops.

References

1. Hoivik ND, Elam JW, Linderman RJ, Bright VM, George SM, Lee YC. Atomic layer deposited protective coatings for micro-electromechanical systems $. 2003;103:100-108.

2. Su Y, Kravets VG, Wong SL, Waters J, Geim a K, Nair RR. Impermeable barrier films and protective coatings based on reduced graphene oxide. *Nat Commun*. 2014;5:4843. doi:10.1038/ncomms5843.

3. Singh BP, Jena BK, Bhattacharjee S, Besra L. Development of oxidation and corrosion resistance hydrophobic graphene oxide-polymer composite coating on copper. *Surf Coatings Technol*. 2013;232:475-481. doi:10.1016/j.surfcoat.2013.06.004.

4. Chen S, Brown L, Levendorf M, et al. Oxidation Resistance of Graphene- Coated Cu and Cu / Ni Alloy. 2011;(2):1321-1327.

5. Lu Y-H, Yang C-W, Fang C-K, Ko H-C, Hwang I-S. Interface-induced ordering of gas molecules confined in a small space. *Sci Rep*. 2014;4:7189. doi:10.1038/srep07189.

6. Schriver M, Regan W, Gannett WJ, Zaniewski AM, Crommie MF, Zettl A. Graphene as a long-term metal oxidation barrier: worse than nothing. *ACS Nano*. 2013;7(7):5763-5768. doi:10.1021/nn4014356.

7. Mayavan S, Siva T, Sathiyanarayanan S. Graphene ink as a corrosion inhibiting blanket for Iron in aggressive chloride environment. *RSC Adv*. 2013;3(47):24868-24871.

8. Walker R, Oliphant R, Walker R, Oliphant R. Corrosion of lead in drinking water. 1982. doi:10.1108/eb007191.

9. Dufo-lópez R, Lujano-rojas JM, Bernal-agustín JL. Comparison of different lead – acid battery lifetime prediction models for use in simulation of stand-alone photovoltaic systems. 2014;115:242-253. doi:10.1016/j.apenergy.2013.11.021.

10. Innocent B, Liaigre D, Pasquier D, Ropital F, Léger J-M, Kokoh KB. Electro-reduction of carbon dioxide to formate on lead electrode in aqueous medium. *J Appl Electrochem*. 2008;39(2):227-232. doi:10.1007/s10800-008-9658-4.

11. Guida G, Marabelli M. f Restoration and Storage of Lead Artifacts. 1980:227-237.

12. Grayburn R a, Dowsett M, De Keersmaecker M, Banerjee D, Brown S, Adriaens A. Towards a new method for coating heritage lead. *Herit Sci*. 2014;2(1):14. doi:10.1186/2050-7445-2-14.

13. 1998 - Tetreault et al - Studies of lead corrosion in acetic acid environments.pdf.

14. Lebedev A V, Engel A, Morozov KI. Measurement of corrosion content of archaeological lead artifacts by their Meissner response in the superconducting state ; a new.

15. Selvaraj M. Stable colloidal dispersion of functionalized reduced graphene oxide in aqueous medium for transparent conductive film. *J Colloid Interface Sci*. 2017;406(May):69-74. doi:10.1016/j.jcis.2013.06.006.

16. Stankovich S, Piner RD, Chen X, Wu N, Nguyen T, Ruoff RS. Stable aqueous dispersions of graphitic nanoplatelets via the reduction of exfoliated graphite oxide in the presence of poly (sodium. 2006:155-158. doi:10.1039/b512799h.

17. Turri S. *Vernici Materiali Tecnologie Proprietà*. 4th ed. (Ambrosiana CE, ed.). Milano; 2011.

18. Crist BV, Crist BV. A Review of XPS Data-Banks. 2007;1:1-52.

19. Baltrusiaitis J, Chen G, Rubasinghege G, Grassian VH. NIH Public Access. *Environ Sci Technol*. 2012;46(23):12806-12813. doi:10.1021/es3019572.Heterogeneous.

20. Kim, K. S, Leary TJ, Winograd N. X-ray Photoelectron Spetra of lead Oxides. *Anal Chem*. 1973;45(13):2215-2218.

21. Dom A, Dom MT. Dating Archeological Lead Artifacts from Measurement of the Corrosion Content Using the Voltammetry of Microparticles. 2011:5639-5644.

22. Ghulinyan M, Bernard M, Bartali R, Pucker G. Applied Surface Science Formation of Mach angle profiles during wet etching of silica and silicon nitride materials. 2015;359:679-686.

23. Rudawska A, Jacniacka E. Analysis for determining surface free energy uncertainty by the Owen–Wendt method. *Int J Adhes Adhes*. 2009;29(4):451-457. doi:10.1016/j.ijadhadh.2008.09.008.

24. Kozbial A, Trouba C, Liu H, Li L. Characterization of the Intrinsic Water Wettability of Graphite Using Contact Angle Measurements : Effect of Defects on Static and Dynamic Contact Angles. *Langmuir*. 2017;33:959-967. doi:10.1021/acs.langmuir.6b04193.

25. Wei Y, Jia CQ. Intrinsic wettability of graphitic carbon. *Carbon N Y*. 2015;87:10-17. doi:10.1016/j.carbon.2015.02.019.

26. Malard LM, Pimenta MA, Dresselhaus G, Dresselhaus MS. Raman Spectroscopy in Graphene. *Phys Rep*. 2015;473(5-6):51-87. doi:10.1016/j.physrep.2009.02.003.

27. Beams R, Canc LG, Novotny L. Raman characterization of defects and dopants in graphene. 2015;27. doi:10.1088/0953-8984/27/8/083002.

28. Kozbial A, Li Z, Sun J, et al. Understanding the intrinsic water wettability of graphite. *Carbon N Y*. 2014;74:218-225. doi:10.1016/j.carbon.2014.03.025.

29. Mittal, K. L. *Contact Angle, Wettability and Adhesion*. (VSP, ed.). Utrech , Netherlands; 1993.

30. Francioso L, Pascali C De, Bartali R, et al. PDMS/Kapton Interface Plasma Treatment E ff ects on the Polymeric Package for a Wearable Thermoelectric Generator. *Appl Mater Interfaces*. 2013;5:6586-6590.

Conclusion and Future remarks

The thesis work was focused on a study of the water-surface interaction of graphitic-materials in different environmental conditions and on the use of graphitic materials as impermeable barriers against the degradation of surface properties induced by water. Water, in fact, is an important source of degradation of the surfaces, even for materials which are water-resistant as PDMS and Lead (Pb). To develop a method to overcome the problem related to the degradation of the surface it is fundamental to study the water- material interaction processes. For this reason, the thesis covers the study of liquid-gas-interaction with graphitic materials and the synthesis of water barrier layers using graphitic-materials on PDMS and Lead (Pb) substrates. Attention was paid to graphene and graphene-based materials which appeared very promising to realise the thinnest water-barrier layers thanks to the 2D structure. Graphene-based materials are material derived from graphite, for this reason, the first part of the dissertation was dedicated to a study of water-gas-graphite interaction. A detailed study of the gas-liquid-solid interactions of graphite was conducted in a wide range of experimental conditions.A first activity was devoted to the investigation of the intrinsic wettability of graphitic materials by water, solvents and different low molecular weight gases. The effect of the addition of oxygen functional group was also explored. We observed that wetting of graphite materials by water was sensitive to the physical-chemical properties of the surface. On unmodified HOPG surface, a small amount of airborne contamination, the layer structuring (e.g. single, multilayer layer) and the gas environment can perturb the intrinsic wettability properties of graphite. Even if part of results were predicted, e.g. the role air contamination, other results as the gasphillicity in the presence of Helium bubbles on graphite immersed in water, was not expected. This led to study the liquid gas-solid interaction. We observed that the HOPG surface had an attractive interaction with bubbles of H_2 and He (gasophilic behaviour) and weaker interaction with air, Ar and N_2 (gasphobic response). The findings show that gasophilic/gasphobic behaviour is related to the polarizability of the gas and of HOPG. Polarizability influences the ratio between the gas–HOPG and gas–gas potential, the χ ratio. A high χ ratio indicates a strong force of interaction at gas-solid interface compared to the effect of gas–gas interaction. Helium shows the lowest captive bubble contact angle and the highest adhesion with HOPG, in relation to the highest value of the χ ratio. Besides the intrinsic properties of HOPG graphite which is an entirely dispersive surface, we investigated the effect of adding polar compounds on the graphite surface. The graphite was modified by oxidizing the surface, creating new functional groups. Oxygen plasma has been used to oxidize the HOPG surface. Polar oxygen-containing groups attached to HOPG surface induced a

significant increase in surface hydrophilicity. The results showed that the epoxy, carbonyl and carboxyl groups created on graphite surface are fundamental to improve the hydrophilicity. We observed too that these functional groups on the surface induced different wetting modes when the surface was immersed in water.

The second part of the dissertation was dedicated to the use of a single layer of graphite, graphene, as water barrier on PDMS. Similarly, to the study of graphite, a detailed study of the interaction of water with PDMS surface in different experimental conditions (in the air and immersed in water) was conducted. The findings show that the air bubbles on graphite surface exhibit a stable behaviour while undergoing on PDMS a dynamic phenomenon. In fact, the air bubble volume on PDMS increased by increasing immersion time in the water. The experimental results indicated that the dynamic evolution of the air bubbles in contact with PDMS was related to the rearrangement of surface polymer chains via the migration of the polar groups. This phenomenon induced a degradation of the surface properties of PDMS when immersed in water. When graphene monolayer was added to PDMS surface, it acted as a barrier against water, suppressing the dynamic evolution of the bubble and preserving the optical transparence and from degradation.

In the last part, we studied the protective properties of graphene-based films deposited on Lead (Pb). We described the effect of water drops and air bubbles in contact with Pb substrates. We observed that Pb surface degradation occurred when Pb was in contact with a drop of water. The surface material was less prone to degradation when it was immersed in water. For this reason, particular interest was focused on the qualitative evaluation of the surface reactivity-degradation using time evolution contact angle and profilometer. The results showed that degradation of Pb surface in contact with water occurred very rapidly, but the graphene-based films were able to significantly reduce degradation of the surface. The best results on fresh samples were obtained with films realised with graphene and graphene oxide, while the membrane realized as a mixture of graphene and graphene oxide showed a defected surface, due to the agglomeration of the graphene flakes. The barrier properties and stability were evaluated after 6 months ageing, and in the case of membranes based on graphene, a reduction of such barrier properties was observed. This was due to the delamination of the graphene layer from the Pb surface while the films based on graphene oxide were more stable upon ageing, indicating that the layer based on graphene oxide is the best candidate to protect Pb surface against differential aeration corrosion induced by water drops.

The study of the interaction of the different kinds of materials with water showed that the degradation of the surface could happen selectively, e,g only when a surface was immersed in water (case of PDMS) or only when a surface was in contact with water drops (case of Pb). The surface

of materials immersed in water showed a behaviour undoubtedly different from water drop in contact with a surface. as observed from the dynamic evolution of the bubbles in contact with PDMS or the behaviour of the gas bubbles with graphite surface. However, independently of the experimental conditions (immersion in water or water contact with the surface), graphene-based materials can be used successfully as barriers against surface degradation induced by water.

Many unclear issues remain unresolved as a precise description of the wetting mode of a surface immersed in water, of the structural change of polymers in contact with water and the role of dissolved CO_2 in all experimental conditions. In any case, we highlight that the interaction of gas bubbles with a surface in water media belongs to the very under-explored scientific field.

It can be underlined that more experiments and computational studies must be done to more deeply understand the behaviour of a bubble in contact with a surface as well as on the use of the 2D materials as a barrier against degradation induced by liquids. In particular, the field of micro- and nanobubbles should be explored, developing new experimental set-up such as in situ AFM to identify in a selective mode the polar groups at the surface or a precise identification of the bubble profile at the micro and nanoscale. We can remark that a deep comprehension of the interactions water and gas with surface could be vital to developing strategies and materials to avoid degradation of surfaces or to avoid embolism in biomedical devices. We believe therefore that the findings of these work can have a significant impact on the protection of historical metal artefacts, in the biomedical field as well as in the development of new microfluidic devices.

List of Publications:

I "Graphene as barrier against the dynamic evolution of air bubbles in contact with PDMS immersed in water". Bartali R. [a,b], Lamberti A. [c], Bianco S. [c], Pirri C. F. [c], Tripathi M., Gottardi G., Micheli V., Speranza G., Pugno N., and Laidani N. [a]
Accepted 10/2017 Langmuir

II "Interaction of the Helium, Hydrogen, Air, Argon, and Nitrogen Bubbles with Graphite Surface in Water." Bartali, R., Otyepka, M., Pykal, M., Lazar, P., Micheli, V., & Gottardi, G. And Laidani N. (2017). *ACS Appl. Mater. Interfaces, 2017, 9 (20), pp 17517–17525 http://doi.org/10.1021/acsami.6b16493*

III "Oxygen plasma treatments of polydimethylsiloxane surfaces: effect of the atomic oxygen on capillary flow in the microchannels."
Ruben Bartali Elisa Morganti;Leandro Lorenzelli;Victor Micheli; Gloria Gottardi ;Marina Scarpa;Mian SafeenRajesh Pandiyan and Nadhira Laidani. *Micro & Nano Letters,5pp. DOI:10.1049/mnl.2017.0230,Online ISSN1750-0443 31 May 2017*

IV "Nanoscale frictional characteristics of few layers graphene over Ni grain and grain boundaries" M. Tripathi[1], F. Awaja[1], G. Paolicelli[2], R. Bartali[1], E. Iacob[1], S. Valeri[3], S. Ryu[4], S. Signetti[5], G. Speranza[1], N. Pugno* [5, 1, 6,] to *Nanoscale, 2016, 8,12, 6646*

V "Effect of glass surface treatments on the deposition of highly transparent reduced graphene oxide films by dropcasting method. "
Van Nguyen, C., Bartali, R., Crema, L., & Speranza, G. (2016). *Colloids and Surfaces A: Physicochemical and Engineering Aspects*, *498*, 231–238. http://doi.org/10.1016/j.colsurfa.2016.03.051

VI "Formation of Mach angle profiles during wet etching of silica and silicon nitride materials."
M. Ghulinyan, M. Bernard , R. Bartali, and G. Pucker , *Applied Surface Science., 2015, 359, 679–686.*

Oral presentations

a) I 23/05/2016 GM-2016 Graphene and related Materials: properties and applications International Conference Paestum, Salerno (Italy),

b) II 02/2015 –Oral presentation, Physics PhD Workshop 2014-2015“ Study of the surface properties of exfoliated highly oriented pyrolytic graphite (HOPG) by means of captive bubble and sessile drop contact angle measurements". .....

Poster presentations

c) Work of adhesion of hydrogen helium argon and nitrogen on highly oriented pyrolitic graphite estimated by means of captive bubble measurements. R. Bartali [1,2], V. Micheli[2], G. Gottardi[2], N. Laidani[2] ” Nanoenergy , Manchester, 02/06/2015 .....

d) Liquid and gas interaction with exfoliated HOPG studied by contact angle measurement R. Bartali [1,2], V. Micheli[2] , G Gottardi[2] , N. Laidani[2,] Nanotechitaly, Venice 27/11/2014 .....

e) c)Surface energy of nano-structurated ZnO films deposited on silicon.Bartali R., Micheli R, Gottardi G.,Speranza G.and Laidani N. PhD Workshop 2014/2015 27/02/20014 .....

Appendix A

Bubble contact angle on Lead

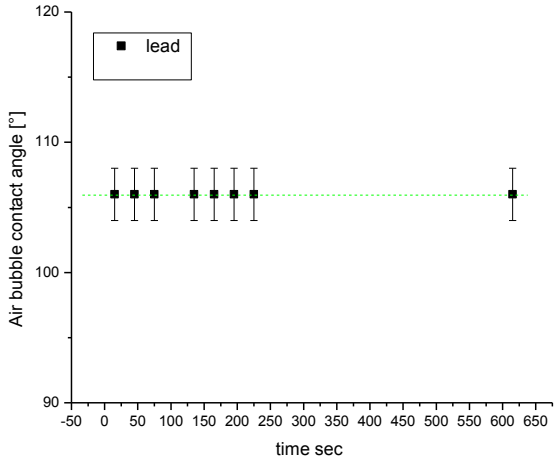

A-1 Bubble contact angle (air) on lead (Pb) immersed in water